A modeling framework for scale-resolving computations of turbulent flow over porous and rough walls

Vom Fachbereich Maschinenbau
an der Technischen Universität Darmstadt
zur
Erlangung des Grades eines Doktor-Ingenieurs (Dr.-Ing.)
genehmigte

D i s s e r t a t i o n

vorgelegt von

Benjamin Elias Krumbein, M.Sc.

aus Frankfurt am Main

Berichterstatter:	Prof. Dr.-Ing. C. Tropea
Mitberichterstatter:	Apl. Prof. Dr.-Ing. S. Jakirlić
	Apl. Prof. Dr. rer. nat. A. Sadiki
Tag der Einreichung:	15.04.2019
Tag der mündlichen Prüfung:	18.06.2019

Darmstadt 2019
D17

Krumbein, Benjamin Elias
A modeling framework for scale-resolving computations of turbulent flow over porous and rough walls
Darmstadt, Technische Universität Darmstadt

Jahr der Veröffentlichung der Dissertation auf TUprints: 2019
URN: urn:nbn:de:tuda-tuprints-88414
Tag der mündlichen Prüfung: 18.06.2019

Abstract

The present work is focused on the development of a modeling framework for scale-resolving simulations of turbulent flow over porous and rough walls. In particular, the investigations and modeling efforts are guided by technical applications involving consequential physical phenomena in the vicinity of rough surfaces. Apart from internal combustion engines, where the near-wall region has been identified as important with respect to the formation of pollutants, turbulent flow over porous or rough walls can be found in a variety of other technical systems as well as the environment.

In order to enable computationally efficient scale-resolving simulations accurately capturing the modification of turbulent flow in the vicinity of rough walls, a RANS-based (RANS: Reynolds-averaged Navier Stokes) sub-scale model and a roughness closure relying on a mathematical framework originating from the field of porous media modeling is proposed. The sub-scale model, termed as eddy-resolving (ER) ζ-f model, is derived on the basis of an elliptic-relaxation RANS model, which is essentially sensitized to resolved turbulent fluctuations by introducing a newly formulated source term motivated by the scale-adaptive simulation concept. With respect to roughness modeling, findings of this study emphasize the importance to consider blockage effects associated with rough surfaces. Consequently, volume-averaged governing equations are applied and a roughness model accounting for the drag roughness elements exert on the flow through a volumetric forcing term in the momentum equation is proposed.

The ER ζ-f model is successfully validated in an extensive computational study. Its high predictive accuracy and computational efficiency is demonstrated by comparison to several sub-scale models from literature. Furthermore, validation results for the proposed roughness model exhibit a high level of qualitative and quantitative agreement with reference data for flow over irregular rough surfaces, both with respect to mean flow and turbulence statistics, as well as predicted friction coefficients.

Kurzfassung

Die vorliegende Arbeit beschäftigt sich mit der Entwicklung von Modellen für die skalenauflösende Simulation turbulenter Strömungen über porösen und rauen Wänden. Die durchgeführten Untersuchungen und die Modellbildung orientieren sich dabei an technischen Anwendungen, bei denen sich wichtige physikalische Prozesse in der Nähe rauer Wände abspielen. Beispielsweise sind hier Verbrennungsmotoren zu nennen, bei denen die wandnahe Region einen entscheidenden Beitrag zur Bildung von Schadstoffen leistet. Darüber hinaus treten turbulente Strömungen über poröse oder raue Wände aber auch in der Umwelt sowie vielen weiteren technischen Systemen auf.

Um den Effekt rauer Wände auf turbulente Strömung im Rahmen von skalenauflösenden Simulationen in einer recheneffizienten Weise abzubilden, wird ein RANS-basiertes (RANS: Reynolds-averaged Navier Stokes) Feinstrukturmodell sowie ein Rauigkeitsmodell entwickelt, das aus einer mathematischen Beschreibungsweise für die Strömung in porösen Medien aufbaut. Das als wirbelauflösendes ζ-f Modell bezeichnete Feinstrukturmodell wird ausgehend von einem auf elliptischer Relaxation basierenden RANS Modell abgeleitet. Ein neuartiger Quellterm, der auf dem Konzept der Skalen-adaptiven Simulation beruht, ermöglicht eine eigenständige Anpassung des Modells an aufgelöste turbulente Fluktuationen. Im Bezug auf die Rauigkeitsmodellierung hat sich im Rahmen dieser Studie gezeigt, dass es wichtig ist die durch raue Oberflächen verursachten Verblockungseffekte zu berücksichtigen. Um diese zu erfassen kommen volumengemittelte Erhaltungsgleichungen zum Einsatz. Der Widerstand, den die Rauigkeit auf die Strömung ausübt wird dabei mithilfe eines Volumenkraftterms in der Impulsgleichung abgebildet.

Das wirbelauflösende ζ-f Modell wurde im Rahmen einer umfangreichen Simulationskampagne erfolgreich validiert. Dabei wurde sowohl die hohe Vorhersagegenauigkeit als auch die Recheneffizienz anhand von Vergleichen mit Feinstrukturmodellen aus der Literatur belegt. Darüber hinaus weisen die mit dem vorgeschlagenen Rauigkeitsmodell gewonnen Ergebnisse für das mittlere Strömungsfeld, Turbulenzintensitäten und Reibungsbeiwerte ein hohes Maß an Übereinstimmung mit Referenzdaten für Strömung über unregelmäßige Rauigkeitsstrukturen auf.

Acknowledgements

First of all I want to express my gratitude to Prof. Dr.-Ing. Cameron Tropea and apl. Prof. Dr.-Ing. Suad Jakirlić for giving me the opportunity to work on this thesis at the Institute for Fluid Mechanics and Aerodynamics of the TU Darmstadt. Particularly, I want to thank my supervisor, Suad Jakirlić, for his valuable advice and encouragement during these last years.

To Dr. Ing. Robert Maduta, I want to express my gratitude for our fruitful discussions on turbulence modeling and his continuous willingness to provide help. I am also grateful to Pourya Forooghi, Ph.D, whose DNS data was invaluable for the present roughness modeling efforts. Furthermore, I would like to thank my former students Vincenzo Termini, Anna Mizobuchi and Michael Ferber for their respective contributions to this work.

Many thanks also go to my former colleagues at the institute for the most pleasant and cooperative atmosphere. In particular, I want to thank Dr.-Ing. Markus Schremb, Dr.-Ing. Matthias Ullrich, Dr.-Ing. Rüdiger Röhrig, Dr.-Ing. Vignesh Thammanna Gurumurthy, Felix Gerlach, Sebastian Wegt and Max Bopp for the enjoyable times and fruitful discussions.

During my time at the institute I also had the great pleasure to work with Dr. rer. nat. Hubert Marschall on exercises and examinations for the lectures on fundamental and advanced fluid mechanics, which was an instructive and very appreciated experience. I would also like to thank Birgit Neuthe for her help in all administrative matters as well as her refreshing sense of humor.

Proofreading by Dr.-Ing. Markus Schremb, Dr.-Ing. Robert Maduta, Dr.-Ing. Matthias Ullrich, Pourya Forooghi, Ph.D. and Dr.-Ing. Daniel Rettenmaier is highly appreciated. Financial support of the German Research Foundation (DFG) in the framework of the Collaborative Research Center/Transregio 150 is gratefully acknowledged. Computations for this work have been performed on the Lichtenberg high performance computer at Technische Universität Darmstadt.

Last but not least, I want to thank my friends and family for their valuable support, kindness and encouragement in the last decades, which essentially rendered this thesis possible in the first place.

Contents

1 Introduction

Turbulent flow over rough surfaces is ubiquitous in many technical systems as well as the environment. In this context, roughness can generally be characterized as high-frequency, small-scale variations in the shape of a surface. With respect to engineering applications, such variations may not only be generated during the manufacturing process, but also throughout the further life cycle of a product, for instance due to erosion, corrosion or deposition processes. Various components of gas turbines and jet engines that are subject to high mechanical and thermal loads are prominent examples, where all of the aforementioned roughness generation mechanisms apply [16, 142]. Further examples include hulls of ships or marine current turbines affected by biofouling [132, 156], components of aircrafts subject to ice accretion [2, 134] as well as undesirable depositions in internal combustion engines [49] and exhaust gas aftertreatment systems. In particular, rough surfaces can affect the performance, safety and efficiency of these systems by increasing friction losses as well as modifying local flow conditions, for instance by triggering laminar-turbulent transition or flow separation. In addition, associated modifications to the flow can have a profound influence on heat transfer characteristics. Finally, in the context of environmental flows, plant and urban canopies in the atmospheric boundary layer are prominent examples of rough surfaces affecting a turbulent flow [9, 30, 31, 41, 92]. In these cases roughness has an impact on meteorological and local climate predictions, for instance with respect to the estimation of wind turbine yields, as well as pollutant dispersion in urban areas.

The effect of roughness on a flow is especially pronounced in the context of turbulent flows. With increasing Reynolds number, the viscous length scale and the boundary layer thickness decrease, thus rendering roughness-related surface features more influential [12]. While turbulence structure modifications associated with smooth walls are nowadays reasonably well understood, the complexity and multitude of realistic

roughness topographies have so far impeded gaining similar levels of insight for turbulent flow over rough walls [42]. Consequently, this subject matter is topic of ongoing research, both with respect to an improved understanding of the relevant physical effects as well as their modeling in the field of computational fluid dynamics (CFD), to which this work aims to contribute.

1.1 Motivation

Enabled by the progress in the field of high-performance computing, CFD is nowadays an indispensable tool in engineering research and development involving fluid flow. In research, validated numerical simulations can facilitate deeper insight into investigated phenomena, due to the availability of spatially and temporally resolved data for all computed physical quantities. With respect to development, CFD is part of the continuing trend towards the virtualization of product development, enabling shorter development cycles as well as cost savings due to reduced prototyping and testing expanses. As a result more complex applications, often involving coupled processes such as heat transfer, multiphase and reactive flow ought to be computed with simultaneously increasing demands in terms of predictive accuracy. In the context of the Collaborative Research Center on "turbulent, chemically reactive, multi-phase flows near walls"[1], which this work is a part of, two guiding examples from the automotive industry involving the aforementioned phenomena have been formulated: internal combustion engines and exhaust gas aftertretmeant systems. In both of these applications, near-wall phenomena have been identified as important. With respect to internal combustion engines it was found that the near-wall region has a profound impact on the formation of pollutants, for instance due to catalytic effects and flame quenching, while in exhaust gas aftertreatment systems based on selective catalytic reduction, wall-films and depositions formed due to the injection of urea solution, can affect the efficiency of the reduction process. In both cases, the turbulent flow in the near wall region is affected by roughness formed predominantly due to deposition processes. Thus, an efficient modeling framework cap-

[1] Collaborative Research Center TRR 150, funded by the German Research Foundation (DFG).

turing the effect of roughness on turbulent flow in the near-wall region is required in order to facilitate CFD computations accounting for the additional coupled processes.

Consequently, the objective of the present work is twofold: firstly, the development and validation of a sub-scale model based on the Reynolds-averaged Navier-Stokes (RANS) concept, enabling computationally more efficient scale-resolving computations of turbulence compared to large eddy simulation (LES), which is often applied in the context of combustion processes, and secondly, the development and validation of a roughness model suitable for scale-resolving computations of turbulence, which accurately captures the effect of roughness on the flow, not only in the outer layer, but also in the directly affected near-wall region.

1.2 Thesis outline

Owing to the aforementioned objectives, a RANS-based scale-resolving turbulence model denoted as eddy-resolving (ER) ζ-f model, relying on the near-wall eddy-viscosity model of Hanjalić *et al.* [59] and the scale-adaptive simulation (SAS) concept of Menter and Egorov [102], is formulated and its performance comparatively assessed. Furthermore, roughness modeling approaches originating in principle from the discrete element method of Taylor *et al.* [147] are evaluated in a data-driven fashion relying on a direct numerical simulation (DNS) data base for open-channel flow over various rough surfaces of Forooghi *et al.* [48]. On that basis, a roughness model based on a reformulation of a drag closure from the field of porous media flow is proposed, which enables a unified computational framework for flow over porous and rough walls. Accordingly, the structure of the present work is as follows:

Chapter 2 summarizes the theoretical background necessary for understanding the physical effects and modeling approaches investigated in this work. After a short review of essential features of turbulent flow, the turbulence modeling frameworks as well as the specific models from literature, employed mainly for a comparative assessment of the results obtained with the ER ζ-f model, are introduced. Specifically, the RANS framework, the concept of LES as well as RANS-based scale-resolving modeling approaches are discussed. Subsequently, the effect of rough-

ness on turbulent flow is reviewed and roughness modeling approaches from literature are classified in order to discuss their advantages and limitations with respect to the present requirements. Finally, a mathematical framework for CFD computations of porous media flow, which relies on the volume averaging technique is introduced, since it provides the foundation for the presently proposed unified modeling approach for flow over porous and rough walls.

Chapter 3 offers an introduction to numerical methods applied in the present work. In particular, the spatial discretization pertinent to the finite-volume method is summarized and the applied interpolation schemes are discussed. The chapter closes with an overview of the applied temporal discretization methods.

Chapter 4 is focused on the formulation and validation of the presently proposed ER ζ-f model. Initially, the ζ-f RANS model is transformed in order to obtain a scale-supplying equation based on the inverse turbulent time scale ω. After a brief validation of the transformed formulation, the model is sensitized to resolved turbulent fluctuations by introducing a source term motivated by the SAS concept in the ω-equation. The ER ζ-f model is subsequently validated on the basis of five generic flow configurations. In addition, computations with a hybrid RANS/LES closure, the VLES model of Chang *et al.* [27], as well as (under-resolved) LES with the dynamic Smagorinsky model of Lilly [94] are performed in order to enable a comparative assessment of the models' performance. Special attention is given to the grid sensitivity of the investigated scale-resolving turbulence models.

Chapter 5 is devoted to roughness modeling in scale-resolving computations of turbulence. Initially, the flow configuration and roughness topographies adopted from the reference DNS of Forooghi *et al.* [48] are introduced. Subsequently, a data-driven methodology making use of the DNS data base is proposed, in order to evaluate a roughness modeling approach relying on a volumetric force term accounting for the viscous and form drag the roughness exerts on the flow. Furthermore, a flow solver based on additionally volume-averaged governing equations for porous media flow is implemented and verified by comparison

with reference DNS data of Breugem *et al.* [21] for turbulent channel flow over porous walls. In addition, the considered scale-resolving turbulence models are adapted for application in the computational framework for porous media flow and their performance is assessed by computing the aforementioned porous channel configuration. The implemented volume-averaged framework enables the comparative evaluation of a second roughness modeling approach, whereby in addition to a volumetric force term, blockage effects are explicitly accounted for in the governing equations. Finally, based on this approach, a porous media model for packed beds is reformulated and calibrated to facilitate the parametrization of a drag closure for rough walls primarily relying on geometrical details of the rough surface.

The present work concludes with Chapter 6, providing a summary of this work as well as suggestions for future investigations and model development.

2 Theoretical background

The following chapter outlines and discusses theoretical aspects necessary for the understanding of physical phenomena and modeling approaches considered in the present work. First, a brief summary of fundamental aspects of fluid mechanics is provided in Section 2.1. For a more comprehensive review, the reader is referred to the textbooks of Batchelor [10] as well as Spurk and Aksel [141]. In Section 2.2 an overview of the phenomenon of turbulence is given, before the various turbulence modeling frameworks considered in this work are discussed. Several turbulence models from literature, which are employed for a comparative assessment of the newly formulated ER ζ-f model are additionally presented in the respective subsections. Subsequently, in Section 2.3, the topic of turbulent flow over rough walls is addressed both in terms of reviewing the effects of roughness on turbulent flows as well as discussing approaches to account for roughness in CFD. The chapter concludes with Section 2.4, where governing equations for a macroscopic description of flow through porous media are presented as basis for the proposed unified modeling framework for flow over porous and rough walls.

2.1 Governing equations of fluid dynamics

Assuming the validity of the continuum hypothesis, the governing equations commonly applied in CFD can be derived from the principal conservation laws of mass, momentum and energy. The resulting equations are formulated based on an Eulerian specification of the flow field, i.e. expressing the relevant physical quantities with respect to locations in space rather than following individual fluid parcels. Various specialized equations suitable for specific types of fluids and/or flow conditions have been derived in the field of fluid mechanics (see e.g. Spurk and Aksel [141]). In the scope of this study, incompressible Newtonian fluids are considered, whose conservation of mass and momentum is described

by the incompressible Navier-Stokes equations. Throughout this work, cartesian index notation for tensors is applied, following the Einstein summation convention. Consequently, the continuity equation implying the conservation of mass, is given by

$$\frac{\partial U_j}{\partial x_j} = 0, \tag{2.1}$$

where U_j represents the velocity components and x_j the spatial coordinates with $j = 1, 2, 3$. Linear momentum is conserved according to

$$\frac{\partial U_i}{\partial t} + U_j \frac{\partial U_i}{\partial x_j} = -\frac{1}{\rho}\frac{\partial P}{\partial x_i} + \frac{\partial}{\partial x_j}\left(\nu \frac{\partial U_i}{\partial x_j}\right), \tag{2.2}$$

where t is the time, ρ the density, P the pressure and ν the kinematic viscosity. Body forces, such as e.g. gravity, are presently not considered.

In case of non-isothermal flow, an equation including the effect of heat transfer in the fluid is necessary to describe the temperature field. Such an equation can be derived in terms of a transport equation for the specific internal energy or enthalpy, based on the principle of energy conservation. Assuming constant fluid properties and neglecting heat generation due to viscous dissipation these equations reduce to a transport equation for the temperature Θ, according to

$$\frac{\partial \Theta}{\partial t} + U_j \frac{\partial \Theta}{\partial x_j} = \frac{\partial}{\partial x_j}\left(\frac{\nu}{\mathrm{Pr}} \frac{\partial \Theta}{\partial x_j}\right), \tag{2.3}$$

where Pr is the dimensionless Prandtl number describing the ratio of viscous to thermal diffusion for a given fluid.

Another important dimensionless quantity in fluid dynamics is the Reynolds number Re, which can be regarded as the ratio of inertial forces to viscous forces. It is defined in terms of problem-specific characteristic velocity and length scales of the flow, denoted as $\mathcal{U}$ and $\mathcal{L}$, respectively:

$$\mathrm{Re} = \frac{\mathcal{U}\mathcal{L}}{\nu}. \tag{2.4}$$

If the Reynolds number of a flow is increased, e.g. by increasing the flow rate in a pipe, at a certain threshold – the critical Reynolds number – seemingly chaotic fluctuations in the flow field arise. This phenomenon

termed *turbulence* is rather the rule then the exception in technical and environmental flows and will be discussed in more detail in the following section.

2.2 Turbulence and associated modeling approaches

Due to its importance for many technical applications, the phenomenon of turbulence has been studied extensively for more than a century. Still, many aspects are not fully understood and no analytical theory fully describing turbulent flows has been found so far. Consequently, turbulence models relying on empirical observations of turbulent flows will most likely remain the state-of-the-art approach for predicting turbulent flow behavior in the foreseeable future.

Some of the difficulties in finding a complete analytical description of turbulence are apparent from the general characteristics of turbulence itself, which have been summarized e.g. by Tennekes and Lumley [148]. One key issue is the inherent irregularity of turbulent flow fields in both space and time, which Pope [118] refers to as "the random nature of turbulence": although the Navier-Stokes equations are deterministic, turbulence is highly sensitive to perturbations in initial and boundary conditions as well as material properties [118], which makes anything but a statistical description difficult. Other general characteristics of turbulence include its diffusive character, which is associated with enhanced momentum and heat transfer compared to laminar flow, the inherent three-dimensional character of turbulent structures and the dissipative nature of turbulence itself [148]. Another important characteristic of turbulence, which is especially challenging with respect to the direct solution of the Navier-Stokes equations, is the broad range of length and time scales associated with turbulent flows. In terms of spatial extent, the largest scales of turbulent motion are primarily determined by the geometry of the flow configuration (i.e. they are in the order of e.g. pipe diameter or channel height), while the smallest scales, according to Kolmogorov's [74] hypothesis, depend on the rate of energy received from larger scales as well as viscosity. The intermediary process of energy transfer to smaller scales is referred to as the *energy*

cascade introduced by Richardson [124].

The energy cascade and turbulent scales

The energy cascade is based on the assumption, that a turbulent flow field can be considered as being composed of superimposed *eddies* of different scales. By means of a spectral view point, the energy content of eddies at a certain wavenumber κ can be described by the energy spectrum $E(\kappa)$, which is qualitatively shown in Fig. 2.1. The energy

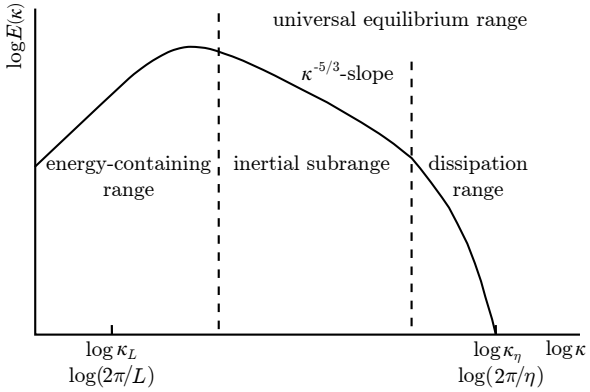

Figure 2.1: Qualitative model spectrum $E(\kappa)$ of turbulent kinetic energy.

contained throughout the entire spectrum is the *turbulent kinetic energy* (TKE)

$$k = \int_0^\infty E(\kappa)\,\mathrm{d}\kappa. \tag{2.5}$$

TKE is drawn from the energy of the mean flow through various production mechanisms of turbulence (i.e. due to mean shear or body forces, see e.g. Hanjalić and Launder [57]). This energy is then supplied into the cascade at low wavenumbers associated with the so-called *energy-containing range*. As the name suggests, most of the turbulent kinetic energy is carried by the large eddies in this wavenumber range, which are characterized by the length scale $L \sim k^{3/2}/\varepsilon$ referred to as *turbulent*

length scale throughout this work. Here ε is the dissipation rate of TKE and thus describes the rate at which TKE is dissipated into heat due to viscous effects.

At sufficiently high Reynolds numbers, the energy supplied to the large eddies exceeds the rate at which TKE can be dissipated due to viscous action on these large scales. Thus, in the so-called *inertial subrange* associated with the characteristic $\kappa^{5/3}$-slope (see Fig. 2.1), larger eddies break up, transferring their energy to smaller and smaller scales primarily by means of inertia effects. This process continues until viscous effects play a decisive role, i.e. the characteristic Reynolds number of the small scales is $\mathrm{Re} \approx 1$ [118]. This is the case in the so-called *dissipation range* and the associated characteristic length, time as well as velocity scales describing the smallest turbulent eddies have been determined by Kolmogorov [74] as

$$\eta = \left(\frac{\nu^3}{\varepsilon}\right)^{1/4}, \quad \tau_\eta = \left(\frac{\nu}{\varepsilon}\right)^{1/2} \text{and} \quad u_\eta = (\varepsilon\nu)^{1/4}, \tag{2.6}$$

respectively. While the large scales in the energy-containing range are affected by the boundary conditions of the flow and consequently exhibit a non-universal and anisotropic character [118], Kolmogorov [74] hypothesized further, that smaller scales formed in the energy cascade process tend to a statistically isotropic state and that the statistics of the scales in the inertial and dissipation range obey a universal form. Thus, inertial and dissipation range together are also referred to as *universal equilibrium range*.

The former of these hypothesis, the concept of *local isotropy*, is a widely employed assumption in turbulence modeling [57]. Especially in the context of this study, where low to moderate Reynolds numbers are considered, it is however important to note that all of Kolmogorov's hypotheses associated with the energy cascade were postulated for a "sufficiently large Reynolds number" [74]. An important consequence of moderate Reynolds numbers is evident from the ratio of the length scales of the small scales η to the scale of the energy containing eddies L, which can be estimated [118] as

$$\frac{\eta}{L} \sim \mathrm{Re}^{-3/4}. \tag{2.7}$$

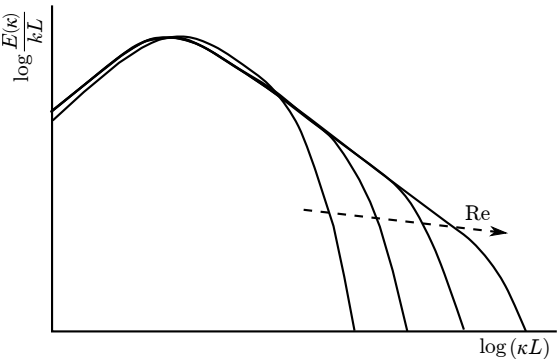

Figure 2.2: Schematic illustration of the Reynolds number dependence of a model spectrum, scaled with TKE k and length scale of energy containing eddies L. Adapted from Pope [118].

Since L remains on the order of the geometrical scale of the flow configuration, a smaller ratio in Eq. (2.7) is associated with a larger η and consequently smaller wavenumbers of the smallest eddies. This notion is reinforced by Fig. 2.2 illustrating model spectra for various Reynolds numbers scaled with the TKE k and the length scale of the energy containing eddies L. Evidently, the energy containing range remains similar, while the extent of the universal equilibrium range grows considerably. This is commonly referred to as increasing *scale separation* – or at low Reynolds number a lack thereof – and is a further important modeling assumption especially in scale-resolving modeling approaches such as LES (see Section 2.2.2).

Near-wall turbulence

Most flows in engineering and the environment are bounded by walls. Due to the no-slip condition inherently enforced by solid walls, viscous effects tend to play an increasingly important role in their vicinity. Furthermore, in addition to viscous damping, impermeable walls directly dampen wall-normal velocity fluctuations due to the reflection of pressure fluctuations, resulting in a strongly non-isotropic state of turbulence [57].

Nevertheless, for many flows, such as fully-developed channel flow, a universal scaling of the mean velocity profile near walls can be introduced based on the so-called *wall friction velocity* defined as

$$u_\tau = \sqrt{\frac{\tau_\mathrm{w}}{\rho}}, \tag{2.8}$$

with the wall shear stress τ_w [118]. The appropriate length scale is the viscous length $\delta_\nu = \nu/u_\tau$. The respective non-dimensional wall distance in this so-called *inner scaling* is consequently given by $y^+ = y/\delta_\nu = yu_\tau/\nu$, while the non-dimensional mean streamwise velocity is obtained from $U^+ = \overline{U}_x/u_\tau$. Here y stands for the wall distance and $\overline{U}_x$ is the time-averaged streamwise velocity. Furthermore, it is at this point convenient to introduce the *friction Reynolds number*

$$\mathrm{Re}_\tau = \frac{u_\tau \mathcal{L}}{\nu}, \tag{2.9}$$

based on the wall friction velocity u_τ and a characteristic length scale $\mathcal{L}$ of the flow, e.g. the half-channel height in channel flow or the radius in pipe flow.

The characteristic velocity profile in inner scaling is illustrated by Fig. 2.3 in terms of DNS data of Moser *et al.* [108] for fully-developed plane channel flow at a friction Reynolds number of $\mathrm{Re}_\tau = 392$. In addition, the linear law describing the velocity profile in the viscosity dominated *viscous sublayer* ($y^+ < 5$) as well as the logarithmic law for the turbulence dominated *log-law region* ($y^+ > 30$) are shown. In the intermediate *buffer region* ($5 < y^+ < 30$) both viscous and turbulent effects contribute in a comparable manner. The expressions for the viscous sublayer and the log-law region introduced by von Kármán [155] are commonly referred to as the *law of the wall* and are given by

$$U^+ = \begin{cases} y^+ & \text{for } y^+ < 5, \\ \frac{1}{\kappa} \ln y^+ + B & \text{for } y^+ > 30. \end{cases} \tag{2.10}$$

The values of B and the Kármán constant κ slightly vary in literature depending on the data set used for their estimation. In the present study the values of $\kappa = 0.41$ and $B = 5.2$ are adopted, which provide a good fit to channel flow data in the presently considered Reynolds number range.

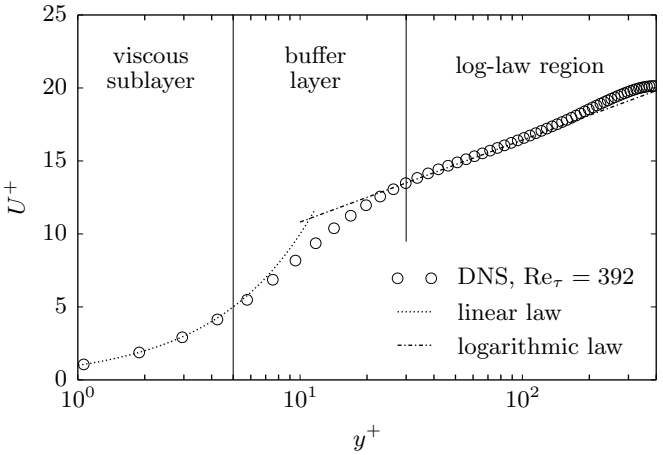

Figure 2.3: Mean velocity profile of fully-developed plane channel flow at $\mathrm{Re}_\tau = 392$ in inner scaling in comparison to the law of the wall. DNS data taken from Moser *et al.* [108].

Turbulence modeling

In principal, the Navier-Stokes equations (2.1) and (2.2) can be solved directly without any turbulence model. For such a *direct numerical simulation* (DNS) it is however necessary to fully resolve the turbulent spectrum down to the Kolmogorov scales (2.6). In addition, based on the length scale ratio given by Eq. (2.7), it is evident that the necessary spatial resolution for a turbulent, and hence three-dimensional flow field, scales with $\mathrm{Re}^{9/4}$. Therefore, DNS is unsuitable for most engineering purposes due to the immense computational costs associated with this approach. Nevertheless, DNS is superior in terms of accuracy and has proven to be a very valuable tool in academic research, that is nowadays applied to increasingly complex flow configurations, such as e.g. model combustion engines [131], thanks to the ever growing capabilities of high performance computers.

In the following sections three approaches to turbulence modeling and the specific models from literature applied as reference in this study are

introduced. The modeling approaches differ primarily in how much of the spectral content of turbulence is resolved in the computed flow field. As will be discussed, they consequently also differ in terms of accuracy, computational cost as well as their applicability to certain types of flow.

2.2.1 Reynolds-averaged Navier-Stokes

In contrast to DNS, where the spectral content of turbulence is fully resolved, in the RANS framework the turbulent spectrum is fully modeled. Consequently, an arbitrary fluctuating quantity Φ is decomposed following Reynolds [123] in its time-averaged part $\overline{\Phi}$ and its fluctuating part ϕ' according to

$$\Phi(x_i, t) = \overline{\Phi}(x_i) + \phi'(x_i, t). \tag{2.11}$$

After insertion of the accordingly decomposed velocity, pressure and temperature fields into Eqs. (2.1), (2.2) and (2.3), subsequent averaging of the equations leads to the RANS equations describing the mean flow field, given by

$$\frac{\partial \overline{U}_j}{\partial x_j} = 0, \tag{2.12}$$

$$\frac{\partial \overline{U}_i}{\partial t} + \overline{U}_j \frac{\partial \overline{U}_i}{\partial x_j} = -\frac{1}{\rho}\frac{\partial \overline{P}}{\partial x_i} + \frac{\partial}{\partial x_j}\left(\nu \frac{\partial \overline{U}_i}{\partial x_j}\right) - \frac{\partial}{\partial x_j}\left(\overline{u_i' u_j'}\right) \tag{2.13}$$

and

$$\frac{\partial \overline{\Theta}}{\partial t} + \overline{U}_j \frac{\partial \overline{\Theta}}{\partial x_j} = \frac{\partial}{\partial x_j}\left(\frac{\nu}{\mathrm{Pr}} \frac{\partial \overline{\Theta}}{\partial x_j}\right) - \frac{\partial}{\partial x_j}\left(\overline{u_j' \theta'}\right). \tag{2.14}$$

It should be noted at this point that the temporal derivative of the time-averaged velocity and temperature actually vanishes. However, in case of time-varying boundary conditions or otherwise globally unstable flows, the $\overline{(\cdot)}$ operator associated with time averaging can be interpreted straightforwardly in a mathematical sense as a time-dependent ensemble average in order to facilitate unsteady RANS (URANS) computations. Thus, the temporal derivative is kept here for a more general description. The last term in Eq. (2.13) stems from the averaging of the non-linear advective term and represents the components of the *Reynolds-stress tensor*. It consists of correlations of unknown velocity fluctuations and

thus has to be modeled. Similarly, the last term in Eq. (2.14) representing the *turbulent heat fluxes* has to be modeled since it additionally contains the unknown temperature fluctuations θ'.

While the Reynolds-stresses can be modeled directly with second-moment closure strategies (see Hanjalić and Launder [57] for an overview), in this study solely models based on Boussinesq's [17] *eddy-viscosity* hypothesis are applied. In this case, the Reynolds stresses are modeled in analogy to viscous stresses as linearly proportional to the rate of strain tensor

$$\overline{S}_{ij} = \frac{1}{2}\left(\frac{\partial \overline{U}_i}{\partial x_j} + \frac{\partial \overline{U}_j}{\partial x_i}\right), \tag{2.15}$$

leading to

$$\overline{u_i' u_j'} = -2\,\nu_\mathrm{t}\overline{S}_{ij} + \frac{2}{3}k\delta_{ij}. \tag{2.16}$$

Here, $k(=1/2\,\overline{u_i' u_i'})$ is the turbulent kinetic energy and δ_{ij} the Kronecker delta. Applying this formulation, the modeling effort reduces to the scalar field ν_t, which is to be predicted by an appropriate *eddy-viscosity model* (EVM). In this framework, the turbulent heat fluxes are conveniently modeled in terms of the eddy-viscosity ν_t by introducing the turbulent Prandtl number Pr_t in analogy to its molecular counterpart. Assuming that turbulent heat fluxes are aligned with the gradient of the mean temperature, the simple gradient diffusion hypothesis (SGDH) can be applied, yielding

$$\overline{u_j'\theta'} = -\frac{\nu_\mathrm{t}}{\mathrm{Pr}_\mathrm{t}}\frac{\partial \overline{\Theta}}{\partial x_j}. \tag{2.17}$$

The turbulent Prandlt number is commonly assumed to be constant and close to unity, which would correspond to the Reynolds analogy [73]. In this study $\mathrm{Pr}_\mathrm{t} = 1$ is assumed for RANS computations.

The RANS framework presently remains the prevalent methodology for simulating turbulent flow for practical engineering applications, mainly due to the manageable computational costs associated with this approach. This advantage can be attributed to relatively low spatial resolution requirements, the possibility to take advantage of symmetries in the mean flow and especially to the fact that time marching is not required for steady computations, while comparatively large time

steps can be applied in URANS simulations. In terms of predictive capabilities, RANS models are considered to be less accurate compared to scale-resolving simulations. While this is a relatively broad statement that may not be universally true, fact is that RANS models rely to a large extent on modeling assumptions as well as calibrated model coefficients. Thus, RANS models are certainly less universal in terms of their applicability to different types of flows, which is well documented throughout literature. Consequently, many RANS models have been proposed, with the most notable examples in terms of popularity being models based on Launder and Spalding's [89] k-ε model as well as Menter's [100] k-ω-SST model. Since the focus of this study is on scale-resolving simulations, only the RANS model underlying the presently proposed RANS-based scale-resolving model is discussed in the following.

Ellipic relaxation ζ-f model

The ζ-f model of Hanjalić *et al.* [59] is a numerically more robust version of Durbin's [39] $\overline{v'^2}$-f model, which pioneered the elliptic relaxation concept for near-wall EVMs. The key element of these models is the application of a different velocity scale in the formulation of the eddy-viscosity: the square root of the wall-normal Reynolds stress $\sqrt{\overline{v'^2}}$ is employed instead of the classical isotropic velocity scale $\sqrt{k}$. Following this approach, the introduction of additional empirical damping functions found in most low Reynolds number RANS models, which compensate for anisotropy effects in the near-wall region, can be avoided.

The model comprises standard transport equations for turbulent kinetic energy k and its dissipation rate ε given by

$$\frac{\partial k}{\partial t} + \overline{U}_j \frac{\partial k}{\partial x_j} = P_k - \varepsilon + \frac{\partial}{\partial x_j}\left[\left(\nu + \frac{\nu_\mathrm{t}}{\sigma_k}\right)\frac{\partial k}{\partial x_j}\right], \tag{2.18}$$

with the production rate $P_k = 2\nu_\mathrm{t}\overline{S}_{ij}\overline{S}_{ij}$, and

$$\frac{\partial \varepsilon}{\partial t} + \overline{U}_j \frac{\partial \varepsilon}{\partial x_j} = \frac{1}{T}\left(C_{\varepsilon 1} P_k - C_{\varepsilon 2}\varepsilon\right) + \frac{\partial}{\partial x_j}\left[\left(\nu + \frac{\nu_\mathrm{t}}{\sigma_\varepsilon}\right)\frac{\partial \varepsilon}{\partial x_j}\right]. \tag{2.19}$$

In order to obtain the velocity scale based on the wall-normal velocity fluctuations, a transport equation for the variable $\zeta = \overline{v'^2}/k$ is solved.

This variable was chosen by Hanjalić *et al.* [59] due to the computationally more robust asymptotic wall behavior of the associated elliptic function f in comparison to Durbin's [39] original model based on an equation for $\overline{v'^2}$. The model equation reads

$$\frac{\partial \zeta}{\partial t} + \overline{U}_j \frac{\partial \zeta}{\partial x_j} = f - \frac{\zeta}{k} P_k + \frac{\partial}{\partial x_j} \left[\left(\nu + \frac{\nu_\mathrm{t}}{\sigma_\zeta} \right) \frac{\partial \zeta}{\partial x_j} \right], \tag{2.20}$$

where the elliptic function f models the redistribution (i.e. pressure-velocity correlation) and anisotropic dissipation terms [39]. The function f is determined based on an elliptic relaxation equation given by

$$L^2 \frac{\partial^2 f}{\partial x_j \partial x_j} - f = \frac{1}{T} \left(C_1 + C_2 \frac{P_k}{\varepsilon} \right) \left(\zeta - \frac{2}{3} \right), \tag{2.21}$$

with the time and length scale switches

$$T = \max \left[\min \left(\frac{k}{\varepsilon}, \frac{a}{\sqrt{6} C_\mu^\zeta |\overline{S}| \zeta} \right), C_\tau \left(\frac{\nu}{\varepsilon} \right)^{1/2} \right] \tag{2.22}$$

and

$$L = C_L \max \left[\min \left(\frac{k^{3/2}}{\varepsilon}, \frac{k^{1/2}}{\sqrt{6} C_\mu^\zeta |\overline{S}| \zeta} \right), C_\eta \left(\frac{\nu^3}{\varepsilon} \right)^{1/4} \right]. \tag{2.23}$$

Finally, the eddy viscosity is computed based on the anisotropic velocity scale as

$$\nu_\mathrm{t} = C_\mu^\zeta \zeta k T. \tag{2.24}$$

All model coefficients are summarized in Tab. 2.1

In simulations performed with the ζ-f model in the scope of this work, Eq. (2.21) was solved for a variable f_t, with the boundary condition $f_{\mathrm{t,w}} = 0$ and f was subsequently obtained from

$$f = f_\mathrm{t} - \frac{2\nu\zeta}{y^2}, \tag{2.25}$$

with the wall distance y, according to the proposal by Hanjalić *et al.* [59].

Table 2.1: Model coefficients in the ζ-f RANS model.

a	C_τ	C_L	C_η
0.6	6.0	0.36	85

C_μ^ζ	C_{ε_1}	C_{ε_2}	C_1	C_2	σ_k	σ_ε	σ_ζ
0.22	$1.4\,(1+0.012/\zeta)$	1.9	0.4	0.65	1	1.3	1.2

2.2.2 Large eddy simulation

The concept of LES is based on the idea to resolve the large energy containing eddies affected by the geometry of the flow and model the remaining, ideally more universal, smaller scales. Thus, a cut-off wavenumber far in the inertial subrange (see Fig. 2.1) is assumed and a low-pass spatial filtering operation is applied to the respective flow fields, represented here by an arbitrary quantity Φ. This leads to the decomposition proposed by Leonard [90]

$$\Phi(x_i,t) = \widetilde{\Phi}(x_i,t) + \phi''(x_i,t), \tag{2.26}$$

with the filtered quantity $\widetilde{\Phi}$ and the unresolved *subgrid-scale* (SGS) contribution ϕ''. After inserting the accordingly decomposed velocity, pressure and temperature fields into Eqs. (2.1) – (2.3), a subsequent filtering of the equations leads to

$$\frac{\partial \widetilde{U}_j}{\partial x_j} = 0, \tag{2.27}$$

$$\frac{\partial \widetilde{U}_i}{\partial t} + \widetilde{U}_j \frac{\partial \widetilde{U}_i}{\partial x_j} = -\frac{1}{\rho}\frac{\partial \widetilde{P}}{\partial x_i} + \frac{\partial}{\partial x_j}\left(\nu \frac{\partial \widetilde{U}_i}{\partial x_j}\right) - \frac{\partial \tau_{ij}}{\partial x_j} \tag{2.28}$$

and

$$\frac{\partial \widetilde{\Theta}}{\partial t} + \widetilde{U}_j \frac{\partial \widetilde{\Theta}}{\partial x_j} = \frac{\partial}{\partial x_j}\left(\frac{\nu}{\mathrm{Pr}} \frac{\partial \widetilde{\Theta}}{\partial x_j}\right) - \frac{\partial q_j}{\partial x_j}, \tag{2.29}$$

with the SGS tensor τ_{ij} and the SGS turbulent heat fluxes q_j describing the influence of the unresolved velocity and temperature fluctuations on

the resolved flow field, defined as

$$\tau_{ij} = \widetilde{U_i U_j} - \widetilde{U}_i \widetilde{U}_j \tag{2.30}$$

and

$$q_j = \widetilde{\Theta U_j} - \widetilde{\Theta}\widetilde{U}_j, \tag{2.31}$$

respectively. In analogy to the Reynolds stress tensor in the RANS framework, the SGS tensor is modeled based on Boussinesq's [17] eddy-viscosity concept as

$$\tau_{ij} = -2\,\nu_\mathrm{t}\widetilde{S}_{ij} + \frac{1}{3}\tau_{kk}\delta_{ij}, \tag{2.32}$$

with the strain-rate tensor $\widetilde{S}_{ij}$ of the resolved flow field and the SGS eddy-viscosity, which is denoted here as ν_t for consistency, while in LES literature usually ν_sgs is used. Again in analogy to the RANS framework, the SGS heat fluxes are modeled with the SGDH as

$$q_j = -\frac{\nu_\mathrm{t}}{\mathrm{Pr}_\mathrm{t}}\frac{\partial\widetilde{\Theta}}{\partial x_j}, \tag{2.33}$$

where the turbulent Prandtl number is set to $\mathrm{Pr}_\mathrm{t} = 0.6$ for all scale-resolving simulations in this study.

Especially in flows where unsteady large scale motions play an important role, models in the LES framework generally provide more accurate results compared to (U)RANS models; not only for higher statistical moments but even for quantities associated with the mean flow. Furthermore, resolving large portions of the turbulent spectrum in the resolved flow field can be beneficial per se in many cases. This includes areas, where instantaneous data with a broad frequency content is of interest, which can simply not be accurately provided by classical URANS models. Specific examples include cases where unsteady forces or thermal loads have to be captured as well as aeroacoustic applications. Another area where LES is advantageous, are applications where additional physical phenomena interact with a turbulent flow, whether it be fluid-structure interaction, chemical reactions or multiphase flows. In such cases – and even if only mean quantities are of interest – a direct coupling with additional model equations through resolved instantaneous flow data is often beneficial compared to the RANS

framework where only mean velocity and e.g. TKE can be provided to the additional model equations.

The benefits of LES in terms of predictive capabilities, come at the price of significantly higher computational costs compared to the RANS framework. This can be attributed to requirements regarding the computational grid, which for a well-resolved LES should, according to Pope [118], be fine enough to resolve 80% of TKE at every location in the computational domain. Similarly, resolution requirements with respect to the temporal discretization necessitate sufficiently small time steps in order to accurately capture the dynamics of resolved turbulent structures. Additionally, it is often required to compute relatively large spans of physical time, e.g. multiple flow through time, to obtain converged mean flow quantities through online averaging of the filtered flow fields.

Another point that should be mentioned here, is that LES is more sensitive to the numerical discretization with its associated errors (e.g. numerical diffusion, commutation and truncation errors, see [50, 127]) compared to RANS models. Such influences are difficult to quantify, highly dependent on the applied grid as well as numerical code and are thus seldom characterized for practical LES computations. However, best practice guidelines alleviating some of these concerns can be readily found in LES literature (e.g. [50, 118, 127]), with the most important being certainly the application of centered high order schemes to limit numerical diffusion as well as the avoidance of grids with high aspect ratio cells or steep gradings, which may introduce truncation errors.

A vast amount of SGS closure models have been proposed in the last decades. Since the LES computations in this work are primarily performed in order to facilitate a comparative assessment of the results obtained with scale-resolving models based on the RANS framework, the likely most frequently applied SGS model, the dynamic Smagorinsky model, is adopted as a representative for the LES framework. This choice is in line with the findings of Röhrig [125], who compared the performance of various SGS models in OpenFOAM, including the dynamic Smagorinsky model, and found “only marginal impact” [125] on turbulent statistics.

Dynamic Smagorinsky model

The dynamic Smagorinsky model is based on the pioneering work of Smagorinsky [137] who first proposed LES with an eddy-viscosity-based SGS model in the context of meteorological applications. In the classical Smagorinsky model, the SGS eddy-viscosity is expressed as

$$\nu_\mathrm{t} = C_S^2 \Delta^2 \widetilde{S}, \tag{2.34}$$

with the filter width Δ, which is conventionally assumed to correspond to the cube root of the cell volume ($\Delta = (\Delta_x \Delta_y \Delta_z)^{1/3}$), and the following norm of the strain-rate tensor of the resolved velocity field:

$$\widetilde{S} = \sqrt{2 \widetilde{S}_{ij} \widetilde{S}_{ij}}. \tag{2.35}$$

One key issue of this simple algebraic model is the constant C_S, which would have to assume different values depending on the considered flow regime and notable also in the vicinity of walls [118]. In practice, researchers found, based on a posteriori analyses, that values in the range $C_S = 0.065...0.24$ have to be applied, which is even more problematic considering that actually the square of the constant is used [50].

In order to overcome this limitation, Germano *et al.* [52] proposed a dynamic procedure to determine an appropriate local value of C_S, which was later modified by Lilly [94]. Essentially, an additional test filter with a larger filter width $\hat{\Delta}$ (here $\hat{\Delta} = 2\Delta$) is introduced, which is denoted by the operator $\widehat{(\cdot)}$. Using a self-consistency criterion in the form of the Germano identity, which relates the SGS stresses on the two filter levels to the fraction of the stresses resolved by the grid but not by the test filter, i.e. the smallest resolved scales, Germano *et al.* [52] obtained

$$L_{ij} = \left(\widehat{\widetilde{U_i U_j}} - \widehat{\widetilde{U}_i} \widehat{\widetilde{U}_j} \right) - \left(\widehat{\widetilde{U_i U_j} - \widetilde{U}_i \widetilde{U}_j} \right) = \widehat{\widetilde{U}_i \widetilde{U}_j} - \widehat{\widetilde{U}_i} \widehat{\widetilde{U}_j}. \tag{2.36}$$

The right-hand side of Eq. (2.36) can be calculated directly based on the resolved velocity field through the explicit test-filtering operation. By modeling the SGS stresses in the middle part of Eq. (2.36) with the Smagorinsky model, an overdetermined set of equations for the constant

C_S is obtained. Lilly [94] proposed to determine C_S in a least-squares sense as

$$C_S^2 = -\frac{1}{2}\frac{L_{ij}M_{ij}}{M_{kl}M_{kl}} \tag{2.37}$$

with the modeled part based on the resolved velocity field

$$M_{ij} = \hat{\Delta}^2\widehat{\widetilde{S}\widetilde{S}}_{ij} - \Delta^2\widehat{\widetilde{S}\widetilde{S}_{ij}}. \tag{2.38}$$

Finally, ν_t can be calculated by supplying the now dynamically estimated Smagorinsky coefficient into Eq. (2.34). One drawback of the dynamic procedure is that large negative values for C_S can occur, leading to a negative eddy-viscosity. While negative values of ν_t can be physically explained by backscatter phenomena, i.e. energy transfer from small to large scales, this can lead to severe numerical instabilities [40]. Thus, in this work, the eddy-viscosity is bound to values $\nu_\mathrm{t} \leq -\nu$ so that an effective viscosity $\nu_\mathrm{eff} = \nu + \nu_\mathrm{t} \geq 0$ is ensured.

2.2.3 RANS-based scale-resolving models

As discussed in more detail in Section 2.2.2, on the one hand the scale-resolving properties of LES are advantageous in many applications, but on the other hand LES is associated with relatively prohibitive computational costs for many practical applications, whether it may be due to high Reynolds numbers, large computational domains or long spans of physical time to cover. Consequently, the goal of any RANS-based scale-resolving modeling approach is to reduce the computational effort compared to an LES with similar accuracy, while gaining at least partly the benefits associated with scale-resolving simulations.

It is at this point important to emphasize that structurally the URANS Eqs. (2.12) – (2.14) are identical to the LES Eqs. (2.27) – (2.29) derived with a filtering operation. Since, as Menter *et al.* [103] put it, the equations retain "no memory of their derivation" [103], the only difference stems from the model applied to the unclosed turbulence related terms. In other words, the ensemble-averaging in the URANS framework or the filtering in the LES framework is generally not explicitly performed but rather a result of the applied model for the Reynolds or SGS stresses. Consequently, there is a common basis enabling the combination of scale-resolving and RANS-based modeling approaches (see

e.g. Chaouat [29] for a theoretical formalism aiming to unify RANS and LES methods). For ease of notation, no additional decomposition operator for RANS-based scale-resolving modeling approaches is introduced. Instead, Eqs. (2.27) – (2.33) and the notation used for LES is adopted. In this generalized formulation, the filtered ($\widetilde{\Phi}$) and the SGS contributions (ϕ'') can be straightforwardly interpreted as simply resolved and unresolved contributions to Φ independent of whether ensemble-averaging or filtering is used in the derivation of the respective model.

Many RANS-based scale-resolving models have been proposed which differ greatly both with respect to their applicability to certain types of flow as well as the employed modeling strategies. Reviews can be found e.g. in Sagaut *et al.* [128], Fröhlich and von Terzi [51] as well as Chaouat [29]. Fröhlich and von Terzi [51] further proposed a comprehensive classification of different strategies to RANS-based scale-resolving modeling, which is adopted here for further discussions:

- In **segregated LES/RANS** strategies, often also referred to as *embedded LES*, the computational domain is split into pure RANS and LES regions. In these respective subdomains classical RANS or SGS models are applied. Coupling is achieved through appropriate boundary conditions, e.g. synthetic turbulence generators for the inlets of LES regions. As a result, the resolved flow field is not continuous at the interface between subdomains.

- **Unified LES/RANS** strategies on the other hand aim to compute the flow field with one global set of momentum equations resulting in a continuous resolved velocity field. This category can be further divided into approaches based on *interfacing LES and RANS*, i.e. switching from LES to RANS modes at defined spatial locations, as well as *blending LES and RANS*, i.e. smoothly transitioning between both frameworks, for instance based on the local grid resolution. As the most prominent example of interfacing LES/RANS, and likely hybrid RANS/LES approaches in general, detached eddy simulation (DES) and delayed DES (DDES) proposed by Spalart *et al.* [138, 139] shall be mentioned. Similar to SGS models in the LES framework, approaches in this category rely on an additional length scale Δ related to the numerical grid.

- In contrast, **second-generation URANS (2G-URANS)** models, also referred to as *sensitized RANS*, rely on physical length scales independent of the numerical grid. Instead, these models are generally based on modifications to the scale-supplying equation enabling the adaption to resolved turbulent fluctuations. Examples for this category are the partially-averaged Navier-Stokes (PANS) concept of Girimaji [53] as well as the scale-adaptive simulation (SAS) concept of Menter *et al.* [103].

As will be discussed in Chapter 4, seamless hybrid approaches based on blending LES and RANS as well as 2G-URANS models appear to be the most suitable choices for the presently developed turbulence and roughness modeling framework for near-wall reactive flow applications. In the following the very large eddy simulation model, which is based on blending LES and RANS is discussed, while a newly formulated 2G-URANS model based on the SAS concept is presented in Chapter 4.2.

Very large eddy simulation

The very large eddy simulation (VLES) model was proposed in Chang *et al.* [27] and later in Chang [26] specifically for flow configurations relevant to internal combustion engines and is thus considered as well suited for the present work. Suppression of the modeled turbulence towards a sub-scale level is achieved, in line with the proposal of Speziale [140], who suggested a direct damping of the Reynolds stress tensor with a grid-spacing-dependent resolution function. Chang *et al.* [27] however applied an EVM, enabling a direct damping of the eddy viscosity according to

$$\nu_\mathrm{t} = F_\mathrm{r}(\Delta)\nu_\mathrm{t}^\mathrm{RANS}, \tag{2.39}$$

where $F_\mathrm{r}(\Delta)$ is the resolution function, depending on a length scale Δ associated with the numerical grid and $\nu_\mathrm{t}^\mathrm{RANS}$ the eddy viscosity predicted by the background RANS model based on the unsteady velocity field. This implies an automatic reduction of the fully-modeled RANS turbulence towards the respective residual scales by interplaying with the local grid resolution. The underlying EVM is based on Hanjalić's [59] ζ-f model, which was already discussed in Section 2.2.1. In order to emphasize the difference between RANS quantities and the respective intermediary quantities based on the unsteady (us) flow field in the

VLES framework, the subscript $(\cdot)_{\mathrm{us}}$ is introduced. The model equations then read

$$\frac{\partial k_{\mathrm{us}}}{\partial t} + \widetilde{U}_j \frac{\partial k_{\mathrm{us}}}{\partial x_j} = P_k - \varepsilon_{\mathrm{us}} + \frac{\partial}{\partial x_j}\left[\left(\nu + \frac{\nu_{\mathrm{t}}}{\sigma_k}\right)\frac{\partial k_{\mathrm{us}}}{\partial x_j}\right], \tag{2.40}$$

$$\frac{\partial \varepsilon_{\mathrm{us}}}{\partial t} + \widetilde{U}_j \frac{\partial \varepsilon_{\mathrm{us}}}{\partial x_j} = \frac{C_{\varepsilon_1} P_k - C_{\varepsilon 2}\varepsilon_{\mathrm{us}}}{T_{\mathrm{us}}} + \frac{\partial}{\partial x_j}\left[\left(\nu + \frac{\nu_{\mathrm{t}}}{\sigma_\varepsilon}\right)\frac{\partial \varepsilon_{\mathrm{us}}}{\partial x_j}\right], \tag{2.41}$$

$$\frac{\partial \zeta_{\mathrm{us}}}{\partial t} + \widetilde{U}_j \frac{\partial \zeta_{\mathrm{us}}}{\partial x_j} = f_{\mathrm{us}} - \frac{P_k}{k_{\mathrm{us}}}\zeta_{\mathrm{us}} + \frac{\partial}{\partial x_j}\left[\left(\nu + \frac{\nu_{\mathrm{t}}}{\sigma_\zeta}\right)\frac{\partial \zeta_{\mathrm{us}}}{\partial x_j}\right] \tag{2.42}$$

and

$$L_{\mathrm{us}}^2 \frac{\partial^2 f_{\mathrm{us}}}{\partial x_j \partial x_j} - f_{\mathrm{us}} = \frac{1}{T_{\mathrm{us}}}\left(C_1 + C_2 \frac{P_k}{\varepsilon_{\mathrm{us}}}\right)\left(\zeta_{\mathrm{us}} - \frac{2}{3}\right). \tag{2.43}$$

Here, $P_k = 2\nu_{\mathrm{t}}\widetilde{S}_{ij}\widetilde{S}_{ij}$ is the production rate based on the rate of strain tensor of the resolved flow field $\widetilde{S}_{ij}$; the length scale switch is given by

$$L_{\mathrm{us}} = C_L \max\left[C_\eta\left(\frac{\nu^3}{\varepsilon_{\mathrm{us}}}\right)^{1/4}, \frac{k_{\mathrm{us}}^{3/2}}{\varepsilon_{\mathrm{us}}},\right] \tag{2.44}$$

and the time scale is presently computed only based on the turbulent time scale

$$T_{\mathrm{us}} = \frac{k_{\mathrm{us}}}{\varepsilon_{\mathrm{us}}}. \tag{2.45}$$

The resolution function F_{r} in Eq. (2.39) has to provide a seamless blending between the DNS limit ($F_{\mathrm{r}} \to 0$, $\nu_{\mathrm{t}} \to 0$) and the RANS limit ($F_{\mathrm{r}} \to 1$, $\nu_{\mathrm{t}} \to \nu_{\mathrm{t}}^{\mathrm{RANS}}$). Between these two limits the VLES operating mode is recovered. Chang *et al.* [27] employ a formulation for F_{r} in line with a proposal by Han and Krajnović [56], which is based on the ratio of a measure for the grid spacing $\Delta = (\Delta x \Delta y \Delta z)^{1/3}$ to the turbulent length scale estimated from the $(\cdot)_{\mathrm{us}}$-quantities:

$$F_r = \min\left[\left(\frac{\Delta}{k_{\mathrm{us}}^{3/2}/\varepsilon_{\mathrm{us}}}\right)^{4/3}, 1\right]. \tag{2.46}$$

Table 2.2: Model coefficients in the VLES model.

C_τ	C_L	C_η
6.0	0.36	85

C_μ^ζ	C_{ε_1}	C_{ε_2}	C_1	C_2	σ_k	σ_ε	σ_ζ
0.22	$1.4\,(1+0.045/\sqrt{\zeta})$	1.9	0.4	0.65	1	1.3	1.2

Finally, the sub-scale eddy viscosity is computed with explicit damping provided by the resolution function as

$$\nu_\mathrm{t} = F_\mathrm{r} C_\mu^\zeta \zeta_\mathrm{us} k_\mathrm{us} T_\mathrm{us}. \tag{2.47}$$

All model coefficients are summarized in Tab. 2.2.

Due to the construction of the VLES model with direct damping of the eddy-viscosity according to Eq. (2.39) instead of a modification of the transport equations, the quantity k_us cannot be considered as the unresolved part k_u of TKE ($k = k_\mathrm{res} + k_\mathrm{u}$). In fact the $(\cdot)_\mathrm{us}$-quantities have to be considered as intermediary between the values corresponding to fully-modeled turbulence (i.e. RANS) and the actual unresolved part, which makes a clear physical interpretation of the $(\cdot)_\mathrm{us}$-quantities difficult. Instead, the unresolved part of TKE is estimated as $k_\mathrm{u} = \sqrt{F_\mathrm{r}} k_\mathrm{us}$, which stems from the derivation of the resolution function [26].

2.3 Turbulent flow over rough walls

In mechanical engineering, surface roughness is typically defined in terms of geometrical deviations in surface normal direction of any real manufactured surface from its ideal predefined geometrical form [38]. In contrast to waviness and inaccuracies in shape, roughness is associated with the short wavelength component of these deviations, typically with ratios of the height of individual *roughness elements* to their spacings in the range 5...100 [38]. These deviations from an ideal surface stem from the mechanical manufacturing process, successive surface treatments and the microstructure of the material [38]. While these types of

surface roughness generation are associated primarily with the production process, roughness affecting a turbulent flow can also be formed during the further life-cycle of a product by mechanical wear and tear as well as various other generation mechanisms. Examples include gas turbines where rough surfaces are generated due to corrosion, erosion and deposition processes [16, 142], aircraft wings where roughness can be formed due to leading edge ice accretion [2, 134], hulls of ships and marine current turbines affected by biofouling (i.e. marine growth of microorganisms, plants, algae and animals) [132, 156] as well as combustion chamber deposits in internal combustion engines [49]. In all theses cases roughness affects the performance, safety or efficiency of the associated technical systems, mainly due to increased drag and altered heat transfer processes. Other examples of relatively homogeneous small scale variations in surface topography which can be considered as a type of roughness can be found in the context of environmental flows: in the atmospheric boundary layer, urban [30, 31, 92] as well as vegetative canopies [9, 41] are frequently considered as rough surfaces. In these cases the effect of roughness on the flow is important for more accurate meteorological and local climate predictions, e.g. for the calculation of wind turbine yields or the estimation of pollutant dispersion in urban areas.

Due to the various generation mechanisms, the geometrical arrangement of roughness topographies differ considerably. The above mentioned examples of rough surfaces generated during use in technical system are generally rather isotropic, three-dimensional and irregular. Roughness topographies formed during the production process vary in their structure depending on the applied manufacturing techniques (see e.g. Strout [143]). While many machined surfaces are also three-dimensional and irregular, processes such as milling and turning can create anisotropic and even two-dimensional surface topographies. Similar arguments can be made in the context of environmental flows, where most naturally occurring roughness is three-dimensional and irregular, while man-made canopies might be rather regularly arranged. Finally, there are evolutionary advantageous as well as purposefully designed structured surfaces that are generally highly regular, such as drag-reducing riblets on shark skin [37] or dimpled surfaces for improved heat transfer [96]. However, such 'functionally' structured surfaces as

well as the often associated class of d-type roughness are beyond the scope of this work and are thus not discussed any further.

Fundamental studies on the effect of a variety of roughness topographies on turbulent flow have been conducted in the past, however, with a focus more towards regular surfaces. This can be attributed to researchers preference for well-defined and easily reproducible surface topographies as well as both, the less complicated manufacturing of regular surface samples for experimental investigations and the easier representation of such surfaces in DNS codes. The roughness elements used in studies of flow over regular arrangements are usually geometrically simple shapes, such as cubes [32, 91, 114], bars [58, 75, 114] or spheres [25, 93, 136] as well as pyramids [133], cylinders [122] or hemispheres and cones [130]. Irregular roughness topographies have also been studied, for example in the pioneering work of Nikuradse [112] who used sieved sand and lacquer to create roughness topographies resembling sandpaper. Similar approaches to create irregular rough surfaces from sand [54, 130] or to simply use practical surfaces like those found in industrial pipes [33] have subsequently followed. However, in these cases the full geometrical details of the surface topographies are often unknown, making it difficult to reproduce the results or use the data for geometry-based roughness models or correlations. More recently, developments in manufacturing techniques, such as in the field of 3D printing, facilitated wind and water tunnel experiments of well-defined irregular surfaces, often obtained from surface scans of real roughness samples [15, 164]. Similarly, advances in numerical methods and available computational power enabled DNS of well-defined geometrically-resolved irregular surfaces, albeit at moderate Reynolds numbers. In this regard Cardillo *et al.* [24] performed DNS of a turbulent boundary layer over a roughness topography based on a surface scan of 24-grit sandpaper. More recently Forooghi *et al.* [48] studied several synthetic roughness topographies covering a range of predefined surface statistics as well as a realistic roughness topography from an internal combustion engine [49]. Finally, based on the methodology developed in Busse *et al.* [22], DNS of rough surfaces obtained from surface scans of various real roughness samples have been performed [149, 150].

In order to effectively quantify the influential geometrical properties of naturally occurring irregular rough surfaces, one usually has to rely

on statistical quantities related to the surface elevation map s. The reference plane for the measurement of this elevation is commonly defined as the *mean* or *melt-down plane* S such that

$$\int_S s \, \mathrm{d}S = 0. \tag{2.48}$$

Based on this, the *root mean square roughness height* can be defined as

$$k_{\mathrm{rms}} = \sqrt{\frac{1}{S} \int_S s^2 \, \mathrm{d}S}, \tag{2.49}$$

which Flack and Schultz [43] found to be an appropriate length scale for scaling the roughness effect on the flow. Various other length scales for the roughness height have been proposed in literature, mainly in the context of roughness correlations relating geometrical properties of the surface to a corresponding friction factor. For most regular rough surfaces made up of uniformly-sized roughness elements, such as e.g. cubes, rods, spheres, hemispheres or cones, a representative length scale can easily be defined based on the roughness elements *peak-to-valley height* $k_{\mathrm{t}} = s_{\max} - s_{\min}$. For irregular surfaces with variable roughness element height, various averaged quantities have been proposed such as the mean height of roughness peaks [154] or mean peak-to-valley height on partitioned tiles of the surface [15, 149]. An additional statistical moment related to the surface elevation that has been shown to be of major influence [43, 48, 109] is the *skewness*, defined as

$$\mathrm{Sk} = k_{\mathrm{rms}}^{-3} \frac{1}{S} \int_S s^3 \, \mathrm{d}S. \tag{2.50}$$

Further less frequently used quantities are the *effective slope*

$$\mathrm{ES} = \frac{1}{S} \int_S \left| \frac{\partial s}{\partial x} \right| \mathrm{d}S \tag{2.51}$$

as well as the *kurtosis* of the surface elevation distribution

$$\mathrm{Ku} = k_{\mathrm{rms}}^{-4} \frac{1}{S} \int_S s^4 \, \mathrm{d}S. \tag{2.52}$$

Finally, several parameters including a quantification of the roughness density have been proposed in literature [130, 135, 154]. Presently, the

simple definition used by Schlichting [130] is adopted, which defines the so-called *frontal solidity* as the ratio

$$\Lambda = \frac{S_\mathrm{p}}{S}, \tag{2.53}$$

where S_p is the total frontal projected area of the roughness elements in streamwise direction.

2.3.1 Roughness effect on the flow

The key issue with respect to turbulent flow over rough walls, is to relate the previously described geometrical properties of a rough surface to its effect on turbulent flow. From an engineering perspective, the most relevant quantity in this regard is the friction coefficient at the rough wall, which is generally larger compared to the smooth wall case. Despite decades of research going back to the pioneering work of Nikuradse [112], no universally reliable way of estimating the friction losses of a previously uncharacterized rough surface has been found, other than conducting hydrodynamic tests or performing geometrically-resolved DNS [42]. However, several empirical correlations for various types of regular and irregular roughness have been proposed based on experimental and DNS data sets (see e.g. [43, 48, 109, 130, 135, 154]).

The Moody chart

A simple correlation relying on Nikuradse's *equivalent sand roughness* for fully-developed pipe flow is available in the form of the well-known Moody [107] chart, which is schematically shown in Fig. 2.4. While this chart is specifically for typical industrial pipes, it provides general insight into characteristics of turbulent flows over rough walls. The Moody chart, Fig. 2.4, shows the friction factor λ as a function of the Reynolds number $\mathrm{Re} = U_\mathrm{b} D/\nu$ for a range of relative roughness heights k_s/D, where k_s is the equivalent sand roughness height, D the pipe diameter and U_b the bulk velocity. Three regimes of turbulent flow over a rough wall can be differentiated: in the *hydraulically smooth regime* the roughness elements are too small to significantly contribute to the friction factor. Thus, as in the smooth case, the friction factor is determined by viscous effects and is merely a function of Reynolds number,

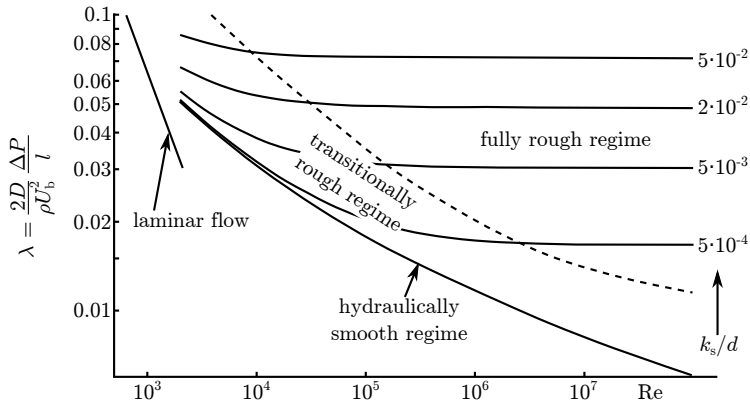

Figure 2.4: Moody chart: friction factor λ in fully-developed pipe flow as function of Reynolds number and relative equivalent sand roughness height k_s/D. Adapted from Moody [107].

$\lambda = \lambda(\mathrm{Re})$. Consequently, this regime collapses to the curve for smooth pipes in Fig. 2.4. In the *transitionally rough regime* both viscous drag as well as form drag on the roughness elements contribute significantly to static pressure losses. Therefore, the friction factor in this regime is a function of Reynolds number as well as the relative roughness height, $\lambda = \lambda(\mathrm{Re}, k_s/D)$. In the *fully rough regime*, the friction factor is controlled solely by the form drag of the roughness elements and is hence independent of the Reynolds number, $\lambda = \lambda(k_s/D)$. A flow can be assigned to one of the three regimes depending on the roughness Reynolds number based on the equivalent sand roughness height $k_s^+ = u_\tau k_s/\nu$. The hydraulically smooth regime can be observed for $k_s^+ < 5$, while the fully rough regime begins at $k_s^+ > 70$, with the transitionally rough regime at intermediate values [119]. However, as pointed out by Flack and Schultz [43] (and references therein), surfaces other than Nikuradse's sand roughness have been reported to exhibit the onset of the transitionally rough regime in the range $k_s^+ = 1.4...15$ and its end in the range $k_s^+ = 18...40$. In any case, these classification, as well as the Moody chart itself, rely on the equivalent sand roughness height k_s. It is important to emphasize, that k_s is not an actual geometrical parameter of the roughness but rather a property of the flow over the

respective surface in the fully rough regime. Specifically, k_s is the height of an equivalent Nikuradse-type sand roughness that would produce the same friction factor in the fully rough regime as the actually considered rough surface [43]. Consequently, the equivalent sand roughness has to be known in advance in order to apply the Moody chart (see e.g. Flack and Schultz [44] for a discussion on its further limitations).

Log-law and roughness function

The effect of roughness on the friction factor is obviously associated with the modification of the mean velocity profile in the near-wall region. In this regard, Nikuradse [112] found that the logarithmic law of the wall can still be applied with the same value for the von Kármán constant κ, however, with a downward shift in the logarithmic region compared to the smooth wall case. In the fully rough regime, this downward shift can be captured by scaling the wall distance y with k_s instead of the viscous length scale ν/u_τ, according to

$$U^+ = \frac{1}{\kappa} \ln\left(\frac{y}{k_\mathrm{s}}\right) + C \tag{2.54}$$

with the constant $C \approx 8.5$. In the transitionally rough regime, where viscous effects play an important role, Nikuradse [112] proposed to adapt the value of C as a function of k_s^+, since the velocity profiles slope in the logarithmic region still remains constant.

Based on this observation, Hama [55] introduced a more straightforward formulation for the logarithmic law over a rough wall by parametrizing directly the shift in the logarithmic region of the velocity profile ΔU^+ compared to a smooth wall, as shown in Fig. 2.5. Including this velocity shift ΔU^+, commonly referred to as *roughness function*, into the smooth wall formulation (2.10) yields

$$U^+ = \frac{1}{\kappa} \ln y^+ + B - \Delta U^+, \tag{2.55}$$

which is fully equivalent to Eq. (2.54). Thus, by combining Eqs. (2.54) and (2.55) an expression for the relation between ΔU^+ and k_s^+ in the fully rough regime can be obtained:

$$\Delta U^+(k_\mathrm{s}^+) = B - C + \frac{1}{\kappa} \ln k_\mathrm{s}^+. \tag{2.56}$$

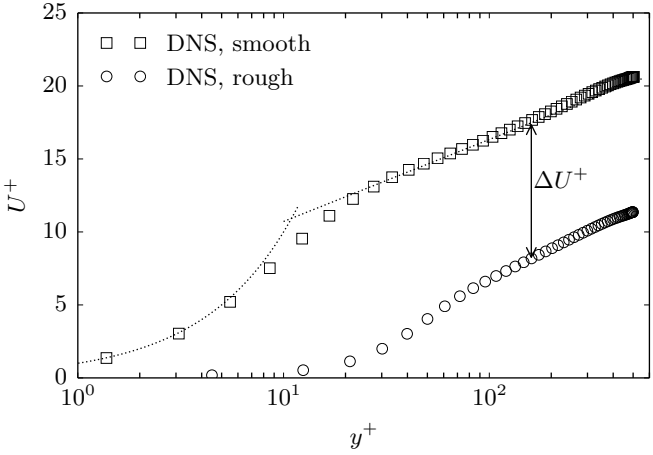

Figure 2.5: Mean velocity profile of fully-developed open channel flow over a smooth and arbitrarily rough wall at $\mathrm{Re}_\tau \approx 500$ in inner scaling with the corresponding roughness function ΔU^+. DNS data taken from Forooghi *et al.* [48].

This correlation provides a linear asymptote of the roughness function in the fully rough regime, when plotted as a function of k_s^+, as illustrated in Fig. 2.6. Additionally, Fig. 2.6 shows Nikuradse's [112] piecewise logarithmic fit for uniform sand roughness as well as Colebrook and White's [33] formula for industrial pipes, which was also used as a basis for the Moody chart [107]. The collapse in the fully rough regime is a consequence of the scaling based on an equivalent k_s and has also been confirmed using experimental data sets of various roughness topographies [43]. As indicated by the two fits from literature, in the transitionally rough regime the roughness function of different types of roughness in general do not collapse due to the scaling with k_s^+. Instead, Colebrook's [33] data indicates a monotonic increase in the roughness function with no critical roughness Reynolds number, implying the nonexistence of a hydraulically smooth regime; Nikuradse's [112] data on the other hand shows a hydraulically smooth regime with $\Delta U^+ = 0$ and a sudden increase marking the onset of the transitionally rough regime.

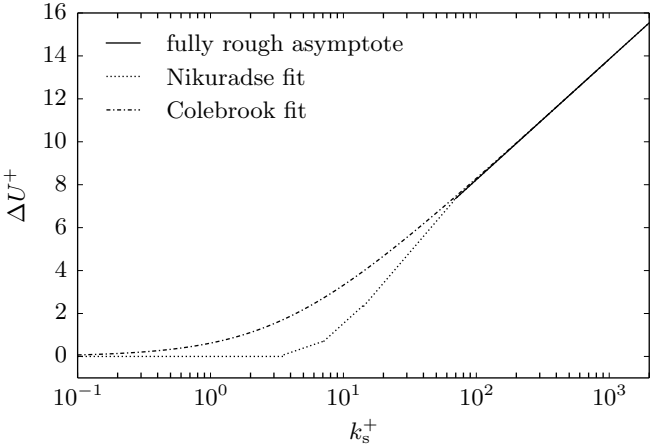

Figure 2.6: Roughness function ΔU^+ over the roughness Reynolds number k_s^+. Fully rough asymptote Eq. (2.56), piecewise logarithmic fit of Nikuradse [112] for uniform sand roughness as well as Colebrook and White's [33] fit for industrial pipes.

While Bradshaw [18] argues based on the Oseen approximation that no critical Reynolds number should exist and Nikuradse's [112] data can be attributed to the rather unnatural, almost mono-disperse distribution in sand-grain size, more recent experimental results for irregular, grit-blasted surfaces reported in Flack *et al.* [45] indeed indicate more of a Nikuradse-type behavior; however, with a slightly earlier onset of roughness effects in the range $k_s^+ = 2...3$ for their surface topographies. Further support for this type of behavior in the transitionally rough regime was recently provided by Thakkar *et al.* [150] who performed DNS of a realistic grit-blasted surface over the entire roughness Reynolds number range from hydrodynamically smooth to fully rough. Consequently, the shape of the roughness function in the transitionally rough regime is most likely dependent on yet to be determined geometrical properties of the roughness topography.

The virtual wall

At this point it is important to clarify the definition of wall distance y used in Eqs. (2.54) and (2.55). Specifically, the question arises where the reference plane or *virtual wall* associated with $y = 0$ is located, considering the variable elevation of the rough surface. Jackson [66] derived that in order for the modified logarithmic law to hold, the virtual wall has to be located at the position where the "mean drag appears to act on the flow" [66]. The position can thus be determined by finding the centroid of the mean drag force profile. Consequently, the origin of y depends not only on the roughness topography, but also on the flow itself. Due to the practical difficulties associated with this definition, many researchers apply different methodologies to determine the position of the virtual wall, e.g. by adjusting the wall distance to obtain the best fit to the logarithmic law (2.55) or use a priori definitions based on the geometry. However, as discussed in Raupach *et al.* [119], these as well as other common approaches are known to be inaccurate. Consequently, special attention should be paid to the applied methodology, when comparing quantities affected by the position of the virtual wall, such as equivalent sand roughness k_s and roughness function ΔU^+.

Outer layer similarity

Another frequently observed characteristic of turbulent flow over rough walls, which is especially important for roughness modeling approaches in the context of CFD discussed in the following section, is *outer layer similarity* of the mean flow. This notion implies that the effect of roughness elements on the flow is confined to a so-called *roughness sublayer* analogously to the viscous sublayer. If this is the case, at high Reynolds number, i.e. in a fully turbulent flow, the turbulent motions in the outer region are unaffected by the roughness sublayer, except for the role it plays in setting the shear stress as quantified by the velocity scale u_τ, the origin of the wall distance y (i.e. the position of the virtual wall) and the boundary layer thickness δ [119]. The dependency on the latter two parameters can be attributed mainly to the blockage effects of the roughness elements resulting in a displacement of the flow away from the wall. This similarity argument first put forward in the context of rough walls by Perry and Abell [117] is based on Townsend's

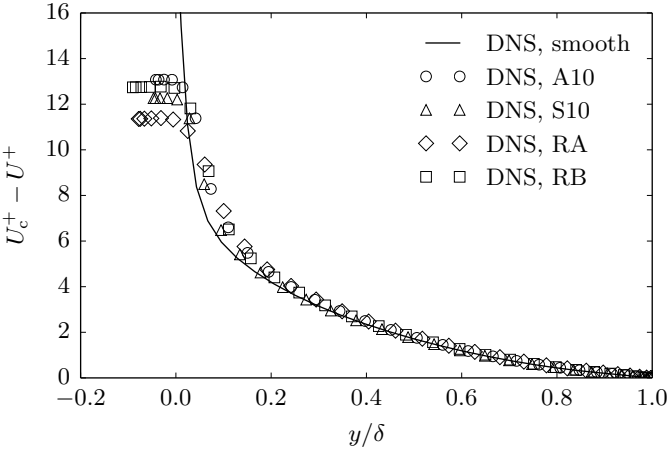

Figure 2.7: Velocity defect profiles based on the center-plane velocity U_c^+ in inner scaling for various regular and irregular roughness topographies at $\mathrm{Re}_\tau \approx 500$. DNS data taken from Krumbein *et al.* [78] (regular samples A10, S10) and Forooghi *et al.* [48] (irregular samples RA, RB corresponding to A7088, B7088).

[151] Reynolds number similarity hypothesis and is thus often simply referred to as *Townsend hypothesis*. Its validity is widely believed to be confirmed by experimental investigations such as the various works reviewed by Raupach *et al.* [119], who concluded that outer layer similarity is "well supported by many kinds of observation" [119], as well as the more recent work of Flack *et al.* [46].

A noteworthy challenge of the Townsend hypothesis was presented in Krogstad *et al.* [76] who could not confirm similarity of the mean velocity with smooth wall data in their experiments over woven mesh roughness. Flack *et al.* [46] argue that this can be attributed to the small ratio of boundary layer thickness to the equivalent sand roughness height $\delta/k_\mathrm{s} \leq 15$. A similar argument is made by Jimenez [70], who suggests that $\delta/k_\mathrm{t} > 40$ is required for similarity laws to hold. However, for the roughness considered in this work, which was studied compu-

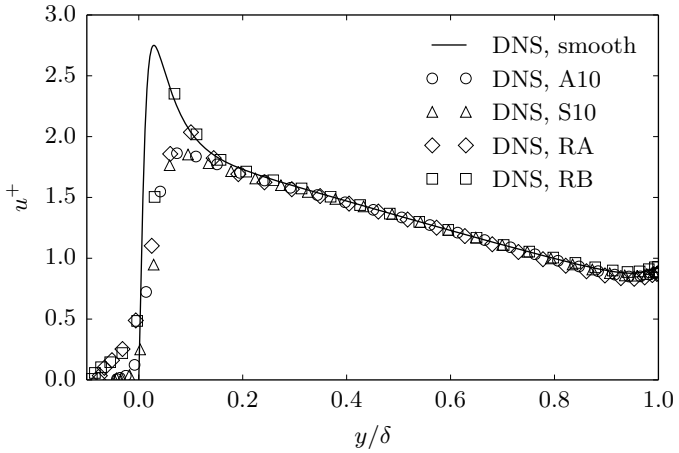

Figure 2.8: Turbulent intensity profiles in inner scaling for various regular and irregular roughness topographies at $\mathrm{Re}_\tau \approx 500$. DNS data taken from Krumbein *et al.* [78] (regular samples A10, S10) and Forooghi *et al.* [48] (irregular samples RA, RB corresponding to A7088, B7088).

tationally by means of the DNS approach of Forooghi *et al.* [48], δ/k_s and δ/k_t are both less than 7. Nevertheless, the velocity defect profiles $U_\mathrm{c}^+ - U^+$ based on the center-plane velocity U_c^+ of various exemplary roughness topographies from this DNS data set exhibit a collapse with smooth wall data in the outer region $y/\delta > 0.3$ [48], as shown in Fig. 2.7. More details on the roughness topographies are provided in Section 2.3. Similarly, the turbulent intensity profiles in inner scaling collapse with the respective smooth wall data in the outer region, as indicated exemplary for the streamwise component in Fig. 2.8. In any case, the requirements on the inverse blockage ratios δ/k_s or δ/k_t postulated by Flack *et al.* [46] and Jimenez [70], respectively, do not seem to be solely indicative of wether the Townsend hypothesis holds.

Spatial averaging and dispersive stresses

Finally, the issue of obtaining mean quantities for the flow over an inherently inhomogeneous rough wall shall be addressed. In general, spatial averaging in layers parallel to the wall is performed in order to gain mean profiles representative for the entire rough wall. Following the DNS study of Forooghi *et al.* [48], which is used as reference data base for rough wall flow computations in this work, the mean velocity profiles are obtained by a *superficial average* of the time-averaged flow field in streamwise direction $\overline{U}_x$. The term superficial, which is often used in the context of porous media or multiphase flow, indicates that spatial averaging is performed disregarding the presence of other phases, i.e. the presence of the roughness elements. Consequently, positions actually occupied by roughness are taken into account in the averaging procedure, with a zero value of the associated quantity, e.g. $\overline{U}_x = 0$. Thus, the velocity profiles U^+ for rough walls in Figs. 2.5 and 2.7 are calculated as $U^+ = \langle \overline{U}_x \rangle^{\mathrm{s},xz} / u_\tau$, where the $\langle\cdot\rangle^{\mathrm{s},xz}$ operator indicates superficial averaging in x and z-directions extending over the entire rough wall.

Further, the spatial inhomogeneity of the time-averaged velocity field $\overline{U}_i$ has to be considered in defining quantities derived from turbulent velocity fluctuations, such as turbulent stresses. Thus, the time-averaged velocity field is further decomposed based on the described spatial average [32], resulting in

$$U_i = \overline{U}_i + u_i' = \underbrace{\langle \overline{U}_i \rangle^{\mathrm{s},xz} + u_i^*}_{\overline{U}_i} + u_i'. \tag{2.57}$$

Here, u_i^* consequently describes the spatial variation of the time-averaged velocity field with respect to its superficial average. In analogy to the Reynolds stresses $\overline{u_i' u_j'}$, the so-called *dispersive stresses* $\langle u_i^* u_j^* \rangle^{\mathrm{s},xz}$ can be defined [121], which describe the additional momentum transfer due to spatial variations. The total turbulent stresses capturing both, the fluctuations in time and space resulting from the double decomposition are given by

$$\langle \overline{u_i u_j} \rangle^{\mathrm{s},xz} = \langle \overline{(u_i' + u_i^*)(u_j' + u_j^*)} \rangle^{\mathrm{s},xz} = \langle \overline{u_i' u_j'} \rangle^{\mathrm{s},xz} + \langle u_i^* u_j^* \rangle^{\mathrm{s},xz}. \tag{2.58}$$

If not explicitly stated otherwise, turbulent intensities for flow over

rough walls in this work, such as u^+ shown in Fig. 2.8, are based on total turbulent stresses.

The role of dispersive stresses has been discussed primarily in the field of atmospheric boundary layer roughness, i.e. for plant and urban canopies. Raupach *et al.* [120] found that dispersive stresses are "practically negligible" above the roughness crest of a model plant canopy. Similar observations were made by Cheng and Castro [30] for urban roughness. Measurements of dispersive stress inside the roughness layer are however scarcely reported, likely due to the difficulties associated with spatially resolved measurements inside the roughness layer. In this regard Moltchanov *et al.* [106] studied the influence of dispersive stresses inside a model forest canopy and found that they have an important influence in non-uniform canopy flow, such as at the upstream edge of a forest, while observations in fully-developed regions indicate also that the Reynolds stresses are dominant. More insight into the role of dispersive stresses could be gained by means of DNS with geometrically resolved rough walls. Such approaches have been however feasible only in recent years due to the associated computational costs. Jelly and Busse [69] performed such DNS for three synthetic roughness topographies and evaluated the influence of dispersive stresses on the roughness function ΔU^+. For two surface topographies with peaks, they found that the contribution from the dispersive stresses are compensated by modified Reynolds stresses; however, this was not the case for a surface consisting solely of pits, which resulted in a more pronounced influence of the dispersive stresses on the roughness function. Overall, the influence of dispersive stresses is not fully understood yet, partly due to the limited amount of data available in literature. Likely as a consequence of this, the confinement to the roughness layer as well as the widely supposed dominance of Reynolds stresses, the dispersive stresses are usually neglected in roughness models [106].

2.3.2 Accounting for roughness in CFD

Fairly diverse approaches to account for roughness in numerical simulations of turbulent flows have been proposed in literature. Specifically, these approaches differ in terms of

- their applicability in combination with different methodologies for

simulating turbulent flow such as fully-resolved turbulence (i.e. DNS), scale-resolving simulations with modeled sub-scale quantities (i.e. LES and hybrid models) or fully-modeled turbulence (i.e RANS);

- the required input, wether it be the exact geometry of the roughness topography, corresponding statistical information or even flow related quantities such as the equivalent sand roughness height;
- the extent of their predictive capabilities with respect to friction factors as well as mean flow and turbulent quantities both inside and outside the roughness-sublayer;
- the additional computational effort required in comparison to a smooth wall at similar Reynolds number.

Consequently, choosing the most suitable modeling approach is highly dependent on the specific application as well as requirements in terms

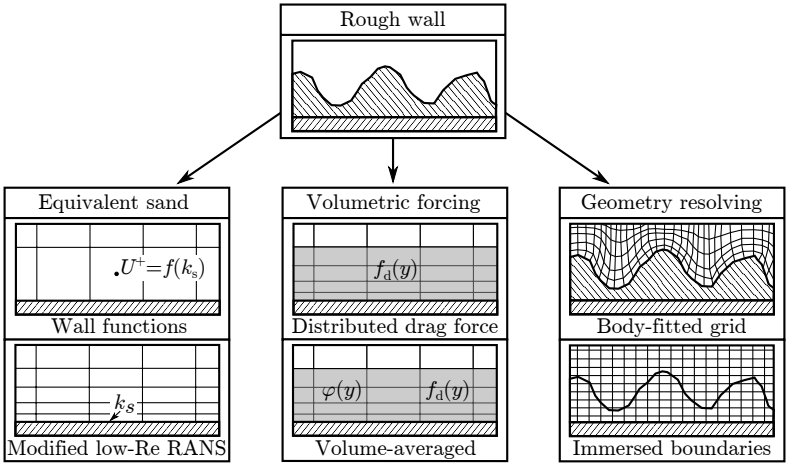

Figure 2.9: Classification scheme for approaches to account for rough walls in numerical computations of turbulent flow. Approaches are sorted with increasing predictive capabilities, accuracy and computational costs from left to right.

of accuracy, the obtainable information concerning the roughness and the available computational resources. In the following an attempt is made to classify approaches from literature in order to discuss their respective advantages and limitations. Fig. 2.9 shows a graphical representation of the classification scheme differentiating between *equivalent sand approaches*, *volumetric forcing approaches* and *geometry resolving approaches*.

Geometry resolving approaches

On the right side, the most accurate but also computationally most intensive category of approaches is listed, which is to numerically resolve the geometry of the roughness topography. This can be done for instance by generating a body-fitted grid or by applying an immersed boundary method (IBM) (see e.g. Mittal and Iaccarino [104] for a review) to enforce wall boundary conditions on the rough surface situated inside the computational domain. The main advantage of IBMs compared to a body-fitted grid is the uncomplicated generation of the background mesh, which is structurally identical to the corresponding smooth wall case (see Fig. 2.9). However, the grid resolution required for an exact geometrical representation of the roughness topography with IBM is likely higher compared to a body-fitted mesh, depending in particular on the specific IBM formulation. Provided that the grid resolution is sufficient to resolve the roughness topography, the accuracy of both approaches can be expected to be solely limited by the applied methodology for computing the turbulent flow.

Depending on the length scales of the roughness and the considered Reynolds number, the required grid resolution for an accurate geometrical representation, especially of realistic irregular surfaces, may already exceed the requirements of a DNS with respect to capturing the smallest turbulent scales (see e.g. [149]). Thus, this approach is often coupled with DNS, resulting in a 'true' DNS resolving both, the geometry of the roughness as well as all turbulent scales. Such computations using IBM have been performed for various regular surfaces (e.g. [25, 91, 114, 115]) and recently also for more realistic irregular surfaces [22, 24, 48, 49, 69, 149, 150]. While 'true' DNS is highly demanding in terms of computational costs, it can be considered as the most accurate fully predictive approach to numerically compute turbulent flow over

a previously uncharacterized rough surface, since the least amount of modeling errors is introduced.

The approach of resolving the geometry of the roughness, which as discussed in Section 2.3.1 has a significant influence on the friction factor, can also be coupled with turbulence modeling approaches from the LES or RANS frameworks. While inherently less accurate due to the introduced modeling errors, especially the combination with highly-resolved LES can still be considered as a fully predictive modeling framework, i.e. friction factors, mean flow fields and turbulence statistics can be predicted accurately relying solely on the geometry of the roughness. LES studies with resolved roughness have been performed using both IBMs (e.g. [3, 166]) as well as body-fitted meshes (e.g. [97, 98, 110, 165]).

Equivalent sand approaches

For practical engineering problems, the computational effort required to accurately resolve the roughness topography generally exceeds the available resources, especially in combination with DNS. Consequently roughness models mimicking the effect of rough surfaces without the need of geometrical representation are necessary. The de-facto standard in this regard – and to date the only available option in major commercial CFD codes, such as Fluent, Star-CCM+ or CFX – are approaches based on Nikuradse's equivalent sand roughness (see Fig. 2.9, left) which are usually applied in combination with RANS models. However, these approaches are associated with major limitations with respect to their predictive capabilities, which are discussed in the following.

Bearing in mind that the equivalent sand roughness height k_s is not an easily obtainable geometrical property of a given rough surface but rather a property of the flow directly correlated with the friction factor in the fully rough regime over the considered rough surface, as discussed in Section 2.3.1, one could argue that these models do not really posses predictive capabilities with respect to the friction factors at all. Instead they rely on a previous characterization of the associated friction over the considered rough surface in the fully rough regime or the availability of an accurate roughness correlation for k_s. Furthermore, equivalent sand approaches are based on Nikuradse's modified formulation of the log-law, Eq. (2.54), which is valid only in the logarithmic region of the velocity profile. Since the velocity profiles in the roughness sub-

layer over different roughness topographies do not collapse due to the scaling with k_s, accurate results in the roughness sublayer can not be expected by relying on this single parameter. The primary goal of these models is rather to set the appropriate shear associated with a given k_s in a region above the roughness sublayer and rely on Townsend's similarity hypothesis in the outer layer – thus effectively bridging the roughness sublayer. A similar argument can be made with respect to the transitionally rough regime: since, as discussed in Section 2.3.1, the shape of the roughness function in this regime does not collapse with k_s but rather depends on geometrical details of the roughness topography, models relying solely on the equivalent sand roughness height are unable to accurately capture the difference between distinct rough surfaces in the transitionally rough regime with an identical value of k_s. Finally, similar to high Reynolds number RANS models, where wall functions are applied to bridge the viscous sublayer, equivalent sand approaches rely to some extent on the existence of a logarithmic region. However, as is well documented throughout literature, the existence of a logarithmic region is based on several conditions, which are not necessarily fulfilled under more complex flow conditions involving e.g. non-equilibrium flows or separation, which introduces additional modeling uncertainties. In summary, equivalent sand roughness models are the most appropriate choice for modeling rough walls in the fully rough regime, which have been previously characterized in terms of k_s, in flow configurations where a logarithmic region can be expected and accurate predictions of flow quantities in the roughness sublayer are not a priority.

Although the discussed limitations render models based on the equivalent sand roughness approach rather unsuitable for consideration in the present work, where a framework for scale-resolving simulations covering the near-wall region is developed, the two major modeling strategies for equivalent sand roughness approaches illustrated in Fig. 2.9 shall be outlined briefly for the sake of completeness. In both cases, the rough wall is replaced by a virtual smooth wall situated below the roughness crest. For the wall function approach, classical wall functions for smooth walls can be modified based on the rough wall log-law Eq. (2.54). An overview of such implementations in various commercial CFD codes can be found e.g. in Blocken *et al.* [14]. More recently, Suga *et al.* [144]

and Apsley [5] proposed more advanced rough wall functions based on the analytical wall function approach of Craft *et al.* [34] which aims to address key issues of the classical wall functions, such as unsatisfactory performance in non-equilibrium flows and sensitivity to the wall distance of the first grid node. The second approach is based on the modification of low Reynolds number RANS models. While in some cases minor changes to the transport equation are necessary, usually only wall boundary conditions are reformulated as function of k_s. Such extensions can be found for various turbulence models including the proposals by Wilcox [162] for the k-ω model, by Aupoix and Spalart [8] for the Spalart-Allmaras model or by Aupoix [6] for the k-ω SST model.

Volumetric forcing approaches

A compromise between the limited capabilities of equivalent sand approaches and the high computational costs associated with geometry resolving approaches is the category in this work termed as volumetric forcing approaches (see Fig. 2.9, middle). In principal these models are based on Schlichting's [130] argument that the flow resistance of a rough surface is due to the form drag individual roughness elements exert on the flow in addition to viscous drag. The basic idea then, is to model the drag force acting on the wetted surface of an individual roughness element based on the following customary expression readily obtained from dimensional analysis:

$$F_\mathrm{D} \sim \rho U_\infty^2 A_\mathrm{p}, \tag{2.59}$$

where U_∞ is the velocity of the incoming fluid and A_p the projected frontal area in streamwise direction. Extending several previous works, where such form drag terms were added to the momentum equation as a distributed volume force in an ad-hoc fashion, Taylor *et al.* [147] formulated two-dimensional boundary layer equations based on a thin wall-parallel control volume penetrated by multiple roughness elements and termed their model *discrete element approach*. The volumetric drag force associated with the roughness elements is parametrized assuming axisymmetric roughness elements with diameter $d(y)$ and a drag coefficient $C_\mathrm{d}(\mathrm{Re}_d)$, depending on the local Reynolds number. Furthermore, they account for the blockage effect of the roughness elements by introducing geometry-dependent blockage factors in their continuity and

momentum equations. The model was validated primarily in terms of predicted friction factors for various regular rough surfaces consisting of axisymmetric roughness elements in conjunction with a mixing length model for the Reynolds shear stress. They found, that the discrete element approach, in contrast to models based on equivalent sand roughness, "applies equally well for both transitionally rough and fully rough flows" [147] and argue that this is due to the model incorporating "more of the basic physics of the interaction between the fluid and the roughness elements" [147].

Following the work of Taylor *et al.* [147], several authors adopted the key concept of a volumetric forcing term accounting for the drag the roughness elements exert on the flow, with some choosing to not explicitly account for blockage effects. Thus, in this work volumetric forcing approaches incorporating solely a drag force term $f_{\mathrm{d},i}$ in the momentum equation are referred to as *distributed drag force* (DDF) approaches, while those additionally including geometry-related blockage factors such as the porosity $\varphi(y)$ in the continuity and momentum equations are labeled as *volume-averaged forcing* (VAF) approaches, since such equations can generally be derived from first principles applying volume averaging techniques.

Various VAF approaches relying on the boundary layer equations of the discrete element approach have been proposed. Tarada [146] developed a low Reynolds k-ε model extended with source terms accounting for roughness effects on the modeled turbulent quantities and a modified drag force closure, while Hosni *et al.* [63] focused on extending the approach to predict rough wall heat transfer. Model validation in both cases was however based primarily on integral quantities such as friction coefficients. Independently, Maruyama [99] proposed full Navier-Stokes equations including a blockage factor in conjunction with a high Reynolds number k-ε model and validated their approach for flow over a staggered array of cubes, also in terms of velocity profiles and TKE in the outer layer. However, their model coefficients have been optimized to fit the measured data and no derivation for their modified Navier-Sokes equations was presented. Thus, Aupoix [7] proposed Navier-Stokes equations for a VAF approach derived relying on Whitaker's [160] volume-averaging technique developed for porous media flow and demonstrated the sensitivity of the model to changes in

the equations stemming from the derivation procedure (i.e. different locations of the blockage factor).

DDF approaches, i.e. approaches not explicitly accounting for blockage effects, have been considered especially in the context of canopy flows. In this regard, Ayotte *et al.* [9] extended a second moment closure RANS model to account for canopy drag, while Belcher *et al.* [11] and Coceal and Belcher [31] proposed parameterizations for the drag closure applicable to vegetative and urban canopies in conjunction with mixing length models. On the other hand Chang *et al.* [28] applied a DDF approach to the flow over an airfoil with regular leading edge roughness in conjunction with a low Reynolds number k-ε model and reported some success in qualitatively predicting aerodynamic performance. Detailed validation results in terms of velocity profiles and turbulent quantities for various roughness topographies have however also not been presented in these studies.

In contrast to VAF approaches, DDF-based models have also been applied in conjunction with scale-resolving computations of turbulence. Miyake *et al.* [105] were among the first to perform DNS of rough channel flow by applying a drag force model for cone-shaped roughness elements in order to numerically study the effect on Reynolds stresses and the budget of TKE. They reported results in qualitatively good agreement with experimental observations, however without a quantitative validation of the roughness modeling approach. A similar numerical experiment focusing on turbulent structures over plant canopies was presented in Watanabe [157] in conjunction with a one-equation subgrid-scale model in the LES framework. More recently, Busse and Sandham [23] systematically studied the effect of a DDF term in conjunction with DNS. Instead of relying on the classical approach of parametrizing the drag force based on geometrical details of a virtual or real rough surface as well as associated drag coefficients, they chose a more abstract mathematical way and expressed the density-specific volumetric force components as

$$f_{\mathrm{d},i} = -\alpha_i \, F(y) \, U_i |U_i|, \tag{2.60}$$

where α_i is a roughness factor with dimension L^{-1} accounting for a combination of roughness density as well as drag coefficient and $F(y)$ is a non-dimensional, normalized shape function accounting for the distribution of the drag term with respect to wall distance. It should be

noted that according to their notation, no summation convention for the index i is applied in Eq. (2.60). Consequently, the components of the drag force are modeled as proportional to the respective velocity component squared instead of the usual definition based on the magnitude of the velocity vector ($f_{\mathrm{d},i} \sim U_i\sqrt{U_k U_k}$), which they argue would impair outer layer similarity of the mean streamwise velocity profile [23]. They then performed an extensive parametric study varying shape function, roughness height as well as roughness factor and found that many effects of roughness with respect to mean velocity profiles and turbulence statistics can be reproduced with the volumetric forcing approach in conjunction with scale-resolving simulations of turbulence [23]. Importantly, they also confirmed that the obtained roughness functions ΔU^+ in the transitionally rough regime span an area between Nikuradse's and Colebook's fits (see Fig. 2.6) [23], indicating that geometry related effects in the transitionally rough regime can be captured with such an approach. However, the question of how the model parameters have to be chosen for a specific rough surface remains open.

Based on the encouraging observations made by Busse and Sandham [23] with respect to their DDF approach in conjunction with scale-resolving simulations of turbulence, the limited predictive capabilities of models relying on equivalent sand roughness height and the excessive computational cost associated with geometry resolving approaches, in this work, roughness models based on volumetric forcing are considered. In order to enable a VAF approach, relying on full three-dimensional Navier-Stokes equations, the proposal of Aupoix [7] is followed and volume averaging techniques originating from the field of porous media modeling are applied. Thus, in the following section, relevant details from this field are presented.

2.4 Turbulent flow over porous media

Flow through porous media can be found in many industrial applications such as in the fields of chemical, petroleum and combustion engineering. A porous medium can be considered as a solid *matrix* with interconnected *pores* saturated with a fluid. In most cases, the geometrical length scales of these pores are very small compared to relevant outer dimensions of the considered system. Consequently, engineering

descriptions of flow through porous media generally rely on a *macroscopic* viewpoint instead of considering the *microscopic* flow details on the order of the pore scale. Thus, either only integral quantities are considered or volume-averaging techniques, such as the one described in the following section, are applied to define continuous macroscopic flow fields.

On a microscopic level, the physical effects associated with flow through porous media are essentially similar to flow over rough walls: the presence of the solid matrix, similarly to roughness elements, results in a blockage effect and a drag force exerted on the surrounding fluid. However, in most cases, the drag force in porous media is dominated by viscous effects instead of form drag, due to the low local Reynolds number based on the typical pore diameter. In the limiting case of Stokes flow in the pores, the well-known Darcy [35] law is valid, which was formulated for steady flow through a homogeneous porous medium with cross-sectional area A. It relates the flow rate Q to the pressure drop $(P_2 - P_1)$ over a length l according to

$$Q = K \frac{A}{\rho\nu} \frac{(P_2 - P_1)}{l}. \tag{2.61}$$

Here, the proportionality coefficient K, commonly referred to as *permeability*, depends on the structure of the porous medium. For cases where inertia effects are not negligible, Forchheimer [47] proposed an extension to Darcy's law with a form drag term proportional to the velocity squared. Introducing Forchheimer's extension in Eq. (2.61) and reformulating in terms of the superficial Darcy velocity U_d yields

$$0 = -\frac{\mathrm{d}P}{\mathrm{d}x} - \frac{\rho\nu}{K} U_\mathrm{d} - \beta\rho U_\mathrm{d}^2, \tag{2.62}$$

with the Forchheimer coefficient β, which again depends on the structure of the porous medium. For further details on flow through porous media the reader is referred to Nield and Bejan [111].

While these one-dimensional equations derived based on empirical observations are helpful to gain some insight into the underlying physical effects, three-dimensional conservation equations for mass and momentum are required for application in CFD. In the following, such equations derived from the Navier-Stokes equations are presented.

2.4.1 Volume-averaged Navier-Stokes framework

Tensorial conservation equations describing macroscopic flow fields can be derived by applying the volume-averaging technique presented in Whitaker [160]. Starting point for such a procedure is the definition

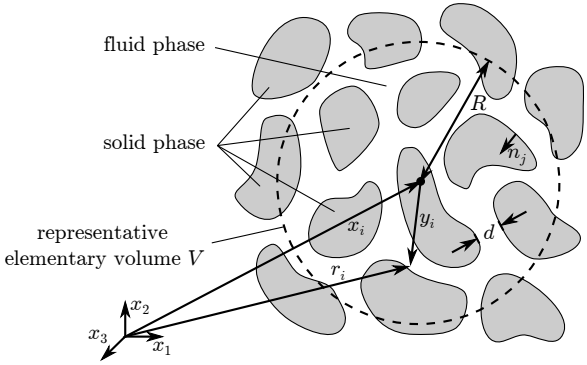

Figure 2.10: Schematic of a spherical representative elementary volume with associated positions vectors for volume averaging.

of a so-called *representative elementary volume* (REV) V, as schematically illustrated in Fig. 2.10. An REV represents the extend of the three-dimensional space whose associated microscopic flow details are considered for the definition of the macroscopic quantity assigned to the position of the REV's centroid x_i. Similarly to the spatial filtering applied to derive governing equations in the LES framework, certain constraints to the dimensions of the REV can be formulated, which essentially imply an assumption of scale separation. Specifically, the typical pore diameter d has to be small compared to the dimension of the REV, e.g. its radius R, in order to ensure smooth macroscopic flow quantities unaffected by spatial variations on the order of the pore scale. On the other hand, the radius R has to be small enough compared to a typical length scale of the macroscopic flow field L so that large scale variations of the macroscopic flow quantities are not smoothed out in the averaging procedure. Consequently, the length scale-constraint is formulated as $d \ll R \ll L$ [159].

For the volume-averaging procedure, first a phase indicator function

is defined as

$$I_\varphi(r_i) = \begin{cases} 1, & \text{in the fluid phase,} \\ 0, & \text{in the solid phase.} \end{cases} \tag{2.63}$$

Integration of $I_\varphi(r_i)$ over V then corresponds to the volume ΔV_f available to the fluid phase in the REV. Thus, the volume fraction of the fluid, which is commonly referred to as *porosity*, is given by

$$\varphi(x_i) = \frac{1}{\Delta V} \int_V I_\varphi(r_i)\,\mathrm{d}V = \frac{\Delta V_\mathrm{f}}{\Delta V}, \tag{2.64}$$

where ΔV is the total volume of the REV.

Two types of volume average are commonly considered in the field of porous media modeling. The superficial average denoted by the averaging operator $\langle\cdot\rangle^s$ of an arbitrary scalar quantity Φ is defined as

$$\langle\Phi\rangle^s(x_i,t) = \frac{1}{\Delta V} \int_V I_\varphi(r_i)\Phi(r_i,t)\,\mathrm{d}V. \tag{2.65}$$

It is based on the total volume of the REV, ΔV, and can thus be considered as an average disregarding the presence of the solid phase, whereas in the definition of the *intrinsic average*, denoted by the operator $\langle\cdot\rangle$, only the volume available to the fluid is considered as a basis, resulting in

$$\langle\Phi\rangle(x_i,t) = \frac{1}{\Delta V_\mathrm{f}} \int_V I_\varphi(r_i)\Phi(r_i,t)\,\mathrm{d}V. \tag{2.66}$$

By combining Eqs. (2.65) and (2.66), the simple expression

$$\langle\Phi\rangle^s = \varphi\,\langle\Phi\rangle. \tag{2.67}$$

relating both types of averages is obtained. Based on the intrinsic average, the arbitrary scalar Φ can be decomposed according to

$$\Phi = \langle\Phi\rangle + {}^\mathrm{i}\phi, \tag{2.68}$$

where ${}^\mathrm{i}\phi$ quantifies the spatial variation with respect to the average value.

Relying on these definitions, the VANS equations of Whitaker [159] for an incompressible Newtonian fluid can be written as

$$\frac{\partial}{\partial x_j}\left(\varphi\langle U_j\rangle\right) = 0 \tag{2.69}$$

and

$$\frac{\partial}{\partial t}\left(\varphi\langle U_i\rangle\right)+\varphi\langle U_j\rangle\frac{\partial\langle U_i\rangle}{\partial x_j}=-\frac{1}{\rho}\frac{\partial}{\partial x_i}\left(\varphi\langle P\rangle\right)+\nu\frac{\partial^2}{\partial x_j\partial x_j}\left(\varphi\langle U_i\rangle\right)-\frac{\partial}{\partial x_j}\left(\varphi\langle{}^{\mathrm{i}}u_i{}^{\mathrm{i}}u_j\rangle\right)+\varphi\langle F_{\mathrm{d},i}\rangle. \quad (2.70)$$

Here, $\langle F_{\mathrm{d},i}\rangle$ represents the components of the density-specific total drag force per unit volume exerted on the fluid by the porous matrix, i.e. the projected contributions of the stress tensor integrated over the fluid-solid interface A in the REV, given by

$$\langle F_{\mathrm{d},i}\rangle=\frac{1}{\varphi\Delta V}\int_A n_j\left(-\frac{P}{\rho}\delta_{ij}+\nu\frac{\partial U_i}{\partial x_j}\right)\mathrm{d}A, \quad (2.71)$$

where n_j are the components of the unit normal vector on A, pointing outward with respect to the fluid phase (see Fig. 2.10). Obviously, the exact expression for $\langle F_{\mathrm{d},i}\rangle$ contains the microscopic pressure and velocity distributions along the fluid-solid interface. Since those microscopic details are unknown from a macroscopic point of view, an appropriate closure model for $\langle F_{\mathrm{d},i}\rangle$ is required. Following arguments presented in Whitaker [158], Breugem *et al.* [21] expanded Eq. (2.71) as

$$\langle F_{\mathrm{d},i}\rangle\approx\underbrace{\frac{1}{\varphi\Delta V}\int_A n_j\left(-\frac{{}^{\mathrm{i}}p}{\rho}\delta_{ij}+\nu\frac{\partial{}^{\mathrm{i}}u_i}{\partial x_j}\right)\mathrm{d}A}_{\langle f_{\mathrm{d},i}\rangle}+\frac{\langle P\rangle}{\varphi\rho}\frac{\partial\varphi}{\partial x_i}-\frac{\nu}{\varphi}\frac{\partial\varphi}{\partial x_j}\frac{\partial\langle U_i\rangle}{\partial x_j}. \quad (2.72)$$

Here, the last two terms are now formulated in terms of macroscopic quantities and can be combined with respective terms in Eq. (2.70). The remaining term denoted as $\langle f_{\mathrm{d},i}\rangle$, is customarily parametrized [159] in line with the Darcy and Forchheimer laws generalized for the three-dimensional case as

$$\langle f_{\mathrm{d},i}\rangle=-\nu\left(K^{-1}\right)_{ij}\varphi\left\langle U_j\right\rangle-\nu\left(K^{-1}\right)_{ij}F_{jk}\,\varphi\left\langle U_k\right\rangle, \quad (2.73)$$

where $(K^{-1})_{ij}$ represents the components of the inverse of the permeability tensor and F_{jk} are the components of the Forchheimer tensor.

In order to apply scale-resolving turbulence models based on the RANS framework, an additional ensemble averaging of the VANS equations is required. Recalling from Section 2.2.3 that the $\widetilde{(\cdot)}$ operator is

in this work used to indicate ensemble averaging, an arbitrary scalar Φ is decomposed as

$$\Phi = \widetilde{\Phi} + \phi'', \tag{2.74}$$

where $\widetilde{\Phi}$ and ϕ'' can be considered as the resolved and unresolved contributions to Φ, respectively. Due to the two consecutive averaging operations, the double-decomposition concept of de Lemos [36] is applied to Eq. (2.68) resulting in

$$\Phi = \underbrace{\langle\widetilde{\Phi}\rangle + \langle\phi''\rangle}_{\langle\Phi\rangle} + \underbrace{{}^{\mathrm{i}}\widetilde{\phi} + {}^{\mathrm{i}}\phi''}_{{}^{\mathrm{i}}\phi}. \tag{2.75}$$

After insertion of this decomposition into Eqs. (2.69) – (2.70) and performing an ensemble averaging, the double-averaged equations in intrinsic form are obtained after a slight rearrangement as

$$\frac{\partial}{\partial x_j}\left(\varphi\langle\widetilde{U}_j\rangle\right) = 0 \tag{2.76}$$

and

$$\frac{\partial\langle\widetilde{U}_i\rangle}{\partial t} + \frac{1}{\varphi}\frac{\partial}{\partial x_j}\left(\varphi\langle\widetilde{U}_i\rangle\langle\widetilde{U}_j\rangle\right) = -\frac{1}{\rho}\frac{\partial\langle\widetilde{P}\rangle}{\partial x_i} + \frac{\nu}{\varphi}\left(\varphi\frac{\partial^2\langle\widetilde{U}_i\rangle}{\partial x_j\partial x_j} + \frac{\partial\varphi}{\partial x_j}\frac{\partial\langle\widetilde{U}_i\rangle}{\partial x_j} + \langle\widetilde{U}_i\rangle\frac{\partial^2\varphi}{\partial x_j\partial x_j}\right) - \frac{1}{\varphi}\frac{\partial}{\partial x_j}\left(\varphi\langle\widetilde{u_i''u_j''}\rangle + \varphi\langle{}^{\mathrm{i}}\widetilde{u}_i{}^{\mathrm{i}}\widetilde{u}_j\rangle\right) + \langle\widetilde{f}_{\mathrm{d},i}\rangle, \tag{2.77}$$

with

$$\langle\widetilde{f}_{\mathrm{d},i}\rangle = -\nu\,(K^{-1})_{ij}\,\varphi\,\langle\widetilde{U}_j\rangle - \nu\,(K^{-1})_{ij}\,F_{jk}\,\varphi\,\langle\widetilde{U}_k\rangle. \tag{2.78}$$

Here, $\langle\widetilde{u_i''u_j''}\rangle$ is the macroscopic residual stress tensor (MRST) and $\langle{}^{\mathrm{i}}\widetilde{u}_i{}^{\mathrm{i}}\widetilde{u}_j\rangle$ represents the dispersion due to spatial variations in the ensemble-averaged velocity field [36], analogous to the dispersive stresses defined with respect to the time average discussed in Section 2.3.1. Similarly to roughness modeling, dispersive stresses are often neglected, with Breugem *et al.* [21] arguing based on an order-of-magnitude analysis that sub-scale dispersion is generally negligible compared to the drag force and Reynolds stresses of the volume-averaged flow field. Based on this argument, i.e. with $\langle{}^{\mathrm{i}}\widetilde{u}_i{}^{\mathrm{i}}\widetilde{u}_j\rangle \approx 0$, the closure problem reduces to the MRST whose modeling is addressed in the following section.

2.4.2 Turbulence modeling in porous media

Various RANS-based turbulence models for flow through porous media have been proposed. Since the focus of the present work is on scale-resolving turbulence modeling approaches, no detailed discussion on RANS-based models is provided at this point. Instead, the reader is referred to de Lemos [36] and references therein for an overview. Nevertheless, some brief remarks concerning porous media RANS models shall be made. Structurally, two key differences compared to their single-phase counterparts can be identified: firstly, the inclusion of the porosity φ in the turbulence model equations either explicitly, or implicitly through a formulation based on superficially-averaged quantities, and secondly, the addition of modeled source terms accounting for the modification of the respective turbulent quantity due to drag exerted on the flow by the solid matrix. However, there is no consensus about the structure of the turbulence model equations and the source terms associated with the drag closure. A further problem is that porous media RANS models are often derived and calibrated assuming constant porosity. This is especially problematic for computations of hybrid domains, i.e. domains including both porous and clear-fluid regions, due to the associated gradient of φ at the interface between these regions. For such cases, various authors proposed so-called interfacial jump conditions which have to be imposed at the interface and often include calibrated coefficients with questionable universality. Moreover, jump conditions are difficult to apply when the transition between porous and clear fluid zones is rather smooth or when parts of the turbulent spectrum shall be resolved. Furthermore, preliminary investigations with porous media RANS models that have previously been applied to hybrid domains without jump conditions, indicated highly unsatisfactory performance. Overall, the validation basis for porous media RANS models appears to be fairly limited in comparison to their single-phase counterparts. Thus, the scale-resolving models applied to the VANS framework in this work, are modified single-phase turbulence models where porosity is subsequently introduced in the model equations.

Since EVM's are applied, the MRST is modeled as proposed by Antohe and Lage [4] in analogy to Boussinesq's eddy-viscosity assumption

extended for the double-averaged Navier-Stokes framework as

$$\varphi\widetilde{\langle u_i'' u_j'' \rangle} = -2\nu_\mathrm{t}\langle\widetilde{S}_{ij}\rangle + \frac{2}{3}\varphi\langle k_\mathrm{u}\rangle\delta_{ij}, \tag{2.79}$$

where

$$\langle\widetilde{S}_{ij}\rangle = \frac{1}{2}\left[\frac{\partial}{\partial x_j}\left(\varphi\langle\widetilde{U}_i\rangle\right) + \frac{\partial}{\partial x_i}\left(\varphi\langle\widetilde{U}_j\rangle\right)\right] \tag{2.80}$$

is the rate of strain tensor based on the double-averaged velocity field. As indicated by the $\widetilde{(\cdot)}$ operator, which is in this work applied in conjunction with scale-resolving turbulence models from the LES and hybrid RANS/LES frameworks, $\langle k_\mathrm{u}\rangle = 1/2\,\widetilde{\langle u_i'' u_j'' \rangle}$ describes the unresolved or sub-scale contribution to the total volume-averaged TKE $\langle k\rangle$ and ν_t the corresponding sub-scale eddy-viscosity. In the case of RANS-based models, transport equations for $\langle k_\mathrm{u}\rangle$, $\langle \varepsilon_\mathrm{u}\rangle$, $\langle \omega_\mathrm{u}\rangle$, $\langle \zeta_\mathrm{u}\rangle$ and $\langle f_\mathrm{u}\rangle$ are solved, depending on the applied model, in order to estimate the sub-scale eddy-viscosity. Further details on the modified single-phase turbulence models will be provided in Section 5.3.1.

3 Numerical methods

The governing equations in CFD, in particular, the Navier-Stokes and associated scalar transport equations discussed in Section 2.1, constitute a system of coupled (non-linear) partial differential equations (PDEs). Since analytical solutions for the Navier-Stokes equations have so far only been found for a limited number of geometrically simple and/or laminar flows, a numerical method is required in order to obtain an approximate solution by spatially discretizing the problem, and thus transforming the system of coupled PDE's into a system of linear equations. In the scope of this work, the open-source continuum mechanics library OpenFOAM (version 2.4.x) [113], developed by the OpenFOAM Foundation Ltd and released under the GNU General Public License 3 (GPLv3), is employed. As most engineering CFD software, OpenFOAM's fluid mechanics libraries are based on the finite-volume method (FVM) for spatial discretization. The FVM is commonly applied in CFD due to its inherent conservative properties and its flexibility regarding different grid types (e.g. unstructured, polyhedral cells), which facilitates the discretization of complex geometries [40]. In the following sections, the principles of the FVM and associated interpolation schemes, as well as the temporal discretization methods applied in this work, are outlined. For a more comprehensive overview of numerical methods in CFD, the reader is referred to Schäfer [129] or Ferziger and Perić [40].

3.1 Finite-volume method

Following the above-cited literature, the spatial discretization procedure of the FVM is discussed in terms of a generic advection-diffusion equation for an arbitrary scalar quantity Φ given by

$$\frac{\partial}{\partial x_i}\left(\rho U_i \Phi - \Gamma \frac{\partial \Phi}{\partial x_i}\right) = q, \tag{3.1}$$

with Γ and q denoting the diffusion coefficient and the source term, respectively. For the time being, the local time derivative term is neglected, as its treatment has no effect on the spatial discretization and will be discussed separately in Section 3.2.

In the first step, a numerical grid is generated: the problem domain is decomposed into a finite number of well-defined control volumes (CVs). Each CV (or *cell*) is associated with a computational node at its centroid, where discretized values of the continuous fields ought to be computed. For the sake of simplicity, the two-dimensional cartesian grid shown in Fig. 3.1 is adopted for further considerations. The computational nodes in the neighborhood of the grey reference CV with node P are labeled in compass notation as N, E, EE, S and W. Furthermore, each of the faces to the neighboring cells of P, denoted by the respective lower case letter (n, e, s and w), are associated with an outward pointing unit normal vector n_i.

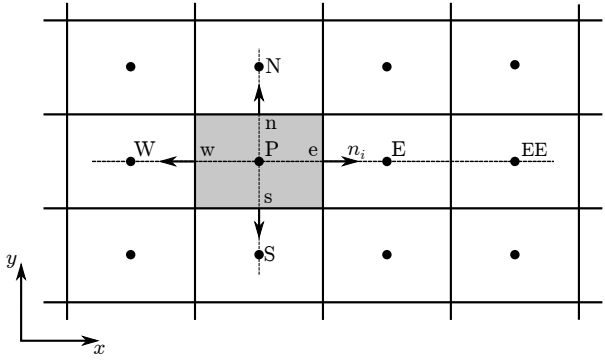

Figure 3.1: Sketch of a two-dimensional cartesian grid. Nomenclature in compass notation with respect to the grey control volume.

For the spatial discretization in the FVM framework, the integral balance equation for the CVs have to be formulated. This is achieved by integration of Eq. (3.1) and subsequent application of Gauss's theorem to the left-hand side, yielding

$$\int_S \left(\rho U_i \Phi n_i - \Gamma \frac{\partial \Phi}{\partial x_i} n_i \right) \mathrm{d}S = \int_V q \, \mathrm{d}V, \tag{3.2}$$

where V denotes the volume of the CV and S its surface. Further, the surface integral can be written as the sum over the faces S_c (c = n, e, s, w):

$$\sum_c \int_{S_c} \left(\rho U_i \Phi n_i - \Gamma \frac{\partial \Phi}{\partial x_i} n_i \right) \mathrm{d}S_c = \int_V q \, \mathrm{d}V. \tag{3.3}$$

In order to obtain a fully discretized set of equations, the surface and volume integrals have to be approximated using numerical quadrature. Thereby, the integrands of the surface integrals, which contain values at the faces, have to be expressed in terms of nodal values by means of interpolation. These issues are addressed in the following two sections.

3.1.1 Approximation of the integrals

For the approximation of the integrals in the context of the FVM, the midpoint rule is adopted. Hence, the integral is approximated by evaluating the value of the integrand in the center (or midpoint) of the integration domain and multiplying with the integration area. This yields a second-order accurate approximation, i.e. the integration is exact for a constant or linear integrand. While higher order approximations such as the Simpson rule could generally be applied, the midpoint rule is usually adopted due to its simplicity, especially in terms of requiring only one value in the center of the integration domain, which limits the necessity for additional interpolation steps.

For the volume integral of the source term over a CV, the application of the midpoint rule yields

$$\int_V q \, \mathrm{d}V \approx q_\mathrm{P} \Delta V, \tag{3.4}$$

where q_P is the value of the source term at the centroid P and ΔV the volume of the CV. Since all variables are already stored at the centroid, no further interpolation is required for the volume integral.

The advective flux over the CV face S_c, representing the first summand in the surface integral in Eq. (3.3), is again approximated by applying the midpoint rule. With the area ΔS_c of the face and the

mass flow rate $\dot{m}_c = (\rho U_i n_i)_c \, \Delta S_c$ over the face, one obtains

$$\int_{S_c} \rho U_i \Phi n_i \, \mathrm{d}S_c \approx (\rho U_i n_i)_c \, \Delta S_c \Phi_c = \dot{m}_c \Phi_c, \tag{3.5}$$

with the value Φ_c at the center of S_c initially unknown. The second summand in Eq. (3.3), representing the diffusive flux, is approximated analogously as

$$-\int_{S_c} \Gamma \frac{\partial \Phi}{\partial x_i} n_i \, \mathrm{d}S_c \approx -(\Gamma n_i)_c \, \Delta S_c \left(\frac{\partial \Phi}{\partial x_i} \right)_c . \tag{3.6}$$

Both, Φ_c as well as the partial derivative $(\partial \Phi / \partial x_i)_c$ represent values on CV faces and consequently have to be expressed in terms of nodal values by means of an appropriate interpolation scheme. In the following, an overview of the interpolation schemes used in this work is given.

3.1.2 Interpolation schemes

As will be discussed in this section, the choice of interpolation scheme for the advective term in the Navier-Stokes equation has a significant impact on the accuracy of the results – in particular of scale-resolving simulations. A vast amount of interpolation schemes have been proposed in literature, which can be classified according to their numerical properties such as order of accuracy, stability or boundedness of the solution. Apart from the usage of different stencils, i.e. the choice of nodes contributing to the interpolated value, many schemes differentiate by blending contributions from various basic interpolation schemes in order to achieve certain numerical properties. Hereafter, the two basic interpolation schemes representing the bounds of all schemes applied in this work, the upwind and the central differencing scheme, are summarized. Furthermore, two of OpenFOAM's blended high-resolution schemes based on flux limiters, the total variation diminishing *limitedLinear* scheme and the *filteredLinear3* scheme are introduced. All considerations in the following sections are made exemplary for the approximation of the value at the eastern CV face e. A more comprehensive discussion on numerical properties, blending procedures and flux limiters for interpolation schemes can be found e.g. in Hirsch [62].

3.1.2.1 Upwind differencing scheme

The upwind differencing scheme (UDS) directly uses the value of the closest upstream computational node in order to approximate the corresponding face value. For the value at the eastern face Φ_e, this yields

$$\Phi_\mathrm{e} = \begin{cases} \Phi_\mathrm{P} & \text{if } \dot{m}_\mathrm{e} > 0, \\ \Phi_\mathrm{E} & \text{if } \dot{m}_\mathrm{e} < 0, \end{cases} \tag{3.7}$$

depending on the direction of the mass flow rate $\dot{m}_\mathrm{e}$ over the CV face S_e. Inherently to its construction, UDS is unconditionally bounded, i.e. no local maxima or minima are introduced, which otherwise could result in non-physical oscillations in the solution [129]. On the other hand, UDS is only first-order accurate and the leading error term – which can be derived by means of a Taylor series expansion – is proportional to the local derivative of Φ, resulting in a diffusion-like interpolation error commonly denoted as *numerical diffusion*. Especially in the context of scale-resolving simulations, where larger gradients of the advected velocity will be present in comparison to a RANS solution describing only the mean flow field, the application of UDS-based schemes for the advective fluxes will provide an additional dissipation term competing with the physical sub-scale model (see e.g. Sagaut [127]) which can significantly reduce the accuracy of the solution. Hence, wherever possible centered higher order schemes should be applied.

3.1.2.2 Central differencing scheme

Due to the second-order accurate approximation of the integrals, the application of a higher than second-order interpolation scheme would be of questionable benefit. Hence, the central differencing scheme (CDS) is adopted as the higher order scheme. With CDS, the value Φ_e at the eastern CV face is approximated by linear interpolation between the neighboring nodal values according to

$$\Phi_\mathrm{e} = \Phi_\mathrm{E} \frac{x_\mathrm{e} - x_\mathrm{P}}{x_\mathrm{E} - x_\mathrm{P}} + \Phi_\mathrm{P} \frac{x_\mathrm{E} - x_\mathrm{e}}{x_\mathrm{E} - x_\mathrm{P}}, \tag{3.8}$$

where x denotes the coordinate of the respective computational node or CV face. While second-order accurate, boundedness of the solution can

not be guaranteed, i.e. non-physical oscillations might be introduced [129].

In the context of this work, a central differencing formula is also applied in terms of a differential quotient for the estimation of the face-normal gradient term appearing in the diffusive fluxes, yielding

$$\left(\frac{\partial \Phi}{\partial x_i}\right)_{\mathrm{e}} \approx \frac{\Phi_{\mathrm{E}} - \Phi_{\mathrm{P}}}{x_{\mathrm{E}} - x_{\mathrm{P}}}. \tag{3.9}$$

This approximation is only second-order accurate for an equidistant grid, while otherwise being associated with a first-order error term proportional to the deviation of the expansion ratio from unity [129].

3.1.2.3 High-resolution schemes

In order to combine the accuracy of high-order schemes such as CDS with the boundedness properties of UDS, a variety of high-resolution schemes based on flux limiters have been proposed following the pioneering work of van Leer [153]. The basic idea is to blend the value obtained with a lower order scheme $\Phi_{\mathrm{e}}^{\mathrm{LO}}$, usually based on UDS according to Eq. (3.7), with the higher-order interpolation value $\Phi_{\mathrm{e}}^{\mathrm{HO}}$, presently obtained with CDS according to Eq. (3.8), yielding

$$\Phi_{\mathrm{e}} = \Phi_{\mathrm{e}}^{\mathrm{LO}} - \gamma(\Phi_{\mathrm{e}}^{\mathrm{LO}} - \Phi_{\mathrm{e}}^{\mathrm{HO}}). \tag{3.10}$$

Here, γ is the limiter function in the range $0 \leq \gamma \leq 1$, which is determined for each face at each time step based on the local flow conditions. The limiter function γ is in general constructed with the goal to prevent spatial gradients from exceeding certain realizability constraints or changing sign between adjacent nodes [62]. In the following, the limiter functions for the high-resolution schemes applied in this work are summarized.

OpenFOAM's *limitedLinear* scheme employs a modified Sweby [145] limiter as blending function between UDS and CDS. The limiter is defined as

$$\gamma = \max\left(\min\left(\frac{2r}{C_{\mathrm{lim}}}, 1\right), 0\right), \tag{3.11}$$

where r is the so-called *ratio of successive gradients* given by

$$r = \frac{2d_i \left(\partial\Phi/\partial x_i\right)_C}{\Phi_\mathrm{E} - \Phi_\mathrm{P}} - 1, \tag{3.12}$$

with $C = \mathrm{P}$, if $\dot{m}_\mathrm{e} > 0$ and $C = \mathrm{E}$ otherwise, corresponding to the upwind transport concept. Furthermore, d_i denotes the vector between the centroids P and E. Finally, C_lim is an input parameter enabling the user to adapt the scheme's level of accuracy and boundedness. Setting $C_\mathrm{lim} = 0$ essentially results in a shift towards the higher-order CDS scheme ($\gamma \to 1$), resulting in the highest accuracy yet least bounded solution. In this work, the scheme is used exclusively with $C_\mathrm{lim} = 1$, rendering the scheme compliant with the properties of the total variation diminishing (TVD) class of interpolation schemes (see e.g. Hirsch [62]), ensuring a bounded, non-oscillatory solution. However, *limitedLinear* is still associated with levels of numerical diffusion impeding the application in the discretization of the advective term in the momentum equation for scale-resolving computations of turbulence and is presently used solely for the energy equation.

OpenFOAM's *filteredLinear3* scheme was designed specifically for the advective term in the Navier-Stokes equation in the context of scale-resolving simulations, with the aim to "remove high-frequency modes with 'staggering' characteristics" [113]. Fig. 3.2 illustrates the problem of these 'staggering' characteristics by means of the mean streamwise velocity field for the case of flow over a two-dimensional fence, which will be discussed in more detail in Section 4.3.2. With CDS (see Fig. 3.2, left) pronounced non-physical oscillations originating from the separation point at the upper left corner of the fence and propagating further upstream are obtained. These oscillations, which can also be observed in the instantaneous velocity field, impact the accuracy of the results such as e.g. the length of the recalculation zone behind the fence, mainly by modifying resolved turbulent structures. As illustrated in Fig. 3.2 (right), this problem is effectively mitigated by applying the *filteredLinear3* scheme, which locally introduces up to 100% of the UDS value ($\gamma \to 0$) in order to damp these oscillations. However, due to the very selective local damping, only a small amount of UDS – and thus little numerical diffusion – is introduced globally. Specifically, in

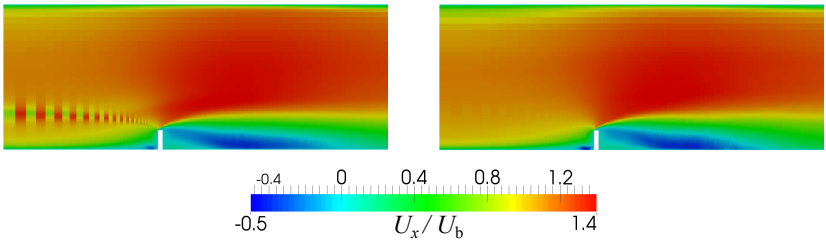

Figure 3.2: Mean streamwise velocity field normalized by the bulk velocity U_b of the flow over a two-dimensional fence, obtained with different interpolation schemes for the advective term in the momentum equation: central differencing scheme (left) and *filteredLinear3* with $C_\mathrm{lim} = 0.5$ (right).

the present computation the application of *filteredLinear3* results in an average of 96% CDS, which can be regarded as a typical value for the flow configurations considered in this work.

Since no reference to the scheme is provided with the source code by the primary developers of OpenFOAM, the scheme is discussed in some detail in the following. *filteredLinear3*'s selective local damping is achieved through a limiter function detecting high-frequency oscillations on the scale of the grid spacing by comparing the face gradient, represented here by the difference across the face e ($\Phi_\mathrm{E} - \Phi_\mathrm{P}$), with the neighboring nodal gradients $(\partial\Phi/\partial x_i)_\mathrm{E}$ and $(\partial\Phi/\partial x_i)_\mathrm{P}$ according to

$$\begin{aligned}\gamma = \max(&\\ &\min(\\ &1 - C_\mathrm{lim}\frac{\left[2d_i\left(\partial\Phi/\partial x_i\right)_\mathrm{E} - \left(\Phi_\mathrm{E} - \Phi_\mathrm{P}\right)\right]\left[2d_i\left(\partial\Phi/\partial x_i\right)_\mathrm{P} - \left(\Phi_\mathrm{E} - \Phi_\mathrm{P}\right)\right]}{\left[2d_i\left(\partial\Phi/\partial x_i\right)_\mathrm{E} + 2d_i\left(\partial\Phi/\partial x_i\right)_\mathrm{P}\right]^2},\\ &1),\\ &0).\end{aligned} \tag{3.13}$$

In principle, this formulation provides limiting to the CDS interpolation if the denominator is comparatively small. This would be the case either if the sign of the neighboring nodal gradient changes or if both

gradients are small. Additionally, the numerator has to assume comparatively large values, which would e.g. not be the case for nearly constant values across the CVs. This point, as well as the further influence of the nominator, can be more easily illustrated by applying CDS in terms of Eq. (3.9) for the discretization of the gradients in the nominator, yielding

$$\begin{aligned}\gamma = \max(&\\ &\min(\\ &\quad 1 - C_{\mathrm{lim}} \frac{(\Phi_{\mathrm{EE}} - \Phi_{\mathrm{E}})(\Phi_{\mathrm{P}} - \Phi_{\mathrm{W}})}{\left[2d_i \left(\partial\Phi/\partial x_i\right)_{\mathrm{E}} + 2d_i \left(\partial\Phi/\partial x_i\right)_{\mathrm{P}}\right]^2},\\ &\quad 1),\\ &0).\end{aligned} \tag{3.14}$$

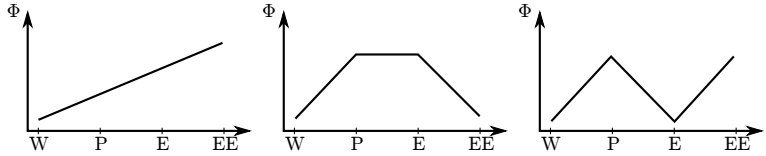

Figure 3.3: Illustration of exemplary scenarios for the explanation of the *filteredLinear3* limiter function

With this formulation in mind, some illustrative situations depicted in Fig. 3.3 can be discussed to gain further insight into the construction of the limiter function. A monotone profile of Φ, as shown in Fig. 3.3 (left), is associated with a positive nominator but at the same time a larger denominator resulting effectively in a high value of γ. The situation depicted in Fig. 3.3 (middle) is associated with changing signs of the gradients and hence a relatively small denominator. In this case however, the differences in the nominator change sign as well, resulting in $\gamma \to 1$. In the situation with staggering characteristics on the order of the grid spacing illustrated in Fig. 3.3 (right) a CDS approximation of the gradients around P and E results in a small value of the denominator. Simultaneously, the differences in the nominator have a finite value with the same sign, resulting finally in an activation of

the limiter ($\gamma < 1$). Thus, *filteredLinear3* provides an effective limiter function mitigating the problem of spurious oscillations by selectively introducing UDS contributions in the interpolation procedure. The appropriate value of C_{lim} is in this work determined on a case-by-case basis by gradually increasing the respective coefficient until no staggering can be observed in the flow field.

3.2 Temporal discretization

For the computation of transient flows or even globally-stable flows in conjunction with a scale-resolving turbulence modeling approach, the local time derivative previously omitted in Eq. (3.1) has to be added to the generic transport equation, resulting in

$$\frac{\partial}{\partial t}\left(\rho\Phi\right) + \frac{\partial}{\partial x_i}\left(\rho U_i \Phi - \Gamma \frac{\partial \Phi}{\partial x_i}\right) = q. \tag{3.15}$$

After completion of the spatial discretization procedure described in Section 3.1, the problem reduces to a set of first order initial value problems for each of the N CVs. For ease of notation, the spatial discretization is expressed by the operator $\mathcal{S}$ such that

$$\frac{\partial \Phi_i}{\partial t} = \mathcal{S}_i(\Phi_j), \quad \Phi_i(t_0) = \Phi_i^0, \quad i = 1...N, \tag{3.16}$$

with the initial conditions Φ_i^0 at the starting time t_0. For the sake of simplicity, a constant time step Δt is assumed in the following.

OpenFOAM employs implicit schemes for time marching, i.e. schemes relying on the spatial discretization operator being evaluated at the new time step t_{n+1} and thus containing the initially unknown values $\Phi_i^{n+1} = \Phi_i(t_{n+1})$. Consequently, a system of linear equations has to be solved. In contrast, this is not the case with explicit methods, which rely exclusively on previously computed values for the temporal discretization procedure. However, implicit schemes are advantageous in terms of stability and numerical constraints regarding the allowed time step width [129]. The most basic implicit method is the so-called *implicit Euler method*, which approximates the time derivative at time t_{n+1} as

$$\left(\frac{\partial \Phi_i}{\partial t}\right)_{t_{n+1}} \approx \frac{\Phi_i^{n+1} - \Phi_i^n}{\Delta t} \approx \mathcal{S}_i(\Phi_i^{n+1}). \tag{3.17}$$

In order to carry over the second-order accuracy in terms of spatial discretization to time marching, the second-order accurate backward differencing formula (BDF) is applied for all scale-resolving simulations in the context of this work. The temporal derivative is then approximated as

$$\left(\frac{\partial \Phi_i}{\partial t}\right)_{t_{n+1}} \approx \frac{3\Phi_i^{n+1} - 4\Phi_i^n + \Phi_i^{n-1}}{2\Delta t} \approx f(\Phi_i^{n+1}). \tag{3.18}$$

In comparison to the implicit Euler method, this formula additionally requires the values Φ_i^{n-1} at the penultimate time level which is simply stored in memory.

Finally, the Courant number, a non-dimensional quantity suitable for the determination of an appropriate time step width is introduced. Originally formulated as a convergence criterion for explicit time marching schemes, the Courant number can be considered as a factor quantifying how far in terms of multiples of the cell size a material point is transported within the time step Δt. Considering for the sake of simplicity a one-dimensional formulation, the Courant number is defined as

$$\mathrm{Co}_x = \frac{U_x \Delta t}{\Delta x}, \tag{3.19}$$

where U_x and Δx are the velocity and cell size in x-direction, respectively. While the applied implicit discretization schemes provide stable time marching for values $\mathrm{Co} > 1$, in scale-resolving computations commonly values $\mathrm{Co} < 1$ are applied in order to ensure that the dynamics of resolved turbulent eddies are captured accurately. In this work, OpenFOAM's adaptive time stepping algorithm is used, which adapts the step size Δt in each time step so that a prescribed maximum Courant number is maintained. The specific values for the computations presented in this work are in the range $\mathrm{Co} = 0.3...1$ and will be provided in Chapters 4 and 5.

4 Towards an eddy-resolving ζ-f model

The present chapter focuses on a computationally efficient scale-resolving turbulence modeling approach suitable for near-wall reactive flow applications. Specifically, internal combustion engines and exhaust gas aftertreatment systems are prominent examples guiding the development of the presently proposed modeling framework. From a fluid mechanics perspective, the intended applications can thus generally be described as internal flows at low to moderate Reynolds numbers. Due to the significance of the near-wall region with respect to the formation of pollutants and undesirable depositions, accurate predictions of turbulent statistics in the vicinity of wall are required as a basis for additional models accounting for these effects. Consequently, only wall-resolving turbulence modeling approaches are considered in this work.

While scale-resolving computations of turbulence are inherently more demanding in terms of computational resources compared to the classical RANS framework, the additional computational effort can be justified by improved predictive capabilities in terms of the flow field as well as significantly reduced modeling uncertainties in conjunction with coupled problems (e.g. multiphase flow, heat transfer and combustion/chemical reactions). Especially in academia, LES on highly resolved grids is frequently performed in this context. RANS-based scale-resolving models aim to reduce the required computational effort compared to LES by providing similar levels of accuracy on coarser grids by means of more sophisticated turbulence models. With respect to the RANS-based modeling strategies discussed in Section 2.2.3, approaches based on blending LES and RANS as well as 2G-URANS models would be the most suitable choices for the intended applications. The main reason for this restriction to 'seamless' models is that interfaces between LES and RANS zones would be located in the vicinity of the wall and therefore just in those areas that have been identified as important in

the context of the broader research questions related to near-wall reactive flows, that shall be addressed in the context of the collaborative research center this work is a part of. Specifically, interfaces and associated rapid changes in modeled quantities would introduce uncertainties and additional complexity with respect to the modeling of coupled phenomena such as combustion.

Based on these arguments the VLES model of Chang *et al.* [27] (see Section 2.2.3), which belongs to the category of blending LES and RANS, was identified as a suitable choice, especially since it was originally proposed in the context of internal combustion engines. However, as will be shown in Section 4.3, the model exhibits somewhat unsatisfactory performance on coarse grids compared to the dynamic Smagorinsky model. Various modifications to the VLES model have been investigated, however, with little success. Thus, in this chapter a new 2G-URANS model based on the same underlying RANS model – the ζ-f model of Hanjalić *et al.* [59] (see Section 2.2.1) – is formulated and validated. This new model, termed ER ζ-f, is sensitized relying on the SAS concept of Menter and Egorov [102] by introducing an additional production term in the scale-supplying equation.

As a starting point, the underlying RANS model is transformed to an ω-based formulation in Section 4.1. In Section 4.2, the transformed model is subsequently sensitized by introducing the newly formulated SAS term into the ω-equation. Finally, the model is validated and its performance is comparatively assessed by computing several generic flow configurations; corresponding results are presented in Section 4.3. Parts of the results and discussion presented in this chapter have been previously published or accepted for publication in the following articles or conference contributions: [79–82, 85, 86].

4.1 ω-based ζ-f RANS model

In a first step, the original ζ-f model is reformulated by transforming the scale-supplying equation from an equation for the dissipation rate ε to the specific rate of dissipation $\omega(=\varepsilon/k)$ in order to facilitate the sensitization of the model through introduction of a source term based on the SAS concept (see Section 4.2). While it is possible to apply a modified and recalibrated SAS term in the original ε-equation, preliminary

investigations indicated better model performance in fully-developed channel flow computations using an ω-based formulation. In the RANS framework, several researchers such as Wilcox [161, 162] and Menter *et al.* [100] advocate ω-based models in the near-wall region, mainly due to their superior performance for separating flows and under adverse pressure gradient conditions. A further advantage comes from the possibility to straightforwardly integrate the ω-equation through the viscous sublayer without additional empirical damping functions found in most low Reynolds k-ε models [161], which is however of minor concern with respect to the adopted elliptic-relaxation-based model. In this work, where the main focus is placed on the application of the present RANS model as a sub-scale model in scale-resolving simulations, the simpler wall boundary condition for ω is primarily considered advantageous: while the boundary condition for the dissipation rate according to Jones and Launder [71] is a finite value depending on the wall-normal gradient of the square root of TKE given by $\varepsilon_\mathrm{w} = 2\nu(\partial k^{1/2}/\partial y)^2|_\mathrm{w}$, the wall boundary condition for the specific dissipation rate is $\omega_\mathrm{w} \to \infty$. While an infinite value might seem numerically problematic, in practice, simply a value based on a hyperbolic variation [57] with $\omega_\mathrm{P} = 2\nu/y_\mathrm{P}^2$ is prescribed at the first wall adjacent grid node P, provided the first cell is located inside the viscous sublayer with $y_\mathrm{P}^+ \approx 1$. In any case, the boundary condition is less sensitive i.e. independent of additional modeled quantities, namely the TKE k, which in scale-resolving simulations would be made up of both modeled and resolved contributions. Consequently, transforming the scale-supplying equation is considered preferable compared to transforming the SAS term. A similar route was taken by Maduta [95] in his SAS-based instability-sensitive Reynolds stress model, which was derived also by transforming the scale-supplying equation of the Jakirlic and Hanjalić [67] Reynolds stress model to an ω-based formulation.

Thus, the ω-equation is derived by inserting the definition $\omega = \epsilon/k$ into the material derivative and utilizing the quotient rule according to

$$\frac{\mathrm{D}\omega}{\mathrm{D}t} = \frac{\mathrm{D}(\varepsilon/k)}{\mathrm{D}t} = \frac{1}{k}\frac{\mathrm{D}\varepsilon}{\mathrm{D}t} - \frac{\varepsilon}{k^2}\frac{\mathrm{D}k}{\mathrm{D}t}. \tag{4.1}$$

The material derivatives of ε and k are given by the right hand sides of the respective transport equations of the original ζ-f model, Eqs. (2.18) and (2.19), respectively. In order to limit the amount of additional terms

stemming from the transformation procedure, the coefficients in the diffusion terms are assumed to be equal ($\sigma_k = \sigma_\varepsilon = \sigma$). The transformed equation then reads

$$\frac{\partial \omega}{\partial t} + \overline{U}_j \frac{\partial \omega}{\partial x_j} = C_{\omega_1} \frac{\omega}{k} P_k - C_{\omega_2} \omega^2 + \frac{\partial}{\partial x_j} \left[\left(\nu + \frac{\nu_\mathrm{t}}{\sigma} \right) \frac{\partial \omega}{\partial x_j} \right] + CD, \quad (4.2)$$

with the coefficients $C_{\omega_1} = C_{\varepsilon_1} - 1$ and $C_{\omega_2} = C_{\varepsilon_2} - 1$. The cross-diffusion term CD emerges from the transformation procedure as

$$CD = \frac{2}{k} \left(\nu + \frac{\nu_\mathrm{t}}{\sigma} \right) \frac{\partial k}{\partial x_j} \frac{\partial \omega}{\partial x_j}. \quad (4.3)$$

The transformation of the scale-supplying equation necessitates the recalibration of the diffusion terms, since the coefficients have been unified as $\sigma_k = \sigma_\varepsilon = \sigma$ in the transformation procedure. In order to retain as much as possible the original model coefficients, the diffusion process is primarily recalibrated through modification of the additional cross-diffusion term. In the models of Wilcox [163] and Menter *et al.* [100] the cross-diffusion includes only the contribution of Eq. (4.3) associated with the eddy viscosity ν_t, which is dominant in the RANS framework. With regard to the application of the model for scale-resolving simulations, where the ratio ν_t/ν is generally smaller, presently both viscous and turbulent contributions are kept and calibrated by introducing the coefficients σ_{cd_ν} and $\sigma_{\mathrm{cd}_\mathrm{t}}$, similarly to the approach taken by Maduta [95]. Finally, the turbulent contribution to the cross-diffusion is bounded to positive values following Wilcox's [163] argument, that the term has to be suppressed close to solid boundaries in wall-bounded flows. Thus, the modeled cross-diffusion term is given by

$$CD = \frac{2}{k} \frac{\nu}{\sigma_{\mathrm{cd}_\nu}} \frac{\partial k}{\partial x_j} \frac{\partial \omega}{\partial x_j} + \max \left(\frac{2}{k} \frac{\nu_\mathrm{t}}{\sigma_{\mathrm{cd}_\mathrm{t}}} \frac{\partial k}{\partial x_j} \frac{\partial \omega}{\partial x_j}, 0 \right). \quad (4.4)$$

The model equation for k, ζ and f remain unchanged compared to the original ζ-f model described in Section 2.2.1 and shall not be repeated here. Consequently, the full ω-based ζ-f RANS model is given by Eqs. (2.18) and (2.20) – (2.25) together with the new scale supplying equation (4.2). The recalibrated model coefficients are summarized in Tab. 4.1.

Table 4.1: Model coefficients in the ω-based ζ-f RANS model.

a	C_τ	C_L	C_η
0.6	6.0	0.36	85

C_μ^ζ	C_{ω_1}	C_{ω_2}	C_1	C_2	σ	$\sigma_{\mathrm{cd_t}}$	σ_{cd_ν}	σ_ζ
0.22	$0.4\,(1+0.042/\zeta)$	0.9	0.4	0.65	1.1	1.2	1.6	1.2

4.1.1 Computations with the ω-based RANS model

Some illustrations of the performance of the ω-based model in comparison to the original ζ-f model shall be given in order to demonstrate the success of the transformation and recalibration procedure. All flow configurations from the test case library considered in this work have been computed with the transformed model. However, since RANS computations are not the focus of this work, only selected results for fully-developed channel flow at a range of Reynolds numbers and flow over a two-dimensional fence are presented here for the sake of brevity. These two flow configurations have been selected since they offer an impression of the similarity between the results obtained with the ω-based and original ζ-f models, while at the same time representing cases where RANS models provide reasonable results in comparison to scale-resolving simulations. Few details on the flow configurations are provided at this point. Instead, the reader is referred to Sections 4.3.1 and 4.3.2, where full details are given along with the results obtained with scale-resolving models.

Channel flow

Fully-developed turbulent channel flow is a geometrically simple, yet important generic flow configuration which is generally computed as a first validation case with any turbulence model. Presently, moderate friction Reynolds numbers based on the half channel height of $\mathrm{Re}_\tau = 180$, 392 and 640 are considered, for which DNS reference data is available from Kawamura *et al.* [72], Moser *et al.* [108] and Abe *et al.* [1], respectively. The RANS computations are performed on computational grids taking

Table 4.2: Reynolds numbers, non-dimensional grid spacing $\Delta y^+ = \Delta y u_\tau/\nu$ and total number of cells N for RANS computations of fully developed channel flow.

Re_τ	Re_b	Δy^+	N
180	5692	2...20	46
392	13758	2...20	100
640	24428	2...20	162

advantage of the spatial homogeneity of the mean flow, i.e. consisting of one cell in streamwise and spanwise directions. Periodic boundary conditions are applied in both these directions and the flow is driven by imposing a pressure gradient in the momentum balance corresponding to the respective bulk Reynolds number, presently defined in terms of

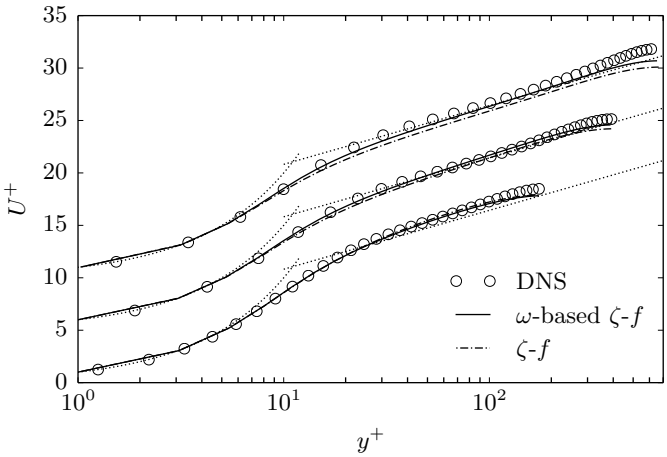

Figure 4.1: Mean streamwise velocity profiles for fully developed channel flow at $\mathrm{Re}_\tau = 180$, 392 and 640. Profiles shifted upwards by $\Delta U^+ = 5$ increments for clarity purposes. DNS data taken from Kawamura *et al.* [72] ($\mathrm{Re}_\tau = 180$), Moser *et al.* [108] ($\mathrm{Re}_\tau = 392$) and Abe *et al.* [1] ($\mathrm{Re}_\tau = 640$).

the channel height H as $\mathrm{Re_b} = U_\mathrm{b} H/\nu$. In line with the requirements of the applied near-wall models, the grids are set up with the first wall adjacent computational node situated in the viscous sublayer at $y^+ \approx 1$. Towards the center plane, the cells are coarsened uniformly with a total expansion ratio of 10. Details of the applied grids, which have found to provide grid-independent results, are summarized in Tab. 4.2. In terms of the applied numerical schemes, CDS was used for the convective term in the momentum equation, while UDS was employed for the respective terms in the turbulence model equations.

First order statistics in the form of mean velocity profiles in inner scaling ($U^+ = \overline{U}_x/u_\tau$) obtained with the ω-based as well as the original ζ-f model are presented in Fig. 4.1 together with the respective DNS reference data. As expected, both models capture the velocity profile fairly accurately with only minor deviations between the two EVM's. Specifically, the ω-based version is with increasing Reynolds number

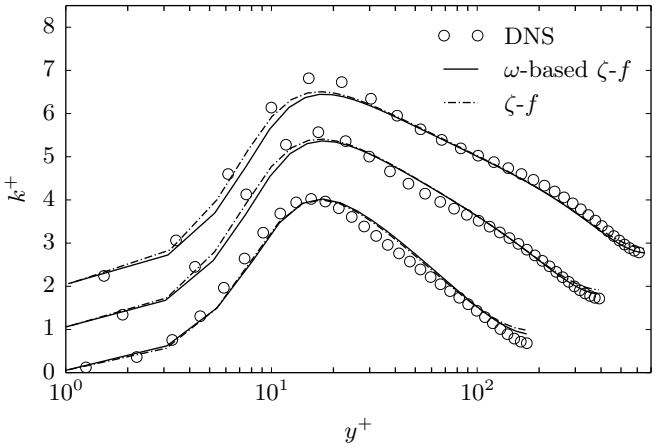

Figure 4.2: Mean TKE profiles for fully developed channel flow at Re_τ = 180, 392 and 640. Profiles shifted upwards by $\Delta k^+ = 1$ increments for clarity purposes. DNS data taken from Kawamura *et al.* [72] ($\mathrm{Re}_\tau = 180$), Moser *et al.* [108] ($\mathrm{Re}_\tau = 392$) and Abe *et al.* [1] ($\mathrm{Re}_\tau = 640$).

slightly more accurate in its prediction of the wall friction velocity u_τ, resulting in better agreement with the reference DNS data in the logarithmic region.

The associated profiles of TKE in inner scaling ($k^+ = k/u_\tau^2$) for the three Reynolds numbers are illustrated in Fig. 4.2. Here as well, only minor differences between the two models can be observed, with the ω-based formulation predicting slightly lower values of k^+ in the buffer layer at the two higher Reynolds numbers. In terms of accuracy, a comparison with the reference DNS reveals that both models provide very reasonable results for TKE.

Flow over a two-dimensional fence

The second flow configuration for which results with the ω-based ζ-f model are presented is the flow over a two-dimensional fence at a Reynolds number of $\mathrm{Re}_H = U_\mathrm{b} H/\nu = 22500$, based on the channel height H and the bulk velocity U_b. Further details on the flow configuration, which was investigated experimentally in Larsen *et al.* [88], are provided in Section 4.3.2. RANS computations are performed on a two-dimensional grid taking advantage of the spatial homogeneity of the mean flow in spanwise direction. The grid is refined towards the wall in order to ensure a non-dimensional distance of the first wall-adjacent grid node of $y^+ < 1$. The computational domain with dimensions $82/15H \times H$ in streamwise and wall-normal directions, is discretized by 65×115 cells upstream the fence, 16×75 cells above the fence and 200×115 cells downstream of the fence; in total 31675 cells. At the inflow boundary, profiles of fully-developed channel flow at the corresponding bulk Reynolds number are prescribed, while zero-gradient conditions are assumed at the outlet for all quantities but the pressure, for which a fixed mean value is imposed. In contrast to the previously discussed channel flow computations, a blended discretization scheme with equal weighting of CDS and UDS is applied for the convective term in the momentum equation for stability purposes.

Fig. 4.3 shows mean streamwise velocity profiles normalized by the bulk velocity, i.e $\overline{U}_x/U_\mathrm{b}$, at various positions x/h, where $h = 2/15H$ is the height of the fence. Both EVM's predict very similar velocity profiles at positions $x/h \leq 0$, which are in good agreement with the experimental reference data. Downstream of the fence, in the region

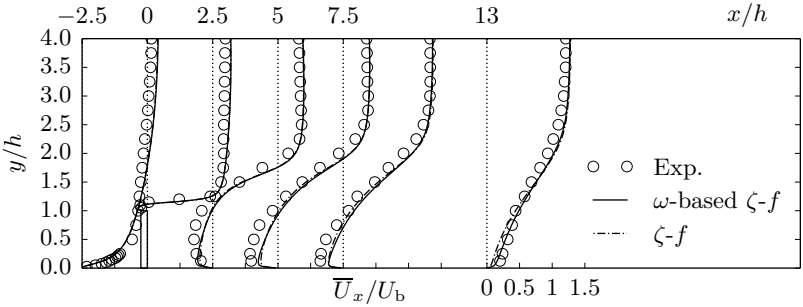

Figure 4.3: Mean streamwise velocity profiles for flow over a two-dimensional fence at $\mathrm{Re}_H = 22500$. Exp. data taken from Larsen *et al.* [88].

$2.5 \leq x/h \leq 7.5$ very minor discrepancies between the two models can be observed. In terms of accuracy, both models noticeably overpredict the velocity in the recirculation zone located below $y/h = 1$. At $x/h = 13$, i.e. after flow reattachment, the ω-based model more accurately captures the velocity profile close to the bottom wall, which can be attributed mainly to a better prediction of the reattachment point with the transformed model. Specifically, the experimentally obtained reattachment point is located at $x_\mathrm{r}/H = 11.7$ which is coincidentally the same value predicted by the ω-based model. The baseline ζ-f model exhibits a slightly longer recirculation zone with reattachment occurring at $x_\mathrm{r}/H = 12.4$. Jakirlic and Maduta [68] obtained $x_\mathrm{r}/H = 14.5$ with their low Reynolds second moment closure model. Thus, the recirculation lengths obtained with the present EVM's can be regarded as surprisingly accurate for RANS models. However, considering the overall mediocre level of agreement with the experimental database (also anticipating the result for TKE and Reynolds shear stress presented in the following) suggests that this level of accuracy can most likely be attributed to a cancelation of errors.

The TKE profiles normalized by the bulk velocity displayed in Fig. 4.4 exhibit more pronounced differences between the two EVM's. While both models are unable to capture the wall peak above the fence, the ω-based model predicts higher levels of TKE in the separating shear layer

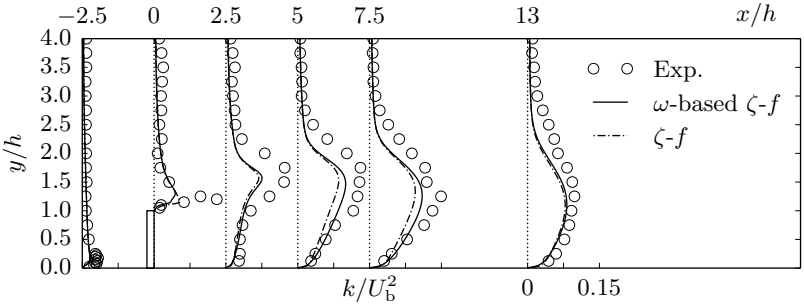

Figure 4.4: Mean TKE profiles for flow over a two-dimensional fence at $\mathrm{Re}_H = 22500$. Exp. data taken from Larsen *et al.* [88].

and recirculation region, which is in closer agreement to the experimental database. The correspondingly higher level of momentum transfer through the separating shear layer can be considered as the main reason for the shorter recirculation zone obtained with the ω-based model. Overall both models noticeably underpredict TKE levels in the entire region downstream of the fence.

Associated profiles of the Reynolds shear stress $\overline{u'v'}$, as usual normalized with the bulk velocity, are shown in Fig. 4.5. Both models are

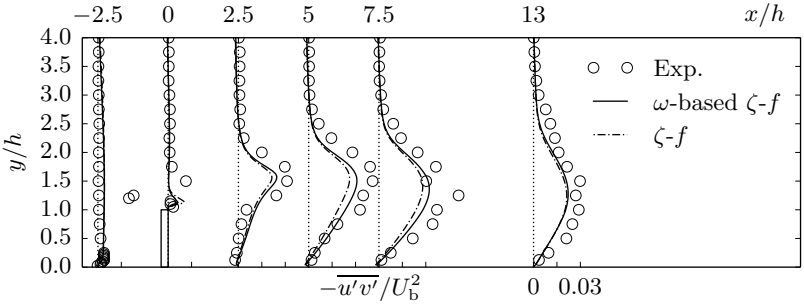

Figure 4.5: Mean Reynolds shear stress profiles for flow over a two-dimensional fence at $\mathrm{Re}_H = 22500$. Exp. data taken from Larsen *et al.* [88].

unable to capture the sign change above the fence. Other than that, comparable observations to the TKE profiles can be made: both models underpredict the turbulent activity in the vicinity of the separating shear layer, with the ω-based model exhibiting slightly better results compared to the original ζ-f model.

Conclusion

In summary, the presented results for channel flow and flow over a two-dimensional fence indicate that both EVM's perform very similar, with the ω-based variant exhibiting slightly better model performance in terms of predicting turbulence related quantities in the latter test case. While it is unclear wether this can be attributed to the application of an ω-equation or the recalibrated model constants, the results provide confidence for the application of the ω-based variant in the eddy-resolving ζ-f model, discussed in the following section.

4.2 Sensitizing the model: the SAS term

As previously outlined, the ω-based ζ-f RANS model is sensitized by introducing an additional source term based on the SAS concept of Menter *et al.* [103] into the scale-supplying ω-equation. Unlike the transport equation for TKE, which is generally modeled on a term-by-term basis starting from the exact transport equation, the scale supplying equation is rather formulated as a whole, in analogy to the TKE equation, instead of modeling the complex correlations in the exact ε or ω-equations directly [102]. For their SAS concept, Menter *et al.* [103] thus proposed the inclusion of an additional production term motivated by Rotta's [126] derivation of a scale supplying equation based on the product of TKE and the integral length scale, i.e. kL. Rotta defined kL in terms of the two-point correlation tensor R_{ij} assuming shear flow with a dominant gradient of the mean velocity in y-direction. The detailed derivation procedure given in [126] shall not be repeated here; instead only the production term, from which Menter and Egorov [102] derived the SAS term, is considered in the following. Rotta applied a Taylor series expansion with respect to the spatial shift r_y in the two-point

correlation to the respective production term, resulting in

$$-\frac{3}{16}\int_{-\infty}^{\infty}\frac{\partial\overline{U}(x_i+r_y\delta_{i2})}{\partial y}R_{12}\mathrm{d}r_y \approx \frac{\partial\overline{U}}{\partial y}\int_{-\infty}^{\infty}R_{12}\mathrm{d}r_y + \frac{\partial^2\overline{U}}{\partial y^2}\int_{-\infty}^{\infty}R_{12}r_y\mathrm{d}r_y + \frac{1}{2}\frac{\partial^3\overline{U}}{\partial y^3}\int_{-\infty}^{\infty}R_{12}r_y^2\mathrm{d}r_y + \mathcal{O}(r_y^3). \tag{4.5}$$

While Rotta kept the first and third term in their model kL equation, Menter and Egorov [101] present arguments that actually the term containing the second derivative of the velocity field should be kept as the leading order term. Following Rotta's modeling approach for the third term, the second term, presently denoted as $Q_{\mathrm{SAS},kL}$, can be approximated as

$$Q_{\mathrm{SAS},kL} = \frac{\partial^2\overline{U}}{\partial y^2}\int_{-\infty}^{\infty}R_{12}r_y\mathrm{d}r_y \approx const.\,\overline{u'v'}\,L^2\,\frac{\partial^2\overline{U}}{\partial y^2}. \tag{4.6}$$

For their k-ω SST SAS model, Menter and Egorov [102] modeled $\overline{u'v'} \sim \sqrt{k}L\overline{S}$ based on the Boussinesq eddy-viscosity assumption (2.16) with $\nu_\mathrm{t} \sim \sqrt{k}L$. The usage of the norm of the strain rate tensor $\overline{S} = \sqrt{2\overline{S}_{ij}\overline{S}_{ij}}$ instead of the respective components associated with $\overline{u'v'}$ can be considered as the first step towards the generalization of the model term formulated by Rotta for the special case of shear flow aligned with the x-direction. Maduta [95] adopted the same modeling strategy for a Reynolds stress model (RSM) based on the SAS concept (termed instability-sensitive RSM), but later suggested[1] modeling the turbulent shear stress component $\overline{u'v'} \sim k$ as a measure for the overall turbulence activity.

In order to introduce the additional production term into the ω-equation, the transformation rule

$$\frac{\mathrm{D}\omega}{\mathrm{D}t} = \frac{3}{2}\frac{\omega}{k}\frac{\mathrm{D}k}{\mathrm{D}t} - \frac{1}{C_\mu^{3/4}}\frac{\omega^2}{k^{3/2}}\frac{\mathrm{D}(kL)}{\mathrm{D}t}, \tag{4.7}$$

[1] R. Maduta, personal communication, 2017.

making use of the relation $\omega = C_\mu^{3/4} k^{3/2}/(kL)$ is applied to the kL-equation [95]. Again, only the additional term instead of the complete kL-equation is considered here for the sake of brevity. Inserting $\overline{u'v'} \sim k$ as well as $L \sim k^{1/2}/\omega$ into Eq. (4.6) and applying the transformation rule results is

$$Q_{\mathrm{SAS},kL} \xrightarrow{\text{Eq.(4.7)}} Q_{\mathrm{SAS}} = const.\, \frac{\omega^2}{k^{3/2}}\, k\, L^2\, \frac{\partial^2 \overline{U}}{\partial y^2} = const.\, \sqrt{k}\, \frac{\partial^2 \overline{U}}{\partial y^2}, \tag{4.8}$$

where Q_{SAS} is the transformed term for the ω-equation.

At this point, a change in notation is made to retain the notation introduced in Section 2.2.3 for scale-resolving turbulence models and emphasize that the final model describes the unresolved contributions to total TKE, i.e. k_u instead of k. The complementary velocity field associated with the sub-scale or unresolved TKE k_u is thus $\widetilde{U}_i$. Further, generalizing the second derivative in Eq. (4.8) for the three-dimensional case yields

$$Q_{\mathrm{SAS}} = const.\, \sqrt{k_\mathrm{u}}\, U'' \tag{4.9}$$

with

$$U'' = \sqrt{\frac{\partial \widetilde{U}_i}{\partial x_j^2}\, \frac{\partial \widetilde{U}_i}{\partial x_k^2}}. \tag{4.10}$$

Finally, the complete SAS term for the ω-equation is formulated analogously to Maduta [95] with exception of the Q_{SAS} part as

$$P_{\mathrm{SAS}} = C_{\mathrm{SAS},1} \max\Bigg(\underbrace{\sqrt{k_\mathrm{u}} U''}_{Q_{\mathrm{SAS}}} - C_{\mathrm{SAS},2}\, Q_2, 0 \Bigg), \tag{4.11}$$

with

$$Q_2 = 3 k_\mathrm{u} \max\left(\frac{1}{k_\mathrm{u}^2} \frac{\partial k_\mathrm{u}}{\partial x_j} \frac{\partial k_\mathrm{u}}{\partial x_j}, \frac{1}{\omega_\mathrm{u}^2} \frac{\partial \omega_\mathrm{u}}{\partial x_j} \frac{\partial \omega_\mathrm{u}}{\partial x_j} \right). \tag{4.12}$$

Here, all constants stemming from the derivation procedure have been absorbed in the model coefficients $C_{\mathrm{SAS},1}$ and $C_{\mathrm{SAS},2}$ for ease of notation. The basis for the Q_2 correction emerges from the transformation procedure given by Eq. (4.7) (see e.g. [95]); its derivation is however not repeated here, since the present formulation is adopted directly from Menter and Egorov [102], who proposed this specific bounding in order

to avoid changes to the performance of the underlying RANS model in boundary layer flows [102].

The P_{SAS} term ultimately results in a reduction of modeled TKE k_{u} in areas where inhomogeneity pertinent to resolved turbulent scales is indicated by the second derivative of the velocity field. The model consequently balances resolved and unresolved contributions of turbulence by appropriately decreasing modeled momentum diffusion through the eddy-viscosity ν_{t}, thus allowing for turbulent fluctuations to be resolved. Importantly, this behavior is achieved without introducing an additional length scale Δ based on the grid spacing as commonly practiced in the LES or hybrid RANS/LES framework. Instead, the additional length scale associated with resolved turbulent eddies is implicitly provided through the second derivative of the velocity field. While it can be argued that grid spacing is at least an implicitly relevant numerical factor considering the discrete approximation of the second velocity derivative is limited by the resolution pertinent to the numerical grid, in the SAS context, commonly more physical arguments based on the von Kármán length scale defined in terms of the second velocity derivative as

$$L_{\mathrm{vK}} = \kappa \frac{U'}{U''}, \tag{4.13}$$

with

$$U' = \widetilde{S} = \sqrt{2\widetilde{S}_{ij}\widetilde{S}_{ij}} \tag{4.14}$$

are presented. Consequently, the SAS term in the k-ω SST SAS [102] as well as the IS-RSM [95] is expressed in terms of the ratio of the RANS length scale as defined in the SST model $L_{\mathrm{SST}} = k_{\mathrm{u}}^{1/2}/(C_{\mu}^{1/4}\omega_{\mathrm{u}})$ and the von Kármán length scale L_{vK} representing a measure for the resolved turbulent scales. In order to facilitate a comparison with the respective SAS term formulations, the present SAS expression (4.11) can be similarly rewritten in terms of the $L_{\mathrm{SST}}/L_{\mathrm{vK}}$ ratio as

$$P_{\mathrm{SAS}} = C^{*}_{\mathrm{SAS},1} \max\left(\widetilde{S}\omega_{\mathrm{u}} \frac{L_{\mathrm{SST}}}{L_{\mathrm{vK}}} - C^{*}_{\mathrm{SAS},2}\, Q_2, 0\right). \tag{4.15}$$

It should be noted, that in this formulation the model coefficients are defined differently since additional constants stemming from the expansion with L_{SST} are absorbed. Differences can be identified in the

Q_{SAS} term, which in the k-ω SST SAS model of Menter and Egorov [102] is $Q_{\mathrm{SAS}} \sim \widetilde{S}^2(L_{\mathrm{SST}}/L_{\mathrm{vK}})^2$ and in Maduta's [95] IS-RSM $Q_{\mathrm{SAS}} \sim \widetilde{S}^2(L_{\mathrm{SST}}/L_{\mathrm{vK}})^{1/2}$. Following the present modeling strategy, a linear relation with respect to the length scale ratio is obtained similar to earlier proposals of Menter and Egorov [101]. In later publications (e.g. [102]) they changed the exponent to 2, arguing that in homogeneous turbulence not only the complete term Eq. (4.6) should be zero, which is naturally provided by $\partial^2\overline{U}/\partial y^2 = 0$ under theses conditions, but also the model expression for the integral over the two-point correlation tensor should be zero per-se based on Rotta's [126] symmetry argument. Maduta [95] however choose to replace the exponent with $1/2$ in order to flatten the additional production term with respect to the length scale ratio in order to prevent the depletion of modeled Reynolds stresses resulting from the application of the quadratic formulation in conjunction with their near-wall RSM. An additional difference is that $\widetilde{S}\omega_{\mathrm{u}}$ appears as the factor for the length scale ratio instead of $\widetilde{S}^2$ due to the modeling based on k_{u} for the turbulence activity in the Q_{SAS} term instead of the Boussinesq approach followed in other works.

Finally, the full model equations for the ER ζ-f model are summarized in the following. The model equation for sub-scale TKE reads

$$\frac{\partial k_{\mathrm{u}}}{\partial t} + \widetilde{U}_j \frac{\partial k_{\mathrm{u}}}{\partial x_j} = P_k - \varepsilon_{\mathrm{u}} + \frac{\partial}{\partial x_j}\left[\left(\nu + \frac{\nu_{\mathrm{t}}}{\sigma}\right)\frac{\partial k_{\mathrm{u}}}{\partial x_j}\right], \tag{4.16}$$

with the production term $P_k = \nu_{\mathrm{t}}\widetilde{S}_{ij}\widetilde{S}_{ij}$ and dissipation rate $\varepsilon_{\mathrm{u}} = \omega_{\mathrm{u}}k_{\mathrm{u}}$. Here, the sub-scale specific dissipation rate is governed by the transformed scale-supplying equation

$$\begin{aligned}\frac{\partial \omega_{\mathrm{u}}}{\partial t} + \widetilde{U}_j \frac{\partial \omega_{\mathrm{u}}}{\partial x_j} = C_{\omega_1}\frac{\omega_{\mathrm{u}}}{k_{\mathrm{u}}}P_k - C_{\omega_2}\omega_{\mathrm{u}}^2 \\ + \frac{\partial}{\partial x_j}\left[\left(\nu + \frac{\nu_{\mathrm{t}}}{\sigma}\right)\frac{\partial \omega_{\mathrm{u}}}{\partial x_j}\right] + CD + P_{\mathrm{SAS}},\end{aligned} \tag{4.17}$$

with the cross diffusion term

$$CD = \frac{2}{k_{\mathrm{u}}}\frac{\nu}{\sigma_{\mathrm{cd}_\nu}}\frac{\partial k_{\mathrm{u}}}{\partial x_j}\frac{\partial \omega_{\mathrm{u}}}{\partial x_j} + \max\left(\frac{2}{k_{\mathrm{u}}}\frac{\nu_{\mathrm{t}}}{\sigma_{\mathrm{cd}_{\mathrm{t}}}}\frac{\partial k_{\mathrm{u}}}{\partial x_j}\frac{\partial \omega_{\mathrm{u}}}{\partial x_j}, 0\right). \tag{4.18}$$

and the additional production term P_{SAS} as given by Eq. (4.11). The model equations for ζ_{u} and f_u remain unchanged compared to the orig-

inal formulation; merely the notation is adapted to comply with the scale-resolving nature of the ER ζ-f model. They are thus given by

$$\frac{\partial \zeta_\mathrm{u}}{\partial t} + \widetilde{U}_j \frac{\partial \zeta_\mathrm{u}}{\partial x_j} = f_\mathrm{u} - \frac{\zeta_\mathrm{u}}{k_\mathrm{u}} P_k + \frac{\partial}{\partial x_j}\left[\left(\nu + \frac{\nu_\mathrm{t}}{\sigma_\zeta}\right)\frac{\partial \zeta_\mathrm{u}}{\partial x_j}\right], \tag{4.19}$$

$$L_\mathrm{u}^2 \frac{\partial^2 f_\mathrm{u}}{\partial x_j \partial x_j} - f_\mathrm{u} = \frac{1}{T_\mathrm{u}}\left(C_1 + C_2 \frac{P_k}{\varepsilon_\mathrm{u}}\right)\left(\zeta_\mathrm{u} - \frac{2}{3}\right), \tag{4.20}$$

with $L_\mathrm{u} = C_L k_\mathrm{u}^{3/2}/\varepsilon_\mathrm{u}$ and $T_\mathrm{u} = 1/\omega_\mathrm{u}$. The length and time scale switches constrained by the Kolmogorov scales applied in the ζ-f RANS model are not retained in the ER version, since Kolmogorov scale estimates based solely on unresolved quantities describing only parts of the turbulent spectrum have been found to not provide reasonable physical scales. While this impairs the capability of the model to asymptotically reduce to the ω-based ζ-f model, this is a minor concern, considering that the goal of the ER ζ-f model is to resolve the majority of turbulent fluctuations on coarse grids and even in globally stable flow configurations. This represents a major distinction compared to the k-ω SST SAS model which is calibrated to provide RANS results even on sufficiently fine grids if the flow is globally stable (e.g. channel flow). The model coefficients correspond to the ω-based ζ-f RANS model summarized in Tab. 4.1. The coefficients in the P_SAS term are in this work set to $C_{\mathrm{SAS},1} = 0.35$ and $C_{\mathrm{SAS},2} = 0.034$. These values have been determined based on parameter studies conducted for the case of channel flow at $\mathrm{Re}_\tau = 392$ and the impinging jet discussed in Section 4.3.4. In order to apply the numerically convenient boundary conditions of $f_\mathrm{u,w} = 0$ at solid boundaries, the procedure described in Section 2.2.1 for the original ζ-f model is followed accordingly.

4.3 Validation and comparative assessment

In the following sections the ER ζ-f model is validated by computing various generic flow configurations which are unambiguously characterized in terms of geometry as well as boundary conditions. This is important in order to limit as much as possible any outside influences, i.e. influences not associated with the turbulence model, affecting the significance of the validation results. Furthermore, the availability of

accurate data for mean velocity and turbulent intensities at various positions throughout the domain is a necessary requirement. Focus was also given to cases, where heat transfer was considered in order to investigate model performance with respect to scalar transport. Some configurations viewed as benchmark cases in the field of turbulence modeling have been selected in order to facilitate comparisons with literature.

While the accordingly considered cases are certainly simplified compared to practical engineering applications, focus was placed on covering Reynolds numbers and flow features relevant for the intended application of the model in the context of internal combustion engines as well as exhaust gas after treatment systems. Due to the formulated requirements and the low to moderate Reynolds numbers relevant for the intended application, most of the considered reference data is based on DNS. Specifically, model performance is evaluated for channel flow at a range of Reynolds numbers, flow over a two-dimensional fence as well as a periodic hill, jet impingement onto a wall and turbulent mixing in a T-junction.

Since the performance of scale-resolving turbulence models is inherently depending on the spatial resolution, relevant grid studies have been conducted including especially coarse meshes appropriate for RANS-based scale-resolving approaches. Additionally to the ER ζ-f model, computations for the validation cases in this section have been performed with the VLES model, a model based on blending LES and RANS as described in Section 2.2.3 and the dynamic Smagorinsky model (denoted as 'dynS' in the following figures), a classical SGS model from the LES framework presented in Section 2.2.2, in order to enable a comparative assessment of the results. Even though RANS computations are not necessarily relevant with respect to the intended application of the proposed modeling framework, results obtained with the original ζ-f model described in Section 2.2.1 are also included at appropriate locations.

4.3.1 Channel flow

As in the validation of the ω-based RANS model, the first considered case is fully-developed plane channel flow at a range of friction-based Reynolds numbers, i.e. $\mathrm{Re}_\tau = 180$, 392 and 640 based on the half-channel height. Corresponding bulk Reynolds numbers can be found in

Tab. 4.2. As reference the DNS data bases of Kawamura *et al.* [72] ($\mathrm{Re}_\tau = 180$), Moser *et al.* [108] ($\mathrm{Re}_\tau = 392$) and Abe *et al.* [1] ($\mathrm{Re}_\tau = 640$) are used. In this section results obtained with the three scale-resolving turbulence models on three grid refinement levels are discussed mainly in terms of the predicted values of u_τ as well as mean velocity and TKE profiles. For the lowest and highest Reynolds numbers, where heat transfer was considered in the reference DNSs, mean temperature profiles are additionally presented.

Computational setup

The computational setup is identical for all computations presented in this section. The computational domain is schematically shown in Fig. 4.6. Its spatial extend relative to the height of the channel H corresponds to $L_x/H = 2$ and $L_z/H = 1$, which is smaller compared to the domains applied in the reference DNSs but was found to be sufficient to appropriately capture large scale turbulent structures. The flow is driven by imposing a pressure gradient in x-direction, adapted in each time step to enforce a mean velocity U_b corresponding to the respective bulk Reynolds number Re_b. In streamwise and spanwise directions, periodic boundary conditions (i.e. the *cyclic* variant in OpenFOAM) are applied, while wall boundary conditions are enforced at the top and bottom walls. In cases where heat transfer is considered, a constant heat flux q_w is prescribed at the walls. Similar to the imposed pressure gradient driving the flow, an analogous term is introduced in the energy equation (2.29) in order to enforce a constant mean temperature distribution in streamwise direction, which is necessary for the application of periodic boundary conditions. The respective source/sink term

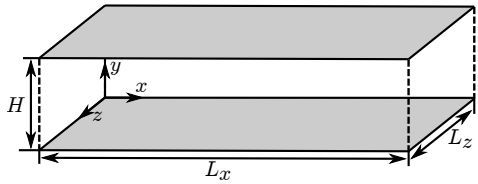

Figure 4.6: Sketch of the computational domain for fully developed channel flow.

introduced in Eq. (2.29) reads

$$S_q = -\frac{\widetilde{U}_x}{H}\frac{q_\mathrm{w}}{\rho c_p U_\mathrm{b}}, \tag{4.21}$$

where c_p is the fluid's specific heat capacity at constant pressure.

Computational grids of three refinement levels are generated for each Reynolds number. This is done such that non-dimensionalized grid spacings in inner scaling are constant between Reynolds numbers, as indicated in Tab. 4.3, which summarizes metrics for the 9 grids. In all cases, the first wall adjacent node is situated at $y^+ \approx 1$ in line with the requirement of the considered near-wall models.

Table 4.3: Grid metrics for scale-resolving computations of fully developed channel flow. Grid spacings are normalized with the viscous length scale from DNS, e.g. $\Delta x^+ = \Delta x\, u_{\tau,\mathrm{DNS}}/\nu$.

				Number of cells		
	Δx^+	Δy^+	Δz^+	$\mathrm{Re}_\tau = 180$	$\mathrm{Re}_\tau = 392$	$\mathrm{Re}_\tau = 640$
coarse	50	2...30	30	6120	63232	267546
medium	35	2...30	20	17388	180000	756864
fine	25	2...20	12	40020	409600	1768068

The convective term in the momentum equation is discretized with CDS, while UDS is applied for the respective terms in the turbulence model equations. In terms of temporal discretization, the second-order BDF (see Section 3.2) is used with adaptive time stepping ensuring a maximum Courant number of $\mathrm{Co} \leq 0.7$. Quantitative results presented in the following are averaged in time over a span of 400 flow-through times ($400 L_x/U_\mathrm{b}$) as well as spatially in streamwise and spanwise directions. Prior to this, and solely with the goal to quickly generate fluctuating initial fields, OpenFOAM's *limitedCubic* scheme is applied for a few flow-through times to the convective term in the momentum equation. This approach followed throughout this work for the generation of fluctuating initial fields, was found to be more convenient then the common approach of prescribing an artificially perturbed velocity field. Instead, the formation of turbulent structures is swiftly triggered

by numerical instabilities associated with the cubic interpolation applied in this scheme.

Results

In order to gain an impression of the instantaneous results provided by the ER ζ-f model on different grid refinement levels, iso-contours of the Q-criterion are shown in Fig. 4.7. Thereby Q is the second invariant of

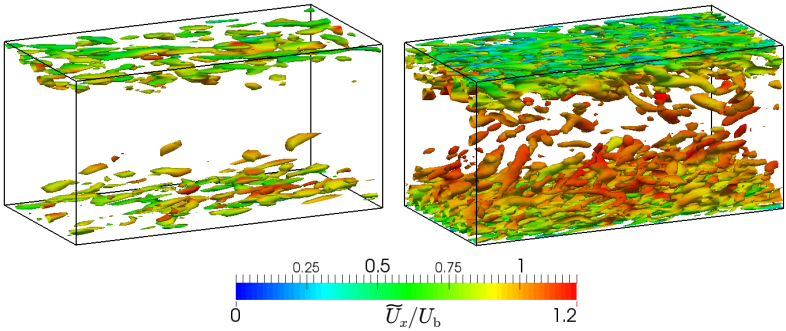

Figure 4.7: Iso-contours of the Q-criterion at $Q = 2.5\,(U_\mathrm{b}/H)^2$ for channel flow at $\mathrm{Re}_\tau = 392$ on the coarse (left) and fine (right) grids. Colors correspond to the instantaneous velocity in streamwise directions normalized with the bulk velocity.

the velocity gradient tensor given by

$$Q = \frac{1}{2}\left(\widetilde{\Omega}_{ij}\widetilde{\Omega}_{ij} - \widetilde{S}_{ij}\widetilde{S}_{ij}\right), \text{with } \widetilde{\Omega}_{ij} = \frac{1}{2}\left(\frac{\partial \widetilde{U}_i}{\partial x_j} - \frac{\partial \widetilde{U}_j}{\partial x_i}\right) \tag{4.22}$$

and was proposed by Hunt *et al.* [64] as an indicator for vortex structures or eddies in turbulent flows. The criterion is based on the condition, that in vortices strain is small compared to vorticity ($Q > 0$), whereby the value of Q used for the iso-contours is a somewhat arbitrary threshold parameter. Fig. 4.7 thus visualizes resolved vortex structures associated with a value of $Q = 2.5\,(U_\mathrm{b}/H)^2$ on the coarse (left) and fine grid (right) for the case of $\mathrm{Re}_\tau = 392$. The iso-contours are colored by the instantaneous velocity in streamwise direction as an indicator

for the associated momentum. As expected, the fine grid enables the resolution of smaller and overall more vortical structures especially in the low-momentum near-wall region. Complementing this observation, the ratio of modeled TKE (k_u) to total TKE ($k = k_\mathrm{res} + k_\mathrm{u}$) including the resolved contribution

$$k_\mathrm{res} = \frac{1}{2}\overline{\left(\widetilde{U}_i - \overline{\widetilde{U}}_i\right)^2}, \tag{4.23}$$

determined via online averaging, is shown in Fig. 4.8. In addition to ER ζ-f, the model ratios for VLES and the dynamic Smagorinsky model are presented. As can be expected from the previously presented visualization of turbulent structures, the modeling ratio with the ER ζ-f model is higher on the coarse grid (coarse grid results are indicated by the additional markers), reaching $k_\mathrm{u}/k \approx 0.2$ in the vicinity of the wall, which is slightly more than double compared to the fine mesh. The VLES model exhibits very similar values in the viscous sublayer but higher

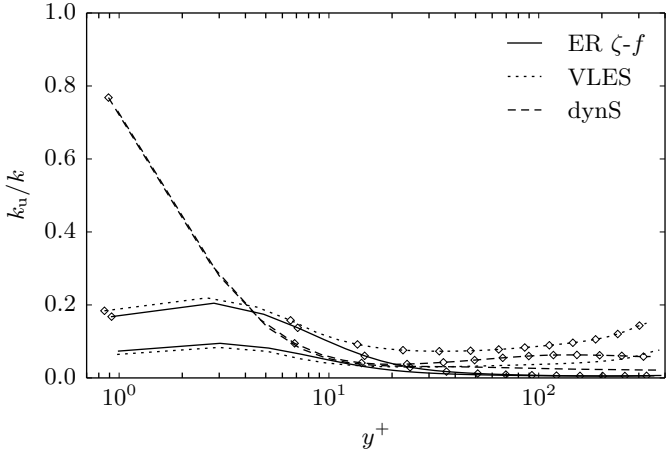

Figure 4.8: Ratio of unresolved (or modeled) TKE k_u to total predicted TKE k on the coarse and fine grid in channel flow at $\mathrm{Re}_\tau = 392$. Lines with markers indicate results obtained employing the coarse grid.

values in the core region compared to the ER ζ-f model. The reason for this increase towards the center of the channel with the VLES model is most likely the increasing grid spacing Δ, which directly influences the estimated sub-scale quantities through the resolution function, see Eq. (2.46). The dynamic Smagorinsky model exhibits a somewhat different behavior: the model ratio in the near-wall region is virtually identical on the coarse and fine grids, approaching a high value of $k_\mathrm{u}/k \approx 0.8$ at the first wall adjacent node; merely in the region $y^+ > 20$ a higher modeling level is obtained on the coarse grid.

In the following, results for the mean streamwise velocity in inner scaling ($U^+ = \widetilde{U}_x/u_\tau$) and TKE ($k^+ = \overline{(k_\mathrm{res} + k_\mathrm{u})}/u_\tau^2$) are presented. The wall friction velocity u_τ used for normalization in inner scaling is the most important quantity in this regard, since it is also a measure for the skin friction coefficient $C_\mathrm{f} = 2(u_\tau/U_\mathrm{b})^2$. It is determined for each computation based on the gradient of the mean streamwise velocity at the wall. Tab. 4.4 summarizes the relative deviations of the obtained values from the DNS reference value $u_{\tau,\mathrm{DNS}}$. Several observations can be made here: generally, friction is slightly underpredicted, except for the fine grid at the highest Reynolds number. As can be expected, the application of a finer mesh thereby generally results in more accurate predictions with all considered sub-scale models. Noticeably, the largest

Table 4.4: Relative deviation of the wall friction velocity ($\Delta u_\tau = (u_\tau - u_{\tau,\mathrm{DNS}})/u_{\tau,\mathrm{DNS}}$) for the various Reynolds numbers and computational grids.

Re_τ	grid	ER ζ-f	VLES	dynS
180	coarse	−10.8%	−21.0%	−15.5%
	medium	−4.6%	−10.6%	−8.5%
	fine	−1.0%	−3.9%	−3.8%
392	coarse	−6.4%	−13.5%	−9.5%
	medium	−2.2%	−5.8%	−4.0%
	fine	−0.8%	−2.4%	−1.9%
640	coarse	−3.3%	−8.3%	−5.9%
	medium	−0.5%	−3.0%	−1.5%
	fine	1.6%	0.1%	0.9%

deviations are obtained for the lowest Reynolds number, $\mathrm{Re}_\tau = 180$, with the spread of deviations reducing significantly at higher Re_τ. Fig. 4.9 illustrates the results for the lowest Reynolds number ($\mathrm{Re}_\tau = 180$) on the coarse, medium and fine grids from top to bottom, respectively. Velocity profiles are shown on the left with the associated TKE profiles on the right. In terms of TKE, all models overpredict k^+, which is expected behavior for under-resolved scale-resolving computations. On the coarse grid, the dynamic Smagorinsky model performs worst, overpredicting the wall peak by more than a factor of 2. VLES performs slightly better in this regard, but nevertheless exhibits the highest deviation with respect to the mean velocity profile in the logarithmic region. The results obtained with the ER ζ-f model are closest to the reference data, both with respect to the mean velocity profile, where deviations in the logarithmic region are noticeable, as well as the wall peak of TKE. This is in line with the most accurate prediction of u_τ, with a deviation of $\Delta u_\tau = -10.8\%$ with ER ζ-f compared to -21% and -15.5% with VLES and dynamic Smagorinsky, respectively. Results clearly improve on the medium and fine grids. All observations made with respect to the coarse grid results are qualitatively also applicable to the finer grids, with ER ζ-f consistently performing best, as coincidentally apparent from the deviations of u_τ summarized in Tab. 4.4. Corresponding results for $\mathrm{Re}_\tau = 392$ are presented in Fig. 4.10. Overall trends are similar to the lower Reynolds number, however the level of accuracy is generally higher. ER ζ-f again performs best in all cases, which is especially noticeable on the coarser grids and with respect to the prediction of u_τ (Tab. 4.4). On the fine grid, the results obtained with all models are in good agreement with the reference DNS data base. For the highest Reynolds number ($\mathrm{Re}_\tau = 640$), good results are already obtainable on the medium grid with all considered models. With a deviation of $\Delta u_\tau = -3.3\%$, ER ζ-f is able to provide reasonable results on the coarse mesh compared to the -8.3% and -5.9% deviation obtained with VLES and dynamic Smagorinsky, respectively.

Finally, results for the temperature profiles in inner scaling, i.e. $\Theta^+ = (\Theta_\mathrm{w} - \widetilde{\Theta})/\Theta_\tau$ with $\Theta_\tau = q_\mathrm{w}/(\rho c_p u_\tau)$, are presented in Fig. 4.12 for the cases of $\mathrm{Re}_\tau = 180$ (left) and 640 (right). The obtained profiles are in terms of their accuracy very similar to the velocity profiles shown in Figs. 4.9 and 4.11. While for $\mathrm{Re}_\tau = 640$ reasonable results are

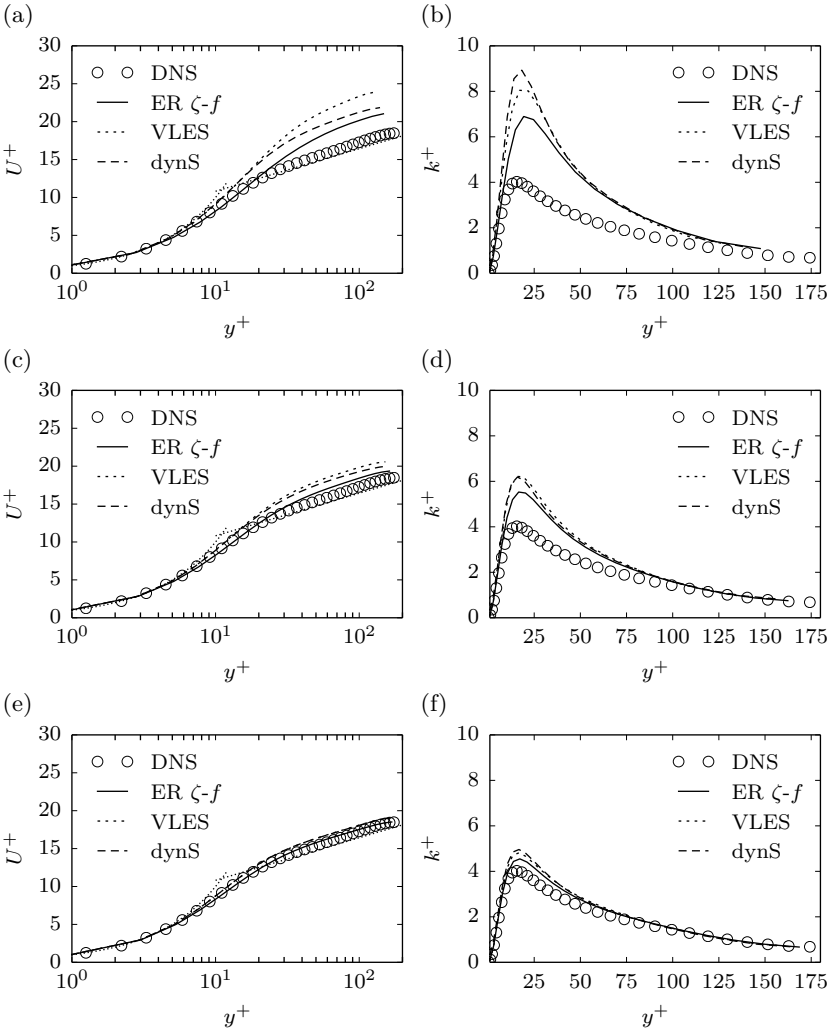

Figure 4.9: Mean streamwise velocity (left) and mean TKE (right) profiles for fully developed channel flow at $\mathrm{Re}_\tau = 180$ on the coarse, medium and fine grids (top to bottom). DNS data taken from Kawamura *et al.* [72].

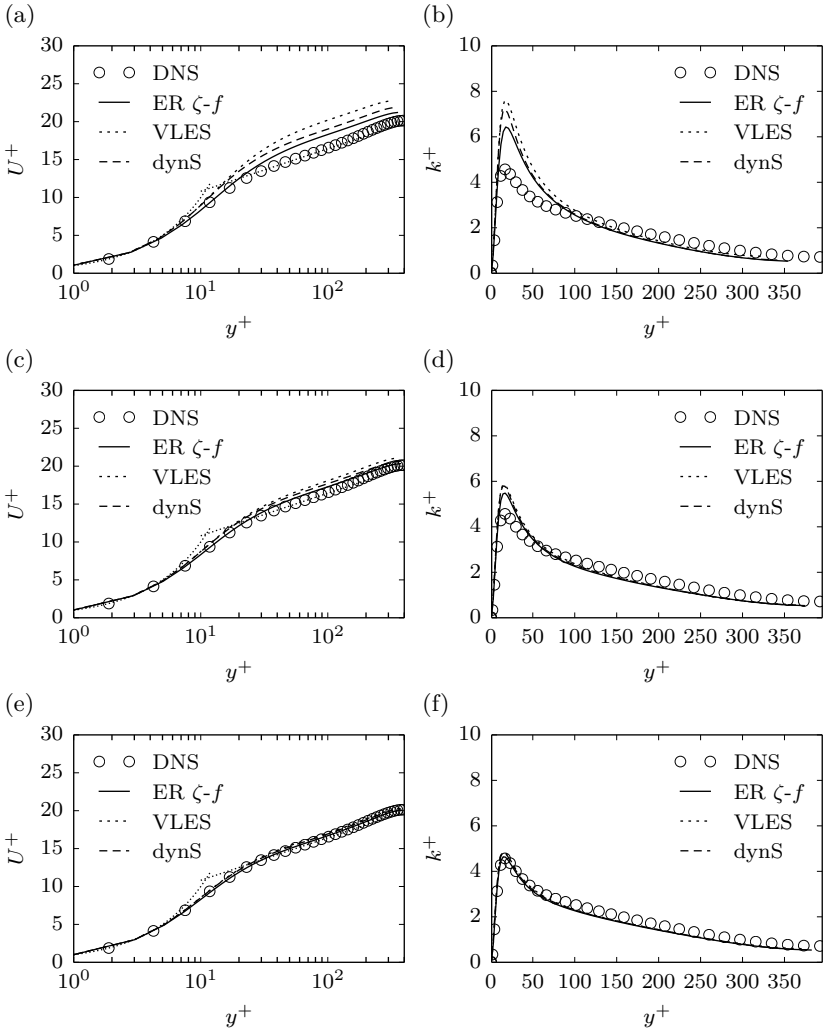

Figure 4.10: Mean streamwise velocity (left) and mean TKE profiles (right) for fully developed channel flow at $\mathrm{Re}_\tau = 392$ on the coarse, medium and fine grids (top to bottom). DNS data taken from Moser *et al.* [108].

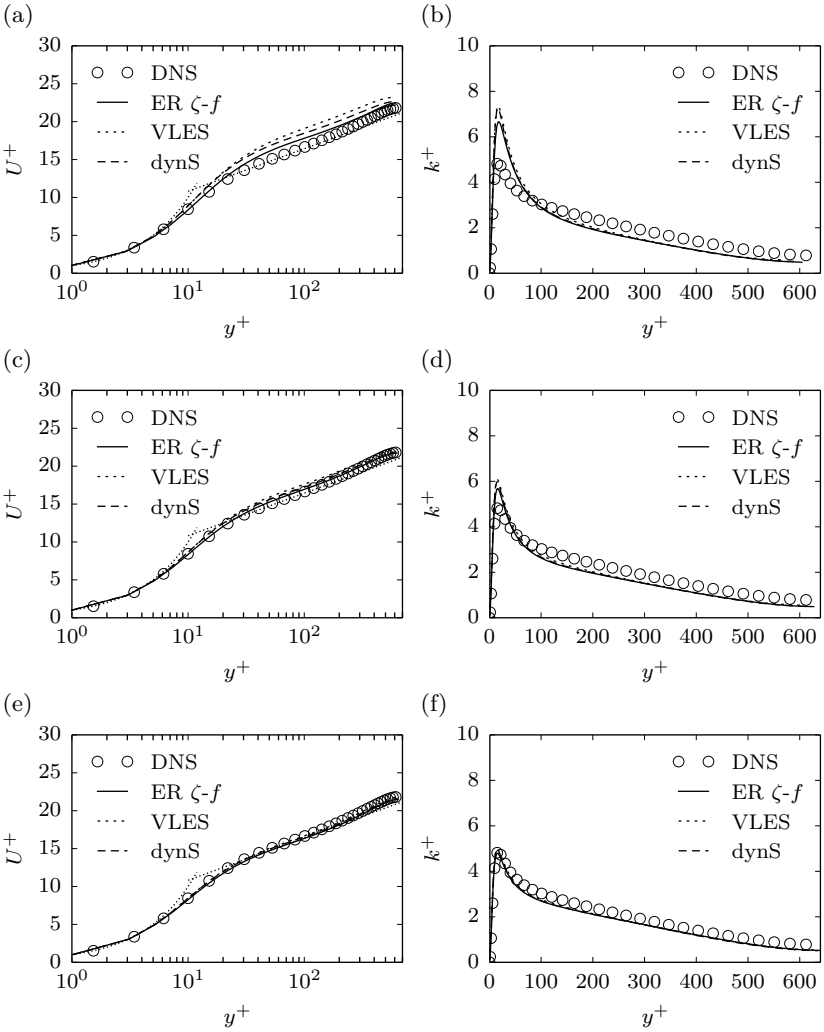

Figure 4.11: Mean streamwise velocity (left) and mean TKE profiles (right) for fully developed channel flow at $\mathrm{Re}_\tau = 640$ on the coarse, medium and fine grids (top to bottom). DNS data taken from Abe *et al.* [1].

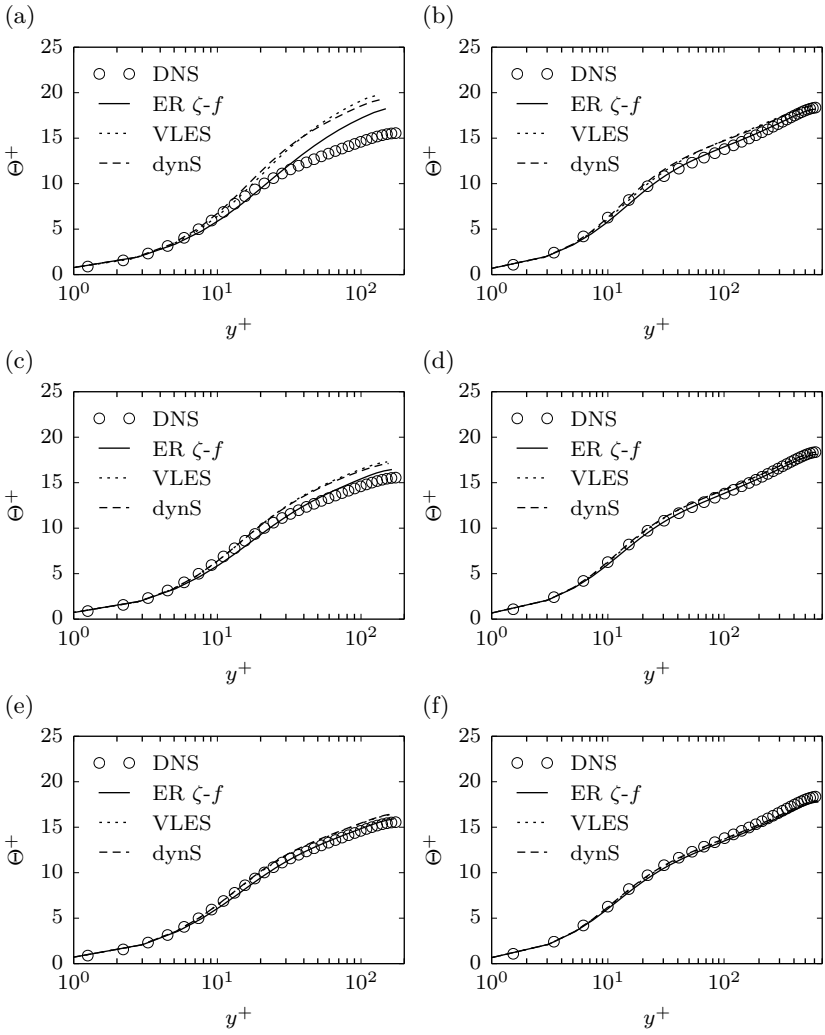

Figure 4.12: Mean temperature profiles for fully developed channel flow at $\mathrm{Re}_\tau = 180$ (left) and $\mathrm{Re}_\tau = 640$ (right) on the coarse, medium and fine grids (top to bottom). DNS data taken from Kawamura *et al.* [72] ($\mathrm{Re}_\tau = 180$) and Abe *et al.* [1] ($\mathrm{Re}_\tau = 640$).

obtained on all meshes, the higher grid dependency attributable to the lower Reynolds number is again apparent. Thus, the advantage of the ER ζ-f model is especially noticeable at the low Reynolds number and on the coarse mesh at $\mathrm{Re}_\tau = 640$.

Conclusion

In summary, the ER ζ-f model performs best, especially with respect to the accuracy of the obtained wall friction velocity u_τ, which in particular affects the agreement of the velocity profiles with the reference data in the logarithmic region. The performance of the VLES model on the other hand is somewhat unsatisfactory for the considered case, especially in comparison to the dynamic Smagorinksy model, which generally provides more accurate results, even on coarser grids. The advantage of the ER ζ-f model is thereby achieved while maintaining a low modeling ratio comparable to the VLES model, thus ensuring that the majority of turbulent fluctuations are resolved even in the near-wall region. This differentiates the model from hybrid approaches based on interfacing LES and RANS, such as DES, which generally suppress the majority of resolved turbulent fluctuations in the near-wall region. The present grid study further emphasizes that for a given level of accuracy, finer meshes in terms of non-dimensional grid spacing are required for lower Reynolds numbers. The necessity for finer grids is most likely associated with the weak separation of scales at low Reynolds numbers (see Section 2.2). ER ζ-f somewhat alleviates this effect by providing reasonable results over a wider range of grid resolutions, indicating an overall reduced grid sensitivity compared to the other two models. This can most likely be attributed to two properties of the ER ζ-f model: Firstly, due to the modification of the scale-supplying equation with the additional production term motivated by the SAS concept, the model is nominally able to directly adapt the modeled sub-scale turbulence to resolved velocity fluctuations. Or in other words, the resolved and modeled turbulence complement each other directly. This is not the case in the VLES model, where the transport equations remain structurally unchanged in comparison to the underlying RANS model. Instead the modeled quantities ($(\cdot)_{\mathrm{us}}$-quantities) represent intermediary values, which have to be rescaled based on the resolution function in order to gain sub-scale quantities corresponding to the unresolved tur-

bulent spectrum (see Section 2.2.3). Secondly, VLES and the dynamic Smagorinsky model rely on the filter width Δ determined by the numerical grid as a length scale characterizing the smallest resolved or largest modeled turbulent eddies. ER ζ-f on the other hand, adapts to the resolved turbulence based on the second derivative of the velocity field, which is associated with the von Karman length scale L_{vK}. This physical length scale is evaluated in every time step and for each computational node based on the neighboring cells. The model thus relies to a higher extent on spatiotemporal information pertinent to the local flow conditions compared to models relying on the grid spacing Δ for similar purposes.

4.3.2 Flow over a two-dimensional fence

The second validation case for which RANS results have already been presented in Section 4.1.1 is flow over a two-dimensional fence at a Reynolds number of $\mathrm{Re}_H = U_{\mathrm{b}}H/\nu = 22500$, based on the channel height H and the bulk velocity U_{b}. The configuration studied experimentally by Larsen *et al.* [88] corresponds to a channel with a wall-mounted fence of height $h = 2/15\,H$ and an aspect ratio of 4 blocking the incoming wall parallel mean flow. This results in a separation of the flow at the sharp edged corner of the fence and the formation of a recirculation region with an associated free shear layer.

Computational setup

The computational domain is schematically sketched in Fig. 4.13. The

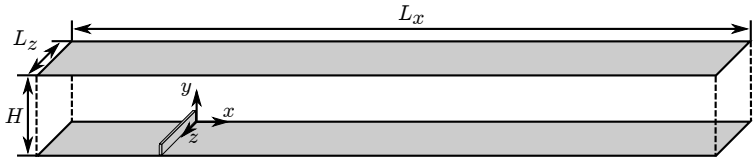

Figure 4.13: Sketch of the computational domain for flow over a two-dimensional fence.

domain dimensions in streamwise and spanwise directions correspond to $L_z/H = 1$ and $L_x/H \approx 5.4$, whereby the fence is positioned approximately one channel height after the inlet plane. Inlet boundary conditions are generated by applying a simultaneous precursor simulation on a mesh generated by extruding the first grid plane over a length of $2H$ in negative x-direction. In this way, an additional computational domain corresponding to Fig. 4.13 is generated, where the same computational setup described in Section 4.3.1 for plane channel flow is applied to generate fully developed inflow data at the corresponding bulk Reynolds number. This data is then mapped as a boundary condition onto the inlet plane of the main computational domain, with the exception of the pressure for which a zero gradient boundary condition is prescribed. In turn, an arbitrary fixed mean value is prescribed for the pressure at the outlet, while zero gradient conditions are applied for the remaining quantities. In spanwise direction, periodic boundary conditions are prescribed corresponding to the assumption of two-dimensional mean flow. Two grid refinement levels are considered with the coarse mesh consisting of 273504 cells and the fine mesh of 1583750 cells. The grid is structured in three blocks: one in front of the fence, one above the fence and one after the fence. Details on the amount of cell in the respective blocks are summarized in Tab. 4.5. In compliance with the requirements of the considered near-wall models, the grids are refined towards the channel walls as well as the fence.

The convective term in the momentum equation is discretized with OpenFOAM's *filteredLinear3V* scheme with $C_{\mathrm{lim}} = 0.1$ based on the arguments presented in Section 3.1.2. As in all scale-resolving computations in this work, the second-order BDF (see Section 3.2) is applied

Table 4.5: Details on the distribution of grid cells for the case of flow over a two-dimensional fence.

	coarse	fine
before fence	$43 \times 98 \times 16$	$65 \times 115 \times 50$
over fence	$10 \times 63 \times 16$	$16 \times 75 \times 50$
after fence	$125 \times 98 \times 16$	$200 \times 115 \times 50$
total	273504	1583750

for time marching. Adaptive time stepping is used to enforce Co ≤ 1. Quantitative results presented in the following are averaged over a span of approximately 57 flow-through timess ($57\, L_x/U_\mathrm{b}$) as well as spatially in z-direction.

Results

To get an impression of the mean flow field, Fig. 4.14 shows streamlines of the mean flow field together with the mean velocity magnitude $|\widetilde{\overline{U}}| = \overline{(\widetilde{U}_i \widetilde{U}_i)^{1/2}}$ normalized by the bulk velocity as obtained with ER ζ-f on the fine grid. The flow separates at the sharp corner of the fence forming a recirculation bubble as well as two small corner bubbles in front of and after the fence. Between the recirculation bubble and the accelerated core flow, a highly unsteady separating shear layer spreads throughout the domain.

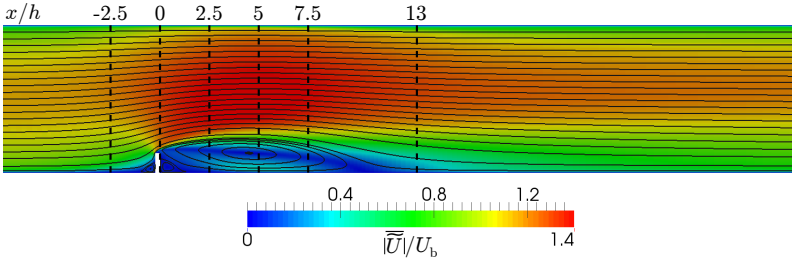

Figure 4.14: Streamlines and magnitude of the mean velocity field for flow over a two-dimensional fence, obtained with the ER ζ-f model on the fine grid. Vertical dashed lines mark positions for which quantitative results are presented in the following.

Associated mean velocity profiles normalized with U_b on the coarse and fine grids are presented in Fig. 4.15. On the coarse mesh, Fig. 4.15 (a), all models predict very similar velocity profiles, which overestimate the velocity in and after the recirculation bubble. On the fine grid, Fig. 4.15 (b), all scale-resolving models again show very similar results, this time in good agreement with the experimental reference data base. As can be expected, the scale-resolving models more accurately capture

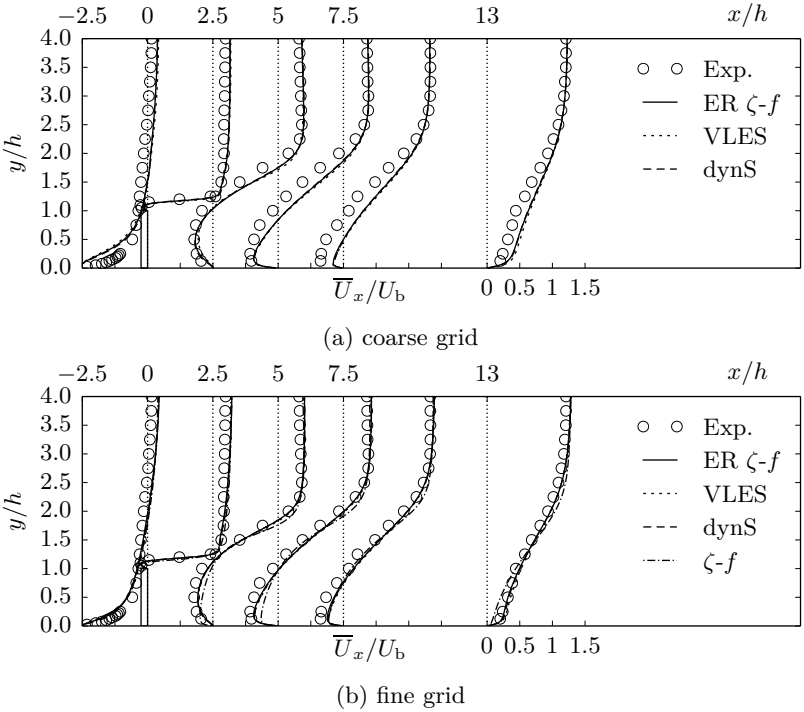

(a) coarse grid

(b) fine grid

Figure 4.15: Mean streamwise velocity profiles for flow over a two-dimensional fence at $\mathrm{Re}_H = 22500$ on the coarse and fine grid. Exp. data taken from Larsen *et al.* [88].

the shape of the recirculation bubble compared to the ζ-f RANS model. One reason for this, is that the extent and intensity of the counterrotating corner bubble after the fence is poorly represented in the RANS solution, as indicated also by Fig. 4.16 (b), illustrating the development of the friction coefficient $C_\mathrm{f} = \tau_\mathrm{w}/(0.5\rho U_\mathrm{b}^2)$ along the bottom wall. The scale-resolving models exhibit slightly too short recirculation zones on the fine grid: the experimentally determined reattachment point is located at $x_\mathrm{r}/H = 11.7$, with the ER ζ-f model being closest with $x_\mathrm{r}/H = 11.2$ compared to $x_\mathrm{r}/H = 11.0$ and $x_\mathrm{r}/H = 10.9$ with the VLES and dynamic Smagorinsky model, respectively. On the coarse grid, Fig.

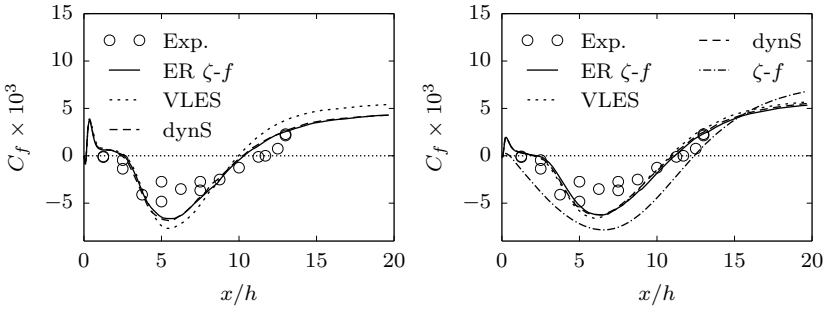

(a) coarse grid (b) fine grid

Figure 4.16: Friction coefficient along the bottom wall for flow over a two-dimensional fence at $\mathrm{Re}_H = 22500$ on the coarse and fine grid. Exp. data taken from Larsen *et al.* [88].

4.16 (a), the recirculation zones are even shorter, with the VLES results deviating more noticeably from the other two computations in terms of the magnitude of C_f. Reattachment is predicted similarly with all models, i.e. $x_\mathrm{r}/H = 10.3$, $x_\mathrm{r}/H = 10.2$ and $x_\mathrm{r}/H = 10.0$ with ER ζ-f, VLES and the dynamic Smagorinksy model, respectively.

TKE profiles normalized with U_b obtained on both grids are presented in Fig. 4.17. On the coarse mesh, 4.17 (a), the turbulence activity in the separating shear layer is captured reasonably well by all models, however with some overestimation in the recirculation region. Despite the somewhat lower TKE levels predicted by the VLES model, it is recalled that the recirculation zone obtained with VLES is the shortest. On the fine grid, Fig. 4.17 (b), the near-wall region is more accurately captured. However, TKE is lower in the separating shear layer then the experimentally obtained values. Nevertheless, the mean velocity field is better predicted on the fine grid in conjunction with somewhat too low TKE levels then on the coarse mesh, where a better agreement of k with the experimental data is obtained in the separating shear layer.

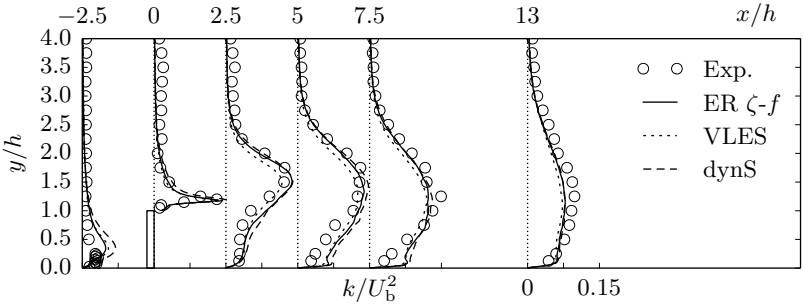

(a) coarse grid

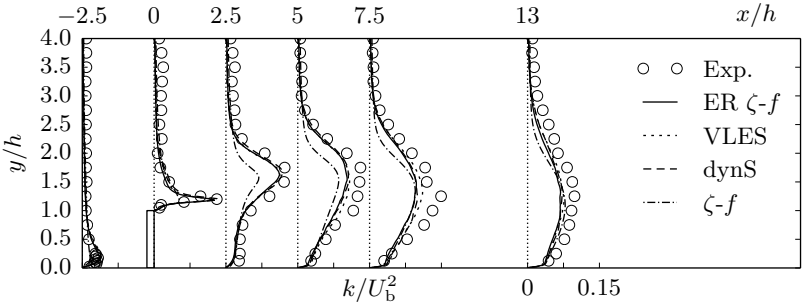

(b) fine grid

Figure 4.17: Mean TKE profiles for flow over a two-dimensional fence at $\mathrm{Re}_H = 22500$ on the coarse and fine grid. Exp. data taken from Larsen *et al.* [88].

Conclusion

While the scale-resolving models clearly demonstrate their advantage over the RANS approach, only very minor differences between the models are found for the case of flow over a two-dimensional fence. Nevertheless, the ER ζ-f model performs slightly better compared to the VLES model in predicting the length of the recirculation bubble on both grids. However, a clear advantage over the dynamic Smagorinsky model can not be attested for this flow configuration.

4.3.3 Flow over periodic hills

Flow over periodic hills is an often computed benchmark case for scale-resolving and hybrid RANS/LES models. Flow features are similar to the previous validation case in that the flow separates after the hill resulting in the formation of a recirculation bubble. However, the location of the separation point is not fixed due to the smooth contour of the hill compared to the sharp edge of the fence. Presently, the flow at a Reynolds number of $\mathrm{Re}_h = U_\mathrm{b} h/\nu = 10595$ is considered, where h corresponds to the height of the hill and U_b is the bulk velocity in the plane above the hill crest. As reference data base, the highly resolved LES of Breuer *et al.* [19] is used, which was conducted on a grid consisting of approximately 13 million cells.

Computational setup

A schematic illustration of the flow configuration is shown in Fig. 4.18. The size of the computational domain is given by $H/h = 2.036$, $L_x/h = 9$ and $L_z/h = 4.5$. Boundary conditions as well as the numerical mechanism to drive the flow are identical to the setup for channel flow described in Section 4.3.1.The computational grid considered here is fairly coarse comparatively (see e.g. [68]) and consists of $52 \times 50 \times 30$ cells in streamwise, wall-normal and spanwise directions, respectively; in total 78000 cells. Nevertheless, the grid is refined towards the top and bottom wall in order to meet the requirements of the considered near-wall models.

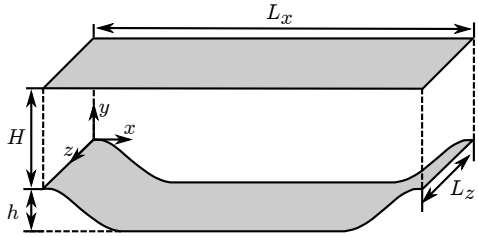

Figure 4.18: Sketch of the computational domain for flow over periodic hills.

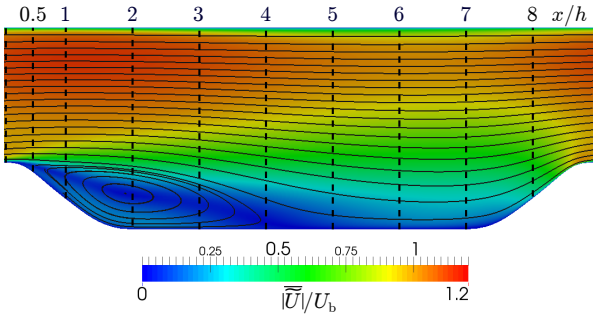

Figure 4.19: Streamlines and magnitude of the mean velocity field for flow over periodic hills, obtained with the ER ζ-f model on the fine grid. Vertical dashed lines mark positions for which quantitative results are presented in the following.

As in the previous case, OpenFOAM's *filteredLinear3V* scheme (see Section 3.1.2) is adopted for the convective term in the momentum equation, in this case with $C_{\mathrm{lim}} = 0.2$. The second-order BDF formula is applied for time marching with adaptive time stepping maintaining $\mathrm{Co} \leq 0.7$. The results presented in the following are averaged over 250 flow-through times ($250\, L_x/U_{\mathrm{b}}$) as well as spatially in z-direction.

Results

The development of the mean flow field is illustrated in Fig. 4.19 in terms of the mean velocity field normalized by the bulk velocity as well as associated streamlines obtained with the ER ζ-f model on the fine grid.

In the reference LES, the flow separates shortly after the hill at $x_{\mathrm{s}}/h = 0.22$ forming a recirculation bubble with subsequent reattachment at $x_{\mathrm{r}}/h = 4.7$. Corresponding values from the present computations are summarized in Tab. 4.6. Flow separation occurs slightly too late with all models, which is however more pronounced with the VLES model. ER ζ-f and VLES similarly predict a too late reattachment location compared to the reference LES, while application of the dynamic Smagorinsky model results in a too short recirculation zone. Associated mean velocity profiles normalized by the bulk velocity U_{b}

Table 4.6: Separation (x_s/h) and reattachment points (x_r/h) obtained with the scale-resolving models.

	x_s/h	x_r/h
reference LES	0.22	4.7
ER ζ-f	0.28	5.1
VLES	0.31	5.1
dynS	0.28	4.5

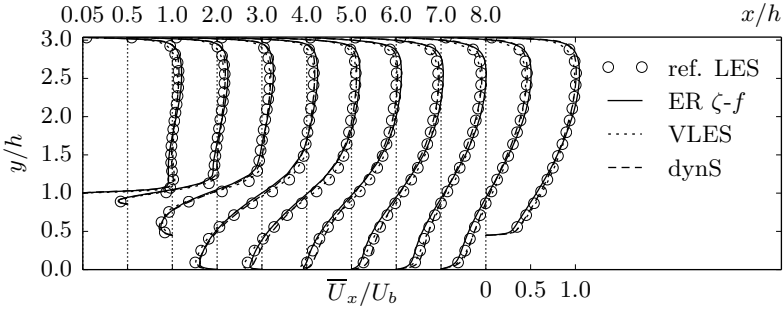

Figure 4.20: Mean streamwise velocity profiles for flow over periodic hills at $\mathrm{Re}_h = 10595$. Reference LES data taken from Breuer *et al.* [19].

are presented in Fig. 4.20. The VLES results exhibit the best level of agreement with the reference data throughout the entire domain. The dynamic Smagorinsky model performs similar, but tends to overpredict the velocity close to the bottom wall at $3 < x/h < 6$ which is in line with the slightly too short recirculation zone. The ER ζ-f model in turn slightly underpredicts the velocity in the lower part at positions $x/h > 5$ resulting in an overprediction near the top wall, which is most likely enhanced due to the periodicity of the flow. Overall all models are able to capture the mean flow field surprisingly well, considering in particular the relatively low grid resolution.

More pronounced differences between the models can be identified with respect to the TKE profiles normalized with the bulk velocity U_b

as shown in Fig. 4.21. Here, only the ER ζ-f model is able to maintain a level of accuracy comparable to the velocity profiles. VLES performs reasonably well up to $x/h = 2$, but further downstream generally overpredicts the turbulence activity. The dynamic Smagorinsky model on the other hand overestimates TKE throughout the entire domain, which is likely the main reason for the shorter recirculation zone.

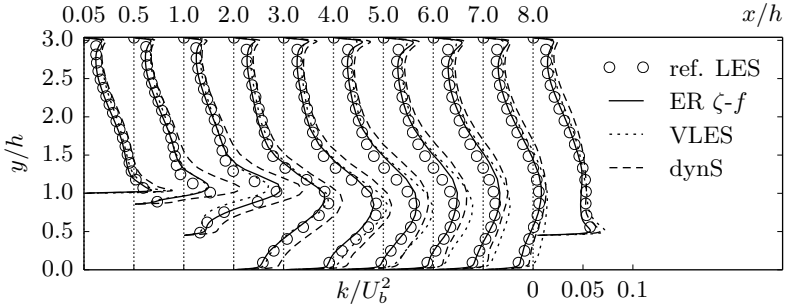

Figure 4.21: Mean TKE profiles for flow over periodic hills at $\mathrm{Re}_h = 10595$. Reference LES data taken from Breuer *et al.* [19].

4.3.4 Jet impingement onto a heated wall

Impinging jets play an important role in a variety of heat transfer applications, with the cooling of turbine blades and electronic components as well as material forming processes representing prominent examples. Furthermore, impinging jets exhibit a number of flow features encountered in the fuel injection process in internal combustion engines. This makes the flow configuration particularly relevant as a generic test case in the framework of model development for near-wall turbulence phenomena under engine and exhaust system conditions. Thus, momentum and heat transfer in a confined impinging jet issuing from a plane channel at a Reynolds number of $\mathrm{Re_b} = U_\mathrm{b} d_\mathrm{h}/\nu = 9120$, based on the bulk velocity and the hydraulic diameter d_h of the inlet channel and a Prandtl number of $\mathrm{Pr} = 0.71$, is considered. The computational results obtained with the presently considered scale-resolving models are analyzed along with reference DNS data by Hattori and Nagano [61]. In addition, for

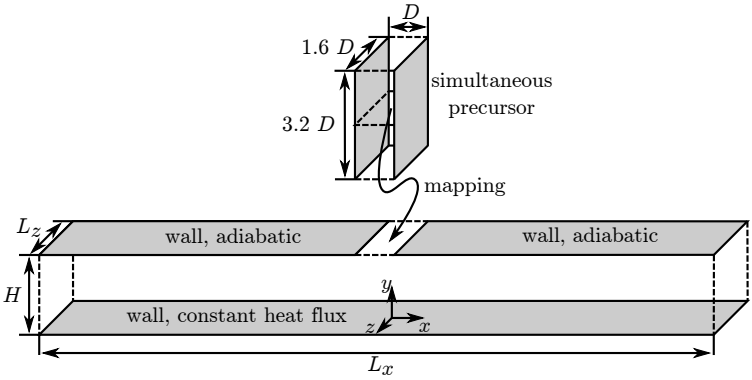

Figure 4.22: Sketch of the computational domain (with precursor) for the impinging jet configuration. Adapted from Hattori and Nagano [61].

the purpose of a comparative assessment, RANS computations employing the ζ-f model are presented.

Computational setup

Fig. 4.22 shows a schematic representation of the computational domain. The dimensions are given by $L_x/H = 13$, $L_z/H = 0.8H$, where H is the distance of the channel outlet to the impingement plate, and by $D/H = 1/2$ as the width of the inlet channel. The dimensions of the computational domain thus comply with the reference DNS. A simultaneous precursor simulation (see Section 4.3.2) is performed in order to generate fully-developed flow properties at the respective Reynolds number, which serve as inlet boundary conditions for the jet. Standard wall boundary conditions are applied at the walls. For the temperature an adiabatic condition is prescribed at the top wall and a constant heat flux q_w at the impingement plate. At the outlets zero-gradient boundary conditions are used for all quantities but the pressure, for which an arbitrary mean value is prescribed. In spanwise direction periodic boundary conditions are applied.

Two grids are considered: the coarser one consists of $218 \times 45 \times 25$

cells in x, y and z-directions, respectively, totaling 245250 cells. The finer mesh is mainly refined in spanwise direction and consists of $220 \times 45 \times 48 = 475200$ cells. Both grids are refined towards the walls in order to ensure a maximum wall distance of $y^+ < 2.5$. Predominantly results obtained on the coarse grid are shown in the following, however, VLES results on the fine mesh have been presented in [82].

Since no staggering characteristic are observed in the flow fields, the CDS scheme is applied for the convective term in the momentum equation. As usual the second-order BDF is used with adaptive time stepping maintaining $\mathrm{Co} \leq 1$ in the present case. The quantitative results presented in the following figures are averaged over approximately 38 flow-through times (estimated as $2\,L_x/U_\mathrm{b}$) as well as spatially in z-direction.

Results

The qualitative structure of the flow field can be observed in Fig. 4.23, showing streamlines and the magnitude of the mean velocity field on the right portion of the computational domain. The typical flow topology of a jet impinging perpendicularly onto a wall, with the stagnation region and highly-curved accelerating flow, proceeded by the wall jet region, can be observed. Due to the confinement by the upper wall, a recirculation region is formed in the upper part which includes a secondary bubble close to the free jet. The dashed lines in Fig. 4.23 represent positions at which results are analyzed quantitatively in the following.

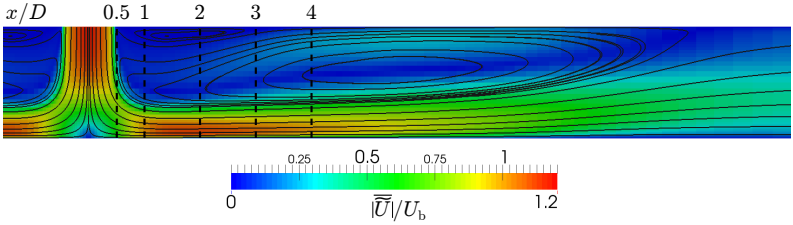

Figure 4.23: Streamlines and magnitude of the mean velocity field for the impinging jet, obtained with the ER ζ-f model on the fine grid. Vertical dashed lines mark positions for which quantitative results are presented in the following.

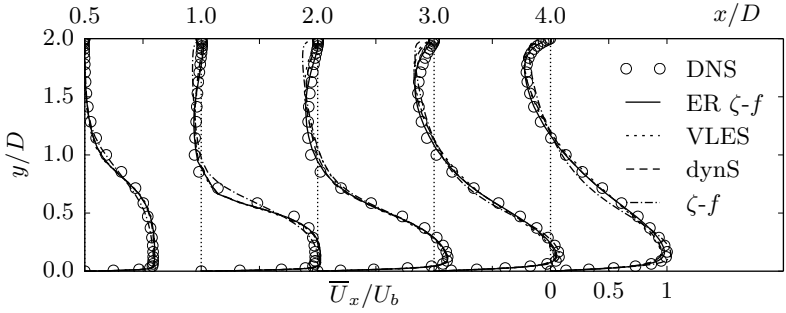

Figure 4.24: Mean streamwise velocity profiles obtained on the coarse grid for the impinging jet configuration. DNS data taken from Hattori and Nagano [61].

Fig. 4.24 shows the associated velocity profiles obtained on the coarse grid at the respective positions x/D, normalized by the bulk velocity U_b of the inlet channel. The formation of the wall jet as well as the recirculation region in the upper part of the channel can be observed correspondingly. While all scale-resolving models perform reasonably well, the ER ζ-f model is most accurate, especially in predicting the shape of the velocity profiles in the recirculation zone at positions $x/D = 2$ and 3. With respect to the RANS framework, elliptic-relaxation-based EVMs are known to perform among the best for impinging jet configurations, as indicated e.g. in the review of Zuckerman and Lior [167] for Durbin's [39] $\overline{v'^2}$-f model. Correspondingly, the ζ-f models results are in fairly good agreement with the reference data, with the exception of the region dominated by the effect of the secondary bubble near the upper wall as well as slight deviations at $x/D = 4$ attributable to an underpredicted spreading of the wall jet. The development of the mean velocity is further illustrated in Fig. 4.25 where profiles at different positions along the impingement plate are plotted in a semi-log manner typical for wall-boundary layers. The profiles are non-dimensionalized by the local wall friction velocity u_τ varying in streamwise direction. The development reveals strong departure from the equilibrium conditions, complying with the existence of a logarithmic region and two associated assumptions: constant stress layer ($\overline{u'v'}/u_\tau^2 = 1$) and local equilibrium ($P_k = \varepsilon$). The high positive pressure gradient associated

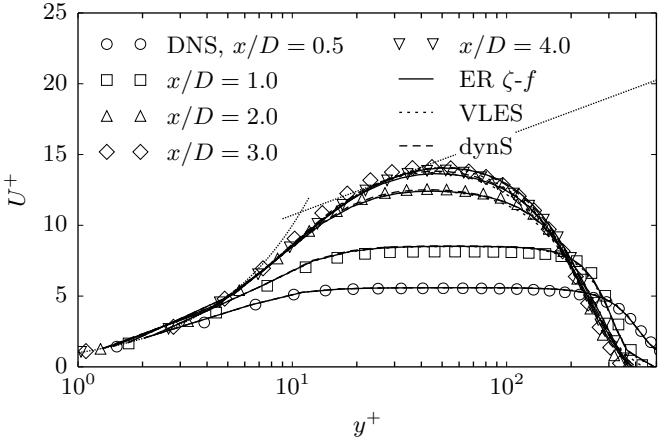

(a) scale-resolving models

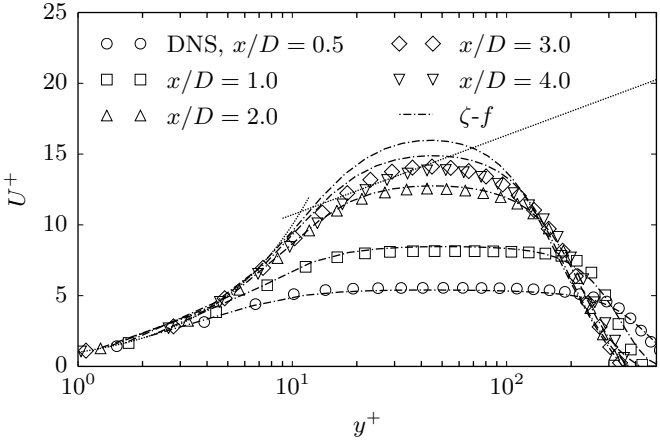

(b) ζ-f RANS model

Figure 4.25: Mean streamwise velocity profiles in inner scaling in the near-wall region of the impingement plate obtained with scale-resolving models (a) and the ζ-f RANS model (b) for the impinging jet configuration. DNS data taken from Hattori and Nagano [61].

with the strong jet deceleration typical of the impingement region and the subsequent deflection of the flow cause large departure from the log-law at $x/D = 0.5$. The consequent flow acceleration pertinent to the wall jet region is documented at the positions $x/D = 1...4$. The results obtained with the scale-resovling models, presented in Fig. 4.25 (a), indicate similarly high levels of agreement with the reference data in the vicinity of the impingement plate up to $x/D = 4$. The velocity profiles corresponding to the two last streamwise locations coincide almost completely indicating a locally fully-developed wall-jet. Whereas the stagnation region and initial acceleration are well predicted by the RANS model, as indicated in Fig. 4.25 (b), significant overprediction of the velocity maximum further upstream at positions $x/D \geq 2$ is obtained due to an underestimation of the local wall friction velocity.

This underestimation associated with the ζ-f model is documented in Fig. 4.26 in terms of the friction coefficient C_f at positions $x/D \geq 2$. VLES and the dynamic Smagorinksy model exhibit a similar underestimation at further downstream positions ($x/D > 3$), while the results obtained with ER ζ-f are in fairly good agreement with the reference data.

Similar observations can be made with respect to mean TKE profiles

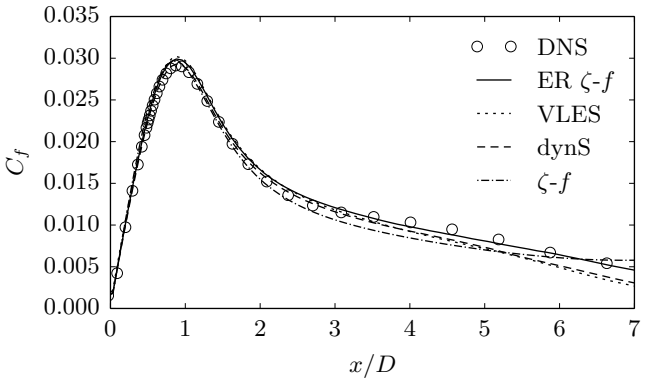

Figure 4.26: Friction coefficient along the impingement plate obtained on the coarse grid for the impinging jet configuration. DNS data taken from Hattori and Nagano [61].

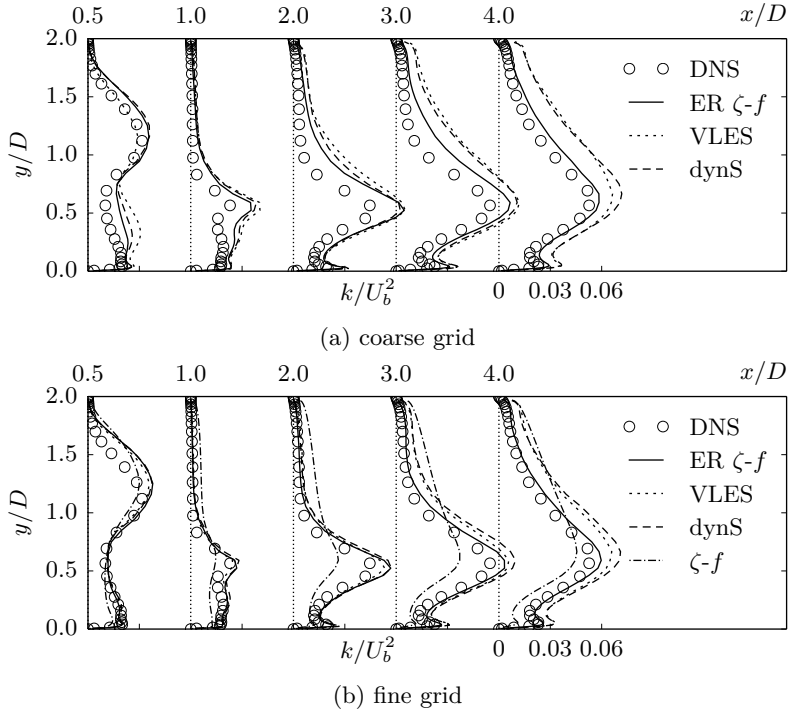

Figure 4.27: Mean TKE profiles obtained on the coarse (a) and fine grid (b) for the impinging jet configuration. DNS data taken from Hattori and Nagano [61].

presented in Fig. 4.27. On the coarse grid, Fig. 4.27 (a), the ER ζ-f model, while generally slightly overpredicting the turbulence activity, provides the most accurate results not only in the vicinity of the recirculation zone, but also with respect to the near-wall peak in the wall jet region, in particular at the two most downstream positions ($x/D = 3$ and 4). At this point, additionally results obtained on the fine grid are presented in Fig. 4.27 (b). At positions $x/D \leq 2$, grid refinement (mainly in spanwise direction) reduces the deviations between the scale-resolving models and improves the overall agreement with the reference data. Improvements are however less pronounced at the further down-

stream positions, where ER ζ-f remains more accurate compared to the other two models. Likely an additional refinement in x-direction would be required for the VLES and dynamic Smagorinsky models in order to reduce the aspect ratio of the cells, which are stretched predominantly in x-direction, and thus improve the validity of the grid-related length scale $\Delta = (\Delta x \Delta y \Delta z)^{1/3}$, on which those models rely. The results obtained with the ζ-f model, as shown in Fig. 4.27 (b), are reasonable only close to the impingement region; poor agreement at further downstream positions demonstrates the advantage of scale-resolving simulations, particularly with the ER ζ-f model, in capturing turbulent statistics.

Regarding thermal fields, mean temperatures and turbulent heat fluxes are analyzed in the following. Fig. 4.28 shows temperature profiles in wall units at different positions along the impingement plate obtained on the coarse grid. The quantity Θ^+ thereby corresponds to the temperature difference $\Theta - \Theta_\mathrm{w}$, with Θ_w representing the local wall temperature, normalized with the friction temperature $\Theta_\tau = q_\mathrm{w}/(\rho c_p u_\tau)$; here q_w is the heat flux prescribed at the impingement plate. Corresponding to the previously discussed velocity profiles in the near-wall region, only minor deviations between the scale-resolving models are obtained at the evaluated positions, while the ζ-f model overpredicts the temperature

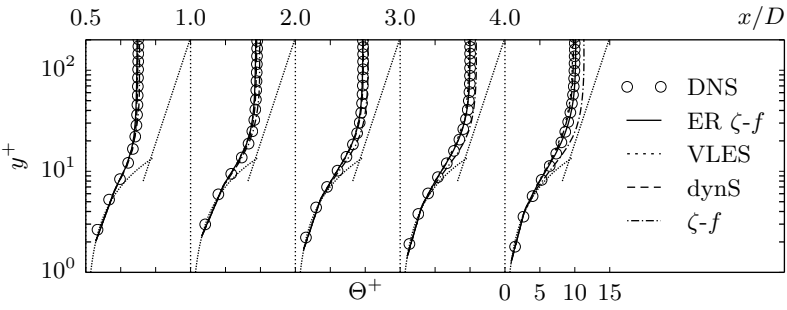

Figure 4.28: Mean temperature profiles in inner scaling in the vicinity of the impingement plate obtained on the coarse grid for the impinging jet configuration. DNS data taken from Hattori and Nagano [61].

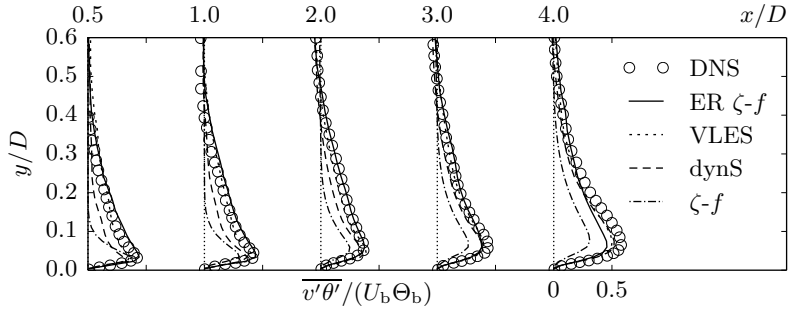

Figure 4.29: Mean turbulent heat flux in wall-normal direction obtained on the coarse grid for the impinging jet configuration. DNS data taken from Hattori and Nagano [61].

levels increasingly at further downstream positions.

Associated profiles of the wall-normal turbulent heat flux component normalized by the bulk velocity U_b and the bulk 'reference temperature' $\Theta_\mathrm{b} = q_\mathrm{w}/(\rho c_p U_\mathrm{b})$ are presented in Fig. 4.29. While the ζ-f model underpredicts the turbulent heat flux, ER ζ-f results exhibit good agreement with the reference data, except for the most downstream position, where an underestimation of the peak value can be observed. The results obtained with the VLES model, while imperfect, represent the best compromise with respect to accuracy at the various positions. Employing the dynamic Smagorinsky model results in an underprediction of the turbulent heat flux, particularly at the further upstream positions.

Concerning heat transfer between the flow and the wall, the local Nusselt number defined as $\mathrm{Nu} = 2\,D\,\alpha/\lambda$ is analyzed. Here, $\alpha = q_\mathrm{w}/(\Theta_\mathrm{w} - \Theta_\mathrm{m})$ is the local heat transfer coefficient, Θ_w the local wall temperature and Θ_m the mean temperature in the inlet channel. Fig. 4.30 illustrates the development of the Nusselt number along the impingement plate. The Nusselt number distribution exhibits its highest values in the stagnation region with a monotonic decrease along the impingement plate. The characteristic peak related to the stagnation point is mainly due to turbulence activity and the relatively thin boundary layer associated with the impingement of the flow. The scale-resolving models reproduce the local Nusselt number distribution well

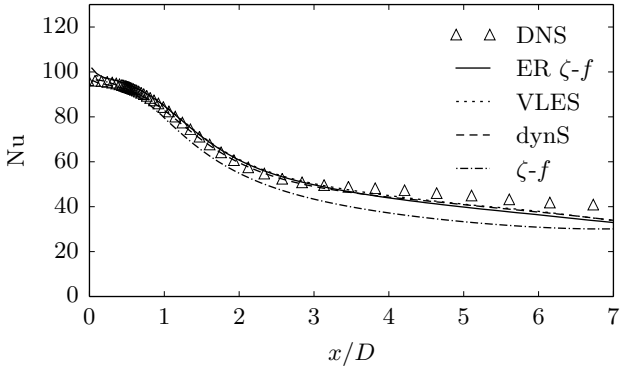

Figure 4.30: Nusselt number along the impingement plate obtained on the coarse grid for the impinging jet configuration. DNS data taken from Hattori and Nagano [61].

up to $x/D \approx 4$, but exhibit deviations further downstream, where the grid is significantly coarsened. The ζ-f model on the other hand more noticeably underpredicts the non-dimensionalized heat transfer at positions $x/D > 1$.

Conclusion

In summary, the ER ζ-f model exhibits the best performance among the applied models. Specifically, turbulence statistics and friction coefficients are more accurately captured compared to the other models, particularly on coarser grids. This is again attributed to a reduced grid sensitivity pertinent to the SAS-based sensitization of the model (see discussion in Section 4.3.1). Furthermore, it should be noted that a relatively crude approach to the modeling of the sub-scale turbulent heat fluxes is presently applied by relying on the SGDH as expressed by Eq. (2.33) as well as a constant turbulent Prandtl number of $\mathrm{Pr_t} = 0.6$ for all scale resolving models. While this approach is sufficient to obtain reasonably good results in the present case, the influence of $\mathrm{Pr_t}$ in conjunction with the respective model should be investigated further. In order to improve predictive capabilities in more complex heat transfer

applications, it might even be beneficial to apply an overall more sophisticated closure strategy to the turbulent heat fluxes, which does not rely on the restrictive assumption that the direction of turbulent heat fluxes is aligned with the gradient of the resolved temperature field.

4.3.5 Turbulent mixing in a T-junction

Flow phenomena encountered during the turbulent mixing of two streams crossing in a T-shaped junction are of interest for a variety of practical applications. While T-junctions can be found in many technical systems in the chemical and petroleum industry, major focus in recent years has been on their application in cooling systems of nuclear power plants, with the goal to more accurately predict thermal fatigue due to cyclic temperature fluctuations induced by the mixing process. Furthermore, T-junctions are relevant for automotive applications, including HVAC (heating, ventilation and air-conditioning) units as well as exhaust gas systems. Presently, the momentum and heat transfer in a two-dimensional T-junction configuration is considered. The junction is fed by two perpendicularly oriented inlet channels issuing fully-developed flow at different temperatures, i.e. a hot steam at Θ_h and a cold stream at Θ_c. The Reynolds number in the inlet channels is $\mathrm{Re}_\mathrm{b} = U_\mathrm{b} H/\nu = 5650$, based on the bulk velocity U_b and the channel height H; the Prandtl number of the fluid is $\mathrm{Pr} = 0.71$. As reference for the validation the DNS database of Hattori et al. [60] is employed. As in the previous case, RANS results obtained with the ζ-f model are additionally presented for comparative assessment.

Computational setup

A sketch of the computational domain is shown in Fig. 4.31. The domain dimensions correspond to $L_x/H = 8$ and $L_z/H = 1$, where H is the height of all channels. In order to generate fully-developed inflow data, simultaneous precursor simulations (see Section 4.3.2) are performed for both inlet channels. Standard wall boundary conditions are applied at the walls for the momentum and turbulence model equations. For the energy equation adiabatic conditions are imposed at the walls while fixed values of Θ_c and Θ_h are prescribed at the inlets corresponding to the main and branch channel, respectively. At the outlet,

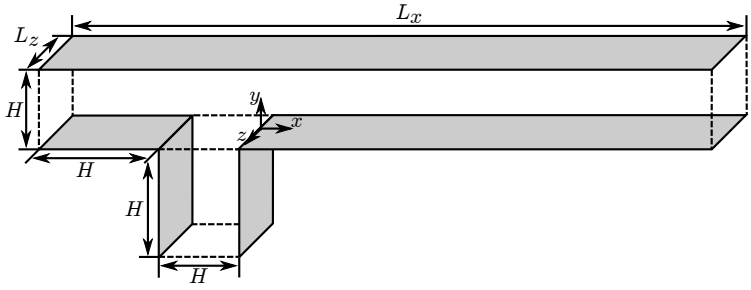

Figure 4.31: Sketch of the computational domain for the T-junction configuration.

zero-gradient conditions are applied for all quantities but the pressure, for which a fixed mean value is prescribed. Due to the two-dimensional configuration, periodic boundary conditions are imposed in spanwise direction.

Regarding the spatial discretization, two computational grids are used: The coarse grid comprises $92 \times 26 \times 19$ cells in x, y and z-directions for the main channel and $26 \times 14 \times 19$ for the branch channel. Thus, the coarse gird consists of merely 52364 cells. The total amount of cells for the fine mesh is 386650 cells, with $181 \times 50 \times 37$ cells in the main channel and $50 \times 28 \times 37$ in the branch. As in all previously considered cases, the grids are refined towards the wall in order to ensure that the first computational node is situated in the viscous sublayer. All computations with the ζ-f RANS model have been performed on a two-dimensional projection of the fine grid.

Due to excessive staggering characteristics being observable in the velocity field in conjunction with the application of CDS for the convective term in the momentum equation, the *filteredLinear3V* scheme (see Section 3.1.2) is applied with $C_{\mathrm{lim}} = 0.9$. Adaptive time stepping enforcing $\mathrm{Co} \leq 1$ is used in combination with the second-order BDF. The instantaneous results are averaged over a span of approximately 200 flow-through times (estimated as $H/U_{\mathrm{b}} + 7\,H/(2\,U_{\mathrm{b}}) = 4.5H/U_{\mathrm{b}}$) as well as spatially in z-direction.

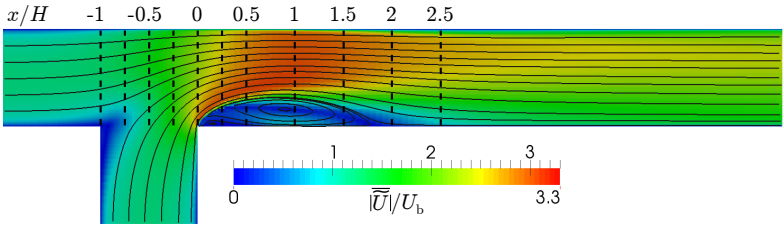

Figure 4.32: Streamlines and magnitude of the mean velocity field for the T-junction configuration, obtained with the ER ζ-f model on the fine grid. Vertical dashed lines mark positions for which quantitative results are presented in the following.

Results

The mean flow field arising from the impingement of the two crossing streams is displayed in Fig. 4.32 in terms of streamlines and the magnitude of the mean velocity field. The flow detaches at the corner located at $x/H = 0$, developing a recirculation zone at the lower wall with associated flow acceleration in the upper part of the channel and the resulting free shear layer, responsible for strong turbulence production, in between. Further downstream at $x/H \approx 2$, the flow reattaches. In the following, flow and thermal field are evaluated quantitatively at different positions x/H marked by the dashed lines in Fig. 4.32.

Fig. 4.33 displays the development of the mean streamwise velocity profiles normalized by the bulk velocity of the inlet channels U_b as predicted by the scale-resolving models on the coarse grid. Additionally, RANS results are presented, which have been computed on a two-dimensional projection of the fine grid, in order to ensure grid independence. Only minor discrepancies between the predictions of the three scale-resolving models as well as the RANS results can be identified. Particularly in the vicinity of the bottom wall at the three most downstream positions, $x/H \geq 1.5$, the results obtained with the ER ζ-f model are closer to the reference data. This advantage of ER ζ-f on the coarse grid is better illustrated by Fig. 4.34 (a) showing the associated evolution of the friction coefficient C_f along the bottom wall. Not

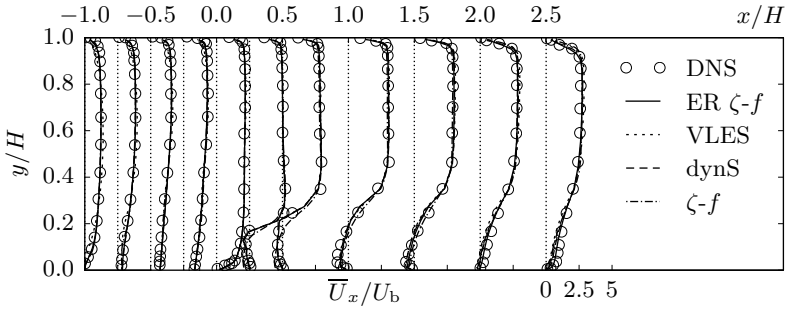

Figure 4.33: Mean streamwise velocity profiles obtained the scale-resolving models (coarse grid) and the ζ-f RANS model (fine grid) for the T-junction configuration. DNS data taken from Hattori *et al.* [60].

only is C_f captured quantitatively correct with the ER ζ-f model at positions $x/H > 2$, but importantly also the extent of the recirculation zone is predicted noticeably better compared to the other models. However, the negative peak of C_f in the recirculation zone is not captured correctly with either one of the models on the coarse grid. As illustrated by Fig. 4.34 (b), mesh refinement leads to better agreement with the reference data with all scale-resolving models, whereby the dynamic Smagorinsky model exhibits slightly more accurate results compared to the other models. The results obtained with the ζ-f RANS model on the other hand exhibit a poor level of agreement with the reference DNS at $x/H < 4$, as well as a too long recirculation zone. Reattachment locations obtained with the various model and grid combinations are summarized in Tab. 4.7.

In terms of turbulence statistics, profiles of TKE are presented in Fig. 4.35. On the coarse grid, Fig. 4.35 (a), at positions $x/H \leq 0$ results obtained with VLES exhibit the best level of agreement with the reference data base. Further downstream however, the turbulence activity in the separating shear layer is clearly underestimated. ER ζ-f and the dynamic Smagorinksy model exhibit more consistent behavior, capturing the TKE levels reasonably well up to $x/H = 1.5$. Further downstream, at $x/H \geq 2$, both models provide too little dissipation,

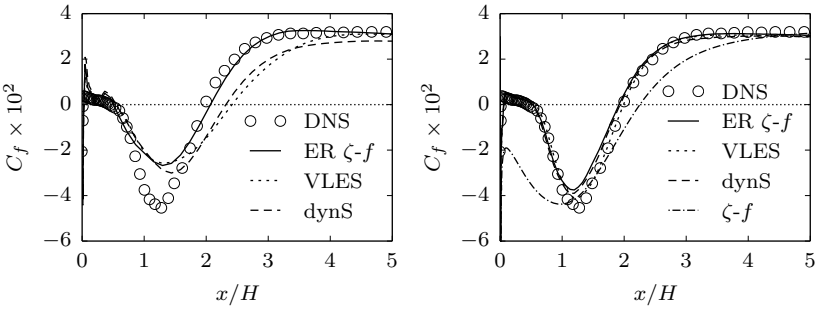

(a) coarse grid (b) fine grid

Figure 4.34: Friction coefficient along the bottom wall for the T-junction configuration on the coarse (a) and fine grid (b). DNS data taken from Hattori *et al.* [60].

resulting in an overprediction of TKE in the lower part of the channel, which is slightly more pronounced with the dynamic Smagorinsky model; similarly, the peak at the upper wall is more intensively overestimated compared to the ER ζ-f model. The VLES results appear more accurate at these positions, which is however mainly a result of the accumulated errors associated with the upstream region. Results obtained on the fine grid are presented in Fig. 4.35 (b). Here, the deviations between the scale-resolving models decrease and an overall good level of agreement is achieved. The ER ζ-f model thereby exhibits the highest level of agreement with the reference data, particularly at po-

Table 4.7: Reattachment points (x_r/H) for the T-junction configuration, obtained on the coarse and fine grids.

	coarse	fine
reference DNS	1.98	
ER ζ-f	2.07	1.92
VLES	2.42	1.94
dynS	2.32	1.99
ζ-f	–	2.25

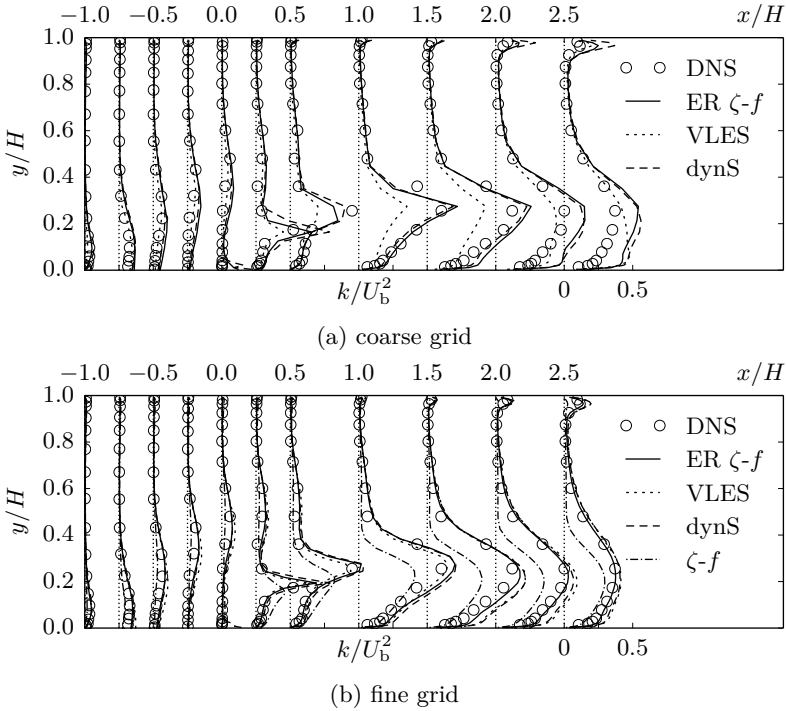

Figure 4.35: Mean TKE profiles obtained on the coarse (a) and fine grid (b) for the T-junction configuration. DNS data taken from Hattori *et al.* [60].

sitions $x/H \geq 1.5$, where the other two scale-resolving models tend to overpredict turbulence levels. The profiles obtained with the classical ζ-f model are qualitatively correct, yet turbulence levels in the separating shear layer and the recirculation region are noticeably underpredicted.

In terms of thermal fields, temperature profiles are presented in Fig. 4.36. Since realistic temperature values are bounded by the minimum temperature Θ_c associated with the cold stream and the maximum value Θ_h of the hot stream, temperature profiles are normalized by the temperature difference $\Delta\Theta = \Theta_\mathrm{h} - \Theta_\mathrm{c}$ as $\Theta - \Theta_\mathrm{c}/\Delta\Theta$. The extend of the thermal mixing region associated with intermediate values of the nor-

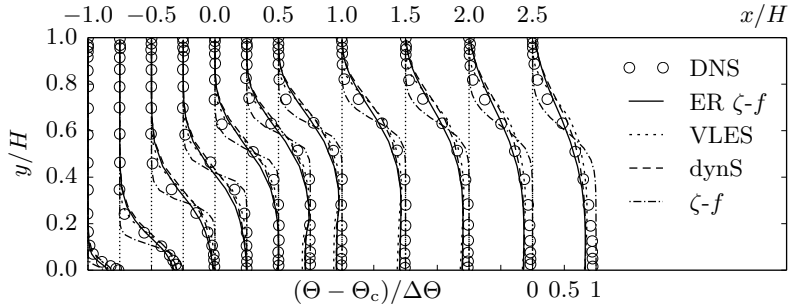

Figure 4.36: Mean temperature profiles normalized by the temperature difference $\Delta\Theta = \Theta_\mathrm{h} - \Theta_\mathrm{c}$ obtained on the coarse grid for the T-junction configuration. DNS data taken from Hattori *et al.* [60].

malized temperature field is clearly undepredicted with the ζ-f RANS model, which is in line with the overall underestimated turbulence activity. The results obtained with the scale-resolving models on the other hand exhibit somewhat too intense mixing in the recirculation bubble. In particular, the slight decrease of the bottom wall temperature indicated by the reference DNS is somewhat too pronounced with all scale-resolving models. As discussed in the previous section, a more advanced model for the turbulent heat fluxes or a tuning of the turbulent Prandtl number could be beneficial to improve the accuracy of the predicted temperature field. This seems especially indicated considering that mean velocity and TKE profiles are reasonably well captured by the ER ζ-f model in the region $x/H \leq 1.5$.

Associated profiles of the wall-normal turbulent heat flux component normalized with the temperature difference $\Delta\Theta$ and the bulk velocity of the inlet channels U_b are presented in Fig. 4.37. In line with the generally underpredicted turbulence activity pertinent to the RANS model, turbulent heat fluxes are clearly underestimated by the ζ-f model. With ER ζ-f and the dynamic Smagorinsky model reasonable agreement with the reference data base is achieved, while VLES results exhibit somewhat lower values, especially in the thermal mixing region.

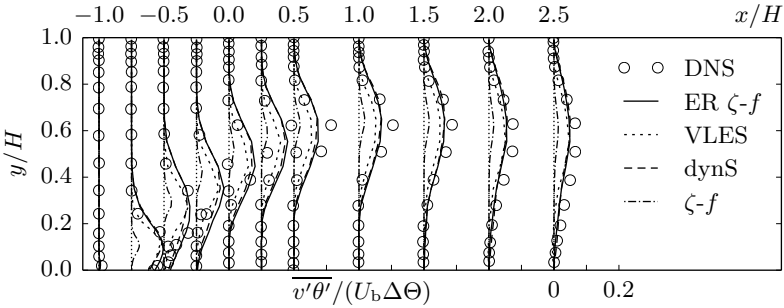

Figure 4.37: Mean turbulent heat flux in wall-normal direction obtained on the coarse grid for the T-junction configuration. DNS data taken from Hattori *et al.* [60].

Conclusion

Overall, the ER ζ-f model is successfully validated for the present case of turbulent mixing in a T-junction. Analogously to previously considered cases, the SAS-based model formulation is demonstrated to be advantageous with respect to predictive capabilities in terms of the spatial structure of the mean flow, distribution of TKE as well as the friction coefficient, in particular but not exclusively on the coarse grid.

4.3.6 A note on computational effort

The superior predictive capabilities in terms of mean flow quantities associated with resolving parts of the turbulent spectrum are well documented in literature, especially with respect to flow separation and highly unsteady effects, such as vortex shedding in free shear layers. This advantage is presently also demonstrated for the considered generic flow configurations, where scale-resolving models generally perform better compared to the ζ-f model. The computational effort required for scale-resolving computations is however significantly higher, mainly due to the necessity to compute extended amounts of physical time in order to obtain converged mean flow fields from the computed instantaneous data. Additionally, symmetries and homogeneity in the mean flow can not be taken advantage of in scale-resolving computations, due to the

necessity to capture the inherently three-dimensional structure of turbulent eddies.

In the case that scale-resolving computations ought to be performed, whether it may be due to accuracy requirements, interest in temporally resolved data or an improved coupling with additional models, RANS-based scale-resolving approaches aim to reduce the required computational effort compared to a well-resolved LES. Since most RANS models are based on at least two differential transport equations whereas in the LES framework mostly algebraic closures are applied, the computational effort on a given grid is generally higher with RANS-based models due to the required effort for solving the additional turbulence model equations. Consequently, the rationale is to obtain a similar level of accuracy on a coarser grid, thus mitigating the additional computational effort. Nevertheless, the predictive capabilities of different models are usually assessed by comparing results obtained on a given grid resolution, as it was done in the previous section.

Table 4.8: Normalized computing time relative to the dynamic Smagorinsky model for channel flow at $\mathrm{Re}_\tau = 392$ on the medium grid and the T-junction configuration on the coarse grid.

	Channel	T-junction
ER ζ-f	114%	109%
VLES	107%	105%
dynS	100%	100%

Complicating matters further, the relative impact of solving turbulence model equations is dependent on a variety of factors including the considered case and associated convergence rates. To give specific examples, Tab. 4.8 summarizes the computing time with the VLES and ER ζ-f model relative to the dynamic Smagorinsky model for the cases of channel flow at $\mathrm{Re}_\tau = 392$ on the medium grid (see Section 4.3.1) and the T-junction configuration on the coarse grid (see Section 4.3.5). The performance measurements have been carried out on the Lichtenberg cluster (MPI2 section, Intel Xeon E5-2680 v3 processors) at TU Darmstadt on an exclusively used computational node. The identical domain

decomposition for parallelization was applied and the same linear equation solvers as well as convergence criteria were set for all models. The computations have been performed for a given physical simulation time, using adaptive time stepping. Output to storage was disabled and at least three runs have been performed in order to ascertain a representative average.

As indicated by Tab. 4.8, employing the ER ζ-f model results in relative computing time penalties of 14% and 9% for the investigated channel and T-junction cases. With the VLES model, respective values of 7% and 5% are obtained. The computational overhead associated with the RANS-based models is moderate, since the majority of computing time is spent on achieving pressure-velocity coupling, or more specifically, on solving the elliptic pressure correction equation employing OpenFOAM's geometric agglomerated algebraic multigrid (GAMG) solver (see [113]). Incidentally, the higher computational effort associated with the ER ζ-f model compared to VLES can also mainly be attributed to solving the pressure correction equation, since with the ER ζ-f model, slightly more GAMG iterations per time step are required to fall below the maximum prescribed residual. The generally lower relative computational overhead in the T-junction case can be attributed to the aforementioned flow-dependent convergence rates, as well as the solution of an additional scalar transport equation for the temperature. For practical applications, the computing time penalty of 9% obtained with the ER ζ-f model in the more complex T-junction configuration is likely more representative, then simple channel flow. Furthermore, it should be emphasized that when additional equations are solved, for instance multiple species transport equations for combustion modeling, the relative effort for solving the turbulence model further decreases. In any case a 9 to 14% increase in computational costs seems manageable with respect to the higher predictive capabilities of the ER ζ-f model at lower spatial resolutions.

A more rigorous way to quantify the efficiency of RANS-based scale-resolving models in terms of computational costs would be to compare the grid resolutions and thus computing time required to achieve the same level of accuracy with different models. While this approach is fairly unpractical for real world applications, since a global quality criterion is often not readily defined, for channel flow this can conveniently be

done based on the relative deviation of the wall friction velocity. Thus, the question arises, how much does the grid have to be refined in order to achieve the same level of accuracy with the dynamic Smagorinksy model compared to ER ζ-f? To answer this question, the result obtained with the ER ζ-f model for channel flow at $\mathrm{Re}_\tau = 392$ on the medium grid consisting of 180000 cells is used as reference. Here, a relative deviation of $\Delta u_\tau = 2.2\%$ (see Tab. 4.4) was obtained. The grid is then gradually refined in streamwise and spanwise directions until the same value of Δu_τ is obtained with the dynamic Smagorinsky model. This is achieved on a mesh consisting of 318000 cells, i.e. a 76% increase. In terms of computing time, this translates to 160% relative to the computing time spent for the ER ζ-f model, i.e. a 60% increase to achieve the same predictive quality. Considering the VLES models performance in terms of Δu_τ is still worse on the fine grid (see Tab. 4.4) compared to the reference case, an even larger computing time increase can be expected with the VLES model. Consequently, the ER ζ-f model is clearly more efficient for the considered case, even though it has the highest penalty for solving the turbulence model equations (see Tab. 4.8).

As discussed, the efficiency gains associated with the ER ζ-f model cannot be quantified in a universal way due to the multitude of influencing factors. However, an estimate is presented for channel flow and the efficiency is expected to increase when additional physical effects (chemical reactions, multiphase models, etc.) are considered for which equations are solved on an accordingly coarser grid. Furthermore, coarser grids pose additional advantages in terms of enabling larger time steps as well as parallelization on fewer processors, which generally improves parallel efficiency.

4.4 Concluding remarks

A newly formulated eddy-resolving ζ-f model based on the SAS concept was proposed. In a first step, the constituent RANS model's scale-supplying equation for the dissipation rate of TKE ε was transformed to an equation for the inverse time scale ω in order to facilitate the subsequent sensitization of the model. The ω-equation was recalibrated accounting for a cross-diffusion term stemming from the transformation procedure and it was demonstrated that the ω-based variant performs

similar or better compared to the baseline ζ-f RANS model in the computed flow configurations. Subsequently, an additional production term motivated by the SAS concept was derived and introduced into the ω-equation in order to allow the model to adapt to resolved turbulent fluctuations. The SAS term was formulated and calibrated in such a way as to enable scale-resolving computations even in globally stable flow configurations at low Reynolds numbers. The model was then validated by computing a test case library comprising several generic flow configurations, whereby special focus was given to relatively coarse grids. The performance of the new 2G-URANS model was furthermore assessed by comparison to results obtained with the VLES and dynamic Smagorinsky models. It could be demonstrated that in most cases the ER ζ-f model provides better results in terms of flow topology, friction factors and TKE levels on coarse grids while maintaining competitive accuracy on fine grids suitable for LES. This effectively indicates a reduced grid sensitivity which is advantageous especially for more complex practical applications such as internal combustion engines, where the appropriate grid resolution is often unclear in advance. The advantage of ER ζ-f is mainly attributed to the SAS-based sensitization, where the second derivative of the velocity field is employed in order to estimate an additional length scale associated with resolved turbulent structures instead of relying on the grid spacing Δ as commonly practiced in LES and hybrid RANS/LES closures. Finally, the computational overhead associated with solving the model equations of the ER ζ-f was quantified to be 14% in the worst case scenario compared to an under-resolved LES with the dynamic Smagorinsky model on the same grid. It was further demonstrated for the example of plane channel flow that in order to achieve the same level of accuracy provided by the ER ζ-f model with respect to wall friction, a finer grid corresponding to an increase of 60% in terms of computational cost is required, when applying the dynamic Smagorinsky model. The VLES model proved less efficient in this regard and requires an even finer spatial resolution then the dynamic Smagorinsky model, which is unsatisfactory considering the computational overhead for solving the turbulence model's equations.

5 Roughness modeling in scale-resolving simulations

This chapter is focused on modeling the effect of rough surfaces on fluid flow in the context of scale-resolving computations of turbulence. Guided by the requirements associated with the intended application of the presently developed modeling framework for near-wall reactive flow applications, a computationally efficient model able to account for the effect of realistic, irregular rough surfaces on turbulent flow, is required. To be more specific, accurate predictions of the mean flow field and turbulent statistics in the roughness sublayer are necessary in order to enable efficient CFD computations of coupled problems, where near-wall phenomena play a significant role. Here, the guiding examples of internal combustion engines and exhaust gas aftertreatment systems shall be mentioned again, where the near-wall region has been identified as crucial with respect to the formation of pollutants and undesirable depositions. In these cases, such depositions can be considered as the main reason for the formation of rough surfaces on a scale that affects the flow. Nevertheless, it should be pointed out that the proposed roughness modeling methodology is also applicable to a variety of other technical and environmental flows, where rough surfaces are generated by different processes, as discussed in Section 2.3.

Due to the requirements with respect to the near-wall region, classical roughness models relying on correlations for Nikuradse's equivalent sand roughness height k_s are deemed unsuitable, especially in conjunction with near-wall, scale-resolving turbulence modeling approaches, such as the presently proposed ER ζ-f model. Thus, in this work, roughness modeling approaches based on volumetric forcing are investigated, which in principle date back to the discrete element approach of Taylor *et al.* [147]. As discussed in Section 2.3.2, two types of volumetric forcing approaches have been applied in the past, which differentiate in whether or not blockage effects are accounted for in the governing

equations. The implications of this choice with respect to predictive quality, are one of the key issues investigated in the present chapter. Since up to now, it is unclear how an optimal volumetric force field or associated drag coefficient profiles for a given rough surface should be shaped, a data-driven methodology relying on geometry-resolving DNS data is proposed and subsequently applied for this investigation. Furthermore, a drag closure originally proposed in the context of flow through porous media is reformulated in order to facilitate modeling of the volumetric force field associated with a rough wall, relying primarily on geometrical details of the roughness topography. This model, termed as equivalent porosity model (EPM), is then calibrated in an a priori fashion based on the proposed data-driven methodology. Hence, a unified modeling approach for flow over porous and rough walls is enabled. As reference data for the assessment of the modeling approaches as well as the validation of the EPM, the DNS data base of Forooghi *et al.* [48] for flow over different roughness topographies in an open-channel flow configuration, is applied.

In Section 5.1, the investigated flow configuration and roughness topographies are introduced. Subsequently, a DDF approach, not explicitly accounting for blockage effects, and the methodology to estimate the shape of the drag coefficient profiles in a data-driven manner is proposed and evaluated in Section 5.2. Thereafter, in Section 5.3 and the corresponding sub-sections, the implementation of a flow solver based on additionally volume-averaged equations from the porous-media-framework is described, and the considered turbulence models are appropriately modified in order to enable the unified modeling approach for porous and rough walls. After verification and validation of the solver and the turbulence models for the case of channel flow over porous walls, the data-driven methodology for rough walls is appropriately adapted to a VAF approach explicitly accounting for blockage effects. Finally, the EPM model is introduced and validated. Parts of the results and discussion presented in this chapter have been previously published or accepted for publication in the following articles or conference contributions: [77, 78, 83, 84].

5.1 Roughness topographies and flow configuration

As a basis for roughness modeling and the associated validation, eight synthetic roughness topographies are considered, for which reference data from geometry-resolving DNS using an immersed boundary method is available. The DNS of Forooghi *et al.* [48] and [78] was performed in an open-channel with a rough bottom wall at friction-based Reynolds numbers in the range $\mathrm{Re}_\tau = H_{\mathrm{eff}} u_\tau / \nu = 461...502$ (depending on the roughness topography). A schematic illustration of the flow configuration is shown in Fig. 5.1. For the present scale-resolving compu-

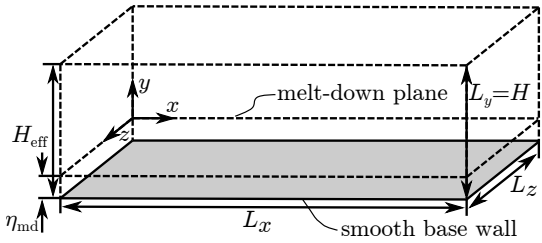

Figure 5.1: Schematic illustration of the computational domain for open-channel flow with a rough bottom wall. Roughness topography is not shown.

tations based on volumetric forcing approaches, domain dimensions of $L_x/H = 4$ and $L_z/H = 2$ are used. Periodic boundary conditions are applied in streamwise and spanwise directions, while standard wall boundary conditions are prescribed at the smooth base wall. At the upper boundary of the domain, a symmetry plane is prescribed corresponding to the open-channel configuration. The roughness topography situated above the smooth base wall is not shown, since it is not geometrically represented in the present computations. However, the corresponding melt-down plane, located at a position η_{md} above the smooth base wall, is sketched. The height of the channel effectively available to the flow is thus given by $H_{\mathrm{eff}} = H - \eta_{\mathrm{md}}$. Forooghi *et al.* [48] adopted the melt-down plane as the virtual wall, i.e. $y = 0$. As discussed in Section 2.3.1, such an a priori definition of the position of the virtual

wall is detrimental for an accurate estimation of the roughness function and the equivalent sand roughness height. However, since this choice is immaterial for the considered roughness modeling approaches as well as the subsequent validation, this simple a priori definition is retained here in order to remain consistent with the data presented in [48] and [78].

The presently investigated synthetic roughness topographies are assembled from axisymmetric roughness elements, which are either regularly or randomly arranged. Fig. 5.2 shows the four regular surfaces.

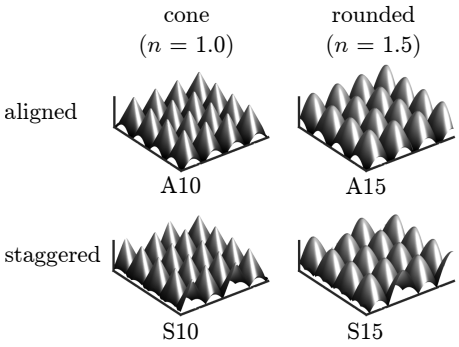

Figure 5.2: Samples of the regularly arranged roughness topographies. Adapted from Krumbein *et al.* [78].

Two arrangement patterns (aligned/staggered) and two element shapes ($n = 1.0$, $n = 1.5$) are considered. In the following, the regular roughness topographies are correspondingly denoted as A10, A15, S10 and S15. A sketch of the roughness elements with the relevant coordinate systems and dimensions is shown in Fig. 5.3. The height distribution of the roughness elements relative to the smooth base wall is given by

$$\eta = k_\mathrm{t} \min\left[1 - \left(\frac{r_0 - r}{r_0 - R_0}\right)^n, 1\right], \tag{5.1}$$

where k_t is the peak-to-valley height and r the radial coordinate with respect to a local coordinate system whose origin is defined by the intersection of the symmetry axis of the considered roughness element

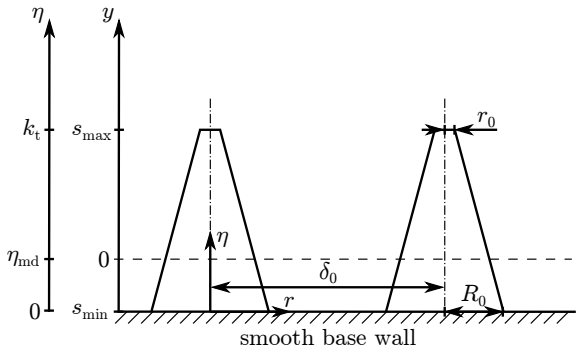

Figure 5.3: Qualitative sketch of two cone-shaped roughness elements with the η-coordinate originating from the smooth base wall and the y-coordinate originating from the melt down plane (as defined by Eq. (2.48)).

with the smooth wall plane located at $\eta = 0$. Furthermore, R_0 and $r_0 = 0.05R_0$ are the radii at $\eta = 0$ and $\eta = k_\mathrm{t}$, respectively, and n is a parameter defining the contour of the surface. The base radius R_0 of the elements as well as the distance δ_0 between the symmetry axes is chosen in such a way, that the frontal solidity is similar ($\Lambda \approx 0.64$) in all cases. The geometrical parameters for the four regularly arranged roughness topographies are summarized in Tab. 5.1.

Illustrations of the four randomly arranged roughness topographies adopted from Forooghi *et al.* [48] are presented in Fig. 5.4. These

Table 5.1: Base radius R_0 and distance of the roughness elements δ_0, both non-dimensionalized with the peak-to-valley height k_t for the four regular roughness configurations.

	R_0/k_t	δ_0/k_t
A10	0.500	0.800
A15	0.555	0.888
S10	0.525	0.800
S15	0.583	0.888

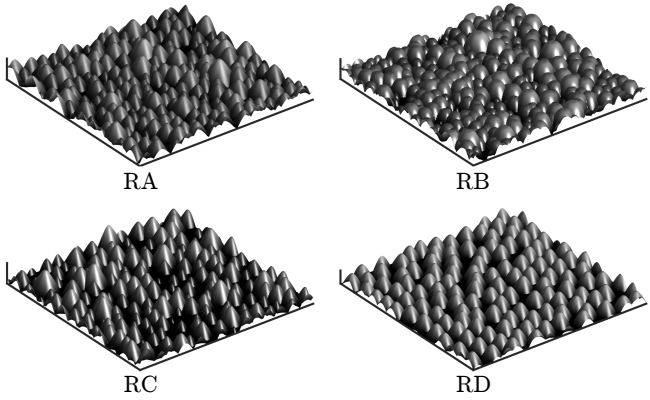

Figure 5.4: Surface samples of the randomly arranged roughness topographies.

surfaces were generated by randomly distributing roughness elements, the shape of which is again described by Eq. (5.1), but with variable height, base radius and shape parameter. The elements were scaled and arranged in such a way that predefined values of statistical properties of the roughness, which are discussed in Section 2.3, are achieved. Thereby, roughness elements were allowed to intersect, which is also the case for the regular arrangements, but is encountered much more frequently for the random surfaces. For a more detailed description of the generation approach for the randomly-arranged rough surfaces the reader is referred to Forooghi *et al.* [48]. The random topographies are denoted as RA, RB, RC and RD in the following.

Tab. 5.2 summarizes the statistical properties for all presently considered surfaces. The random topographies RA, RB and RC share similar surface statistics except for the skewness Sk, which apart from the roughness height has been identified as the most influential parameter with respect to the roughness function (see Section 2.3). The topography RD is statistically similar to RA, with the main difference being that the former surface is made up of roughness elements with uniform shape and height, as it is the case for the regular arrangements. While the roughness topographies adopted from the reference DNS study are

Table 5.2: Statistical properties of the regular and random roughness topographies.

	η_{md}/H	$k_{\mathrm{t}}/H_{\mathrm{eff}}$	$k_{\mathrm{rms}}/H_{\mathrm{eff}}$	Sk	Ku	ES	Λ
A10	0.041	0.104	0.025	0.36	2.39	1.28	0.64
A15	0.052	0.105	0.028	−0.07	2.14	1.28	0.64
S10	0.045	0.105	0.024	0.31	2.42	1.28	0.64
S15	0.056	0.106	0.026	−0.15	2.26	1.28	0.64
RA	0.072	0.248	0.045	0.21	2.62	0.88	0.44
RB	0.084	0.233	0.045	−0.33	2.62	0.88	0.44
RC	0.048	0.222	0.045	0.66	2.62	0.88	0.44
RD	0.056	0.145	0.045	0.22	1.88	0.89	0.44

synthetically generated in order to span a wide parameter range, the values of skewness and kurtosis agree well with values measured for roughness on gas turbine blades generated by depositions, as reported in Bons *et al.* [16].

In the DNS, a fixed streamwise pressure gradient was imposed to drive the flow. Thus, essentially, the friction-based Reynolds number Re_τ was prescribed and the corresponding bulk Reynolds numbers can be considered as results of the computations. In the present work the exact opposite is done, which is more convenient for practical applications; i.e. the flow is driven such that a fixed bulk velocity (or flow rate) is prescribed and the pressure gradient (or corresponding friction-velocity) is a result of the computations. Consequently, bulk Reynolds numbers $\mathrm{Re}_{\mathrm{b}} = U_{\mathrm{b}}^{\mathrm{s}} H_{\mathrm{eff}}/\nu$ are determined based on the superficially-averaged mean streamwise velocity profiles from the DNS data base by defining the superficial bulk velocity as

$$U_{\mathrm{b}}^{\mathrm{s}} = \frac{1}{H}\int_0^H \langle \overline{U}_x \rangle^{\mathrm{s},xz} \mathrm{d}\eta. \tag{5.2}$$

The respective bulk and friction Reynolds numbers from the geometry-resolving DNS computations with the eight roughness topographies as well as a smooth wall are summarized in Tab. 5.3. In addition to the global flow properties, the DNS data base includes superficially-averaged streamwise velocity profiles ($\langle \overline{U}_x \rangle^{\mathrm{s},xz}$) for all cases. In terms

Table 5.3: Bulk and friction Reynolds numbers of the reference DNS for open-channel flow with regular and random roughness topographies as well as a smooth wall.

	Re_b	Re_τ
smooth	9064	501
A10	4624	471
A15	4963	464
S10	4296	468
S15	4548	461
RA	3954	498
RB	4520	501
RC	3855	502
RD	4105	501

of turbulence statistics, only combined Reynolds and dispersive stresses ($\langle\overline{u_i u_j}\rangle^{\mathrm{s},xz}$) have been evaluated for the regular rough surfaces. However, for the random roughness topographies, which have been computed with an optimized DNS workflow, Reynolds ($\langle\overline{u_i' u_j'}\rangle^{\mathrm{s},xz}$) and dispersive stresses ($\langle\overline{u_i^* u_j^*}\rangle^{\mathrm{s},xz}$) have been evaluated separately.

5.2 Data-driven distributed drag force approach

In a first step, a DDF approach is investigated. With respect to implementation and application, such an approach is advantageous since it relies on the same governing equations used for single phase flow computations with merely a volumetric force term added to the momentum equation. The modified momentum equation thus reads

$$\frac{\partial\widetilde{U}_i}{\partial t} + \widetilde{U}_j\frac{\partial\widetilde{U}_i}{\partial x_j} = -\frac{1}{\rho}\frac{\partial\widetilde{P}}{\partial x_i} + \frac{\partial}{\partial x_j}\left(\nu\frac{\partial\widetilde{U}_i}{\partial x_j}\right) - \frac{\partial\tau_{ij}}{\partial x_j} + \widetilde{f}_{\mathrm{d},i}, \tag{5.3}$$

where $\widetilde{f}_{\mathrm{d},i}$ is the additional density specific volumetric force term intended to model blockage effects as well as the viscous and form drag

the roughness elements exert on the flow. The continuity equation (2.27) and the Boussinesq eddy-viscosity ansatz (2.32) remain unchanged.

The presently proposed data-driven approach is motivated by the work of Busse and Sandham [23] who applied a drag force term according to Eq. (2.60), as discussed in Section 2.3.2. The drag term is parametrized relying on a roughness factor α_i in each direction, as well as a non-dimensional and normalized shape function $F(y)$ accounting for a modification of the roughness factor with wall distance. By varying the roughness factor and applying various rather arbitrarily selected shape functions, fulfilling several realizability constraints, they demonstrated qualitatively in an extensive parametric study that many effects a rough wall exerts on turbulent flow can be captured in scale-resolving simulations using such a DDF approach. In terms of a quantitative comparison, they selected one shape function and 'tuned' the roughness factor to fit the roughness function ΔU^+ of the reference DNS for flow over transverse square bars. Consequently, the resulting mean velocity profile exhibits very good agreement in the log-region, but deviations in the roughness sublayer indicate that either the modeling approach or the roughness factor and shape function are not optimal for the considered case. In order to further investigate the performance of the DDF approach in a quantitative way and provide a first step towards modeling the drag term based on geometrical properties of the rough surface, a methodology to determine the drag force directly from geometry-resolving DNS data is proposed in the following.

In the present work, a slightly different parametrization for $\widetilde{f}_{\mathrm{d},i}$ is adopted, which is closer to the customary expression for a drag force compared to the formulation of Busse and Sandham [23]. The parametrization reads

$$\rho\,\widetilde{f}_{\mathrm{d},i} = -\frac{1}{2}\rho\,\widetilde{U}_j\widetilde{U}_j\,\frac{C_\mathrm{d}(y)}{k_\mathrm{t}}\,\frac{\widetilde{U}_i}{(\widetilde{U}_k\widetilde{U}_k)^{1/2}}, \tag{5.4}$$

were the peak-to-valley height k_t was arbitrarily selected as a length scale, since this choice has no impact on the further discussion. The ratio of the sectional drag coefficient $C_\mathrm{d}(y)$ and k_t is proportional to the product of the roughness factor and shape function in the work of Busse and Sandham [23]. A key difference however, is that they did not apply the usual formulation of the drag term proportional to the magnitude of the velocity squared ($\sim \widetilde{U}_j\widetilde{U}_j$) acting in the opposite direction of the

local velocity vector, given by the unit normal vector $-\widetilde{U}_i/(\widetilde{U}_k\widetilde{U}_k)^{1/2}$, but instead formulated a drag force, where each component is proportional only to the respective component of the velocity squared, i.e. $\widetilde{f}_{\mathrm{d},x} \sim \widetilde{U}_x^2$, $\widetilde{f}_{\mathrm{d},y} \sim \widetilde{U}_y^2$ and $\widetilde{f}_{\mathrm{d},z} \sim \widetilde{U}_z^2$, which implies that the resulting drag force is not aligned against the direction of the velocity vector. They argue that this somewhat curious choice was made, since application of the full quadratic formulation "impairs the outer-layer similarity of the mean streamwise velocity profile" [23]. Since this observation could not be reproduced in this work, the customary expression, which seems more consistent, is adopted here.

In order to determine the shape and magnitude of the mean volumetric force necessary to achieve the correct velocity profile and ultimately estimate the sectional drag coefficient C_d, a data-driven approach based on the reference DNS data base is applied. Consistent with the model assumption of a distributed force with constant proportionality coefficient C_d in layers parallel to the wall, the superficially-averaged profiles from the geometry-resolving reference DNS are evaluated using RANS equations. Here, the spatial variations of the time-averaged velocity field, which give rise to the dispersive stresses $\langle u_i^* u_j^* \rangle^{\mathrm{s},xz}$ are neglected (see associated discussion in Section 2.3.1). For the considered case of open-channel flow (see Fig. 5.1), the dominant streamwise component of the time-averaged drag force is thus estimated as

$$\overline{f}_{\mathrm{d},x} \approx \frac{1}{\rho}\left\langle \frac{\partial \overline{P}}{\partial x} \right\rangle^{\mathrm{s},xz} - \nu \frac{\partial^2}{\partial y \partial y}\left(\langle \overline{U}_x \rangle^{\mathrm{s},xz}\right) + \frac{\partial}{\partial y}\left(\langle \overline{u'v'} \rangle^{\mathrm{s},xz}\right). \qquad (5.5)$$

The drag force profile $\overline{f}_{\mathrm{d},x}$ is evaluated for each roughness topography by inserting corresponding DNS data into the right hand side of Eq. (5.5). For the regular surfaces the total turbulent shear stress is used since, as discussed in Section 5.1, Reynolds stresses have not been evaluated separately for these cases in the DNS. However, the impact of this inevitable choice will be demonstrated for the random topographies by computing with sectional drag coefficients based on total and Reynolds stresses, respectively. Finally, the sectional drag coefficient C_d is estimated based on the determined mean drag force profiles by normalizing with the dynamic pressure based on the DNS's velocity profile, accord-

ing to

$$C_{\mathrm{d}}(y) \approx -\frac{\rho \overline{f}_{\mathrm{d},x}\, k_{\mathrm{t}}}{\frac{1}{2}\rho \left(\langle \overline{U}_x \rangle^{\mathrm{s},xz}\right)^2}. \tag{5.6}$$

Since the mean velocity magnitude assumes very small values close to the base wall, predominantly due to blockage and viscous effects, the normalization with the square of the streamwise velocity in Eq. (5.6) results in very large values of C_{d} in this region. In addition, uncertainties associated with the numerical procedure applied to estimate $\overline{f}_{\mathrm{d},x}$ (according to Eq. (5.5)) as well as the evaluated DNS data base are greatly enhanced in the vicinity of the base wall due to the normalization. Thus, the sectional drag coefficient is in this work bound to a maximum value of $C_{\mathrm{d}} = 400$, mainly for numerical stability purposes. The resulting C_{d} profiles are presented in Fig. 5.5. Since the mean velocity is small deep inside the roughness layer, the applied bounding is expected to have a minor influence on the model performance; in any case, simulations with smaller bounding values of down to $C_{\mathrm{d}} = 200$ indicate a negligible influence of the prescribed maximum value, which reinforces this assumption. The C_{d} profiles presented in Fig. 5.5 steeply decrease from the initially bounded levels in the vicinity of the base wall

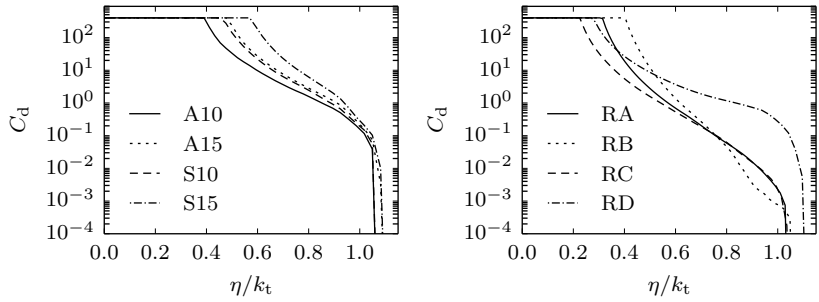

(a) regular roughness (b) random roughness

Figure 5.5: Bounded sectional drag coefficients for the DDF approach. Regular roughness (a) based on combined Reynolds and dispersive stress; random roughness (b) based on Reynolds stress only.

and approach zero slightly above the maximum elevation of the roughness at $\eta/k_\mathrm{t} = 1$. Hence, as can be expected, the volumetric forcing term is only active in the immediate vicinity of the rough surface.

Computational setup

In the following the results obtained with the data-driven DDF approach for the open-channel flow configuration (see Fig. 5.1) are presented. Computations are performed with the ER ζ-f model on a grid corresponding – in terms of non-dimensional grid spacings – to the fine grids applied for smooth channel flow in Section 4.3.1. This grid resolution is chosen in order to assess the performance of the roughness model, while limiting uncertainties associated with the turbulence modeling approach; it is at this point recalled that for the smooth channel computations at the corresponding grid resolution, u_τ is predicted within a 2% error margin by the ER ζ-f model. Based on the friction Reynolds number of $\mathrm{Re}_\tau \approx 500$, the applied grid comprises $80 \times 64 \times 100$ cells in streamwise, wall-normal and spanwise directions, respectively. The remaining computational details correspond to the smooth channel computations presented in Section 4.3.1. Results are averaged in time over a span of at least 130 flow-through time ($130\, L_x/U_\mathrm{b}^\mathrm{s}$). In addition, superficial averaging in streamwise and spanwise directions is performed. The friction velocity u_τ associated with the superficially-averaged mean velocity can not be determined directly based on the wall-normal gradient, since the rough surface is not resolved in the computations. Instead, a global momentum balance is formulated, in order to calculate u_τ from the mean driving pressure gradient, resulting in

$$u_\tau = \sqrt{-\frac{H}{\rho}\overline{\frac{\partial \widetilde{\widetilde{P}}}{\partial x}}}. \tag{5.7}$$

As discussed in Chan-Braun *et al.* [25], this approach is equivalent to the extrapolation of total shear stress to the position of the virtual wall, which was applied in the reference DNS.

Results

Mean velocity profiles normalized by the superficial bulk velocity for the regular and random roughness topographies are presented in Fig.

5.6 (a) and (b), respectively. As previously discussed, the blockage and drag exerted by the roughness elements results in very low velocities below the melt-down plane. Good agreement with the DNS data base is achieved for all topographies, importantly also with respect to the roughness sublayer. For the random topographies results obtained with sectional drag coefficients based on full as well as Reynolds stresses are presented. Only minor differences can be identified, whereby the Reynolds-stress-based results seem slightly more accurate with respect to the initial slope of the velocity profile at $y/H_{\mathrm{eff}} < 0.2$. On the other hand, at $y/H_{\mathrm{eff}} > 0.7$, the full stress results are in closer agreement with the reference DNS.

Velocity profiles normalized by the friction velocity u_τ are shown in Fig. 5.7. Here, more noticeable deviation from the reference data can be observed due to inaccuracies in the prediction of the friction velocity u_τ. Corresponding relative deviations of the predicted values to the reference data $u_{\tau,\mathrm{DNS}}$ are summarized in Tab. 5.4. No general trend can be identified; both under- and overprediction of u_τ occurs depending on the roughness topography, with maximum deviations of approximately 12%. The friction predicted with the Reynolds-stress-based sectional drag coefficient, is generally smaller. However, in terms of accuracy no clear advantage of either estimation approach for C_{d} can be identified.

Table 5.4: Relative deviation of the wall friction velocity ($\Delta u_\tau = (u_\tau - u_{\tau,\mathrm{DNS}})/u_{\tau,\mathrm{DNS}}$) for the various roughness topographies, based on data-driven DDF considering combined Reynolds and dispersive stresses (full stress) or Reynolds stresses only (Re. stress).

	full stress	Re. stress
A10	4.0%	–
A15	11.8%	–
S10	−5.4%	–
S15	−1.7%	–
RA	1.2%	3.8%
RB	7.7%	10.3%
RC	−3.3%	0.9%
RD	2.8%	6.6%

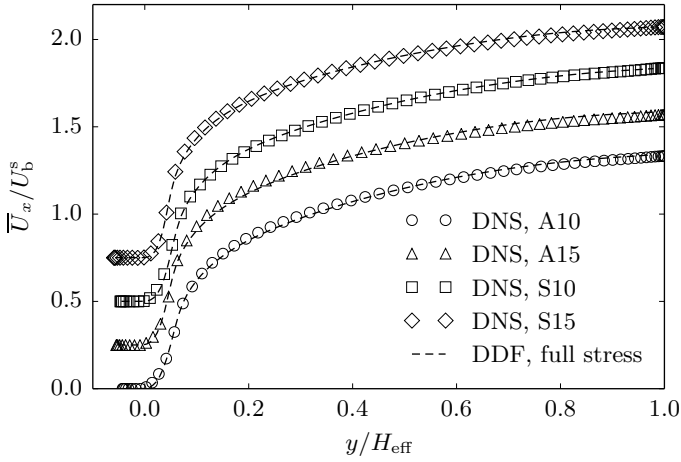

(a) regular roughness

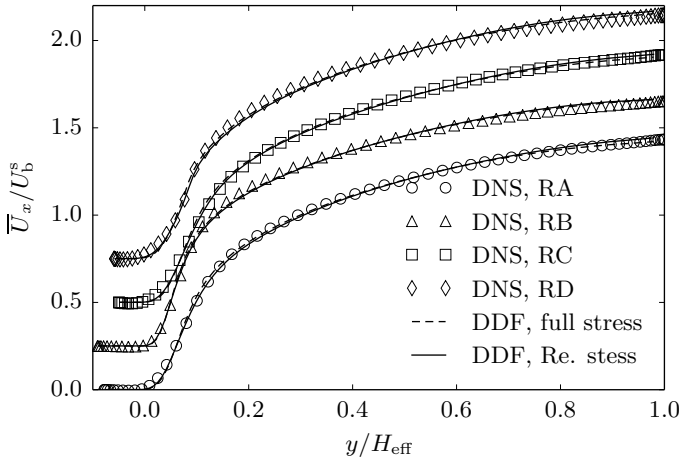

(b) random roughness

Figure 5.6: Mean streamwise velocity profiles normalized by the superficial bulk velocity U_b^s, obtained with the DDF approach for the regular (a) and random (b) roughness topographies. Profiles shifted upwards by $\Delta\overline{U}_x/U_\mathrm{b}^\mathrm{s} = 0.25$ increments for clarity purposes. DNS data taken from Forooghi *et al.* [48] and [78].

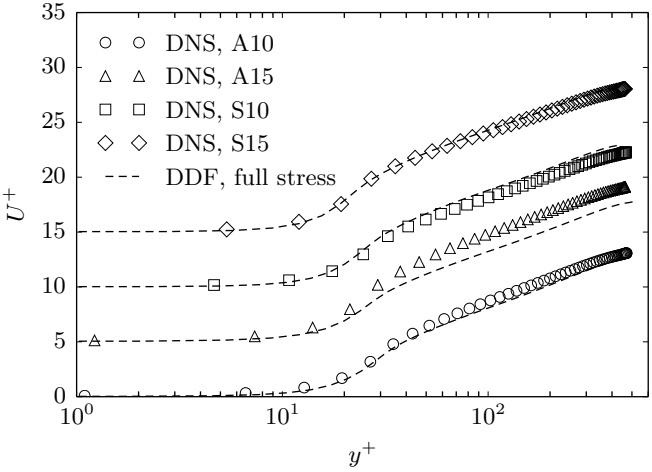

(a) regular roughness

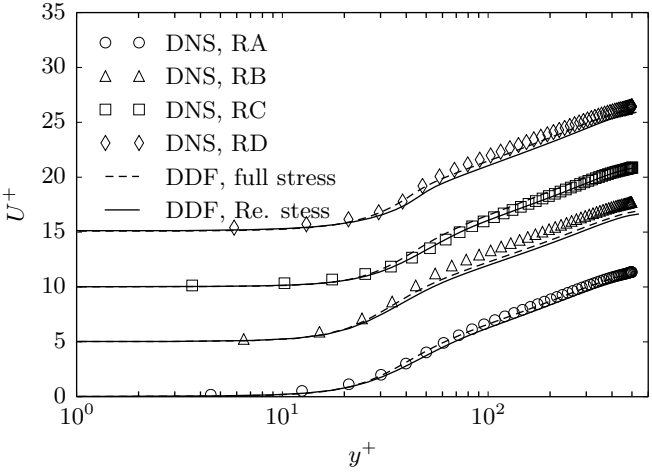

(b) random roughness

Figure 5.7: Mean streamwise velocity profiles normalized with the friction velocity u_τ, obtained with the DDF appraoch for the regular (a) and random (b) roughness topographies. Profiles shifted upwards by $\Delta U^+ = 5$ increments for clarity purposes. DNS data taken from Forooghi *et al.* [48] and [78].

Profiles of turbulent intensity components non-dimensionalized by the friction velocity u_τ are displayed in Fig. 5.8 and 5.9, for the regular and random roughness topographies, respectively. For the regular roughness in Fig. 5.8, the turbulence intensity components $u^+_{i,\mathrm{rms}}$ from the DNS data base are based on combined Reynolds and dispersive stresses. The respective profiles for the random roughness topographies in Fig. 5.9 show the turbulence intensity $u'^+_{i,\mathrm{rms}}$ based only on Reynolds stresses. Regardless of the DNS reference data, the turbulent intensity profiles

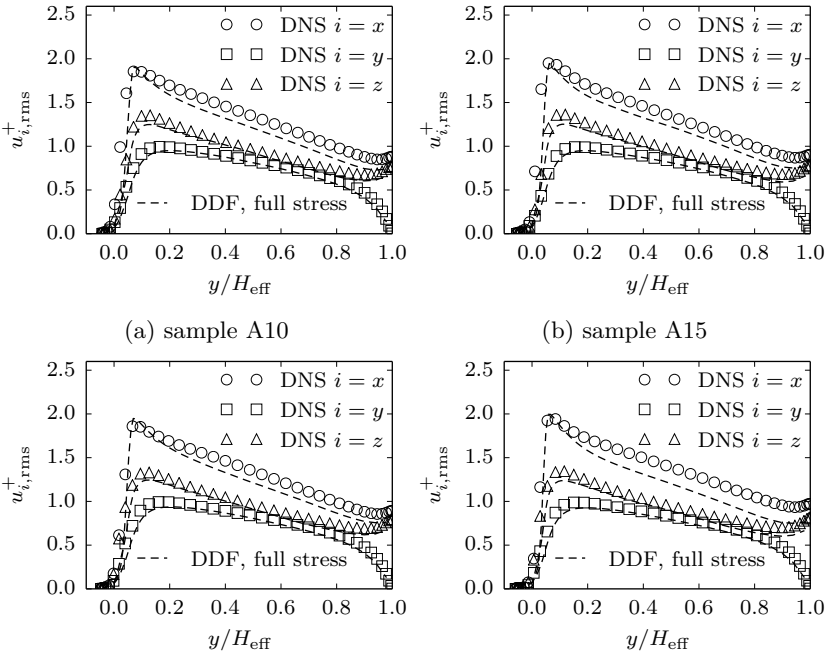

(a) sample A10

(b) sample A15

(c) sample S10

(d) sample S15

Figure 5.8: Turbulence intensity components normalized with the friction velocity, obtained with the DDF approach for the regular roughness topographies, compared to DNS data based on full stresses (e.g. $u^+_{x,\mathrm{rms}} = \sqrt{\overline{u_x u_x}}/u_\tau$). DNS data taken from [78].

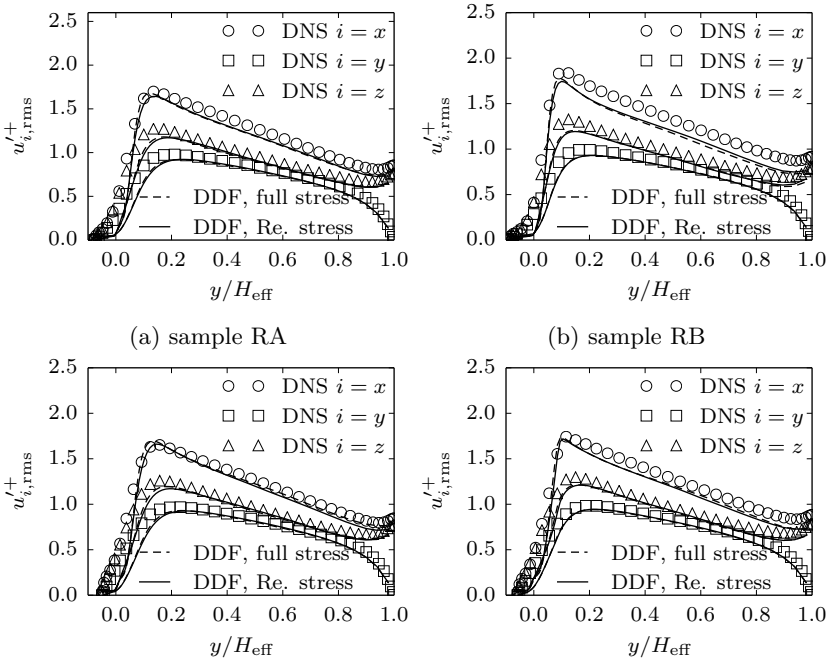

(a) sample RA

(b) sample RB

(c) sample RC

(d) sample RD

Figure 5.9: Turbulence intensity components normalized with the friction velocity, obtained with the DDF approach for the random roughness topographies, compared to DNS data based on Reynolds stresses (e.g. $u'^{+}_{x,\mathrm{rms}} = \sqrt{\overline{u'_x u'_x}}/u_\tau$). DNS data taken from Forooghi *et al.* [48].

obtained with the DDF approach are evaluated in the same way for both regular and random roughness topographies, since the DDF approach is inherently unable to capture dispersive stresses, due to the constant forcing in wall parallel layers. Consequently, for the DDF data $u^{+}_{i,\mathrm{rms}} = u'^{+}_{i,\mathrm{rms}}$. Furthermore, the presented turbulent intensities are based on resolved turbulent fluctuations, i.e. sub-scale contributions on this relatively fine grid are presently neglected. The turbulent structure

modification caused by the rough wall results in a weakening of the turbulence anisotropy for all investigated roughness topographies. This is characterized by a distinct reduction of the peak values of the streamwise intensity components to values ≤ 2 compared to a smooth wall, where generally a peak value of $u'^{+}_{i,\mathrm{rms}} \approx 2.7$ is obtained. Peak values of the normalized spanwise and wall-normal turbulent intensity components are significantly less affected by the presence of the rough wall. Qualitatively these effects are captured well with the data-driven DDF approach. However, the streamwise intensity component in the outer layer is underpredicted to varying degrees in all cases, while wall-normal and spanwise components are in closer agreement with the reference data. Below the highest crests of the roughness topographies, i.e. in the region where the forcing term is active, the resolved turbulence intensity is suppressed too strongly in all spatial directions, especially for the random topographies presented in Fig. 5.9. Considering the accurately predicted mean flow, this overly pronounced damping of turbulence implies an excessive response of the volumetric force closure (5.4) to the temporal turbulent fluctuations relative to the mean value. In any case it seems unlikely that a spatially homogeneous forcing in wall parallel layers could enable accurately resolved turbulent structures, since eddy dynamics and the associated anisotropy state of turbulence in the vicinity of walls are significantly affected by geometry related pressure redistribution effects. Finally, similar to the results for the mean velocity, the influence of the kind of shear-stress applied for the estimation of the sectional drag profiles, can be characterized as minor with respect to the prediction of turbulent intensity levels for the random roughness, as indicated in Fig. 5.9.

Conclusion

In this section, a data-driven approach was applied in order to estimate the shape of time-averaged, non-dimensionalized volumetric force profiles associated with the effect of roughness on turbulent flow over various roughness topographies from geometry-resolving DNS data. These non-dimensional force profiles, presently denoted as sectional drag coefficients $C_{\mathrm{d}}(y)$, were subsequently applied in a DDF approach in conjunction with the ER ζ-f model, in order to quantitatively investigate the performance of the roughness closure term, which is expected to account

for blockage effects as well as the viscous and form drag the roughness elements exert on the flow. It was demonstrated that application of the correspondingly determined sectional drag profiles in the present DDF approach results in an accurate representation of the mean velocity for all roughness topographies. However, relative deviations of the friction velocity from the reference DNS value exhibit some scatter with maximum deviations of up to 12%. While it might be possible to compensate for inaccuracies related to the drag-like roughness closure by modifying the resolved turbulence activity in the roughness layer through an appropriate modification of the turbulence model, in the following, it is investigated whether improved predictive capabilities can be achieved by separating the effect of blockage from the drag closure through the application of volume-averaged governing equations.

5.3 A unified modeling approach for flow over porous and rough walls

In this section, a VAF approach for turbulent flow over rough walls is investigated. Similar to the discrete element approach of Taylor *et al.* [147], which was formulated relying on two-dimensional boundary layer equations, the blockage pertinent to the roughness elements is directly accounted for through blockage factors in the presently applied three-dimensional governing equations. This represents a key difference to the previously investigated DDF approach, where blockage effects are lumped into the volumetric drag closure. As suggested by Aupoix [7], double-averaged Navier-Stokes equations, derived relying on Whitaker's [160] volume averaging technique for flow through porous media, are adopted. Thus, a unified modeling approach for scale-resolving computations of turbulent flow over porous and rough walls is enabled.

In Section 5.3.1, a newly implemented flow solver based on the additionally volume-averaged equations is briefly discussed and the turbulence models considered in this work are adapted to account for blockage effects. Thereafter, in Section 5.3.2, the implementation of the flow solver is verified and the performance of the turbulence models is assessed by computing channel flow over a porous wall. Subsequently, the focus is switched back to the roughness topographies introduced in 5.1

and the data-driven methodology previously discussed in the context of the DDF approach is adapted for the present volume-averaged framework in Section 5.3.3. Finally, in Section 5.3.4, a drag closure originating from the field of porous media modeling is reformulated and calibrated, with the purpose to enable computations of flow over rough walls relying primarily on geometrical data of the roughness topographies.

5.3.1 Flow solver and adapted turbulence models

In a first step, a solver for porous media flow based on double-averaged Navier-Stokes equations is implemented into the applied numerical code (OpenFOAM 2.4.x), in order to facilitate investigation of a VAF approach for scale-resolving computations of turbulent flow over rough walls. For pressure-velocity coupling, the implementation relies on OpenFOAM's PIMPLE algorithm, which is a combination of the SIMPLE and PISO algorithms of Patankar and Spalding [116] and Issa [65], respectively. The solver is thus denoted as *porosityPimpleFoam*. The implemented governing equations are based on Whitaker's [160] volume averaging technique and the double decomposition concept of de Lemos [36], both originated in the field of porous media modeling, as discussed in more detail in Section 2.4. The momentum equation, formulated in terms of the ensemble-averaged intrinsic velocity field $\langle \widetilde{U}_i \rangle$, is implemented according to the expanded form given by Eq. (2.77). Thereby, the two terms containing spatial derivatives of the porosity φ stem from an expansion of the viscous diffusion term and are of significant importance in areas with variable porosity, such as at the interface between porous and clear-fluid regions or rough walls. In clear-fluid regions, where $\varphi = 1$ and $\langle \widetilde{f}_{\mathrm{d},i} \rangle = 0$, the continuity and momentum equations reduce to the standard single-phase equations, thus enabling computations in hybrid domains containing clear-fluid regions, porous regions, interface regions between them as well as roughness. For the computations of the drag term $\langle \widetilde{f}_{\mathrm{d},i} \rangle$ and the MRST $\langle \widetilde{u_i'' u_j''} \rangle$, flexible base classes are implemented. This enables the straightforward implementation of additional drag closures and turbulence models adapted for the volume-averaged computational framework, which can subsequently be selected at run time. The specific drag closures employed for porous media and rough walls will be introduced in the relevant sections.

The scale-resolving turbulence models applied in the volume-averaged framework, are ad-hoc modified versions of the corresponding single-phase models. This route is taken, due to the lack of consensus regarding derivation procedures of the underlying transport equations as well as the limited validation basis for terms that have no counterpart in single-phase turbulence. A similar approach was applied by Ullrich [152] in the context of the two-fluid model (or Euler-Euler) framework for multiphase flow, where two immiscible phases are regarded as interpenetrating continua. Since in this case, a similar averaging procedure is applied in order to circumvent the necessity to resolve the geometric boundary between the two phases, the equations are structurally similar to the volume-averaged framework for porous media flow, if one phase is considered as the stationary porous medium. Hence, it is expected that this approach can be applied successfully to the volume-averaged framework as well. This is especially the case for the present scale-resolving computations, where a considerable part of the interaction between the unresolved solid phase and turbulence is handled directly through the momentum equation. Thus, this pragmatic approach is adopted here and the single-phase turbulence models are adapted by merely introducing the porosity φ in the model equations. In the following, only the modified equations for the ER ζ-f model are presented for the sake of brevity. However, the adaption is completely analogous for the VLES model, which either way shares most of the ER ζ-f's equations.

The model equation for sub-scale TKE of the adapted ER ζ-f model is given by

$$\frac{\partial(\varphi\langle k_\mathrm{u}\rangle)}{\partial t} + \frac{\partial(\varphi\langle\widetilde{U}_j\rangle\langle k_\mathrm{u}\rangle)}{\partial x_j} = \langle P_k\rangle - \varphi\langle\varepsilon_\mathrm{u}\rangle + \frac{\partial}{\partial x_j}\left[\left(\nu + \frac{\nu_\mathrm{t}}{\sigma}\right)\frac{\partial(\varphi\langle k_\mathrm{u}\rangle)}{\partial x_j}\right], \quad (5.8)$$

where the porosity φ is introduced in each term in line with the model equation of de Lemos [36]. Applying the Boussinesq eddy-viscosity assumption adapted for the volume-averaged framework, according to Eq. (2.79), yields $\langle P_k\rangle = \nu_\mathrm{t}/\varphi\,\langle\widetilde{S}_{ij}\rangle\langle\widetilde{S}_{ij}\rangle$ for the production term of sub-scale TKE, where the strain rate tensor $\langle\widetilde{S}_{ij}\rangle$ is given by Eq. (2.80). In the scale-supplying equation, φ is introduced analogously to the correspond-

ing terms in the $\langle k_\mathrm{u}\rangle$-equation, resulting in

$$\frac{\partial(\varphi\langle\omega_\mathrm{u}\rangle)}{\partial t} + \frac{\partial(\varphi\langle\widetilde{U}_j\rangle\langle\omega_\mathrm{u}\rangle)}{\partial x_j} = C_{\omega_1}\frac{\langle\omega_\mathrm{u}\rangle}{\langle k_\mathrm{u}\rangle}\langle P_k\rangle - C_{\omega_2}\varphi\langle\omega_\mathrm{u}\rangle^2 + \frac{\partial}{\partial x_j}\left[\left(\nu + \frac{\nu_\mathrm{t}}{\sigma}\right)\frac{\partial(\varphi\langle\omega_\mathrm{u}\rangle)}{\partial x_j}\right] + \varphi\, CD + \varphi\, P_\mathrm{SAS}. \quad (5.9)$$

Here, the cross diffusion term CD and the P_SAS term remain structurally unchanged compared to the single-phase formulation presented in Section 4.2, apart from their multiplication with φ. This is analogous to the treatment of the respective terms by Ullrich [152] in his SAS-based Reynolds stress model in the context of the two-fluid model framework. Finally, the adapted $\langle\zeta_\mathrm{u}\rangle$ and $\langle f_\mathrm{u}\rangle$-equations read

$$\frac{\partial(\varphi\langle\zeta_\mathrm{u}\rangle)}{\partial t} + \frac{\partial(\varphi\langle\widetilde{U}_j\rangle\langle\zeta_\mathrm{u}\rangle)}{\partial x_j} = \varphi\langle f_\mathrm{u}\rangle - \frac{\langle\zeta_\mathrm{u}\rangle}{\langle k_\mathrm{u}\rangle}\langle P_k\rangle + \frac{\partial}{\partial x_j}\left[\left(\nu + \frac{\nu_\mathrm{t}}{\sigma_\zeta}\right)\frac{\partial(\varphi\langle\zeta_\mathrm{u}\rangle)}{\partial x_j}\right] \quad (5.10)$$

and

$$L_\mathrm{u}^2\frac{\partial^2(\varphi\langle f_\mathrm{u}\rangle)}{\partial x_j\partial x_j} - \varphi\langle f_\mathrm{u}\rangle = \frac{1}{T_\mathrm{u}}\left(C_1 + C_2\frac{\langle P_k\rangle}{\langle\varepsilon_\mathrm{u}\rangle}\right)\left(\varphi\langle\zeta_\mathrm{u}\rangle - \frac{2}{3}\right), \quad (5.11)$$

respectively. Length and time scale definitions as well as model coefficients remain unchanged compared to the single-phase formulation presented in Section 4.2.

5.3.2 Flow over porous walls: verification and validation

In order to verify the implemented flow solver and validate the adapted single-phase turbulence models, channel flow with a porous insert in the lower half of the channel, corresponding to a packed bed, is computed before the modeling framework is applied to the roughness topographies described in Section 5.1. DNS results of Breugem *et al.* [21] are used as reference data for the verification and validation. The reference DNS is also based on volume-averaged equations, however, Breugem and Boersma [20] successfully validated this approach by comparison

to DNS with a geometrically-resolved porous medium. The drag term $\langle \widetilde{f}_{\mathrm{d},i} \rangle$ associated with the volume-averaged equations is modeled using the customary parametrization of a Darcy drag term with Forchheimer extension, according to Eq. (2.78). The permeability and Forchheimer tensors are estimated relying on a modified Ergun equation for packed beds [13, 21], according to

$$K_{ij} = \frac{d_\mathrm{p}^2 \, \varphi^3}{180 \, (1-\varphi)^2} \, \delta_{ij} \tag{5.12}$$

and

$$F_{ij} = \frac{\varphi}{100 \, (1-\varphi)} \frac{d_\mathrm{p}}{\nu} \sqrt{\langle \widetilde{U}_k \rangle \langle \widetilde{U}_k \rangle} \, \delta_{ij}, \tag{5.13}$$

where d_p is the mean particle diameter in the porous medium, which was set to $d_\mathrm{p}/H = 0.01$ in the reference DNS. Using these isotropic formulations of the permeability and Forchheimer tensors, Eq. (2.78) can be rewritten as

$$\langle \widetilde{f}_{\mathrm{d},i} \rangle = -\nu \frac{180 \, (1-\varphi)^2}{d_\mathrm{p}^2 \, \varphi^2} \langle \widetilde{U}_i \rangle - \frac{180 \, (1-\varphi)}{100 \, d_\mathrm{p} \, \varphi} \sqrt{\langle \widetilde{U}_j \rangle \langle \widetilde{U}_j \rangle} \, \langle \widetilde{U}_i \rangle, \tag{5.14}$$

where the first term accounts for viscous drag, while the second term models form drag.

The Reynolds number based on the half-channel height H and the bulk velocity in the clear-fluid region U_b is fixed to $\mathrm{Re}_\mathrm{b} = U_\mathrm{b} H/\nu = 5500$ in all cases. Three values for the porosity of the packed bed in the lower half of the channel are investigated, $\varphi_\mathrm{h} = 0.60, 0.80$, and 0.95. The interface between porous and clear-fluid region is associated with a variable porosity φ transitioning from the corresponding value of φ_h in the porous region to $\varphi = 1$ in the fluid region following a fifth-order polynomial (see [21]).

Computational setup

A sketch of the computational domain, whose dimensions are adopted from the reference DNS and are given by $L_x/H = 5$ and $L_z/H = 3$, is shown in Fig. 5.10. The methodology to drive the flow, as well as boundary conditions, applied numerical schemes and averaging procedures correspond to the methodology described for smooth channel flow in Section 4.3.1.

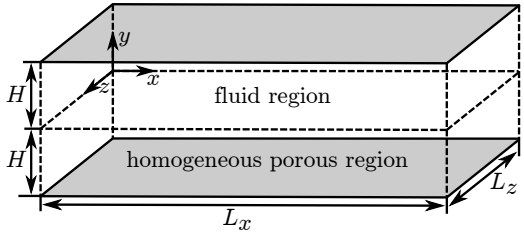

Figure 5.10: Schematic illustration of the computational domain for channel flow over a porous wall.

The employed computational grids also correspond – in terms of the non-dimensionalized grid spacings – to the smooth channel flow computations. Three grid resolutions are considered, denoted as coarse, medium and fine. The grids are refined towards the porous-fluid interface and the top wall in compliance with the applied near-wall models. Due to the significant dependence of the friction Reynolds number associated with the porous-fluid interface on the porosity φ_h, three grids are generated for each porosity. Specifically, the friction Reynolds number $\mathrm{Re}_\tau^\mathrm{p} = u_\tau^\mathrm{p} H/\nu$ based on the friction velocity u_τ^p at the porous-fluid interface assumes values of $\mathrm{Re}_\tau^\mathrm{p} = 353, 398$ and 678 for the porosities of $\varphi_\mathrm{h} = 0.60, 0.80$ and 0.95, respectively. Tab. 5.5 summarizes the corresponding grid metrics.

Table 5.5: Grid metrics for the computations of channel flow over a porous wall. Grid spacings are normalized with the viscous length scale associated with the porous-fluid interface, obtained in the DNS e.g. $\Delta x^+ = \Delta x\, u_{\tau,\mathrm{DNS}}^\mathrm{p}/\nu$.

				Total number of cells		
	Δx^+	Δy^+	Δz^+	$\varphi_\mathrm{h} = 0.60$	$\varphi_\mathrm{h} = 0.80$	$\varphi_\mathrm{h} = 0.95$
coarse	50	2...30	30	66150	102400	494768
medium	35	2...30	20	198750	290700	1444524
fine	25	2...20	12	452625	652800	3375520

Verification of the *porousPimpleFoam* solver

In order to initially verify the implemented solver independently from turbulence modeling, the channel configuration with $\varphi_\mathrm{h} = 0.80$ is computed on a highly-resolved grid without the use of a turbulence model. This computation can be regarded as a quasi-DNS or well-resolved implicit LES (ILES). The term quasi-DNS is used, since computations are performed with OpenFOAM's FVM and discretization schemes with relatively low order for DNS standards (CDS, second-order is uesd). ILES on the other hand is meant in the sense, that additional dissipation is only provided by the numerical discretization rather than by a sub-grid scale model. In terms of the resolution the mesh corresponds to the grid used in the reference DNS with $256 \times 320 \times 192$ cells in streamwise, wall-normal and spanwise directions, respectively; in total 15.7 million cells.

Fig. 5.11 shows the time average of the intrinsically-averaged streamwise velocity, normalized by the bulk velocity U_b for the case with $\varphi_\mathrm{h} = 0.80$. The ILES computation exhibits good agreement with the reference DNS, with minor deviations in the core of the fluid region. Associated turbulent intensity components, normalized by the friction velocity u_τ^t at the top wall, are presented in Fig. 5.12. Here as well, a

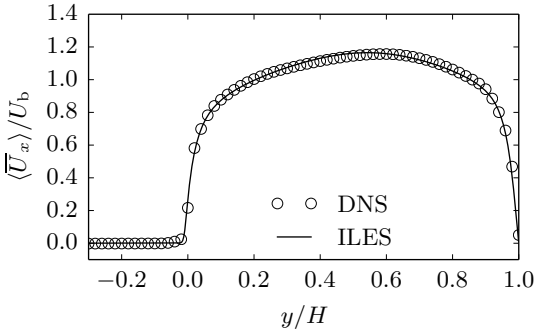

Figure 5.11: Mean streamwise velocity profile normalized by the bulk velocity U_b for the case $\varphi_\mathrm{h} = 0.80$, obtained on the DNS grid without the use of a turbulence model. DNS data taken from Breugem *et al.* [21].

high level of agreement with the reference data base is obtained, even though the spanwise and wall-normal components are slightly underpredicted in the vicinity of the porous-fluid interface at $0 \leq y/H \leq 0.3$. Overall, these deviations can most likely be attributed to the lower code accuracy in comparison to the reference computations, where a pseudo-spectral DNS code was employed. In conclusion, the newly implemented *porousPimpleFoam* solver based on volume-averaged equations is considered as successfully verified.

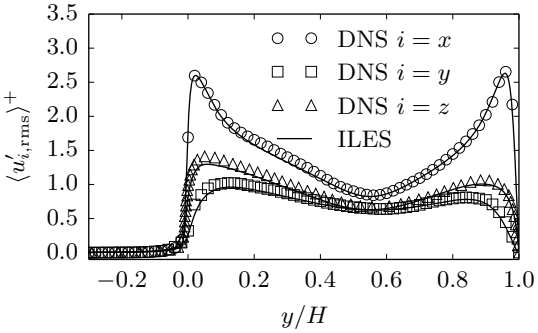

Figure 5.12: Turbulent intensity components normalized with the friction velocity at the top wall (e.g. $\langle u'_{x,\mathrm{rms}} \rangle^+ = \sqrt{\langle \overline{u'_x u'_x} \rangle} / u^{\mathrm{t}}_\tau$) for the case $\varphi_{\mathrm{h}} = 0.80$, obtained on the DNS grid without the use of a turbulence model. DNS data taken from Breugem *et al.* [21].

Validation and comparative assessment

In the following, results from the computations with the various porosities, grids and scale-resolving turbulence models (i.e. ER ζ-f, VLES and dynS) are presented in order to validate the ad-hoc modified model equations and assess the overall performance of the turbulence models. With the VLES model, no reasonable results could be achieved on the coarse grid for the cases $\varphi_{\mathrm{h}} = 0.60$ and 0.80, since turbulent fluctuations decay during run time. Thus, Fig. 5.13 shows the mean streamwise velocity profiles normalized with the bulk velocity for the three porosities,

(a)

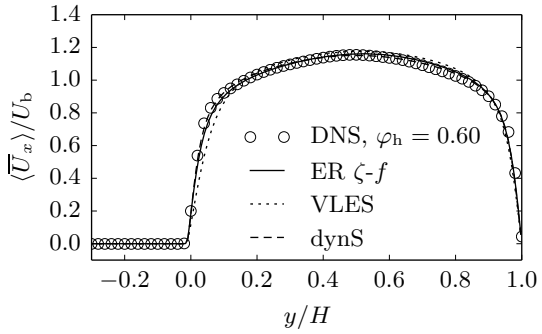

(b)

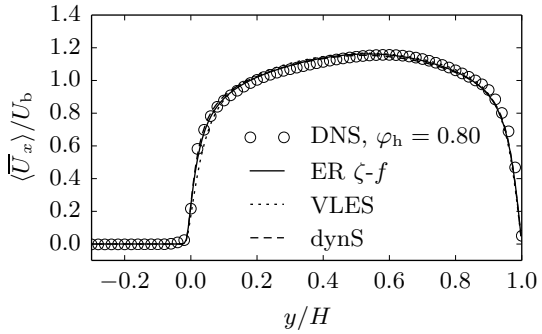

(c)

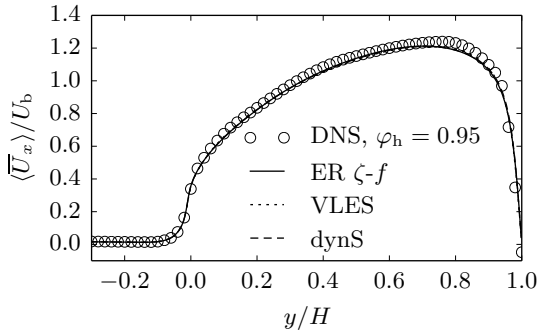

Figure 5.13: Mean streamwise velocity profiles normalized with the friction velocity U_b for $\varphi_\mathrm{h} = 0.60, 0.80$ and 0.95, obtained on the medium grid. DNS data taken from Breugem *et al.* [21].

as obtained on the medium grid. For $\varphi_\mathrm{h} = 0.60$, the velocity profile is highly symmetric with respect to $y = 0.5$ and hence closely resembles the flow over a solid wall. With higher porosity, the porous wall induces an increasingly asymmetric velocity profile with the maximum value shifted towards the top wall, which is in accordance with the previously discussed increase in $\mathrm{Re}_\tau^\mathrm{p}$. For $\varphi_\mathrm{h} = 0.95$ all models predict the velocity profile in outer scaling equally well on the medium grid. This indicates, in line with the observations made for smooth channel flow, that with increasing Reynolds number, a lower grid resolution in terms of non-dimensional grid spacing is required, to achieve good results, which can most likely be attributed to the increasing separation of scales. For the lower porosities however, especially for $\varphi_\mathrm{h} = 0.60$, the VLES model is not able to capture the slope of the velocity over the porous wall at $0 \leq y/H \leq 0.1$ as accurately as ER ζ-f and the dynamic Smagorinsky model. This also results in a slight overestimation of the velocity in the upper part of the fluid region. Similar, though less pronounced, deviations are apparent for the case with $\varphi_\mathrm{h} = 0.80$. As can be expected, the agreement with the reference DNS further improves on the fine grid, while the observations made for the medium grid qualitatively still apply. Thus, the mean velocity profiles obtained on the fine grid are not presented here for the sake of brevity.

The intrinsically-averaged TKE profiles obtained on the medium grid are presented in Fig. 5.14. All models tend to overpredict k^+, with the ER ζ-f model exhibiting the overall best results. For the two lower porosities, $\varphi_\mathrm{h} = 0.60$ and 0.80, the TKE levels in the homogeneous porous region as well as the core of the clear-fluid region are reasonably predicted with both, the ER ζ-f and the dynamic Smagorinsky model. The peak values associated with the porous-fluid interface and the top wall are captured slightly more accurate with the ER ζ-f model for both of these porosities. With the VLES model, a somewhat more pronounced overprediction of TKE is obtained, especially in the vicinity of the porous-fluid interface. Additionally, the VLES results exhibit a significant overestimation of $\langle k \rangle^+$ in the porous medium directly below the porous-fluid interface, especially for the two lower porosities but also less pronounced for $\varphi_\mathrm{h} = 0.95$. The overestimation of $\langle k \rangle^+$ with VLES stems from the unresolved (or modeled) part of TKE $\langle k_\mathrm{u} \rangle^+$, since turbulent fluctuations in the resolved velocity field

(a)

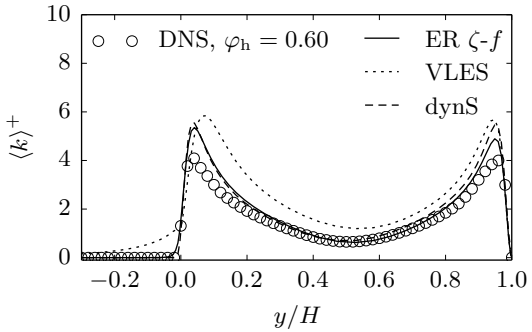

(b)

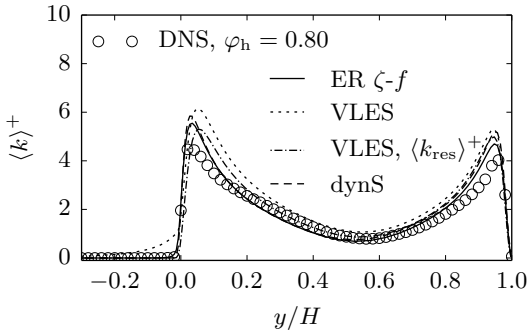

(c)

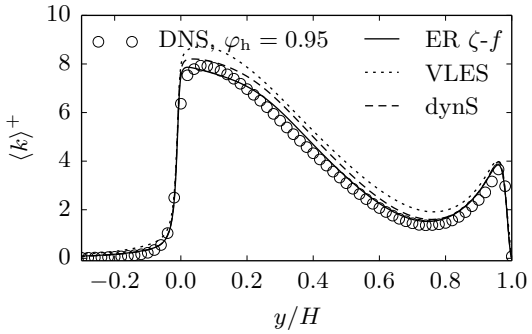

Figure 5.14: TKE profiles normalized by the friction velocity u_τ^t at the top wall for $\varphi_h = 0.60, 0.80$ and 0.95, obtained on the medium grid. DNS data taken from Breugem *et al.* [21].

(a)

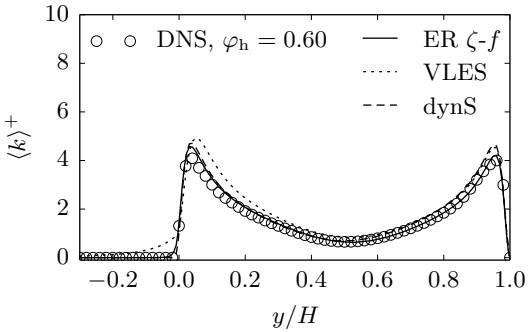

(b)

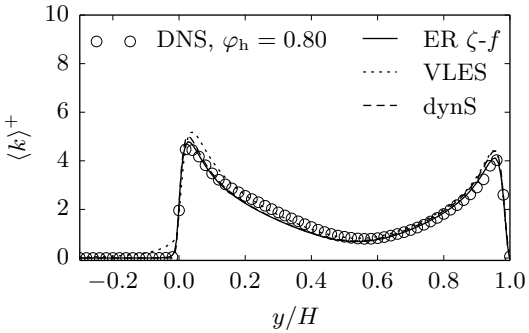

(c)

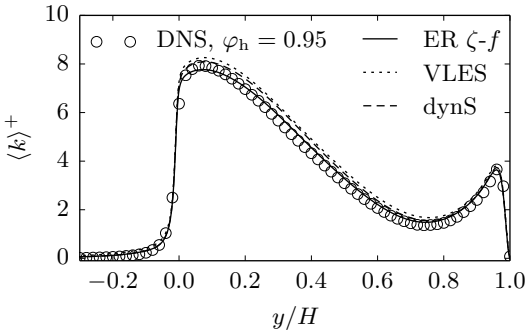

Figure 5.15: TKE profiles normalized by the friction velocity u_τ^t at the top wall for $\varphi_h = 0.60, 0.80$ and 0.95, obtained on the fine grid. DNS data taken from Breugem *et al.* [21].

$\langle \widetilde{U}_i \rangle$ are effectively suppressed due to the damping effect of the Darcy-Forchheimer drag model. This is demonstrated based on the example of the case with $\varphi_\mathrm{h} = 0.80$ in Fig. 5.14 (b), where in addition to total TKE ($\langle k \rangle^+ = \langle k_\mathrm{res} \rangle^+ + \langle k_\mathrm{u} \rangle^+$) the resolved part $\langle k \rangle^+_\mathrm{res}$ obtained with VLES is displayed. Consequently, the VLES model requires additional sink/source terms in the transport equations for $\langle k_\mathrm{us} \rangle$ and $\langle \varepsilon_\mathrm{us} \rangle$ in order to appropriately modify the modeled intermediary $(\cdot)_\mathrm{us}$-quantities. Recalling the relation $\langle k_\mathrm{u} \rangle = \sqrt{F_\mathrm{r}} \langle k_\mathrm{us} \rangle$ suggests a further alternative: the formulation of the resolution function F_r, Eq. (2.46), could be adapted to account for the porous medium e.g. by introducing the porosity φ. For ER ζ-f on the other hand, no additional modifications of the model equations seem indicated, since an effective sink for modeled TKE is provided by the SAS-based production term in the scale-supplying equation. This sensitization of the model implies a closer and more direct coupling between the modeled quantities and the resolved flow field compared to the VLES model. This argument is in line with the conclusion drawn in Section 4.3.1 with respect to the advantages of SAS-based sensitization approach.

In Fig. 5.15 the intrinsically-averaged TKE profiles obtained on the fine grid are presented. As expected, the higher spatial resolution further improves the agreement with the reference data base, especially with respect to the peak values at the porous-fluid interface as well as the top wall. Overall, ER ζ-f still provides slightly more accurate results compared to the other models. The overprediction of TKE in the porous medium close to the porous-fluid interface pertinent to the VLES model is still clearly observable, albeit slightly less pronounced.

Finally, friction losses associated with the porous medium are analyzed. Combined with the contributions associated with the top wall, friction at the porous medium determines the pressure gradient necessary to drive the flow. While the wall shear stress at the top wall can easily be determined based on the wall-normal velocity gradient, friction associated with the porous-fluid interface has to be determined by also taking the turbulent shear stress into account. Specifically, contributions from both, the resolved turbulent motion as well as the modeled turbulence have to be considered. For the presently investigated channel

flow, this yields

$$\frac{\tau_\mathrm{p}}{\rho} = \left[\nu\frac{\partial\langle\overline{U}_x\rangle}{\partial y} - \langle\overline{u'v'}\rangle_\mathrm{res} + \nu_\mathrm{t}\frac{\langle\overline{U}_x\rangle}{\partial y}\right]_{y=0}, \tag{5.15}$$

where the first term is associated with the viscous stress, the second term represents the contribution to the turbulent shear stress from the resolved turbulent motion, and the third term the respective modeled part, all evaluated at the position of the porous wall $y = 0$. The quality of the results is again quantified in terms of the relative deviation of the corresponding friction velocity to the value obtained in the reference DNS, $\Delta u_\tau^\mathrm{p} = (u_\tau^\mathrm{p} - u_{\tau,\mathrm{DNS}}^\mathrm{p})/u_{\tau,\mathrm{DNS}}^\mathrm{p}$, where $u_\tau^\mathrm{p} = \sqrt{\tau_\mathrm{p}/\rho}$. This is of course equivalent to the relative deviation in the obtained Reynolds number based on the friction velocity, since $\mathrm{Re}_\tau^\mathrm{p} \sim u_\tau^\mathrm{p}$. Tab. 5.6 summarizes the relative deviations for all simulations performed for this study, with the exception of the two previously addressed VLES computations. As expected, the accuracy of the predictions improves with spatial resolution, with the exception of the ER ζ-f result on the fine grid for $\varphi_\mathrm{h} = 0.60$. However, with a deviation of 2.5% the obtained wall friction velocity is still in closer agreement to the reference DNS compared to the other models. Thus, the ER ζ-f model provides the overall most accurate results, while simultaneously exhibiting the low-

Table 5.6: Relative deviation of the wall friction velocity at the porous wall ($\Delta u_\tau^\mathrm{p} = (u_\tau^\mathrm{p} - u_{\tau,\mathrm{DNS}}^\mathrm{p})/u_{\tau,\mathrm{DNS}}^\mathrm{p}$) for the various porosities and computational grids.

φ_h	grid	ER ζ-f	VLES	dynS
0.60	coarse	−3.8%	–	−14.9%
	medium	−0.2%	−10.2%	−8.3%
	fine	2.5%	−5.0%	−6.0%
0.80	coarse	−13.6%	–	−21.6%
	medium	−8.9%	−15.3%	−14.0%
	fine	−5.5%	−9.6%	−9.5%
0.95	coarse	3.2%	3.7%	3.5%
	medium	3.2%	2.0%	3.7%
	fine	0.6%	0.9%	0.7%

est grid sensitivity. Consequently, coarser meshes can be applied, while maintaining a reasonable accuracy. The VLES results indicate a slight disadvantage of this hybrid RANS/LES model in comparison to the dynamic Smagorinsky model, which can be attributed to the necessity of additional source/sink terms in the transport equations accounting for the effect of the porous medium on the modeled turbulent quantities.

Conclusion

In summary, *porousPimpleFoam*, a flow solver based on volume-averaged equations was implemented in OpenFOAM and verified by comparing results obtained in a highly-resolved ILES computation of flow over a porous wall to reference DNS data from literature. Subsequent to the successful verification, the performance of three scale-resolving turbulence models, which have been adapted for the volume-averaged computational framework by introducing porosity into the model equations, was investigated. Computations with the three turbulence closures, the ER ζ-f, VLES and dynamic Smagorinsky models, were performed for the case of channel flow over packed beds of various porosity, on three grid refinement levels. The results were analyzed in terms of mean velocity and TKE profiles, as well as the relative deviation of the obtained friction velocity at the porous-fluid interface from the reference DNS. It was thereby demonstrated that the adapted ER ζ-f model provides the overall best results in terms of accuracy, while simultaneously exhibiting the least amount of grid sensitivity. Comparatively, velocity and TKE profiles are also reasonably well predicted with the dynamic Smagorinsky model. However, deviations in terms of the friction velocity are more pronounced compared to ER ζ-f, especially for the two lower porosities. The results obtained with the adapted VLES model indicate, that additional source/sink terms accounting for the effect of porosity on the modeled turbulent quantities could improve its predictive accuracy. The ER ζ-f model on the other hand manages to produce fairly accurate results without additional modifications to the underlying RANS model. This is attributed to the higher sensitivity of the sub-scale model equations to the resolved flow field, facilitated by the SAS-based production term in the scale-supplying equation, which acts as a sufficient sink for modeled TKE in the vicinity of the porous-fluid interface.

5.3.3 Data-driven volume-averaged forcing approach

After the implementation of the flow solver for the porous media framework has been successfully verified and it was demonstrated that the correspondingly adapted ER ζ-f model performs similar to its single-phase counterpart, the data-driven approach to roughness modeling presented in Section 5.2 is now adapted for the VAF approach. Thus, the drag term in the governing momentum equation (2.77) is again modeled analogously to a form drag term as

$$\rho \langle \widetilde{f}_{\mathrm{d},i} \rangle = -\frac{1}{2} \rho \langle \widetilde{U}_j \rangle \langle \widetilde{U}_j \rangle \frac{C_\mathrm{d}(y)}{k_\mathrm{t}} \frac{\langle \widetilde{U}_i \rangle}{(\langle \widetilde{U}_k \rangle \langle \widetilde{U}_k \rangle)^{1/2}}. \tag{5.16}$$

In contrast to the DDF approach, the resulting volumetric drag force is additionally projected on wall-parallel layers, or in other words, force components normal to the smooth base wall are suppressed. For the present configurations, where the wall-normal direction is always aligned with the y-coordinate, this is achieved by simply assuming $\langle \widetilde{f}_{\mathrm{d},y} \rangle = 0$. However, this projection can be straightforwardly generalized for curved surfaces or surfaces not aligned with the main coordinate system based on local normal vectors, which are readily available in CFD codes. Ultimately, the suppression is applied here, since it generally proved to have a positive impact on the accuracy of the predicted mean velocity profiles as well as wall friction in the data-driven VAF approach. It should be noted that this modification was also investigated in the context of the data-driven DDF approach, where it did not prove to be beneficial. A possible explanation for this difference is provided by the previously discussed argument, that in the DDF approach blockage effects are lumped into the drag closure, while they are separately accounted for in the present porous-media-based framework.

Analogous to the procedure described for the data-driven DDF approach, Reynolds-averaged equations are applied in order to estimate the required mean force profile in streamwise direction from the DNS data base. For the present data-driven VAF approach the double-averaged momentum equation is used as a basis, where in a first step the ensemble averaging is straightforwardly replaced by Reynolds averaging. Simplifying this equations for the open-channel configuration,

while again neglecting dispersive stresses, yields

$$\langle \overline{f}_{\mathrm{d},x} \rangle \approx \frac{1}{\rho} \left\langle \frac{\partial \overline{P}}{\partial x} \right\rangle^{xz} + \frac{1}{\varphi} \frac{\partial}{\partial y} \left(\varphi \langle \overline{u'v'} \rangle^{xz} \right) - \frac{\nu}{\varphi} \left[\varphi \frac{\partial^2 \langle \overline{U}_x \rangle^{xz}}{\partial y \, \partial y} + \langle \overline{U}_x \rangle^{xz} \frac{\partial^2 \varphi}{\partial y \, \partial y} + \frac{\partial \varphi}{\partial y} \frac{\partial \langle \overline{U}_x \rangle^{xz}}{\partial y} \right]. \quad (5.17)$$

In line with the assumption of homogeneous forcing in wall-parallel layers, the porosity in each layer is given by the ratio of the area available to the fluid $S_{\mathrm{f}}(\eta)$ to the overall area S, $\varphi(\eta) = S_{\mathrm{f}}(\eta)/S$. All other quantities necessary to estimate $\langle \overline{f}_{\mathrm{d},x} \rangle$ are supplied from the DNS data base, whereby use of expression (2.67) is made to obtain the intrinsically-averaged velocity and Reynolds shear-stress profiles. Finally, the corresponding sectional drag profiles are estimated as

$$C_{\mathrm{d}}(y) \approx -\frac{\rho \langle \overline{f}_x \rangle \, k_{\mathrm{t}}}{\frac{1}{2}\rho \left(\langle \overline{U}_x \rangle^{xz} \right)^2}. \quad (5.18)$$

Figs. 5.16 (a) and (b) display the correspondingly obtained C_{d} profiles

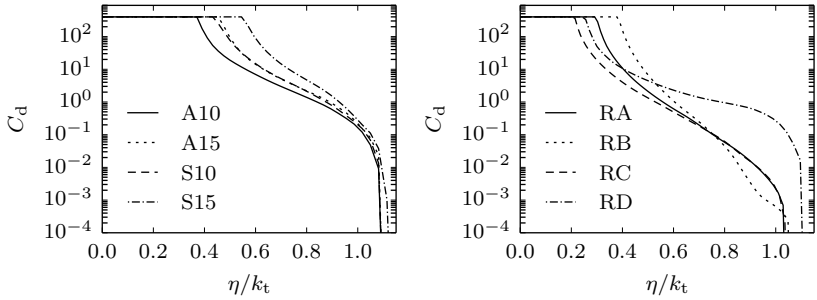

(a) regular roughness (b) random roughness

Figure 5.16: Bounded sectional drag coefficients for the VAF approach. Regular roughness (a) based on combined Reynolds and dispersive stress; random roughness (b) based on Reynolds stress only.

for the regular and random roughness topographies. The values of C_{d}

are again bound to a maximum value of $C_\mathrm{d} = 400$, based on the same arguments previously discussed in Section 5.2. Comparing the present sectional drag coefficients with those obtained in the DDF approach (see Fig. 5.5), reveals that the shape of the profiles is qualitatively very similar with both approaches. In the following, it will be presented how mean velocity and TKE profiles as well as wall friction velocities are affected by the application of volume-averaged governing equations and the correspondingly obtained sectional drag profiles.

Computational setup

In terms of computational domain, applied numerical grid, boundary conditions and averaging times, the computational setup remains unchanged compared to what is reported for the DDF approach in Section 5.2. The key difference is the application of the computational framework for porous media flow, as implemented in the *porousPimpleFoam* solver, as well as the appropriately adapted ER ζ-f model. As a consequence of the volume-averaged momentum equation formulated in terms of the intrinsic velocity $\langle\widetilde{U}_i\rangle$, the flow is driven by a pressure gradient adapted in each time step to maintain a constant intrinsic bulk velocity defined as

$$U_\mathrm{b} = \frac{1}{H}\int_0^H \frac{\langle\overline{U}_x\rangle^{\mathrm{s},xz}}{\varphi}\,\mathrm{d}\eta, \tag{5.19}$$

instead of the superficial bulk velocity U_b^s. Furthermore, the integral momentum balance used for the determination of the wall friction velocity u_τ is reformulated in terms of the intrinsic pressure gradient, resulting in

$$u_\tau = \sqrt{-\frac{H_\mathrm{eff}}{\rho}\overline{\frac{\partial\langle\widetilde{P}\rangle}{\partial x}}}. \tag{5.20}$$

Results

Fig. 5.17 displays the mean velocity profiles obtained with the data-driven VAF approach for the regular and random roughness samples in comparison to the DNS data base of Forooghi *et al.* [48]. For the sake of simplicity and to facilitate comparisons with the data presented for the DDF approach in Section 5.2, superficially-averaged velocity profiles are

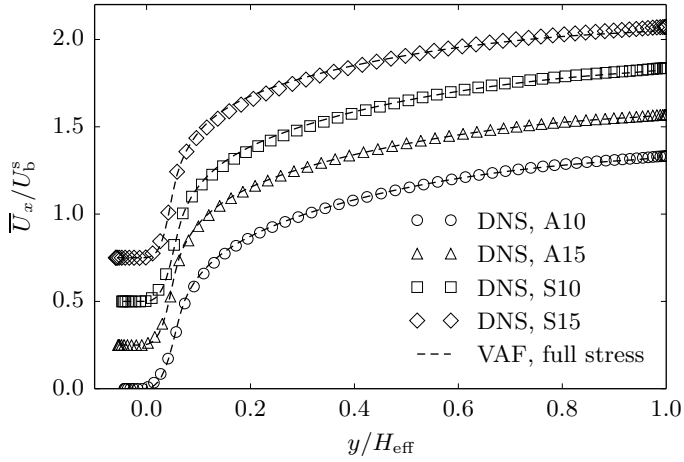

(a) regular roughness

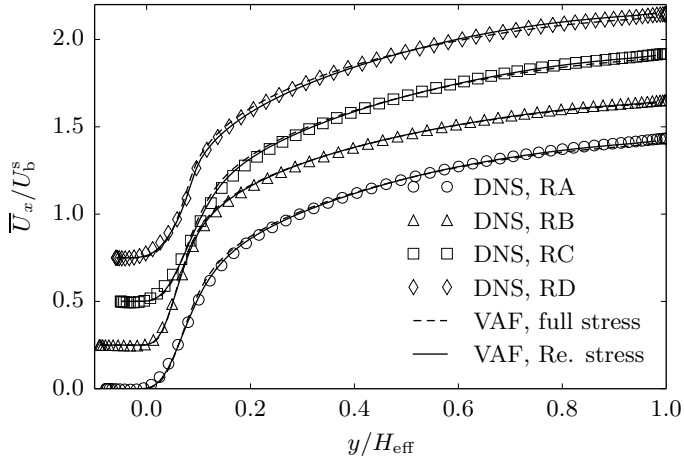

(b) random roughness

Figure 5.17: Mean streamwise velocity profiles normalized by the superficial bulk velocity U_b^s, obtained with the VAF approach for the regular (a) and random (b) roughness topographies. Profiles shifted upwards by $\Delta\overline{U}_x/U_\mathrm{b}^\mathrm{s} = 0.25$ increments for clarity purposes. DNS data taken from Forooghi *et al.* [48] and [78].

presented, i.e. $\overline{U}_x \mathrel{\widehat{=}} \langle \overline{U}_x \rangle^{\mathrm{s},xz}$. The profiles are evaluated by first averaging the intrinsic velocity $\langle \widetilde{U}_x \rangle$ in time. Subsequent spatial-averaging in wall parallel layers is performed and expression (2.67) is applied to obtain the corresponding superficial average. The resulting mean velocity profiles normalized with the superficial bulk velocity $U_{\mathrm{b}}^{\mathrm{s}}$ for the regular roughness topographies are displayed in Fig. 5.17 (a). Analogously to the DDF approach, the sectional drag profiles for the regular surfaces are based on full stresses, i.e. combined Reynolds and dispersive stresses. Overall, the mean velocity profiles are in good agreement with the reference DNS data base and comparable to the results obtained with the DDF approach (see Fig. 5.6). Similar observations can be made regarding the results for the random roughness topographies presented in Fig. 5.17(b). With respect to the impact of the application of full stresses and Reynolds stresses in the data-driven VAF approach, the differences in the mean velocity profiles are again minor. However, in contrast to the DDF approach, the present Reynolds-stress-based results are consistently slightly more accurate compared to those where additionally dispersive stresses have been considered in the methodology to estimate the sectional drag coefficient.

Mean velocity profiles in inner scaling are presented in Fig. 5.18. With respect to the results for the regular roughness topographies presented in Fig. 5.18 (a), it is interesting to note that with the VAF approach good agreement with the reference data is achieved for the aligned configurations, while for the staggered arrangements U^+ is somewhat overpredicted in the logarithmic region. With the DDF approach (see Fig. 5.7), deviations of similar magnitude are obtained; however, no clear trends can be identified, such as the attribution of these deviations to a certain class of roughness topographies. The results for the random roughness displayed in Fig. 5.18 (b), exhibit a high level of agreement with the reference DNS data base. In addition, the previously discussed minor – but consistent – advantage associated with the Reynolds-stress-based sectional drag profiles in the VAF approach is more noticeable here compared to the results presented in outer scaling. Furthermore, in comparison to the DDF approach, a higher level of agreement with the reference data base is obtained for the random roughness samples.

As indicated by the high level of agreement in Fig. 5.17, the devia-

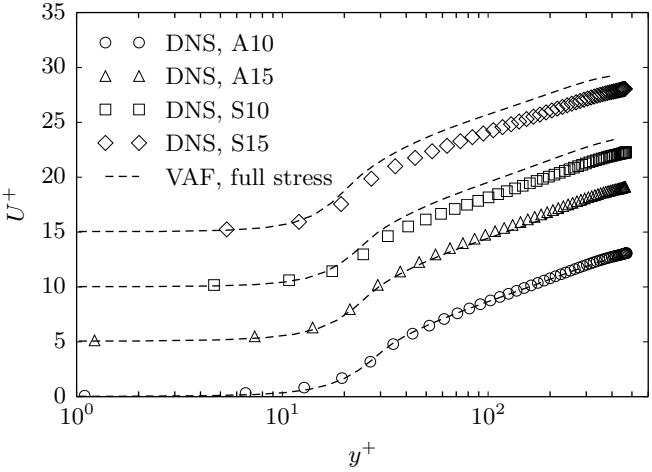

(a) regular roughness

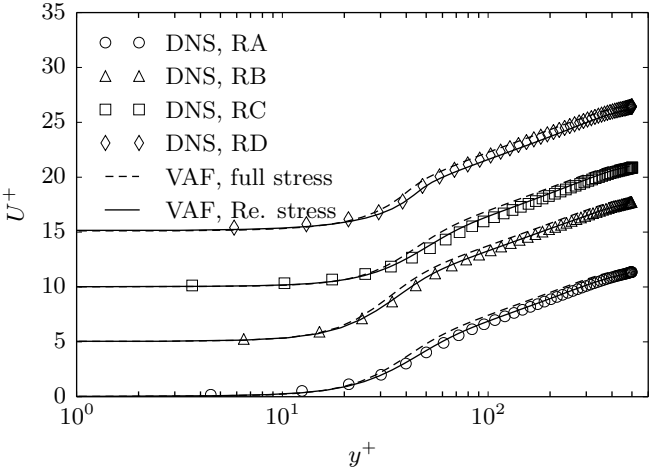

(b) random roughness

Figure 5.18: Mean streamwise velocity profiles normalized with the friction velocity u_τ, obtained with the VAF approach for the regular (a) and random (b) roughness topographies. Profiles shifted upwards by $\Delta U^+ = 5$ increments for clarity purposes. DNS data taken from Forooghi *et al.* [48] and [78].

tions of the velocity profiles in inner scaling from the reference data can be attributed to inaccuracies in the prediction of the wall friction velocity u_τ. Thus, Tab. 5.7 quantifies the relative deviations of u_τ from the reference DNS values for all VAF computations. With the exception of the staggered configurations, very reasonable results with relative deviations of less then 3.6% are obtained, whereby the Reynolds-stress-based cases are considered for the random roughness topographies. Overall, the results are more consistent compared to the DDF approach, especially for the more realistic random topographies, where deviations of less than 2.2% are obtained which is comparable to corresponding smooth channel flow computations with the ER ζ-f model. The larger discrepancies associated with the regular, staggered configurations are somewhat surprising. In principle, one would expect that flow over a staggered arrangement is more similar to flow over random roughness than flow over an aligned arrangement is. The main argument for this point is that in the two former cases the flow moving between two roughness elements will inevitably impinge on a subsequent roughness element blocking the way, while in an aligned arrangement straight, groove-like routes throughout the entire roughness topography are aligned with the main flow direction (see e.g. Orlandi

Table 5.7: Relative deviation of the wall friction velocity ($\Delta u_\tau = (u_\tau - u_{\tau,\mathrm{DNS}})/u_{\tau,\mathrm{DNS}}$) for the various roughness topographies, based on data-driven VAF considering combined Reynolds and dispersive stresses (full stress) or Reynolds stresses only (Re. stress).

	full stress	Re. stress
A10	0.8%	–
A15	3.6%	–
S10	−9.9%	–
S15	−10.2%	–
RA	−4.8%	−0.6%
RB	−3.6%	0.0%
RC	−5.6%	−1.8%
RD	−2.4%	2.2%

and Leonardi [114]). Nevertheless, reasonable results are obtained for the aligned and random arrangements, including sample RD, which is made up of equally high roughness elements. Given the fact that the sectional drag profiles are evaluated in a data-driven fashion based on the DNS data base and that this approach works well for the remaining roughness topographies, the discrepancies associated with the staggered arrangements suggest that the underlying assumption of the constant C_d in wall-parallel layers might be prohibitive for these arrangements. One reason for this could be that spatial variations in the time-averaged flow field, i.e. the cause for dispersive stresses, might be more influential for a staggered arrangement due to the associated spatial periodicity compared to randomly arranged topographies. Since the cause for the comparably high deviations obtained for the two staggered configurations can not be conclusively addressed in this work due to a lack of spatially-resolved data, this observation should be further investigated in future DNS studies.

In order to evaluate the turbulence activity in the data-driven VAF approach, Fig. 5.19 displays the turbulence intensity components normalized with the friction velocity u_τ for the regular roughness topographies. As in the DDF approach, the $u^+_{i,\mathrm{rms}}$ values pertinent to the reference DNS are based on combined Reynolds and dispersive stresses. Compared to the DDF approach (see Fig. 5.8) a better agreement with the reference DNS data base can be attested in the outer layer, especially with respect to the streamwise turbulence activity, which is more severely underpredicted in the DDF approach. Wall-normal and spanwise components are comparatively less affected and remain in similarly good agreement to the reference DNS data. Similar observations can be made with respect to the turbulent intensity components based on Reynolds stresses, obtained for the random topographies, as presented in Fig. 5.20. With the VAF approach, especially the streamwise component is more accurately predicted compared to the DDF approach (see Fig. 5.9). Resolved turbulence activity below the roughness crests is again underpredicted to an extend compared to the regular topographies. With respect to this suppressed turbulence activity close to the base wall, the same arguments presented in Section 5.2 apply for the VAF approach as well. Consequently, if more accurately predicted turbulence levels are required below the roughness crests, a modification of

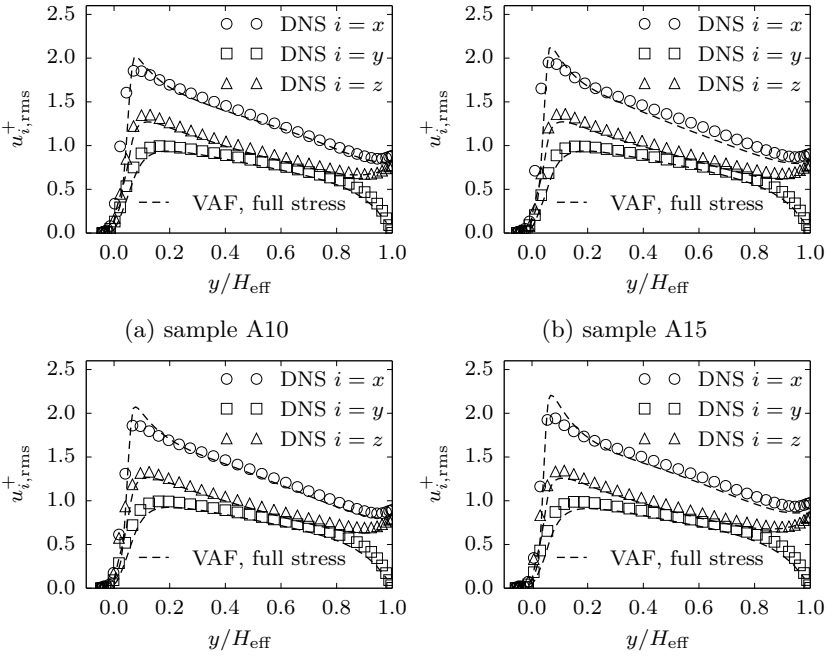

(a) sample A10

(b) sample A15

(c) sample S10

(d) sample S15

Figure 5.19: Turbulence intensity components normalized with the friction velocity, obtained with the VAF approach for the regular roughness topographies, compared to DNS data based on full stresses (e.g. $u^+_{x,\mathrm{rms}} = \sqrt{\overline{u_x u_x}}/u_\tau$). DNS data taken from [78].

the sub-scale turbulence model would be indicated. However, mean flow and friction factors are well predicted, at least for random topographies, even without accurately captured turbulence levels below the roughness crest.

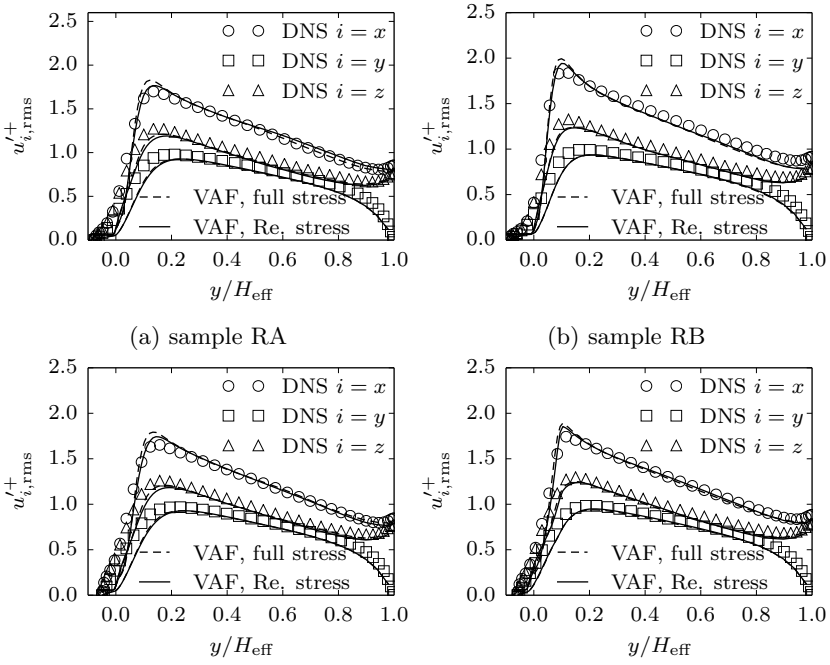

(a) sample RA (b) sample RB

(c) sample RC (d) sample RD

Figure 5.20: Turbulence intensity components normalized with the friction velocity, obtained with the VAF approach for the random roughness topographies, compared to DNS data based on Reynolds stresses (e.g. $u'^{+}_{x,\mathrm{rms}} = \sqrt{\overline{u'_x u'_x}}/u_\tau$). DNS data taken from Forooghi *et al.* [48]

Conclusion

In summary, the data-driven methodology proposed for the DDF approach was adapted for a VAF approach, where blockage effects are now separately accounted for through the porosity φ in the additionally volume-averaged governing equations. Compared to the DDF approach, more accurate results are obtained for the friction at the rough wall, especially with respect to more realistic random roughness, as well as

turbulence intensity components above the roughness crest. Overall, the results obtained with the VAF approach exhibit less scatter in the predicted wall friction with respect to the various roughness topographies and are generally more consistent with respect to the accuracy of the results, including the turbulence intensity components. Thus, it can be concluded, that it is indeed beneficial to separate the effect of blockage from the drag closure by applying governing equations originally proposed for porous media modeling. Furthermore, the results with the DDF approach for the staggered arrangements indicate that the underlying assumptions of the data-driven methodology as well as the homogeneous volumetric forcing, are less valid for regular, periodic roughness arrangements compared to more realistic random roughness.

5.3.4 Modeling roughness as equivalent porosity

Finally, in this last section devoted to the unified modeling approach for flow over porous and rough walls, the drag closure applied in Section 5.3.2 for flow over porous walls, is reformulated and calibrated for the application with rough walls[1]. The main goal in this regard is to enable scale-resolving computations of turbulent flow over rough walls with similar levels of accuracy as provided by the data-driven VAF approach. However, instead of relying on sectional drag profiles evaluated from a geometry-resolving DNS or experimental investigations for each roughness topography, which is at the least restrictive for many practical application, the proposed equivalent porosity model (EPM) aims to provide a similar level of accuracy relying predominantly on geometrical details of the considered rough surface. Based on the previous findings, the EPM is presently only applied in the framework of a VAF approach, i.e. applying additionally volume-averaged governing equations.

In a first step, the modified Ergun equation for packed beds, Eq. (5.14), is rewritten as

$$\langle \widetilde{f}_{\mathrm{d},i} \rangle = -C_{\mathrm{V}}\,\nu \frac{(1-\varphi)^2}{d_{\mathrm{mh}}^2\,\varphi^2} \langle \widetilde{U}_i \rangle - C_{\mathrm{F}}\,\frac{(1-\varphi)}{d_{\mathrm{mh}}\,\varphi} \sqrt{\langle \widetilde{U}_j \rangle \langle \widetilde{U}_j \rangle}\, \langle \widetilde{U}_i \rangle, \qquad (5.21)$$

by introducing the model coefficients C_{V} and C_{F} for the viscous and form drag terms, respectively, as well as replacing the constant particle

[1] A similar approach was independently proposed in the context of DNS in the Lattice Boltzmann framework by Kuwata and Kawaguchi [87].

diameter by the mean hydraulic diameter in wall-parallel layers $d_{\mathrm{mh}}(\eta)$. In contrast to the data-driven approaches, here, the drag closure incorporates a distinct term for viscous drag proportional to the velocity in addition to a quadratic form drag term. This in principle enables application of the model in situations where viscous drag is dominant, e.g. if the effective slope of the roughness is small (sometimes referred to as waviness regime) or at lower Reynolds numbers. Analogously to the data-driven VAF approach, the resulting force according to Eq. (5.21) is subsequently projected on wall-parallel layers by setting $\langle \widetilde{f}_{\mathrm{d},y} \rangle = 0$. In the following, the methodology applied to determine φ, which was already employed for the data-driven VAF approach, as well as the mean hydraulic diameter d_{mh} is summarized.

Processing the roughness topography

Starting point for the determination of the relevant geometrical properties of the rough surface, is the surface elevation map $s(x, z)$. In this work, the surface elevation maps for the eight synthetic roughness topographies described in Section 5.1 were readily available, since they have been prescribed in the geometry-resolving reference DNS of Forooghi *et al.* [48]. Nevertheless, a representative sample of the surface elevation map for a real rough surface can be conveniently obtained with a surface scan (e.g. by applying confocal microscopy). In line with the assumption of homogeneous roughness and a correspondingly homogeneous forcing in layers parallel to the smooth base wall, the porosity φ and the mean hydraulic diameter d_{mh} are evaluated in wall parallel slices. The respective pre-processing is performed relying on image processing algorithms in MathWorks' MATLAB. Fig. 5.21 shows a processed slice for the roughness topography RA at $\eta = \eta_{\mathrm{md}}$. Here, the grey area represents slices through the roughness elements, i.e. solid material, while the white area is available to the fluid. The black line indicates the appropriately tracked wetted perimeter. The mean hydraulic diameter is obtained based on the integrated length of the wetted perimeter P_{w}, as

$$d_{\mathrm{mh}}(\eta) = \frac{4\,(S - S_{\mathrm{f}}(\eta))}{P_{\mathrm{w}}(\eta)}, \tag{5.22}$$

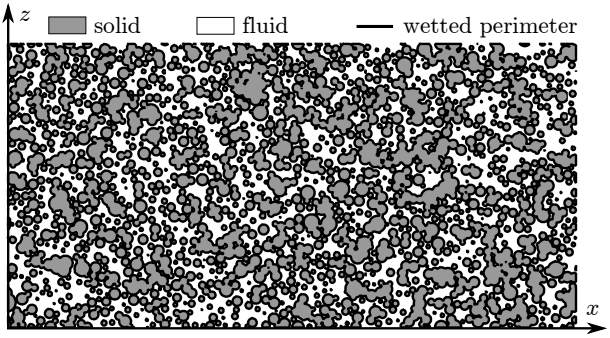

Figure 5.21: Processed slice through the roughness topography RA at $\eta = \eta_{\mathrm{md}}$.

where S is the total area of the slice and $S_{\mathrm{f}}(\eta)$ represents the area available to the fluid at position η. The latter quantity is easily obtained by integration over the white area in Fig. 5.21 and is also used for the determination of the porosity according to the simple expression

$$\varphi(\eta) = \frac{S_{\mathrm{f}}(\eta)}{S}. \tag{5.23}$$

Figs. 5.22(a) and (b) display the corresponding profiles of φ as well as d_{mh} normalized by the peak-to-valley height, again based on the example of the roughness topography RA.

Determination of model coefficients

In the next step, the model coefficients C_{V} and C_{F} are determined. This can be done without performing a single CFD computation in an a priori fashion, based on the mean streamwise force profile $\langle \overline{f}_{\mathrm{d},x} \rangle$, which was previously determined for the data-driven VAF approach, as well as the plane-averaged intrinsic streamwise velocity profile from DNS, $\langle \overline{U}_x \rangle^{xz}$. Specifically, the velocity profile as well as the porosity and mean hydraulic diameter are supplied into Eq. (5.21) and the corresponding curve is 'fitted' to $\langle \overline{f}_{\mathrm{d},x} \rangle$ by manually adapting the coefficients C_{V} and C_{F}. The resulting a priori estimate of the mean streamwise

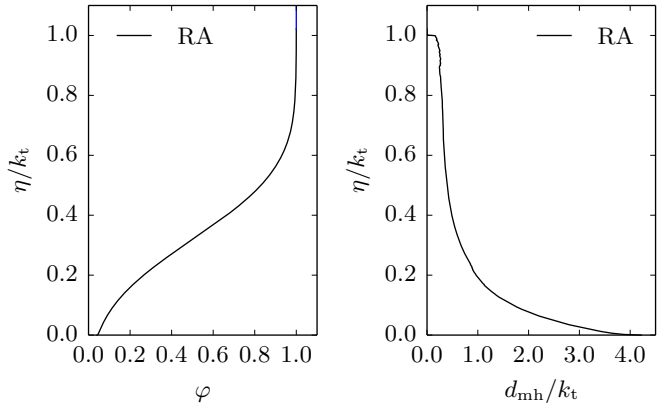

(a) porosity (b) mean hydraulic diameter

Figure 5.22: Evaluated porosity and mean hydraulic diameter profiles for the roughness topography RA.

drag force for the roughness topography RA, obtained with $C_F = 1.4$ and $C_V = 300$, is displayed in Fig. 5.23 in comparison to the respective force profile from the data-driven VAF methodology. Here, a manual 'fitting' approach is favored in order to prioritize the agreement of the fit in areas η that are expected to contribute most significantly to the accuracy of the result. In this regard, the investigations with the data-driven methodology suggest that the drag closure in the region close to the base wall is less influential for an appropriate modification of the flow, likely due to the low momentum content. On the other hand, as discussed in Section 2.3.1, the roughness function scales with the roughness height. Thus, the high momentum region up to the highest elevation of the rough surface at $\eta = k_t$ is prioritized. Specifically, the coefficient C_F associated with form drag, which represents the dominant contribution in this area, is incrementally increased until a good fit with the data-driven $\langle \overline{f}_{d,x} \rangle$ profile is obtained in the area $0.6 \leq \eta/k_t \leq 1$. Subsequently, the value of C_V is adapted to improve the overall quality of the fit, especially in the area below the peak of the volumetric force profile. As an alternative to this manual approach, a weighted fitting

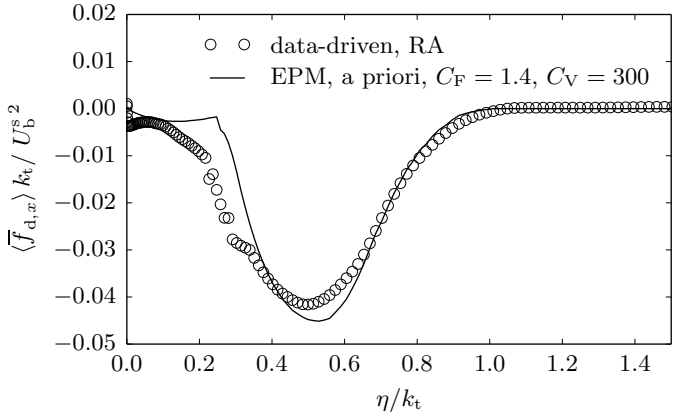

Figure 5.23: Non-dimensionalized mean streamwise drag force from the data-driven VAF approach compared to an a priori estimate of the respective force profile obtained with the EPM.

algorithm could be applied. Furthermore, uncertainties associated with the determined model coefficients, especially those associated with the balance between form drag and viscous drag, could be further reduced by adapting the model coefficients based on data-driven force profiles of the same roughness topography at various Reynolds numbers. However, since the reference DNS for the eight presently considered roughness topographies has been performed at $\mathrm{Re}_\tau \approx 500$, this approach can not be applied in this work.

The determined model coefficients, $C_\mathrm{F} = 1.4$ and $C_\mathrm{V} = 300$, are subsequently applied for all roughness topographies in this work. Corresponding a priori estimates for the remaining roughness topographies (not shown here) are in similar or better agreement with the respective data-driven volumetric force profiles compared to what is shown in Fig. 5.23. This indicates that the parametrization relying on the porosity φ and the mean hydraulic diameter d_mh according to Eq. (5.21) is valid. However, the same limitations as in the previous approaches apply, e.g.

the assumption of homogeneous and isotropic roughness[2]. Furthermore, the validity of the determined model coefficients for different types of roughness element shapes should be investigated in future studies, especially if the shape of the cross sectional areas vastly differs from what is shown in Fig. 5.21, e.g. in the case of cube- of pyramid-shaped roughness elements.

In the following, the results obtained using the EPM are presented in the same fashion as for the two data-driven approaches. Thereby, the applied computational setup is completely analogous to what is described for the data-driven VAF approach in Section 5.3.3, with the only difference being that the drag closure according to Eq. (5.21) is applied with $C_\mathrm{F} = 1.4$ and $C_\mathrm{V} = 300$.

Results

The mean streamwise velocity profiles normalized by the superficial bulk velocity U_b^s for the regular and random roughness topographies are presented in Fig. 5.24. Essentially, a similarly high level of agreement as observed for the data-driven approaches is achieved. Especially the velocity profiles for the random topographies are accurately predicted with the EPM. Fig. 5.25 displays the associated velocity profiles in inner scaling. Overall, the profiles for the random roughness topographies presented in Fig. 5.25 (b) are comparable to the results obtained with the data-driven VAF approach (see Fig. 5.18 (b)). Thus, the predictive quality achieved with the EPM, by relying on geometrical details of the rough surfaces, can be described as superior compared to the data-driven DDF approach. For the regular roughness, Fig. 5.25 (a), all profiles predicted with the EPM exhibit a slight overprediction compared to the results obtained with the data-driven VAF approach (see Fig. 5.18 (a)). Consequently, the velocity profiles for the staggered configurations again display noticeable deviations from the reference DNS data base, as previously discussed in Section 5.3.3, while reasonable results are achieved for the aligned arrangements.

The accuracy of the predicted friction losses associated with the rough wall are again quantified by the relative deviation of the obtained friction

[2]For highly non-isotropic roughness, a generalized EPM formulation based on the drag parametrization from the porous media framework, relying on the permeability and Forchheimer tensors according to Eq. (2.78), would be advantageous.

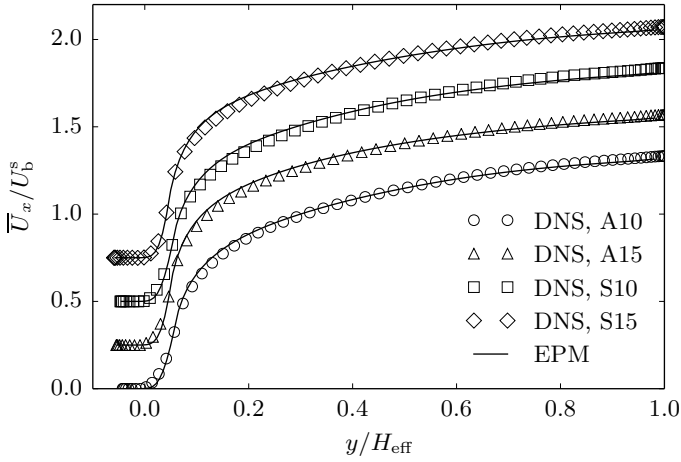

(a) regular roughness

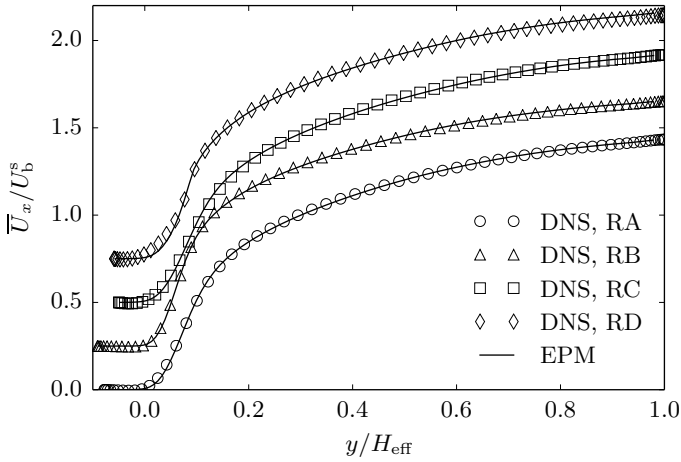

(b) random roughness

Figure 5.24: Mean streamwise velocity profiles normalized by the superficial bulk velocity U_b^s, obtained with the EPM for the regular (a) and random (b) roughness topographies. Profiles shifted upwards by $\Delta\overline{U}_x/U_\mathrm{b}^\mathrm{s} = 0.25$ increments for clarity purposes. DNS data taken from Forooghi *et al.* [48] and [78].

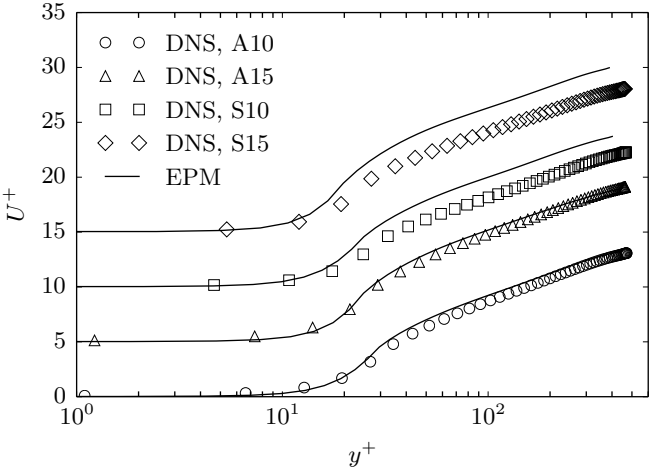

(a) regular roughness

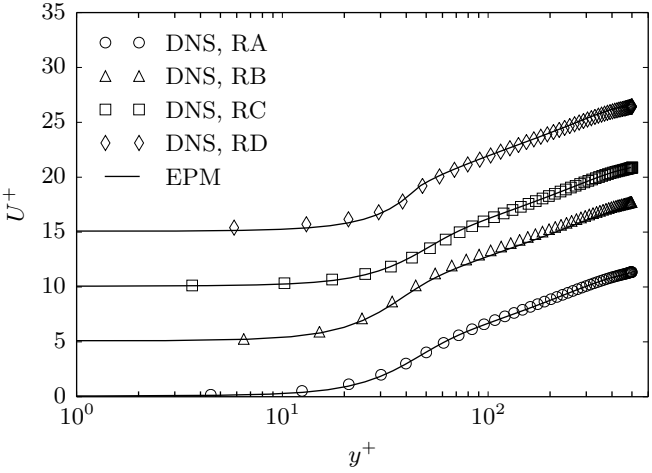

(b) random roughness

Figure 5.25: Mean streamwise velocity profiles normalized with the friction velocity u_τ, obtained with the EPM for the regular (a) and random (b) roughness topographies. Profiles shifted upwards by $\Delta U^+ = 5$ increments for clarity purposes. DNS data taken from Forooghi *et al.* [48] and [78].

Table 5.8: Relative deviation of the wall friction velocity ($\Delta u_\tau = (u_\tau - u_{\tau,\mathrm{DNS}})/u_{\tau,\mathrm{DNS}}$) for the various roughness topographies.

	EPM
A10	−3.0%
A15	−0.8%
S10	−12.5%
S15	−14.0%
RA	0.3%
RB	3.4%
RC	−0.2%
RD	−0.8%

velocity u_τ from the respective DNS reference data. Tab. 5.8 summarizes these relative deviations Δu_τ. In line with the previously discussed velocity profiles in inner scaling, relative deviations Δu_τ for the random topographies are relatively small; only for the topography RB associated with the lowest Sk, a deviation of more than 1% is obtained. On average, the accuracy for the random topographies is very comparable to the data-driven VAF approach. Consequently, the predominantly geometry-based EPM is able to accurately capture the effect of varying skewness Sk in samples RA, RB and RC. This is an important finding, since various researchers concerned with empirical correlations for the equivalent sand roughness height, k_s, have identified Sk as the most influential statistical surface parameter apart from the physical roughness height [43, 48]. The magnitudes of the relative deviations Δu_τ obtained with the EPM for the regular topographies are slightly larger compared to the data-driven VAF approach (see Tab. 5.7), whereby once more reasonable deviations are obtained for the aligned arrangements. Further improvements could be achieved by adapting the model coefficients C_V and C_F for the regular arrangements. However, for practical applications where the main flow direction might vary during computations, the discrepancy between the accuracy associated with regularly aligned and staggered arrangements suggests that a non-isotropic EPM might be required to achieve similar predictive quality as for the random topographies. This argument is based on the fact that in essence a stag-

gered configuration corresponds to an aligned configuration, where the main flow direction is rotated by 45° around the wall-normal direction.

Finally, the turbulence intensity profiles obtained with the EPM for the regular and random topographies are presented in Figs. 5.26 and 5.27, respectively. For the regular arrangements the results are essentially similar to those obtained in the data-driven VAF approach (see Fig. 5.19). Merely the underprediction of the streamwise component for sample S15 is slightly more pronounced with the EPM. For the ran-

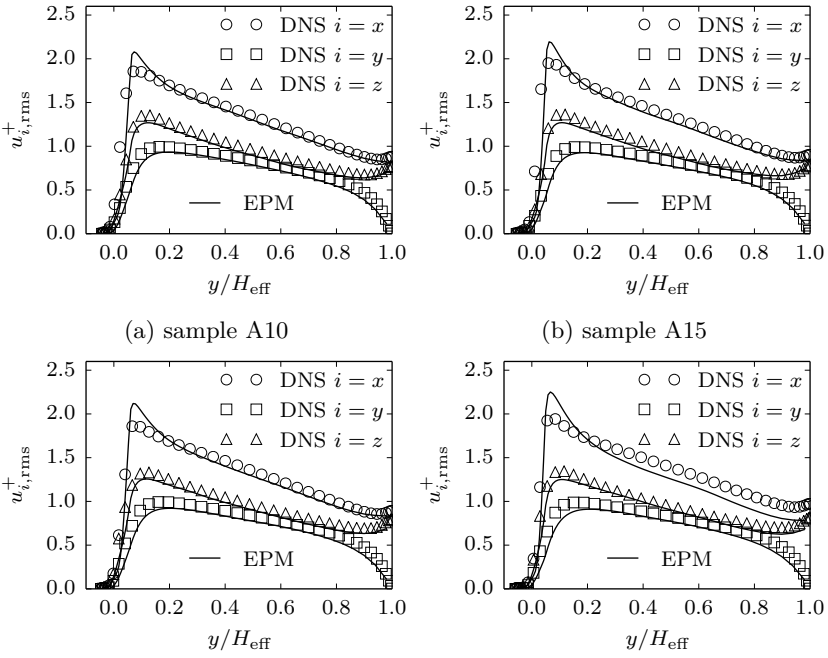

(a) sample A10

(b) sample A15

(c) sample S10

(d) sample S15

Figure 5.26: Turbulence intensity components normalized with the friction velocity, obtained with the EPM for the regular roughness topographies, compared to DNS data based on full stresses (e.g. $u^+_{x,\mathrm{rms}} = \sqrt{\overline{u_x u_x}}/u_\tau$). DNS data taken from [78].

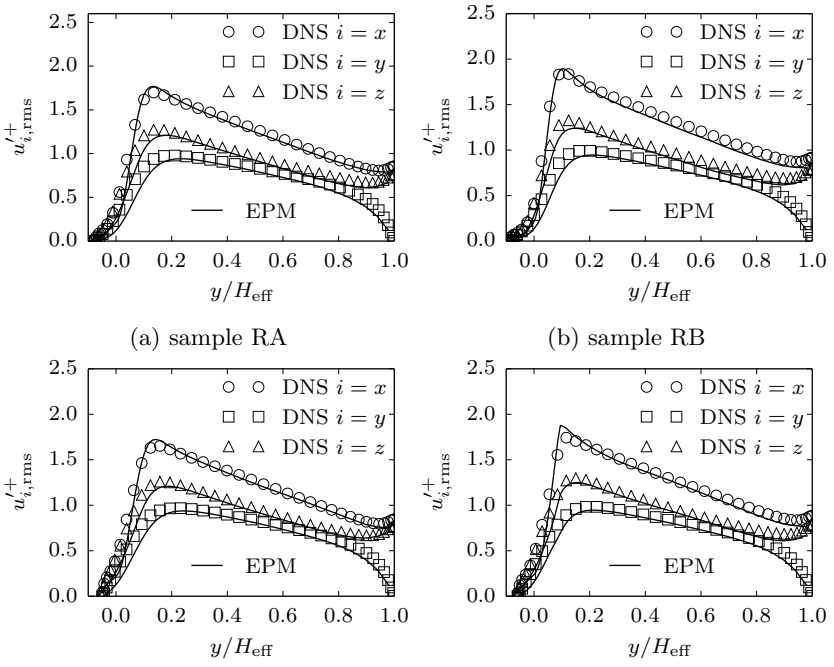

(a) sample RA (b) sample RB

(c) sample RC (d) sample RD

Figure 5.27: Turbulence intensity components normalized with the friction velocity, obtained with the EPM approach for the random roughness topographies, compared to DNS data based on Reynolds stresses (e.g. $u'^{+}_{x,\mathrm{rms}} = \sqrt{\overline{u'_x u'_x}}/u_\tau$). DNS data taken from Forooghi *et al.* [48].

dom roughness topographies presented in Fig. 5.27 the results above the roughness crest are in very good agreement with the reference DNS data base and basically identical to the corresponding profiles from the data-driven VAF approach (see Fig. 5.27). Thus, the impression raised by the good agreement of the a priori estimated volumetric force profiles $\langle \widetilde{f}_{\mathrm{d},x} \rangle$ with those determined employing the data-driven methodology for the VAF approach, is confirmed by the presented results.

Conclusion

In the present section a drag closure originally formulated for flow over porous media, or more specifically packed beds, was reformulated for the application to flow over rough walls. The model, denoted as equivalent porosity model (EPM), relies on profiles for the porosity φ and the mean hydraulic diameter d_{mh} in wall parallel layers as well as two model coefficients associated with viscous and form drag. It was demonstrated how the corresponding profiles are obtained based on surface elevation maps of the rough surfaces and how the model coefficients can be determined in an a priori fashion relying on the previously proposed data-driven methodology. Subsequently, computations for the eight considered roughness topographies were performed, whereby a single set of model coefficients for the EPM was applied. The presented results demonstrate that the geometry-based parametrization of the drag closure provides a similarly high level of accuracy as the data-driven VAF approach. Especially the good agreement with the reference DNS data base for the random topographies, in terms of mean velocity and turbulent intensity profiles as well as friction velocities, indicate that the EPM is able to capture the influence of skewness of the surface height distribution, which has been identified as one of the most influential parameters with respect to the flow modification by a rough surface.

5.4 Concluding remarks

In the present chapter, two roughness modeling approaches based on volumetric forcing were analyzed in terms of their predictive quality with respect to mean velocity and turbulent intensity profiles as well as friction velocities for the case of open-channel flow over various roughness topographies. The main difference between the two approaches is whether blockage effects are lumped into the drag closure (DDF approach) – which is in principle supposed to account for viscous and form drag the roughness elements exert on the flow – or whether blockage is explicitly considered via the application of additionally volume-averaged governing equations (VAF approach). In previous works devoted to volumetric forcing approaches, especially in the context of the RANS framework, drag closures have been primarily parametrized relying on

geometrical considerations for model roughness topographies and calibration of associated drag coefficients to achieve a good agreement with reference data for e.g. the roughness function ΔU^+ or other measures associated with friction losses pertinent to the rough wall. However, this methodology generally does not result in an accurate representation of the mean velocity profile in the near-wall region, which indicates that modeling uncertainties associated with the parametrization of the drag closure are compensated through the calibrated model coefficients. Thus, in this work a data-driven methodology relying on the reference DNS data base was applied in order to estimate sectional drag coefficient profiles that enable an accurate representation of mean velocity profiles over the entire channel height. By applying the correspondingly determined sectional drag profiles in the DDF and VAF approaches and evaluating the obtained turbulence intensities as well as friction velocities, it was found that the latter approach provides a higher level of consistency and overall accuracy, especially for more realistic random roughness topographies.

Prior to the computations with the VAF approach, the present implementation of the volume-averaged computational framework originally proposed for flow through porous media, has been verified and the performance of correspondingly adapted turbulence models was assessed by computing turbulent channel flow over porous walls. The ER ζ-f model proposed in Chapter 4 thereby exhibits the best performance of the considered models, with respect to both grid sensitivity as well as overall predictive quality. It was thus employed for all computations of flow over rough walls in this work.

Finally, the drag closure for packed beds, which was previously applied for the porous channel configuration, was reformulated by introducing the mean hydraulic diameter associated with the cross-sectional areas of the roughness elements in layers parallel to the wall as the relevant length scale. Apart from this geometrical information, the drag closure presently denoted as equivalent porosity model, relies on two calibration coefficients for viscous and form drag terms. A single set of these coefficients for all roughness topographies was determined in an a priori fashion by relying once again on the proposed data-driven methodology. The results obtained with the EPM for the various roughness topographies exhibit a high level of agreement with those from the data-driven

VAF approach, implying that the geometry-based parametrization is valid. With respect to the accuracy of the results, overall good agreement with the reference DNS data base is achieved with respect to mean velocity and turbulent intensity profiles. Friction velocities for regular arrangements exhibit deviations of up to 14% from the reference DNS values. Since similar deviations were obtained with the data-driven VAF approach, this might be an indication that underlying model assumptions of the volumetric forcing approach are less valid for such highly periodic arrangements, thus prompting the need for further investigations. Nevertheless, friction velocities for the more realistic and highly irregular random topographies exhibit relative deviations of less than 3.4%, which is of similar magnitude as for corresponding smooth channel flow computations employing the ER ζ-f model.

6 Conclusions and outlook

The primary objective of the present work was the development and validation of a computationally efficient modeling framework for scale-resolving simulations of turbulent flow over rough walls. In particular, the development is motivated by technical applications involving influential phenomena in the vicinity of rough walls, such as internal combustion engines and exhaust gas aftertreatment systems. In both of these cases, near-wall phenomena associated with turbulent, chemically reactive multiphase flow have been identified as important, for instance with respect to the formation and emission of pollutants. In order to enable predictive computational fluid dynamics simulations capturing the relevant coupled phenomena, an accurate representation of the turbulent flow field in the near-wall region is essential. In particular, modifications of the turbulence structure through the presence of rough surfaces have to be considered. Consequently, the modeling efforts in the present work have been twofold: firstly, the development of a computationally efficient RANS-based sub-scale model, and secondly, the formulation of an appropriate modeling approach for the effect of realistic, irregular rough surfaces on turbulent flow.

With respect to turbulence modeling, the main goals addressed with the presently proposed RANS-based sub-scale model are a reduction of required computational resources compared to the LES framework, as well as improvements with respect to grid sensitivity. These two objectives are very much related, and if achieved, facilitate cost reductions as well as higher levels of robustness and predictive quality, especially for complex applications such as internal combustion engines, where the appropriate grid resolution for a well-resolved LES in the entire computational domain is difficult to estimate in advance.

Due to the significance of the near-wall region, with respect to both developing, non-equilibrium boundary layers as well as possibly additional coupled physical processes (e.g. combustion, heat transfer), wall-

resolving turbulence modeling approaches have been considered exclusively. Specifically, a RANS-based sub-scale model relying on the near-wall elliptic-relaxation EVM of Hanjalić *et al.* [59], commonly referred to as ζ-f model, was proposed. The newly formulated model, termed as eddy-resolving (ER) ζ-f model, was sensitized to resolved turbulent fluctuations by introducing an additional source term motivated by the scale-adaptive simulation (SAS) concept of Menter and Egorov [102] into the scale-supplying equation. In line with most previously proposed models based on the SAS concept, the original scale-supplying equation of the ζ-f RANS model, formulated in terms of the dissipation rate of turbulent kinetic energy ε, was transformed and re-calibrated to rely on the inverse turbulent time scale $\omega(= \varepsilon/k)$ instead. The subsequently introduced SAS production term is presently modeled primarily in terms of the second-derivative of the resolved velocity field. Effectively, it introduces a second physical length scale associated with resolved turbulent eddies into the ω-equation, which enables the ER ζ-f to adapt the modeled quantities to an appropriate sub-scale level. Thereby, the presently proposed SAS term formulation enables scale-resolving computations of globally stable flow configurations, even at relatively low Reynolds numbers – in contrast to the original SAS proposal of Menter and Egorov [102].

In order to validate the newly formulated RANS-based sub-scale model and comparatively assess its performance, several generic flow configurations were computed with the ER ζ-f model, as well as the dynamic Smagorinsky model of Lilly [94] and the VLES model of Chang *et al.* [27]. The latter is a seamless hybrid RANS/LES closure also relying on the ζ-f model, which achieves scale-resolving capabilities through a direct damping of the eddy-viscosity based on the local grid resolution, and has previously been applied to the flow in internal combustion engines. The considered generic configurations represent standard validation test cases, such as fully-developed channel flow, as well as configurations exhibiting flow phenomena relevant to the intended application, comprising flow separation, jet impingement onto a heated wall and non-equilibrium boundary layers. Special attention was payed to the performance of the models on various grid refinement levels. Thereby, it was demonstrated that in most cases, the ER ζ-f model provides more accurate results in terms of flow topology, friction velocities and

turbulent kinetic energy levels, especially on grids unsuitable for a well-resolved LES, while maintaining competitive accuracy on finer grids. Consequently, it can be concluded that grid sensitivity is reduced compared to the other two investigated scale-resolving modeling approaches. Finally, it was demonstrated that while solving the ER ζ-f model's partial differential equations is associated with a computational overhead of up to 14% compared to the algebraic dynamic Smagorinsky model, the lower requirements in terms of spatial resolution enable the application of coarser grids to obtain similar levels of accuracy. In particular, it was demonstrated for the simple case of fully-developed channel flow that with the other two models, finer grids, corresponding to an increase in computational costs of at least 60% compared to ER ζ-f, are required in order to achieve the same level of accuracy with respect to the predicted wall shear stress.

The superior performance of the ER ζ-f model in the presently investigated generic flow configurations can be considered as a basis for future applications to more realistic flow configurations, such as internal combustion engines. Since in the present work, primarily flows at low to moderate Reynolds numbers have been investigated, the performance and computational efficiency of the ER ζ-f model compared to LES should be further investigated at higher Reynolds numbers relevant to e.g. external aerodynamics applications. Furthermore, the results obtained with ER ζ-f with respect to heat transfer applications suggest that further improvements could be achieved through an adjustment of the turbulent Prandtl number in the presently employed simple gradient diffusion approach, or alternatively, through the application of an overall more physical sub-scale model for turbulent heat fluxes.

With respect to roughness modeling, the main objective of the present work was the development of a roughness model suitable for application in conjunction with scale-resolving models of turbulence, such as the proposed ER ζ-f model. In particular, the roughness model should provide an accurate representation of the modified turbulent flow in the near-wall region. The category of roughness modeling approaches originating in principle from the discrete element method of Taylor *et al.*

[147], which account for the viscous and form drag roughness elements exert on the flow by means of a volumetric force term in the momentum equation, have been identified as a suitable starting point. Previously, such models have been applied predominantly in the RANS framework and specific drag closures have generally been parametrized relying on simplified, virtual roughness topographies, instead of geometrical details of the actual rough surface. In addition, model coefficients have usually been tuned in order to achieve good agreement with experimental reference data in terms of wall friction, which generally does not result in an accurate representation of the flow in the near-wall region. Furthermore, Taylor *et al.* [147] explicitly accounted for blockage effects in his modified two-dimensional boundary layer equations, while several following researchers choose to merely apply a volumetric force term.

In the present work, the impact of this choice on the predictive accuracy was initially investigated. A distributed drag force (DDF) approach not explicitly accounting for blockage effects was straightforwardly enabled by adding a volumetric force term to the standard single-phase equations. For the volume-averaged forcing (VAF) approach explicitly accounting for blockage effects, governing equations from the field of porous media modeling, relying on the volume averaging technique of Whitaker [160], were adopted. The volume- and ensemble-averaged equations were implemented into the applied numerical code (OpenFOAM) and the implementation was verified by comparison to DNS reference data of Breugem *et al.* [21] for channel flow over packed beds of different porosities. Furthermore, the presently considered scale-resolving turbulence models were adapted to account for blockage effects and their performance was subsequently assessed based on the aforementioned validation case. Thereby it was demonstrated once again that the ER ζ-f model exhibits the overall best agreement with the reference DNS data base, as well as the lowest grid sensitivity and was thus applied for all remaining computations.

In order to assess the DDF and VAF approaches independently of any calibrated model coefficients for the drag closure, a data-driven methodology relying on the reference DNS data base of Forooghi *et al.* [48] for open-channel flow over various roughness topographies was proposed. In this way, non-dimensionalized force profiles representing the mean effect of the roughness topographies on the flow were deter-

mined based on the respective governing equations. By applying the non-dimensionalized force profiles in the open-channel configuration, it was demonstrated that the proposed methodology results in a good representation of the mean velocity field for all roughness topographies. Furthermore, the results were analyzed in terms of the obtained turbulent intensity profiles as well as the correspondingly predicted friction velocities associated with the rough wall. Thereby it was found that the employed VAF approach provides more consistent results, especially for more realistic, irregularly arranged roughness topographies, emphasizing the importance to account for blockage effects.

Based on this finding, the drag closure from the field of porous media flow, previously employed for the verification and validation of the volume-averaged computational framework, was reformulated for the application to rough walls, enabling a unified modeling framework for flow over porous and rough walls. In particular, this modified drag closure presently denoted as equivalent porosity model (EPM), is parametrized based on the porosity and mean hydraulic diameter associated with the roughness elements in layers parallel to the wall. In addition the drag closure relies on two model coefficients, which were determined in an a priori fashion employing the data-driven methodology. The results obtained with the EPM exhibit a high-level of agreement with the data-driven VAF approach, indicating that the geometry-based parametrization is valid. Furthermore, relative deviations of the predicted friction velocities from the DNS reference for the irregular roughness topographies are on the same order of magnitude as obtained for corresponding smooth wall computations.

For regular, periodic arrangements of roughness elements, noticeably higher deviations in the friction velocities of up to 14% were found. These deviations are similarly obtained with the EPM as well as the data-driven approach, suggesting that underlying model assumptions of spatial homogeneity might be less valid for periodic roughness arrangements. In this regard further DNS studies investigating the effect of spatial variations of the time-averaged velocity field and the associated dispersive stresses are indicated to gain further insights. Furthermore, since the model coefficients for the EPM were determined based on DNS data at a fixed Reynolds number, at which form drag is dominant,

the model coefficient for viscous drag should be recalibrated relying on DNS data at lower Reynolds numbers. In addition, the validity of the determined model coefficients for rough surfaces consisting of roughness elements of vastly different cross-sectional shape should be explored. Finally, for the application of the model in the context of heat transfer applications, a source term accounting for the effect of roughness in the energy equation is required, which can be modeled for instance based on the Reynolds analogy.

To conclude, the presently proposed ER ζ-f model enables scale-resolving computations at lower spatial resolutions compared to the LES framework, thus effectively reducing computational costs and facilitating a higher level of robustness with respect to the applied numerical grid. Furthermore, the data-driven methodology and the EPM represent important contributions to the field of roughness modeling in the context of scale-resolving computations. In particular, the data-driven methodology is expected to promote future model refinements on the basis of geometry-resolving direct numerical simulation studies, which have only been feasible in recent years.

Bibliography

[1] H. Abe, H. Kawamura, and Y. Matsuo. Surface heat-flux fluctuations in a turbulent channel flow up to $\mathrm{Re}_\tau = 1020$ with $\mathrm{Pr} = 0.025$ and 0.71. *International Journal of Heat and Fluid Flow*, 25:404–419, 2004.

[2] D. N. Anderson, D. B. Hentschel, and G. A. Ruff. Measurement and correlation of ice accretion roughness. *AIAA Paper*, 98–0486, 2003.

[3] W. Anderson. Amplitude modulation of streamwise velocity fluctuations in the roughness sublayer: evidence from large-eddy simulations. *Journal of Fluid Mechanics*, 789:567–588, 2016.

[4] B. V. Antohe and J. L. Lage. A general two-equation macroscopic turbulence model for incompressible flow in porous media. *International Journal of Heat and Mass Transfer*, 40(13):3013–3024, 1997.

[5] D. Apsley. CFD calculation of turbulent flow with arbitrary wall roughness. *Flow, Turbulence and Combustion*, 78:153–175, 2007.

[6] B. Aupoix. Roughness corrections for the k-ω shear stress transport model: status and proposals. *Journal of Fluids Engineering*, 137:021202, 2015.

[7] B. Aupoix. Revisiting the discrete element method for predictions of flows over rough surfaces. *Journal of Fluids Engineering*, 138:031205, 2016.

[8] B. Aupoix and P. R. Spalart. Extensions of the Spalart-Allmaras turbulence model to account for wall roughness. *International Journal of Heat and Fluid Flow*, 24:454–462, 2003.

[9] K. W. Ayotte, J. J. Finnigan, and M. R. Raupach. A second-order closure for neutrally stratified vegetative canopy flows. *Boundary-Layer Meteorology*, 90:189–216, 1999.

[10] G. K. Batchelor. *An introduction to fluid mechanics*. Cambridge University Press, 2000.

[11] S. E. Belcher, N. Jerram, and J. C. R. Hunt. Adjustment of a turbulent boundary layer to a canopy of roughness elements. *Journal of Fluid Mechanics*, 488:369–398, 2003.

[12] K. Bhaganagar, J. Kim, and G. Coleman. Effect of roughness on wall-bounded turbulence. *Flow, Turbulence and Combustion*, 72:463–492, 2004.

[13] R. B. Bird, W. E. Stewart, and E. N. Lightfoot. *Transport phenomena*. John Wiley, 2006.

[14] B. Blocken, T. Stathopoulos, and J. Carmeliet. CFD simulation of the atmospheric boundary layer: wall function problems. *Atmospheric Environment*, 41:238–252, 2007.

[15] J. P. Bons. St and c_f augmentation for real turbine roughness with elevated freestream turbulence. *Journal of Turbomachinery*, 124:632–644, 2002.

[16] J. P. Bons. A review of surface roughness effects on gas turbines. *Journal of Turbomachinery*, 132(2):021004, 2010.

[17] J. Boussinesq. Essai sur la théorie des eaux courantes. *Mémoires présentés par divers savants à l'Académie des Sciences de l'Institut national de France*, 23(1), 1877.

[18] P. Bradshaw. A note on "critical roughness height" and "transitional roughness". *Physics of Fluids*, 12:1611–1614, 2000.

[19] M. Breuer, N. Peller, C. Rapp, and M. Manhart. Flow over periodic hills - numerical and experimental study in a wide range of Reynolds numbers. *International Journal of Computational Fluid Dynamics*, 38(2):433–457, 2009.

[20] W. P. Breugem and B. J. Boersma. Direct numerical simulations of turbulent flow over a permeable wall using a direct and continuum approach. *Physics of Fluids*, 17:025103, 2005.

[21] W. P. Breugem, B. J. Boersma, and R. E. Uittenbogaard. The influence of wall permeablility on turbulent channel flow. *Journal of Fluid Mechanics*, 562:35–72, 2006.

[22] A. Busse, M. Lützner, and N. D. Sandham. Direct numerical simulation of turbulent flow over a rough surface based on a surface scan. *Computers Fluids*, 116:129–147, 2015.

[23] A. Busse and N. D. Sandham. Parametric forcing approach to rough-wall turbulent channel flow. *Journal of Fluid Mechanics*, 712:169–202, 2012.

[24] J. Cardillo, Y. Chen, G. Araya, J. Newman, K. Jansen, and L. Castillo. DNS of a turbulent boundary layer with surface roughness. *Journal of Fluid Mechanics*, 729:603–637, 2013.

[25] C. Chan-Braun, M. García-Villalba, and M. Uhlmann. Force and torque acting on particles in a transitionally rough open-channel flow. *Journal of Fluid Mechanics*, 684:441–474, 2011.

[26] C.-Y. Chang. *Development and validation of scale-resolving computational models relevant to IC-engine flow configurations*. PhD thesis, Technische Universtität Darmstadt, 2015.

[27] C.-Y. Chang, S. Jakirlić, K. Dietrich, B. Basara, and C. Tropea. Swirling flow in a tube with variably-shaped outlet orifices: an LES and VLES study. *International Journal of Heat and Fluid Flow*, 49:28–42, 2014.

[28] Y. H. Chang, K. Toda, and M. Yamamoto. Modeling and verification of virtual-force-based roughness turbulence model. In *Turbulence, Heat and Mass Transfer 5. Proceedings of the International Symposium on Turbulence, Heat and Mass Transfer - Dubrovnik, Croatia, September 25 - 29*, pages 385–388, 2006.

[29] B. Chaouat. The state of the art of hybrid RANS/LES modeling for the simulation of turbulent flows. *Flow, Turbulence and Combustion*, 99:279–327, 2017.

[30] H. Cheng and I. P. Castro. Near wall flow over urban-like roughness. *Bounday-Layer Meteorology*, 104:229–259, 2002.

[31] O. Coceal and S. E. Belcher. A canopy model of mean winds through urban areas. *Quarterly Journal of the Royal Meteorological Society*, 130:1349–1372, 2004.

[32] O. Coceal, T. G. Thomas, I. P. Castro, and S. Belcher. Mean flow and turbulence statistics over groups of urban-like cubical obstacles. *Bounday-Layer Meteorology*, 121:491–519, 2006.

[33] C. F. Colebrook and C. White. Experiments with fluid friction in roughened pipes. *Proceedings of the Royal Society A: Mathematical and Physical Sciences*, 161:367–381, 1937.

[34] T. J. Craft, A. V. Gerasimov, H. Iacovides, and B. E. Launder. Progress in the generalisation of wall-function treatments. *International Journal of Heat and Fluid Flow*, 23:148–160, 2002.

[35] H. Darcy. *Les Fontaines Publiques de la Ville de Dijon.* Victor Dalmond, Paris, 1856.

[36] M. J. S. de Lemos. *Turbulence in porous media.* Elsevier, 2012.

[37] B. Dean and B. Bhushan. Shark-skin surfaces for fluid-drag reduction in turbulent flow: a review. *Philosophical Transactions of the Royal Society A: Mathematical, Physical and Engineering Sciences*, 368:4775–4806, 2010.

[38] DIN 4760:1982-06. Gestaltabweichungen; Begriffe, Ordnungssystem.

[39] P. A. Durbin. Near-wall turbulence closure modeling without "damping functions". *Theoretical and Computational Fluid Dynamics*, 3:1–13, 1991.

[40] J. H. Ferziger and M. Perić. *Computational methods for fluid mechanics.* Springer-Verlag Berlin Heidelberg, 2002.

[41] J. Finnigan. Turbulence in plant canopies. *Annual Review of Fluid Mechanics*, 32:519–571, 2000.

[42] K. A. Flack. Moving beyond Moody. *Journal of Fluid Mechanics*, 842:1–4, 2018.

[43] K. A. Flack and M. P. Schultz. Review of hydraulic roughness scales in the fully rough regime. *Journal of Fluids Engineering*, 132:041203, 2010.

[44] K. A. Flack and M. P. Schultz. Roughness effects on wall-bounded turbulent flows. *Physics of Fluids*, 26:101305, 2014.

[45] K. A. Flack, M. P. Schultz, J. M. Barros, and Y. Kim. Skin-friction behavior in the transitionally-rough regime. *International Journal of Heat and Fluid Flow*, 61:21–30, 2016.

[46] K. A. Flack, M. P. Schultz, and T. A. Shapiro. Experimental support for Townsend's Reynolds number similarity hypothesis on rough walls. *Physics of Fluids*, 17:035102, 2005.

[47] P. Forchheimer. Wasserbewegung durch Boden. *Zeitschrift des Vereins Deutscher Ingenieure*, 45:1781–1788, 1901.

[48] P. Forooghi, A. Stroh, F. Magagnato, S. Jakirlić, and B. Frohnapfel. Towards a universal roughness correlation. *Journal of Fluids Engineering*, 139:121201, 2017.

[49] P. Forooghi, A. Weidenlener, F. Magagnato, B. Böhm, H. Kubach, T. Koch, and B. Frohnapfel. DNS of momentum and heat transfer over rough surfaces based on realistic combustion chamber deposit geometries. *International Journal of Heat and Fluid Flow*, 69:83–94, 2018.

[50] J. Fröhlich. *Large Eddy Simulation turbulenter Strömungen*. Teubner Verlag, 2006.

[51] J. Fröhlich and D. von Terzi. Hybrid LES/RANS methods for the simulation of turbulent flows. *Progress in Aerospace Sicences*, 44(349-377), 2008.

[52] M. Germano, U. Piomelli, P. Moin, and W. H. Cabot. A dynamic subgrid-scale eddy viscosity model. *Physics of Fluids A*, 3:1760–1765, 1991.

[53] S. S. Girimaji. Partially-averaged Navier-Stokes model for turbulence: a Reynolds-averaged Navier-Stokes to direct numerical simulation bridging method. *Journal of Applied Mechanics*, 73:413–421, 2006.

[54] A. J. Grass. Structural features of turbulent flow over smooth and rough boundaries. *Journal of Fluid Mechanics*, 50(2):233–255, 1971.

[55] F. R. Hama. Boundary-layer characteristics for rough and smooth surfaces. *Transactions of the Society of Naval Architects and Marine Engineers*, 62:333–351, 1954.

[56] X. Han and S. Kranjonić. An efficient very large eddy simulation model for simulation of turbulent flow. *International Journal for Numerical Methods in Fluids*, 71(11):1341–1360, 2012.

[57] K. Hanjalić and B. Launder. *Modelling turbulence in engineering and the environment*. Cambridge University Press, 2011.

[58] K. Hanjalić and B. E. Launder. Fully developed asymmetric flow in a plane channel. *Journal of Fluid Mechanics*, 51(2):301–335, 1972.

[59] K. Hanjalić, M. Popovac, and M. Hadžiabdić. A robust near-wall elliptic-relaxation eddy-viscosity turbulence model for CFD. *International Journal of Heat and Fluid Flow*, 25:1047–1051, 2004.

[60] H. Hattori, M. Iwase, T. Houra, and M. Tagawa. DNS and LES for turbulent heat transfer and mixing in T-junction channel flow. In *10th International ERCOFTAC Symposium on Engineering Turbulence Modelling and Measurements (ETMM11), Marbella, Spain, September 17-19*, 2014.

[61] H. Hattori and Y. Nagano. Direct numerical simulation of turbulent heat transfer in plane impinging jet. *International Journal of Heat and Fluid Flow*, 25(749-758), 2004.

[62] C. Hirsch. *Numerical computation of internal and external flows: the fundamentals of computational fluid dynamics*. Butterworth-Heinemann, 2007.

[63] M. H. Hosni, H. W. Coleman, and R. P. Taylor. Measurements and calculations of rough-wall heat transfer in the turbulent boundary layer. *International Journal of Heat and Mass Transfer*, 34(4/5):1067–1082, 1991.

[64] J. C. R. Hunt, A. A. Wray, and P. Moin. Eddies, streams and convergence zones in turbulent flows. In *Center for Turbulence Research, Proceedings of the Summer Programm*, 1988.

[65] R. I. Issa. Solution of the implicitly discretised fluid flow equations by operator-splitting. *Journal of Computational Physics*, 62:40–65, 1986.

[66] P. S. Jackson. On the displacement height in the logarithmic velocity profile. *Journal of Fluid Mechanics*, 111:15–25, 1981.

[67] S. Jakirlić and K. Hanjalić. A new approach to modelling near-wall turbulence energy and stress dissipation. *Journal of Fluid Mechanics*, 459:139–166, 2002.

[68] S. Jakirlić and R. Maduta. Extending the bounds of 'steady' RANS closures: toward an instability-sensitive Reynolds stress model. *International Journal of Heat and Fluid Flow*, 51:175–194, 2015.

[69] T. O. Jelly and A. Busse. Reynolds and dispersive shear stress above highly skewed roughness. *A. Busse*, 852:710–724, 2018.

[70] J. Jiménez. Turbulent flows over rough walls. *Annual Review of Fluid Mechanics*, 36:173–196, 2004.

[71] W. P. Jones and B. E. Launder. The prediction of laminarization with a two-equation model of turbulence. *International Journal of Heat and Mass Transfer*, 15:301–314, 1972.

[72] H. Kawamura, K. Ohsaka, H. Abe, and K. Yamamoto. DNS of turbulent heat transfer in channel flow with low to medium-high Prandtl number. *International Journal of Heat and Fluid Flow*, 19:482–491, 1998.

[73] W. M. Kays. Turbulent Prandtl number - where are we? *Journal of Heat Transfer*, 116:284–295, 1994.

[74] A. Kolmogorov. The local structure of turbulence in incompressible viscous fluid for very large Reynolds numbers. *Proceedings of the Royal Society A: Mathematical and Physical Sciences*, 434(1890):9–13, 1991.

[75] P.-Å. Krogstad, H. Andersson, O. Bakken, and A. Ashrafian. An experimental and numerical study of channel flow with rough walls. *Journal of Fluid Mechanics*, 530:327–352, 2005.

[76] P.-Å. Krogstad, R. A. Antonia, and L. Browne. Comparison between rough- and smooth-wall turbulent boundary layers. *Journal of Fluid Mechanics*, 245:599–617, 1992.

[77] B. Krumbein, P. Forooghi, S. Jakirlić, F. Magagnato, and B. Frohnapfel. VLES modeling of flow over walls with variably-shaped roughness by reference to complementary DNS. In *11th International ERCOFTAC Symposium on Engineering Turbulence Modelling and Measurements (ETMM11), Palermo, Italy, September 21-23*, 2016.

[78] B. Krumbein, P. Forooghi, S. Jakirlić, F. Magagnato, and B. Frohnapfel. VLES modeling of flow over walls with variably-shaped roughness by reference to complementary DNS. *Flow, Turbulence and Combustion*, 99:685–703, 2017.

[79] B. Krumbein and S. Jakirlić. Scale-resolving modeling of convective heat transfer in impinging and separating flows accounting for near-wall turbulence. In *7th European Conference on Computational Fluid Dynamics (ECFD7), Glasgow, UK, June 11-15*, 2018.

[80] B. Krumbein, S. Jakirlić, V. Termini, A. Mizobuchi, and C. Tropea. Flow and heat transfer in cross-stream type T-junctions: a computational study. In *10th International Symposium on Turbulence and Shear Flow Phenomena (TSFP10), Chicago, USA, July 6-9*, 2017.

[81] B. Krumbein, S. Jakirlić, and C. Tropea. Jet impingement onto a heated wall: a VLES study. In *11th International ERCOFTAC Symposium on Engineering Turbulence Modelling and Measurements (ETMM11), Palermo, Italy, September 21-23*, 2016.

[82] B. Krumbein, S. Jakirlić, and C. Tropea. VLES study of a jet impinging onto a heated wall. *International Journal of Heat and Fluid Flow*, 68:290–297, 2017.

[83] B. Krumbein, S. Jakirlić, and C. Tropea. A unified modeling approach for flow over porous and rough walls in scale-resolving simulation methods. In *11th International Symposium on Turbulence and Shear Flow Phenomena (TSFP11) Southampton, UK, July 30 - August 2*, 2019, (accepted).

[84] B. Krumbein, R. Maduta, S. Jakirlić, and C. Tropea. Performance assessment of scale-resolving models in computing turbulent flow over a porous wall. In *12th International ERCOFTAC Symposium on Engineering Turbulence Modelling and Measurements (ETMM12), Montpellier, France, September 26-28*, 2018.

[85] B. Krumbein, R. Maduta, S. Jakirlić, and C. Tropea. A scale-resolving elliptic-relaxation-based eddy-viscosity model: development and validation. In *New Results in Numerical and Experimental Fluid Mechanics XII*. Springer International Publishing, 2019, (in press).

[86] B. Krumbein, V. Termini, S. Jakirlić, and C. Tropea. Flow and heat transfer in cross-stream type T-junctions: a computational study. *International Journal of Heat and Fluid Flow*, 71:179–188, 2018.

[87] Y. Kuwata and Y. Kawaguchi. Lattice Boltzmann direct numerical simulation of turbulence over resolved and modelled walls with irregularly distributed roughness. In *10th International Symposium on Turbulence and Shear Flow Phenomena (TSFP10), Chicago, USA, July 6-9*, 2017.

[88] P. S. Larsen, J. J. Schmidt, and U. Ullum. Experimental study of temporal and spatial structures in fence-on-wall test case. In *IUTAM Symposium on Simulation and Identification of Organized Structures in Flows, Fluid Mechanics and its Applications*, volume 52, pages 25–37, 1999.

[89] B. E. Launder and D. B. Spalding. The numerical computation of turbulent flows. *Computer Methods in Applied Mechanics and Engineering*, 3(2):269–289, 1974.

[90] A. Leonard. Energy cascade in large-eddy simulations of turbulent fluid flows. *Advances in Geophysics*, 18:237–248, 1975.

[91] S. Leonardi and I. P. Castro. Channel flow over large cube roughness: a direct numerical simulation study. *Journal of Fluid Mechanics*, 651:519–539, 2010.

[92] F. S. Lien, E. Yee, and Y. Cheng. Simulation of mean flow and turbulence over a 2D building array using high-resolution CFD and a distributed drag force approach. *Journal of Wind Engineering and Industrial Aerodynamics*, 92:117–158, 2004.

[93] P. M. Ligrani and R. Moffat. Structure of transitionally rough and fully rough turbulent boundary layers. *Journal of Fluid Mechanics*, 162:69–98, 2006.

[94] D. K. Lilly. A proposed modification of the Germano subgrid-scale closure model. *Physics of Fluids A*, 4:633–635, 1992.

[95] R. Maduta. *An eddy-resolving Reynolds stress model for unsteady flow computations: development and application.* PhD thesis, Technische Universtität Darmstadt, 2013.

[96] G. I. Mahmood and P. Ligrani. Heat transfer in a dimpled channel: combined influences of aspect ratio, temperature ratio, Reynolds number, and flow structure. *International Journal of Heat and Mass Transfer*, 45:2011–2020, 2002.

[97] M. D. Marchis, B. Milici, and E. Napoli. Numerical observations of turbulence structure modification in channel flow over 2D and 3D rough walls. *International Journal of Heat and Fluid Flow*, 56:108–123, 2015.

[98] M. D. Marchis and E. Napoli. Effects of irregular two-dimensional and three-dimensional surface roughness in turbulet channel flows. *International Journal of Heat and Fluid Flow*, 36:7–17, 2012.

[99] T. Maruyama. Optimization of roughness parameters for staggered arrayed cubic blocks using experimental data. *Journal of Wind Engineering and Industrial Aerodynamics*, 46/47:165–171, 1993.

[100] F. R. Menter. Two-equation eddy-viscosity turbulence models for engineering applications. *AIAA Journal*, 32(8):1598–1605, 1994.

[101] F. R. Menter and Y. Egorov. Revisiting the turbulent scale equation. In *IUTAM Symposium on One Hundred Years of Boundary Layer Research*. Springer Netherlands, 2006.

[102] F. R. Menter and Y. Egorov. The scale-adaptive simulation method for unsteady turbulent flow predictions. Part 1: theory and model description. *Flow, Turbulence and Combustion*, 85(1):113–138, 2010.

[103] F. R. Menter, M. Kuntz, and R. Bender. A scale-adaptive simulation model for turbulent flow predictions. *AIAA Paper*, 2003-0767, 2003.

[104] R. Mittal and G. Iaccarino. Immersed boundary methods. *Annual Review of Fluid Mechanics*, 37:239–261, 2005.

[105] Y. Miyake, K. Tsujimoto, and Y. Agata. A DNS of a turbulent flow in a rough-wall channel using roughness elements model. *JSME Internation Journal Series B*, 43(2):233–241, 2000.

[106] S. Moltchanov, Y. Bohbot-Raviv, and U. Shavit. Dispersive stresses at the canopy upstream edge. *Bounday-Layer Meteorology*, 139:333–351, 2011.

[107] L. F. Moody. Friction factors for pipe flow. *Transactions of the American Society of Mechanical Engineers*, 66:671–684, 1944.

[108] R. D. Moser, J. Kim, and N. N. Mansour. Direct numerical simulation of turbulent channel flow up to $\mathrm{Re}_\tau = 590$. *Physics of Fluids*, 11(4):943–945, 1999.

[109] A. J. Musker. Universal roughness function for naturally-occuring surfaces. *Transactions of the Canadian Society for Mechanical Engineering*, 6(1):1–6, 1980.

[110] E. Napoli, V. Armenio, and M. D. Marchis. The effect of the slope of irregularly distributed roughness elements on turbulent wall-bounded flows. *Journal of Fluid Mechanics*, 613:385–394, 2008.

[111] D. A. Nield and A. Bejan. *Convection in porous media*. Springer Science+Business Media, 2006.

[112] J. Nikuradse. Strömungsgesetze in rauhen Rohren. *VDI-Forschungsheft*, 361, 1933.

[113] OpenFOAM Foundation Ltd. OpenFOAM 2.4.x source code, URL: https://github.com/openfoam/openfoam-2.4.x (accessed 31.08.2018).

[114] P. Orlandi and S. Leonardi. DNS of turbulent channel flows with two- and three-dimensional roughness. *Journal of Turbulence*, 7(53):1–22, 2006.

[115] P. Orlandi and S. Leonardi. Direct numerical simulation of three-dimensional turbulent rough channels: parametrization and flow physics. *Journal of Fluid Mechanics*, 606:399–415, 2008.

[116] S. V. Patankar and D. B. Spalding. A calculation procedure for heat, mass and momentum transfer in three-dimensional parabolic flows. *International Journal of Heat and Mass Transfer*, 15(10):1787–1806, 1972.

[117] A. E. Perry and C. J. Abell. Asymptotic similarity of turbulence structures in smooth- and rough-walled pipes. *Journal of Fluid Mechanics*, 79:785–799, 1977.

[118] S. B. Pope. *Turbulent flows*. Cambridge University Press, 2000.

[119] M. R. Raupach, R. Antonia, and S. Rajagopalan. Rough-wall turbulent boundary layers. *Applied Mechanics Review*, 44(1):1–25, 1991.

[120] M. R. Raupach, P. A. Coppin, and B. J. Legg. Experiments on scalar dispersion within a model plant canopy. Part 1: the turbulence structre. *Bounday-Layer Meteorology*, 35:21–52, 1986.

[121] M. R. Raupach and R. Shaw. Averaging procedures for flow within vegetation canopies. *Bounday Layer Meteorology*, 22:79–90, 1982.

[122] M. R. Raupach, A. S. Thom, and I. Edwards. A wind-tunnel study of turbulent flow close to regularly arrayed rough surfaces. *Bounday-Layer Meteorology*, 18(4):373–397, 1980.

[123] O. Reynolds. On the dynamical theory of incompressible viscous fluids and the determination of the criterion. *Philosophical Transactions of the Royal Society of London A*, 186:123–164, 1895.

[124] L. F. Richardson. *Weather prediction by numerical process*. Cambridge University Press, 1922.

[125] R. Röhrig. *Jet-stratification interaction: a computational study of containment-relevant flow configuration*. PhD thesis, Technische Universtität Darmstadt, 2017.

[126] J. C. Rotta. *Turbulente Strömungen*. Universitätsverlag Göttingen, 2010.

[127] P. Sagaut. *Large eddy simulation for incompressible flows - an introduction*. Springer-Verlag Berlin Heidelberg, 2006.

[128] P. Sagaut, S. Deck, and M. Teraccol. *Multiscale and multiresolution approaches in turbulence*. Imperial College Press, 2006.

[129] M. Schäfer. *Computational engineering - inroduction to numerical methods*. Springer-Verlag Berlin Heidelberg, 2006.

[130] H. Schlichting. Experimentelle Untersuchungen zum Rauhigkeitsproblem. *Ingenieur-Archiv*, 7(1):1–34, 1936.

[131] M. Schmitt. *Direct numerical simulations in engine-like geometries*. PhD thesis, ETH Zurich, 2014.

[132] M. P. Schultz. Effects of coating roughness and biofouling on ship resistance and powering. *Biofouling*, 23(5):331–341, 2007.

[133] M. P. Schultz and K. A. Flack. Turbulent boundary layers on a systematically varied rough wall. *Physics of Fluids*, 21:015104, 2009.

[134] J. Shin. Characteristics of surface roughness associated with leading edge ice accretion. *Journal of Aircraft*, 33(2):316–321, 1996.

[135] A. Sigal and J. Danberg. New correlation of roughness density effect on the turbulent boundary layer. *AIAA Journal*, 28(3):554–556, 1990.

[136] K. M. Singh, N. D. Sandham, and J. Williams. Numerical simulation of flow over a rough bed. *Journal of Hydraulic Engineering*, 133(4):386–398, 2007.

[137] J. Smagorinsky. General circulation experiments with the primitive equations: I. the basic experiment. *Montly Weather Review*, 91(3):99–164, 1963.

[138] P. R. Spalart, S. Deck, M. L. Shur, K. D. Squires, M. K. Strelets, and A. Travin. A new version of detached-eddy simulation, resistant to ambiguous grid densities. *Theoretical and Computational Fluid Dynamics*, 20:181–195, 2006.

[139] P. R. Spalart, W.-H. Jou, M. Strelets, and S. R. Allmaras. Comments on the feasibility of LES for wings and on the hybrid RANS/LES approach. In C. Liu and Z. Liu, editors, *Advances in DNS/LES*, pages 137–147. Greyden Press, 1997.

[140] C. Speziale. Turbulence modeling for time-dependent RANS and VLES: a review. *AIAA Journal*, 36(2):173–184, 1998.

[141] J. Spurk and N. Aksel. *Strömungslehre*. Springer-Verlag Berlin Heidelberg, 2010.

[142] M. Stripf, A. Schulz, and H.-J. Bauer. Modeling of rough-wall boundary layer transition and heat transfer on turbine airfoils. *Journal of Turbomachinery*, 130:021003, 2008.

[143] K. J. Strout, E. J. Davis, and P. Sullivan. *Atlas of machined surfaces*. Springer Netherlands, 1990.

[144] K. Suga, T. J. Craft, and H. Iacovides. An analytical wall-function for turbulent flows and heat transfer over rough walls. *International Journal of Heat and Fluid Flow*, 27:852–866, 2006.

[145] P. K. Sweby. High resolution schemes using flux limiters for hyperbolic conservation laws. *SIAM Journal on Numerical Analysis*, 21(5):995–1011, 1984.

[146] F. Tarada. Prediction of rough-wall boundary layers using a low Reynolds number k-ε model. *International Journal of Heat and Fluid Flow*, 11(4):331–345, 1990.

[147] R. P. Taylor, H. W. Coleman, and B. K. Hodge. Prediction of turbulent rough-wall skin friction using a discrete element approach. *Journal of Fluids Engineering*, 107:251–257, 1985.

[148] H. Tennekes and J. L. Lumley. *A first course in turbulence*. The MIT Press, 1972.

[149] M. Thakkar, A. Busse, and N. Sandham. Surface correlations of hydrodynamic drag for transitionally rough engineering surfaces. *Journal of Turbulence*, 18(2):138–169, 2017.

[150] M. Thakkar, A. Busse, and N. D. Sandham. Direct numerical simulation of turbulent channel flow over a surrogate for Nikuradse-type roughness. *Journal of Fluid Mechanics*, 837:R1, 2018.

[151] A. A. Townsend. *The structure of turbulent shear flow*. Cambridge University Press, 1976.

[152] M. Ullrich. *Second-moment closure modeling of turbulent bubbly flows within the two-fluid model framework*. PhD thesis, Technische Universtität Darmstadt, 2017.

[153] B. van Leer. Towards the ultimate conservative difference scheme. i: the quest of monotinicity. *Lecture notes in physics*, 18:163–168, 1973.

[154] J. A. van Rij, B. J. Belnap, and P. M. Ligrani. Analysis and experiments on three-dimensional, irregular surface roughness. *Journal of Fluids Engineering*, 124:671–677, 2002.

[155] T. von Kármán. Mechanische Ähnlichkeit und Turbulenz. *Nachrichten von der Gesellschaft der Wissenschaften zu Göttingen - Mathematisch-physikalische Klasse*, 5:58–76, 1930.

[156] J. M. Walker, K. A. Flack, E. E. Lust, M. P. Schultz, and L. Luznik. Experimental and numerical studies of blade roughness and fouling on marine current turbine performance. *Renewable Energy*, 66:257–267, 2014.

[157] T. Watanabe. Large-eddy simulation of coherent turbulence structures associated with scalar ramps over plant canopies. *Bounday-Layer Meteorology*, 112:307–341, 2004.

[158] S. Whitaker. Flow in porous media I: A theoretical derivation of Darcy's law. *Transport in Porous Media*, 1:3–25, 1986.

[159] S. Whitaker. The Forchheimer equation: a theoretical development. *Transport in Porous Media*, 25:27–61, 1996.

[160] S. Whitaker. *The method of volume averaging*. Springer Netherlands, 1999.

[161] D. C. Wilcox. Reassessment of the scale-determining equation for advanced turbulence models. *AIAA Journal*, 26:1299–1310, 1988.

[162] D. C. Wilcox. *Turbulence modeling for CFD*. DCW Industries, Inc., 2006.

[163] D. C. Wilcox. Formulation of the k-ω turbulence model revisited. *AIAA Journal*, 46(11):2823–2838, 2008.

[164] Y. Wu and K. T. Christensen. Outer-layer similarity in the presence of a practical rough-wall topography. *Physics of Fluids*, 19:085108, 2007.

[165] Z.-T. Xie, O. Coceal, and I. P. Castro. Large-eddy simulation of flows over random urban-like obstacles. *Bounday-Layer Meteorology*, 129:1–23, 2008.

[166] J. Yuan and U. Piomelli. Estimation and prediction of the roughness function on realistic surfaces. *Journal of Turbulence*, 15(6):350–365, 2014.

[167] N. Zuckerman and N. Lior. Jet impingement heat transfer: physics, correlations, and numerical modeling. *Advances in Heat Transfer*, 39:565–631, 2006.

Nomenclature

Latin letters

Lower case

Symbol	SI unit	Description
c_p	$\mathrm{m^2/(s^2\,K)}$	specific heat capacity at constant pressure
d	m	diameter
d_h	m	hydraulic diameter
d_i	m	component of vector between adjacent computational nodes
d_mh	m	mean hydraulic diameter
d_p	m	particle diameter
f	1/s	elliptic relaxation function (ζ-f model)
$f_{\mathrm{d},i}$	$\mathrm{m/s^2}$	density-specific volumetric drag force component
f_t	1/s	transformed elliptic relaxation function (ζ-f model)
h	m	height
k	$\mathrm{m^2/s^2}$	turbulent kinetic energy
k_rms	m	root mean square roughness height
k_s	m	equivalent sand roughness height
k_t	m	peak-to-valley roughness height
l	m	length
n	–	shape parameter for roughness elements
n_i	m	unit normal vector component
q	–	source term of an arbitrary quantity
q_i	K m/s	sub-scale turbulent heat flux component
q_w	$\mathrm{kg/s^3}$	heat flux at the wall
r	–	ratio of successive gradients
r	m	radial coordinate

r_i	m	position vector component
r_0	m	radius of a roughness element at $\eta = k_\mathrm{t}$
s	m	surface elevation map
t	s	time
u_η	m/s	Kolmogorov velocity scale
u_τ	m/s	wall friction velocity
x_i	m	component of cartesian coordinates
y	m	cartesian coordinate, wall distance
y_i	m	position vector component

Upper case

Symbol	SI unit	Description
A	m^2	cross-sectional area
A_p	m^2	projected frontal area in streamwise direction
B	–	log-law constant
C	–	roughness log-law constant
C_d	–	(sectional) drag coefficient
$C\,D$	$1/\mathrm{s}^2$	cross-diffusion term (ER ζ-f model)
C_f	–	skin friction coefficient
Co	–	Courant number
D	m	Diameter
E	$\mathrm{m}^3/\mathrm{s}^2$	energy spectrum function
ES	–	effective slope
F	–	shape function
F_D	$\mathrm{kg\,m/s}^2$	drag force
$F_{\mathrm{D},i}$	$\mathrm{m/s}^2$	density-specific volumetric drag force component
F_{ij}	–	component of the Forchheimer tensor
F_r	–	resolution function (VLES model)
H	m	height
H_eff	m	effective height
I_φ	–	phase indicator function
K	m^2	permeability
K_{ij}	m^2	component of the permeability tensor

$(K^{-1})_{ij}$	$1/\mathrm{m}^2$	component of the inverse of the permeability tensor
Ku	–	kurtosis
L	m	turbulent length scale
$\mathcal{L}$	m	characteristic length scale
L_{ij}	$\mathrm{m}^2/\mathrm{s}^2$	resolved stress component (dynS model)
L_{SST}	m	turbulent length scale in the SST model
L_{vK}	m	von Kármán length scale
L_x	m	length in x-direction
L_y	m	length in y-direction
L_z	m	length in z-direction
M_{ij}	$\mathrm{m}^2/\mathrm{s}^2$	modeled stress component (dynS model)
N	–	total number of cells
P	$\mathrm{kg}/(\mathrm{m\,s}^2)$	pressure
P_k	$\mathrm{m}^2/\mathrm{s}^3$	production of turbulent kinetic energy
Pr	–	Prandtl number
Pr_t	–	turbulent Prandtl number
P_{SAS}	$1/\mathrm{s}^2$	bounded SAS production term (ER ζ-f model)
P_w	m	wetted perimeter
Q	m^3/s	flow rate
Q	$1/\mathrm{s}^2$	second invariant of the velocity gradient tensor
Q_{SAS}	$1/\mathrm{s}^2$	SAS production term for the ω-equation
$Q_{\mathrm{SAS},kL}$	$\mathrm{m}^3/\mathrm{s}^3$	SAS production term for the kL-equation
Q_2	$1/\mathrm{s}^2$	SAS correction term (ER ζ-f model)
R	m	radius
Re	–	Reynolds number
Re_τ	–	friction Reynolds number
R_{ij}	$\mathrm{m}^2/\mathrm{s}^2$	component of the two-point correlation tensor
R_0	m	radius of a roughness element at $\eta = 0$
S	m^2	melt-down plane
S	$1/\mathrm{s}$	norm of the strain-rate tensor
S_f	m^2	area available to the fluid
S_{ij}	$1/\mathrm{s}$	strain-rate tensor component
Sk	–	Skewness

S_p	m^2	total frontal projected area
S_q	K/s)	source/sink term in the temperature equation
T	s	turbulent time scale
$\mathcal{U}$	m/s	characteristic velocity scale
U_d	m/s	Darcy velocity
U_i	m/s	velocity vector component
U'	1s	first spatial derivative of the velocity field according to Eq. (4.14)
U''	$1/(\mathrm{m\,s})$	second spatial derivative of the velocity field according to Eq. (4.10)
U_∞	m/s	far-field velocity magnitude
V	m^3	volume

Greek letters

Lower case

Symbol	SI unit	Description
α	$\mathrm{kg}/(\mathrm{s}^3\,\mathrm{K})$	local heat transfer coefficient
α_i	1/m	roughness factor component
β	1/m	Forchheimer coefficient
γ	–	limiter function
δ	m	boundary layer thickness
δ_ν	m	viscous length scale
δ_0	m	distance between two roughness elements
ε	$\mathrm{m}^2/\mathrm{s}^3$	dissipation rate of turbulent kinetic energy
ζ	–	measure for turbulence anisotropy (ζ-f model)
η	m	cartesian coordinate
η	m	Kolmogorov length scale
η_md	m	coordinate of the melt-down plane
φ	–	porosity
φ_h	–	porosity in the homogeneous region

κ	$1/\mathrm{m}$	wave number
κ	–	von Kármán constant
λ	–	Darcy-Weisbach friction factor
λ	$\mathrm{kg\,m/(s^3\,K)}$	thermal conductivity
ν	$\mathrm{m^2/s}$	kinematic viscosity
ν_{eff}	$\mathrm{m^2/s}$	effective viscosity
ν_{sgs}	$\mathrm{m^2/s}$	subgrid-scale eddy-viscosity
ν_{t}	$\mathrm{m^2/s}$	(sub-scale) turbulent/eddy-viscosity
$\nu_{\mathrm{t}}^{\mathrm{RANS}}$	$\mathrm{m^2/s}$	eddy-viscosity predicted by the background RANS model (VLES model)
ρ	$\mathrm{kg/m^3}$	density
τ_{ij}	$\mathrm{m^2/s^2}$	sub-scale stress tensor component
τ_{w}	$\mathrm{kg/(m\,s^2}$	wall shear stress
τ_η	s	Kolmogorov time scale
ω	$1/\mathrm{s}$	inverse turbulent time scale

Upper case

Symbol	SI unit	Description
Γ	–	diffusion coefficient of an arbitrary quantity
Δ	m	filter width or measure for the grid spacing
$\hat{\Delta}$	m	test filter width
Δt	s	time step width
Δu_τ	–	relative deviation of the wall friction velocity
Δx	m	grid spacing in x-direction
Δy	m	grid spacing in y-direction
Δz	m	grid spacing in z-direction
ΔS	$\mathrm{m^2}$	area
ΔU^+	–	roughness function
ΔV	$\mathrm{m^3}$	volume
ΔV_{f}	$\mathrm{m^3}$	partition of volume available to the fluid
$\Delta\Theta$	K	temperature difference
Θ	K	temperature

Θ_τ	K	friction temperature
Λ	–	frontal solidity
Φ	–	arbitrary quantity
Ω_{ij}	1/s	rotation-rate tensor component

Sub- and superscripts

Symbol	Description
$(\cdot)_\mathrm{b}$	bulk value
$(\cdot)_\mathrm{c}$	center or center-plane value
$(\cdot)_\mathrm{e}$	value at the easter face (compass notation)
$(\cdot)_\mathrm{max}$	maximum value
$(\cdot)_\mathrm{min}$	minimum value
$(\cdot)_\mathrm{n}$	value at the northern face (compass notation)
$(\cdot)_\mathrm{r}$	flow reattachment
$(\cdot)_\mathrm{res}$	resolved contribution
$(\cdot)_\mathrm{rms}$	root mean square
$(\cdot)_\mathrm{s}$	value at the southern face (compass notation)
$(\cdot)_\mathrm{s}$	flow separation
$(\cdot)_\mathrm{u}$	unresolved contribution
$(\cdot)_\mathrm{us}$	intermediary quantity based on unsteady flow field (VLES model)
$(\cdot)_\mathrm{w}$	wall value
$(\cdot)_\mathrm{w}$	value at the western face (compass notation)
$(\cdot)_\mathrm{E}$	value at the eastern computational node (compass notation)
$(\cdot)_\mathrm{DNS}$	value from DNS
$(\cdot)_\mathrm{N}$	value at the northern computational node (compass notation)
$(\cdot)_\mathrm{P}$	value at the computational node
$(\cdot)_\mathrm{S}$	value at the southern computational node (compass notation)
$(\cdot)_\mathrm{W}$	value at the western computational node (compass notation)
$(\cdot)^\mathrm{p}$	value at the porous-fluid interface

$(\cdot)^{\mathrm{s}}$	superficially-averaged value
$(\cdot)^{\mathrm{t}}$	value at the top wall
$(\cdot)^{\mathrm{HO}}$	higher order
$(\cdot)^{\mathrm{LO}}$	lower order

Mathematical symbols

Symbol	Description
$\mathrm{D}/\mathrm{D}t$	material derivative
$\mathcal{S}$	spatial discretization operator
δ_{ij}	Kronecker delta
ϵ_{ijk}	permutation or Levi-Civita symbol
$\overline{(\cdot)}$	time averaging
$\widetilde{(\cdot)}$	ensemble averaging or filtering operation
$\langle\cdot\rangle$	intrinsic volume averaging
$\langle\cdot\rangle^{\mathrm{s}}$	superficial volume averaging
$\langle\cdot\rangle^{\mathrm{s},xz}$	superficial volume averaging in xz-layers
ϕ'	fluctuating part of Φ with respect to time averaging
ϕ''	fluctuating part of Φ with respect to ensemble averaging or filtering
ϕ^*	spatial variation of $\overline{\Phi}$ with respect to superficial averaging
${}^{\mathrm{i}}\phi$	spatial variation of Φ with respect to intrinsic averaging

Abbreviations

Abbreviation	Description
2G-URANS	second-generation unsteady Reynolds-averaged Navier-Stokes
BDF	backward differencing formula

CDS	central differencing scheme
CFD	computational fluid dynamics
CV	control volume
DDES	delayed detached eddy simulation
DDF	distributed drag force
DES	detached eddy simulation
DNS	direct numerical simulation
dynS	dynamic Smagorinsky
ER	eddy-resolving
EVM	eddy-viscosity model
FVM	finite volume method
IBM	immersed boundary method
LES	large eddy simulation
MRST	macroscopic resiudal stress tensor
PANS	partially-averaged Navier-Stokes
PDE	partial differential equation
RANS	Reynolds-averaged Navier Stokes
REV	representative elementary volume
RSM	Reynolds stress model
SAS	scale-adpative simulation
SGDH	simple gradient diffusion hypothesis
SGS	subgrid-scale
SST	shear-stress transport
TKE	turbulent kinetic energy
TVD	total variation diminishing
UDS	upwind differencing scheme
URANS	unsteady Reynolds-averaged Navier Stokes
VAF	volume-averaged forcing
VANS	volume-averaged Navier-Stokes
VLES	very large eddy simulation

List of Figures

List of Tables